MICROSTRUCTURE AND MECHANICAL PROPERTIES

OF

Al-Si CASTING ALLOYS

A Thesis submitted to

THE VICTORIA UNIVERSITY OF MANCHESTER

in the Faculty of Science for

the degree of

DOCTOR OF PHILOSOPHY

by

QAIS SADIC HAMED

B.Sc. (Phy.), M.Sc. (Met.)

MATERIALS SCIENCE CENTRE

UNIVERSITY OF MANCHESTER

INSTITUTE OF SCIENCE AND TECHNOLOGY

JANUARY 1993

CONTENTS

DECLARATION

No portion of the work referred to in the thesis has been submitted in support of an application for another degree or qualification of this or any other University or other institute of learning.

To

my father and mother

my wife

my brothers and sisters

my son and daughter

ABOUT THE AUTHOR

The author has graduated from Physics department, Science collage, Baghdad University in 1987. He started his M.Sc in October 1988 and he got the M.Sc. degree in 1989 from Materials Science department (UMIST). From the first of April he was engaged in two years postgraduate study leading to the degree of Ph.D.

ABSTRACT

This thesis comprises of a study of the microstructures, solidification conditions and mechanical property relationships of directionally solidified, treated and untreated commercial purity LM25 and eutectic alloys. A thermal valve furnace was used to produce a specimen with low temperature gradient. A Bridgman furnace was used to generate a higher temperature gradient. Directional solidification studies with strontium modified eutectic alloys identified the influence of solidification conditions on the development of the scalloped interface and associated porosity. Temperature gradient was shown to play an important role. This undesirable aspect of strontium modification can be overcome with suitable changes to the solidification pattern. The results for the untreated, commercial purity LM25 casting alloys show that secondary dendrite arm spacing can be described by the equation;

$$\lambda_f = 10.27 \pm 0.55 t_f^{0.30 \pm 0.01}$$

where t_f is the total solidification time. (λ, μm – t, sec)

Specimens quenched during solidification are used to follow the coarsening of secondary dendrite arms during solidification. It is shown that coarsening behaviour can be represented adequately by an average coarsening parameter, M, in the equation;

$$\lambda = [\lambda_o^3 + B.\bar{M}.t]^{0.33}$$

Factors influencing the value of λ_o are defined and its influence on the coarsening behaviour is described. The addition of TiBAL, Sr, Sb into the LM25 alloys refined the dendrite arm spacing and is associated with reduction in the primary tip temperature and average coarsening parameter. The mechanical property studies of the LM25 alloys show that 60% of strength is due to the Al-primary phase. Also it was found that the addition of 0.04%Sr enhanced the strength and the ductility of the alloys, but that overmodification has the opposite effect. The addition of Sb improves the mechanical properties of the LM25 alloys. The UTS-DAS has a Hall-Petch type relationship but the hardness and proof stress does not.

ACKNOWLEDGEMENTS

This research was conducted under the supervision of Dr. R. Elliott. Senior Lecturer, Materials Science Centre, University of Manchester. I would like to express my sincere appreciation to Dr. R. Elliott for his great help during the course of this research.

I would like to express my appreciation to the head of the department and to all members of the department of Metallurgy and Material Science, staff and students.

I would like to thank the Ministry of Higher Education in Iraq for financial support for the first year of the course, and to the London and Scandinavian Metallurgical Co.Ltd, for their support to this project.

The author also wishes to thank his friends and colleagues, specially Mr. Ali Ourdjini for his assistance during the work.

CHAPTER ONE

GENERAL INTRODUCTION

CHAPTER ONE

GENERAL INTRODUCTION

Solidification is a phase transformation which is important because of its major practical application, that of casting. Casting is a very economic method of forming a component. Cast metal products can be produced economically from alloys having melting points as high as 1660 ^{0}C.

Al-Si alloys are widely used in applications where good strength and light weight are required or where corrosion resistance or castability are desired. If high strength is needed, magnesium addition make these alloys heat treatable. Also the strength and ductility for these Al-Si alloys can be improved by modification of the eutectic phase. The modification of Al-Si alloys can be achieved by rapid solidification or, more usually, by the addition of a third component such as sodium, strontium or some alkali and alkaline earth metals and elements of group VB of the periodic table. If the modification is achieved, the flake changes to a fine fibrous structure; these fibres appear to be small individual particles on a conventionally polished surface.

A knowledge of the triangular relationship between microstructure, properties and solidification parameters is essential for realization of the outstanding properties of Al-Si casting alloys.

LM25 alloy is a hypoeutectic Al-Si alloy containing about 7%Si-0.3%Mg with miner elements such Mn, Fe, Ti and Zn. This alloy has been used to produce aircraft pump parts, automotive transmission cases, aircraft fittings and control parts, water-cooled cylinder blocks and also used in other application where excellent castability and good weldability, pressure tightness and good resistance to corrosion are required.

The primary Al phase dendritic network in these alloys contributes to their strength by providing barriers to the propagation of cracks through the matrix. Several studies have shown that this leads to a relationship between spacing (DAS) and tensile properties. To utilize this relationship in practice requires a knowledge of the relationship between DAS and the solidification conditions.

In the present work the relationship between the solidification conditions and modification behaviour of the eutectic Al-Si alloy has been examined in the first part of this project. Then in the second part the relationship between the solidification time and secondary dendrite arm spacing has been established for untreated and treated LM25 alloys. In the last part mechanical property measurements have been presented for different alloys.

CHAPTER TWO

LITERATURE REVIEW

SECTION I

2-1-1 PRINCIPLES OF EUTECTIC SOLIDIFICATION.

There is an alloy of specific composition that melts at a lower temperature than other compositions in many binary systems. The alloy of this composition is called eutectic (see Figure 2.1.1). The system of three phases and two components has one degree of freedom, and at constant pressure, the three phases can co-exist at only one temperature and their composition is fixed according to Gibb s phase rule. So, an invariant equilibrium is established in the binary system at the eutectic isotherm, the end of which coincides with the terminal solid solutions forming at the two ends of the phase diagram, with liquid phase having an intermediate composition. Below the eutectic temperature the equilibrium is non-variant between the two solid phases since the liquid has disappeared. The liquid phase will change into two different solids, when the cooling takes place through the eutectic isotherm.

$$L \rightarrow \alpha + \beta \qquad (2\text{-}1)$$

where L is the liquid phase and α & β are the two solid phase. The reverse reaction will take place isothermally on heating the eutectic. The eutectic solidification starts with nucleation followed by growth. Usually the first phase nucleates heterogeneously in the liquid, then the second phase nucleates adjacent to the first phase but not necessarily epitaxially showing a preferred orientation relationship between the phases.[1] The structural features develop during growth when both phases have nucleated in the liquid. They will grow cooperatively at roughly equal rates or at different rates and growth is controlled by the rate of heat extraction, the composition of alloy, growth rate and temperature gradient. Although the nucleation event may have an influence on the eutectic structure, it is generally accepted that the growth process has a greater influence.

2-1-2 THE CLASSIFICATION OF BINARY EUTECTICS.

In the past many attempts have made to classify eutectic systems.[2-6] These early classifications were based on either limited evidence from the solidification process or in terms of single features of the solidification process. Hunt and Jackson[7] followed the earlier work of Jackson[8] who explained the structure of the solid-liquid interface in terms of the parameter α. When these considerations are applied to the binary eutectic they suggest three possible configurations.

I Eutectic in which both phases grow in a non-faceting manner.

II One phase grows in a faceted manner, the second phase in a non-faceted manner.

III Both phases grow faceted.

Facets form when there is an energy barrier for the addition of a new solid layer on an existing solid. Croker's[9-12] suggested an entropy of solution value of the order of 23 J mol^{-1} K^{-1} to indicate faceting behaviour and, on this basis the eutectic microstructure is classified into two groups; one is normal, the second is anomalous. If one phase has an entropy of solution > 23 J mol^{-1} K^{-1} an anomalous eutectic structure will result, but if it is less than that value normal structures are obtained. Figures 2.1.2 and 2.1.3 illustrate the main feature of this classification and represent a section taken through the three dimensional model constructed by Croker. The main eutectic structures forming under these conditions (some of them are shown in the above figures) are summarized[12] as follows.

I. Normal structures:-

1. Lamellar: An arrangement of plates which is regular over a large distance but usually containing intersecting faults.

2. Rod: Similar to a lamellar structure but the rods may be polygonal in cross section.

II. Anomalous structures:-

1. Irregular: The spatial arrangements such as isolated unbranched and branched are not regular over large distances.

2. Broken lamellar: A near regular array of broken plates.

3. Fibrous: An array of interconnected fibres of low aspect ratio which may sometimes display microfacets.

4. Complex regular: An array of fibres or plates which are regular over small areas.

5. Chinese script: An array of discrete, finely-branched sheets of the faceting minor phase in the non-faceting matrix phase.

6. Quasi-regular: An array of sheets and or fibres of the non-faceting minor phase in the matrix of a faceting phase.

2-1-3 THE Al-Si EUTECTIC ALLOYS.

The Al-Si system is non-faceted/faceted and the unmodified eutectic microstructure is " irregular". This Al-Si eutectic has α of less than 1 and approximately 5 for the aluminum and silicon phases, respectively and is a typical anomalous eutectic. The phase diagram for this alloy is shown in Figure 2.1.4. This system is comprised of f.c.c. metal Al and a diamond cubic metalloid Si. No stable intermetallic phases are formed and solid solubility is limited, 1.65%Si in aluminum at the eutectic temperature and less than 0.01%Al in silicon.

At 550 ^{0}C the solid solubility of silicon in aluminum decreases to 1.3%wt and to 0.8 at 300 ^{0}C. The eutectic point was put at 11.7%Si at 577 ^{0}C according to the earlier studies but the currently accepted values for the eutectic points are 12.7%Si and at 577 ^{0}C[13] while another study suggests the eutectic temperature is 577.2 ^{0}C. The average liquidus slope for aluminum and silicon are;

$$\text{aluminum} = 6.54\ ^0\text{C/wt.\%}$$

$$\text{silicon} = 9.5\ ^0\text{C/wt.\%}$$

The system is commercially important because of its structural modification. The modification produces improved mechanical properties and Al-Si based alloys are used widely in the motorcar industry.

A typical micrograph of untreated eutectic alloy is shown in Figure 2.1.5. The microstructure is seen to consist of irregular flakes of the silicon phase dispersed in an aluminum matrix. Being an anomalous eutectic, the microstructure of aluminum-silicon alloys is sensitive to both growth velocity and composition. Day and Hellawell[14,15] presented the various microstructures in Al-Si alloy in terms of alloy composition, growth rate and temperature gradient. Three particular structural regions with distinct silicon morphologies were determined.

Region A:	Large particles of silicon at a planar aluminium front growing with a relatively long range diffusion process.
Region B:	The silicon particles grow at a short range diffusion front with a < 100 > preferred growth direction.
Region C:	Silicon particles grow by a short range diffusion process with multiple twins.

Figure 2.1.6 summarizes these findings and emphasizes the fact that the growth mechanism of the faceting phase plays a vital role in determining the Al-Si structures. It can be seen that in region (A) the temperature gradient is high and the growth rate is low enough for the two eutectic phases to grow independently at a planar interface by a long range diffusion process. Large particles of silicon are formed as result of a high G/V ratio.

In region (B) the instability of the planar interface of the Al phase appears. The conditions lead to cooperative or semicoupled growth between the 'Al and Si phases by a short range diffusion process. In region (C) the microstructure is predominately a flake Si structure as shown in Figure 2.1.5. Additional morphologies have been charted for this system as a function of freezing rate and imposed temperature gradient. Steen and Hellawell[16] indicated region D in which they found interconnected fibres.

2-1-4 THE MODIFICATION OF THE Al-Si ALLOYS.

There have been several suggestions as to how modification takes place with impurity additions (Na/Sr) based on changes in the phase diagram, differential nucleation and changes in the growth kinetics of the silicon phase. The experimental observations reported that;[17,18]

1. The impurity (Na/Sr) is partly soluble in the liquid and the form of the ternary phase diagram influences modification.
2. The impurity depresses nucleation so the growth of the eutectic and primary silicon begin at a lower temperature.
3. The fibres modified by impurity are heavily twinned and are microfaceted.
4. Sodium activity in an aluminium melt is sharply reduced by the addition of silicon.[19] Also the observation shows that Na is associated with the silicon phase and not with the Al matrix.[20]
5. Impurity modifies the actual growth process, quite distinct from the effect on nucleation either by, (I) surface adsorption which may poison the growth mechanism of the silicon, (II) by changing the solid-solid or solid-liquid interfacial energy and consequently changing the solid-liquid profile, (III) by changing the liquid diffusion to depress the reaction rate.[17]

The theories that have been proposed so far have been categorized into three types by Fredrikson et al.[21]

A) Theories based on Al-Si-(Na/Sr) phase diagram.

B) Theories based on the nucleation behaviour.

C) Theories based on the growth behaviour.

The theories based on the phase diagram suggested that the binary Al-Na monotectic, which occurs at a concentration level of 0.014% Na and about 1 degree below the freezing point of the eutectic Al-Si alloy,[22] and a ternary Al-Si-Sr eutectic, which is occurs at a concentration of 1.8% Sr at 2 to 3 degrees below the eutectic Al-Si alloy,[23] are responsible for the modification. A complete modification in the case of addition of Na occurs at 0.014%Na in the binary Al-Na system whereas with the Sr addition modification can be produced at concentrations far below the ternary eutectic point.[24,25] Evidence is not available to show that these observations are related to the modification problem.

The theories based on the nucleation behaviour were based on the misinterpretation of metallographic information which led to the belief that Si occurred as isolated particles in the modified alloys. Such information was interpreted so as to involve repeated nucleation of the Si phase. This idea first came from the fact that the action of sodium lay in the poisoning the alumina and silica which were assumed as the operative heterogeneous sites in unmodified alloys. The existence of the unmodified structure in high purity alloys and again the existence of the modified structure at high freezing rate without any addition cannot be explained on this basis. Many authors[14,25-32] pointed out that the impurity modification of the Al-Si alloys is due to the change in the growth behaviour.

2-1-6 GROWTH MECHANISM OF SILICON PHASE IN THE Al-Si EUTECTIC ALLOY.

2-1-6-1 UNMODIFIED EUTECTIC SILICON.

Nucleation sites which produce interconnected flakes are separated by at least an order of magnitude greater than the mean interflake spacing . The eutectic growth is dominated by {111} faceting of the Si phase at lower growth rates, the Si phase growing ahead of the Al phase with a non-isothermal front. Such flakes have the {111} habit and

are generally twinned on a few {111} planes parallel to the plane of the flake.[33] These twins intersect the interface creating re-entrant edges and grooves on the growing edge of the flake as shown in Figure 2.1.7. Shu-Zu-Lu et al.[34] have reported that twin spacing is larger than the estimated distance between intrinsic steps and hence it needs to be resolved as to whether atomic attachment occurs at intrinsic steps or is initiated at the twin plane re-entrant angles. The kinetic undercooling for intrinsic growth by the T.P.R.E. mechanism is shown in Figure 2.1.8.

2-1-6-2 IMPURITY MODIFIED EUTECTIC SILICON.

Investigations[34-36] have established that fibres formed in impurity modified alloys are microfaceted to various degrees. This effect is due to heavy twinning on up to four {111} systems. The twin spacing is much smaller than the estimate of the distance between intrinsic steps. Therefore it is concluded[34] that the T.P.R.E. mechanism for kinetic attachment plays a vital role in the growth process, whereas the intrinsic steps are not very important. The high incidence of twinning at growth rates and undercoolings at which a flake morphology occurs in an unmodified alloy must imply that growth on intrinsic steps has been effectively poisoned by impurity absorption at the solid-liquid interface making such a growth process least preferable. The alternative growth process will be by the T.P.R.E. mechanism.

The kinetic undercooling rises to a level where twinning occurs frequently (see Figure 2.1.8). The modified element is incorporated preferentially into the Si-phase to an extent that depends on the growth velocity and the nature of the Al-modifier phase diagram.[37] Shu-Zu-Lu et al.[18-38] have shown the size factor requirement for modification (the ratio of the atomic radius of the modifier/atomic radius of Si should be greater than 1.65). The interface undercooling is greater for fibrous growth than that required for flake growth at a particular growth velocity.

2-1-7 THE SOLIDIFICATION OF BINARY Al-Si ALLOYS.

2-1-7-1 THE RELATIONSHIP BETWEEN THE SECONDARY DENDRITE ARM SPACING AND SOLIDIFICATION TIME.

Our understanding of the solidification of the dendrite network is well advanced and can be traced back to the pioneering work of Flemings.[39] There are two stages in the solidification process. A dendrite skeleton of primary and secondary arms forms initially. The scale of this structure depends on the solidification process. A dendrite skeleton of primary and secondary arms forms initially. Not all of the arms formed on the initial skeleton grow. During the second stage of the solidification process larger arms tend to grow at the expense of smaller arms. This "dendrite coarsening" stage is driven by surface energy and coarsening kinetics can be of overriding importance in determining the final dendrite arm spacing. Most kinetic studies have focused on Al-Cu alloys for which it has been established that the final secondary dendrite arm spacing, λ_f, is related to solidification time, t_f, by the equation,

$$\lambda_f = K_1 * t_f^n \qquad (2\text{-}2)$$

where K_1 is 10 $\mu m/s^n$ and n is 0.33. The solidification time is the time required for the casting to cool from the solidification temperature to the solidus temperature at a given location. It is inversely proportional to the average cooling rate. Several microstructural models have been proposed for the coarsening process but the kinetics depend on two factors irrespective of the model. The first factor is that the liquid composition in equilibrium with a solid surface depends on the surface curvature. The difference in liquid composition from that in equilibrium with a planar interface is proportional to the curvature. Consequently, local liquid composition differences increase approximately with the inverse of the DAS. Hence,

$$\Delta C \propto \lambda^{-1} \tag{2-3}$$

where ΔC is the mean composition difference over the distance λ. The second consideration relates to the diffusion of solute from the smaller to larger arms that promotes the growth of the latter.

The rate of growth depends on the solute gradient, $\Delta C_L / \lambda$. Hence,

$$\frac{d\lambda}{dt} \propto \frac{\Delta C_L}{\lambda} \tag{2-4}$$

Combining the equation (2-3) and (2-4) and integrating from an initial spacing of λ_o gives an equation of the form,

$$\lambda_f^3 - \lambda_o^3 = K_2 * t_f \tag{2-5}$$

where t_f is the total solidification time.

The precise form of this equation depends on the model assumed and the mathematical simplifications made.

2-1-8 THE EFFECT OF TEMPERATURE GRADIENT AND PRIMARY ARM TIP VELOCITY ON SECONDARY DENDRITE ARM SPACING.

As it is well known, the secondary dendrite arm spacing λ changes during solidification. This fact can be explained by dendrite arm coarsening[40-44]. There is a driving force for coarsening which is inversely proportional to the dendrite arm spacing λ. Since the diffusion distance increases proportionally to λ, the coarsening rate is inversely proportional to λ^2. Therefore, λ varies with time according to;[45,46]

$$\lambda^3=\lambda_0{}^3+\int_0^t BM[T(t)]dt \qquad (2\text{-}6)$$

where

$$M[T(t)]=\frac{D_L(T)T\sigma}{m(T)[1-k(T)]\Delta H\rho C_L^*(T)} \qquad (2\text{-}7)$$

where B is a numerical constant of the order of 33 related to the particular geometry of the dendrites. Table 2.1.1 shows the other symbols.

The M(T(t)) function is so complicated that it is impossible to integrate the equation in a closed form. However, if the functions $D_L(T)$, $m_L(T)$, k(T), C_L^* and T(t) are known, the integration of equation (2-1) will be easy to solve. For this purpose, equation (2-6) can be written with finite differences of time.

$$\lambda^3=\lambda_0{}^3+\sum_{j=1}^{l} BM[T_j(t_j)]\Delta t_j \qquad (2\text{-}8)$$

The effect of G_L and V are examined mostly under steady state conditions of solidification. Idealised T(x) and T(t) functions are plotted in Figure 2.1.9 for steady state condition solidification. Through the mushy zone, the temperature gradient in the liquid phase is;

$$G_L=\frac{T_L-T_S}{X_m}=\frac{T_L-T_i}{X_i} \qquad (2\text{-}9)$$

The primary tip velocity is;

$$V=\frac{X_m}{t_f}=\frac{X_i}{t_i} \qquad (2\text{-}10)$$

Using equation (2-9) and (2-10), t_i, Δt_i, X_i can be calculated as described belc

$$t_i=\frac{T_L-T_i}{G_L V} \tag{2-11}$$

$$\Delta t_i=\frac{T_{i-1}-T_i}{G_L V} \tag{2-12}$$

$$X_i=\frac{T_L-T_i}{G_L} \tag{2-13}$$

By using the average coarsening parameter the final dendrite arm spacing can be calculated;

$$\lambda_f=(\lambda_o^3+B\bar{M}t_f)^{\frac{1}{3}} \tag{2-14}$$

or if $\lambda = 0$

$$\lambda_f=(B\bar{M}t_f)^{\frac{1}{3}} \tag{2-15}$$

where

$$\bar{M}=\frac{1}{t_f}\sum_{i=1}^{n} M(T_i)t_i \tag{2-16}$$

M at a given C_o depends very little on C_L and V. Therefore, a plot of $\log\lambda_f$ as a function of $\log t_f$ becomes a straight line for all G_L and V with a slope of 0.33. The final solidification time t_f can be expressed with V and G_L or X_m;

$$t_f=\frac{T_L-T_s}{G_l V} \tag{2-17}$$

$$t_f=\frac{X_m}{V} \tag{2-18}$$

and then;

$$\lambda_f=[B\bar{M}\frac{T_L-T_s}{G_L V}]^{\frac{1}{3}} \qquad (2\text{-}19)$$

$$\lambda_f=[B\bar{M}\frac{X_m}{V}]^{\frac{1}{3}} \qquad (2\text{-}20)$$

Therefore the final dendrite arm spacing can be calculated if the parameters in the equation (2-20) are known.

TABLE 2.1.1. System parameters used in the numerical calculations.

σ	surface energy	λ	Secondary dendrite arm spacing
ρ	density	λ_o	Initial secondary dendrite arm spacing
ΔH	latent heat of solidification	λ_f	Final secondary dendrite arm spacing
m_L	liquidus slope	M	Coarsening parameter
k	partition coefficient	T	Temperature
B	geometric factor	T_s	Solidus temperature
C_o	average concentration of alloy	t	Time
C_E	eutectic composition	t_f	Local solidification time
T_L	liquidus temperature	t_i	Time at the end of the i-th step
T_E	eutectic temperature	t_i	i-th time interval
D_L	diffusion coefficient	X	Distance behind the primary arm tips
X_m	Width of the mushy zone	G_L	Temperature gradient in liquid phase
V	Primary growth velocity	C^*_L	Concentration in liquid phase at solid/liquid interface

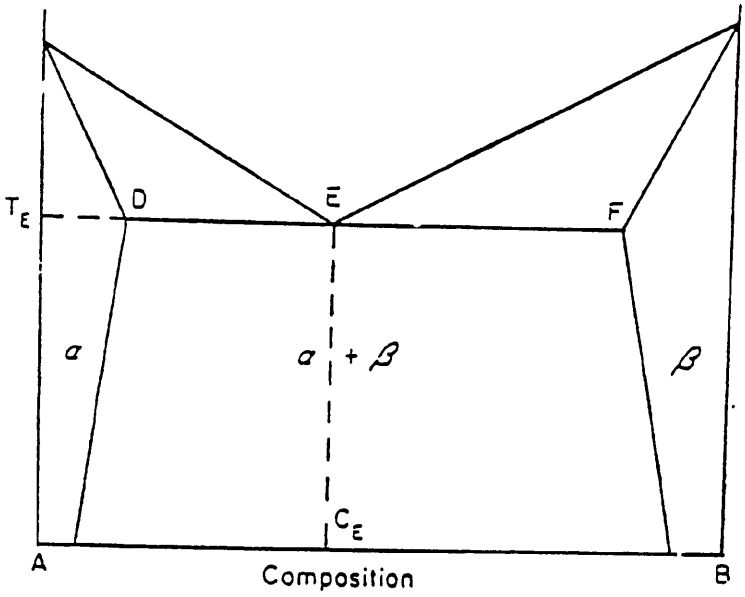

Figure.2.1.1 Typical eutectic type of phase diagram.

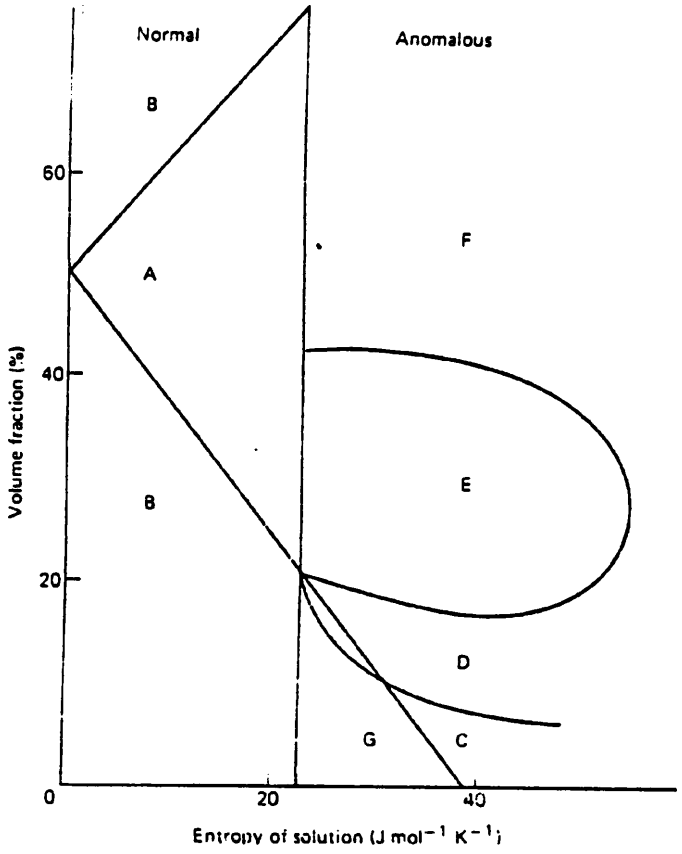

Figure.2.1.2 Classification of eutectic microstructure in terms of volume fraction and entropy of solution for a growth velocity 5 μm sec^{-1}. A) Normal Lamellar; B) Normal rod; C) Anomalous broken lamellar; D) Anomalous irregular flake; E) Anomalous complex regular; F; Anomalous quasi-regular; G; Anomalous fibrous structure.[9]

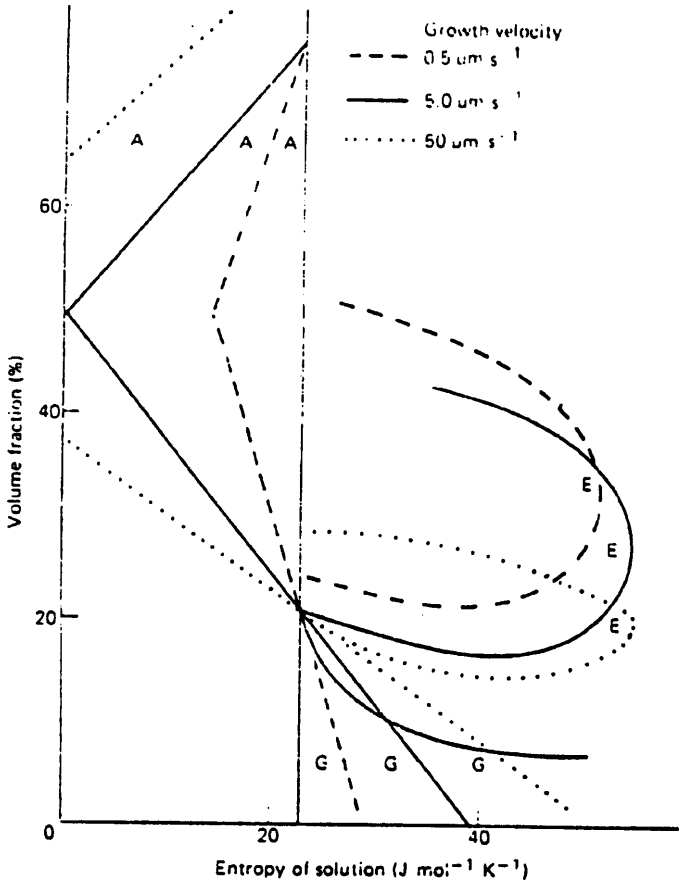

Figure.2.1.3 Effect of growth velocity on the classification in Figure 2.1.2.[9]

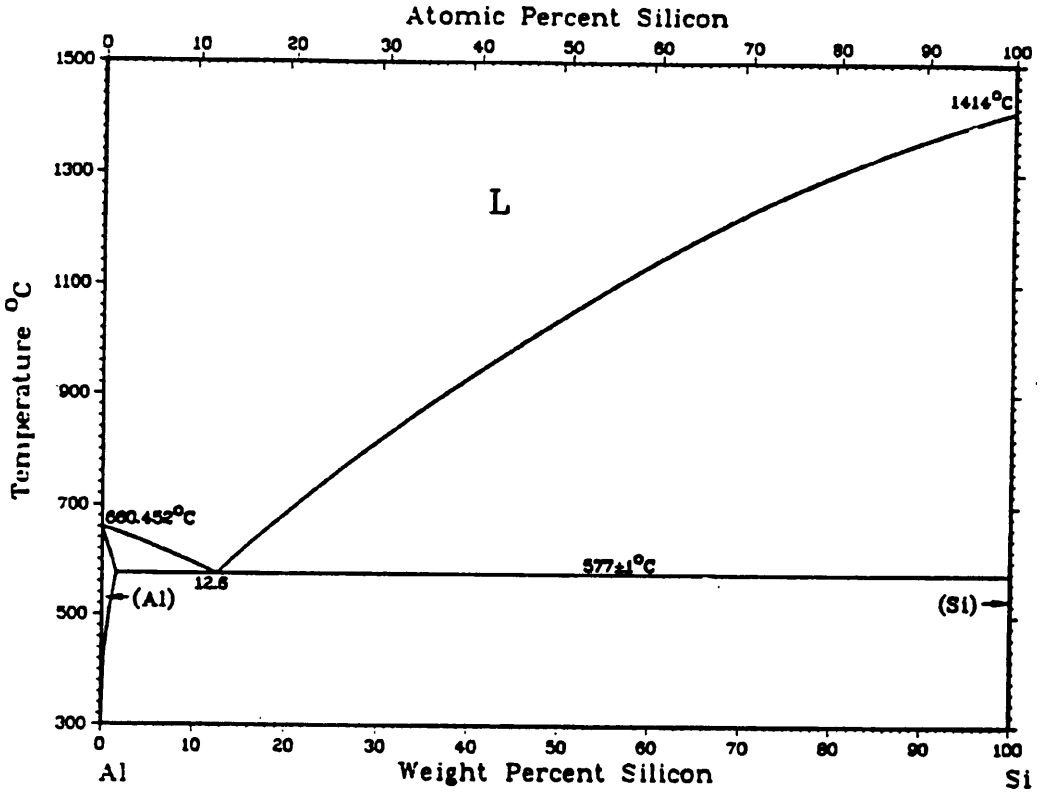

Figure.2.1.4 The phase diagram of the Al-Si eutectic system.

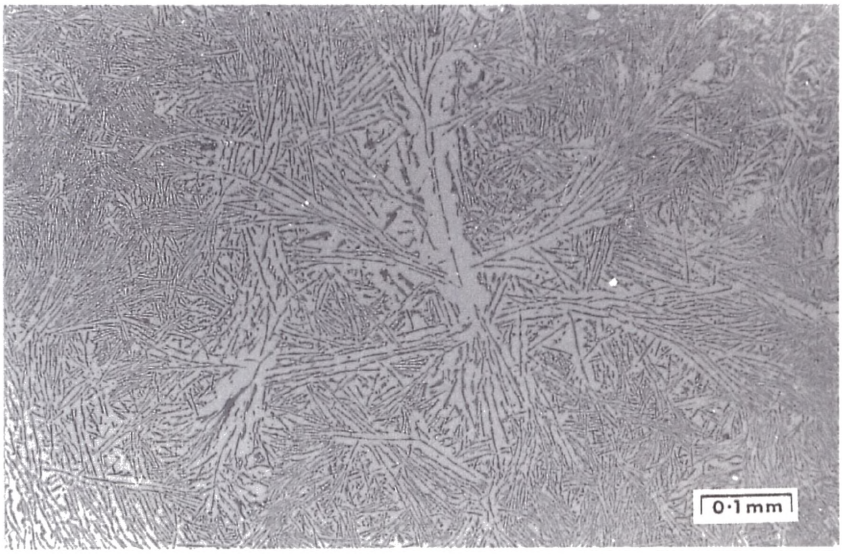

Figure.2.1.5 Micrograph of the aluminium-silicon eutectic showing the flake structure.

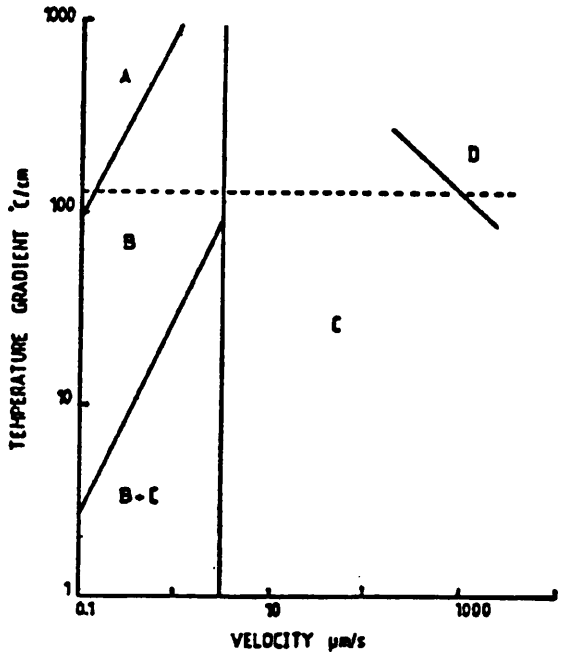

Figure.2.1.6 Microstructure of directionally solidified Al-Si eutectic alloys; Region A - separate growth; region, B - [100] Si structures; region, C - [111] flake Si structure; region, D - fibrous Si structure.[14]

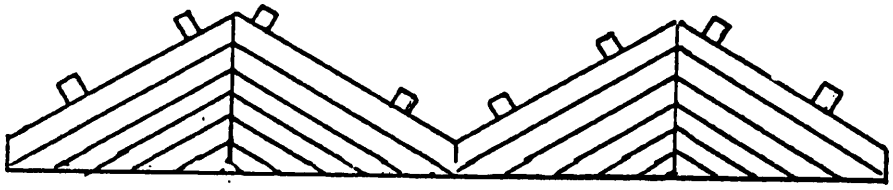

Flake Si

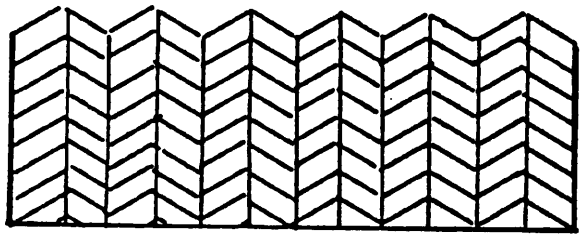

Impurity Modified Si

Figure.2.1.7 Schematic representation of Si phase growth mechanism.

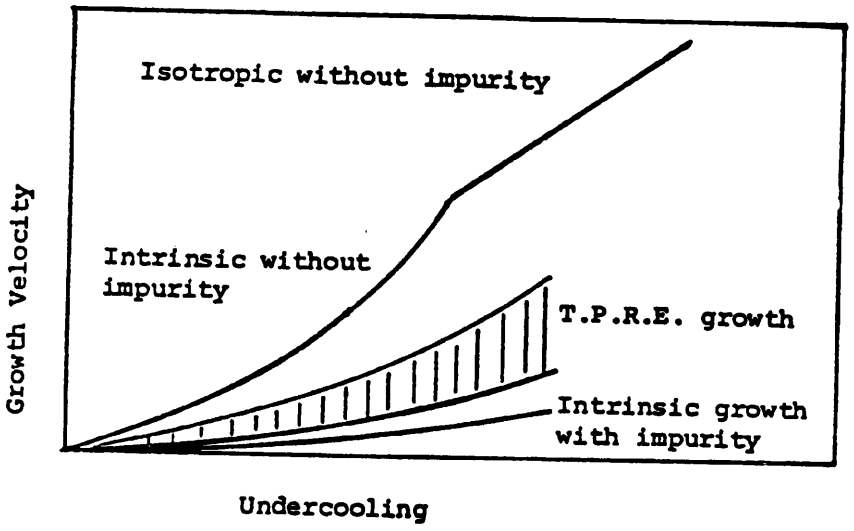

Figure.2.1.8 Kinetic undercooling relationships for different Si phase growth modes.[34]

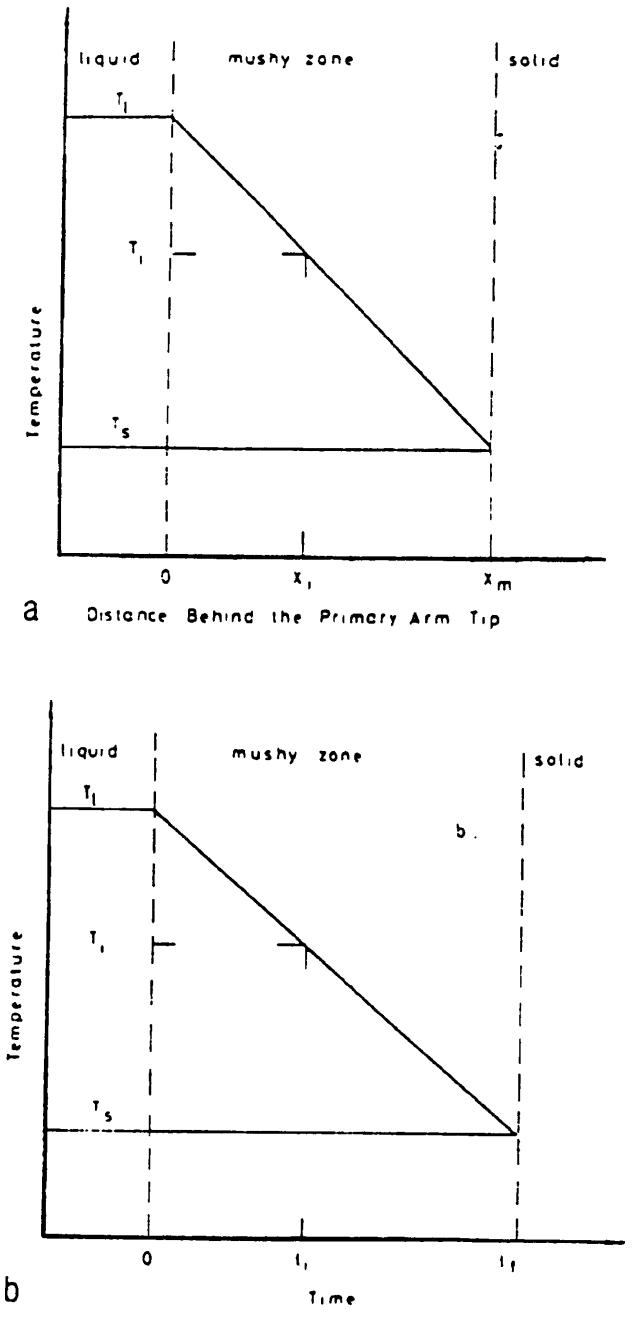

Figure.2.1.9. a) The temperature distribution as a function of distance behind the primary arm tips,

b) as a function of time during steady state conditions solidification.[46]

SECTION TWO

2-2 THE TRIANGULAR RELATIONSHIP

In foundry practice there is a need for a deeper understanding of the relationship between the processing parameters such as alloy composition, casting process, solidification conditions, metal quality, mould filling conditions, etc, and the properties of the castings. However, such a detailed understanding will only become possible if the relationships between the process parameters and the microstructure and the mechanical properties are taken into consideration. Therefore, for completeness, a study of the relationship between the production parameters and the mechanical properties should be included in a study of triangular relationship, which below is shown;

PRODUCTION PARAMETERS	PROPERTIES
Solidification conditions	Mechanical properties
Melt quality	Tensile properties
Alloy composition	Fracture toughness
Melt treatment	Fatigue properties
Casting process	
Mould filling conditions	
Heat treatment	

MICROSTRUCTURE

Qualitative description of microconstituents

Quantitative description of microstructure

2-2-1 MELT COMPOSITION

The control of the melt composition is a very important factor in the improvement of mechanical and physical properties of Al-Si alloys. The chemical composition of the melt prior to casting is determined primarily by the purity of charge materials. There are several specifications which differ only slightly in composition, see Table 2.2.1.[47] This emphasises the importance of alloy composition particularly the minor elements; slight differences in their content result in significant differences in microstructure which, in turn, result in differences in mechanical properties. Therefore, it's important to study each of the effect of these elements, how they operate and how they effect the mechanical properties.

2-2-1-1 SILICON.

Al-Si alloys are essentially composite materials consisting of hard and discontinuous particles and fibres (Si) embedded in a ductile matrix. The strength values of the hard second phase and the soft matrix are of the order of 1520 N mm^{-2} and 546 N mm^{-2}, respectively[48]. Both ultimate tensile strength and yield strength increase with Si additions of up to about 7%, while the ductility decreases[49]. At Si concentrations greater than 7%, the rate of increase in strength properties decreases significantly. Tsukude[50] et al showed that the elongation and charpy impact values of Al-Si-0.15%Sb alloys decrease rapidly at Si contents greater than about 6 to 8%.

The mechanical properties of the cast component are determined largely by the shape and distribution of Si particles in the matrix. Depending on the growth conditions the Si can adopt a variety of morphologies and this is significant with respect to the mechanical properties[51-53]. At low cooling rates (low growth velocity) Si forms coarse, acicular flakes. A flake-fibre transition occurs with growth velocities exceeding 500 $\mu m\ sec^{-1}$. The fibrous form minimizes stress concentration effects and, in addition to

improving strength, also improves ductility appreciably[54]. Usually permanent moulded castings rely on this chill modification process to modify the eutectic Si structure. However, the modification process can be achieved at all cooling rates by impurity modification. This is achieved by addition of Na or Sr. The amount of Na or Sr required for optimum structural modification falls in a narrow band defined by the type of modifier and the concentration of any elements present that poison the effect. Approximately 0.005 to 0.01%Na and 0.01 to 0.02%Sr achieve modification. There are handling difficulties with Na which is leading to the increased use of Sr. Sr concentration above 0.015% can lead to a coarsening of Si particles. A refinement of the flake structure is achieved by addition of Sb. This is favoured in some foundries because Sb improves the castability considerably.

Al-Si casting alloys are usually heat treated for long times for solutionizing and changing the Si particle morphology from flake to spheroidize Si through thermal modification processes. Plate-like particles in unmodified alloys are resistant to shape perturbations and spheroidize very slowly. Spheroidization occurs rapidly in Sr modified alloys and, consequently, chemical modification can be used effectively to reduce solution treatment times and overall heat treatment costs[48].

Vorren et al.[56] plotted the secondary dendrite arm spacing for Al-7%Si, Al-10%Si and Al-12%Si, as function of solidification time and local solidification rate by using his results and the equation presented by Feurer and Wunderlin[57], as shown in Figure 2.2.1. They reached a conclusion which indicates that the silicon content has a strong influence on the secondary dendrite arm spacing in permanent mould castings. Dendrite arm spacing close to the surface is smaller and less sensitive to thickness for Al-12%Si than for Al-7%Si. This is due to the smaller freezing range.

2-2-1-2 MAGNESIUM

Magnesium is introduced to aluminium-silicon alloys in order to increase the tensile strength of the alloy. The most popular of the Al-Si alloys containing Mg are A356 [LM25 (Al-7%Si-0.3%Mg)] and A357 with a higher Mg level (0.5%). These two alloys are heat treatable due to Mg_2Si (Magnesium Silicide) hardening. The hard particles of Mg_2Si are precipitated uniformly throughout the aluminium matrix after solution treatment followed directly by quenching and aging. The hardening effect, however, is useful only to approximately 0.7%Mg, beyond which point no further strengthening in the aluminium matrix takes place and the loss of ductility is even more pronounced[58].

A confusion exists in the literature about the exact effect of Mg on the eutectic microstructure. Gruzleski and co-workers[59] found that in commercial alloys with higher Mg contents (A357), the eutectic phase is somewhat finer than in alloys with lower Mg level (A356). On the other hand, Bercovici[60] has reported that Mg coarsens the eutectic microstructure for the same alloys. Recently Joenoes[61] and Gruzleski have reported that by introducing a small amount of Mg (0.13%) the eutectic temperature is decreased. A further increase of the Mg content results in a lowering of the eutectic temperature and a noticeable increase in the undercooling and they concluded that Mg neither clearly refines nor clearly coarsens the eutectic, but definitely reduces the degree of homogeneity of the microstructure. Furthermore, Mg has a negative effect on Strontium modification, such that its presence changes the microstructure from a fully modified to a partially modified one.

Dasgupta et al.[62] have studied the effect of the Mg content on the mechanical properties of A319 (6-6.5%Si, 3.7%Cu, 0.07-0.5%Mg) and they reached a conclusion that the increase in Mg content has a negligible effect on the mechanical properties of this alloy. Furthermore, no significant microstructure changes occur with increasing Mg

concentration. Murali et al.[63] mentioned that at lower Fe content in A356, a rise in Mg content from 0.32 to 0.65% increases hardness and strength, while ductility is decreased. Baily[64] has investigated the effects of Mg on the properties of A356-T6 alloys. Higher strengths were obtained with increasing Mg content and depending on cooling rate, the elongation showed a corresponding decrease. Granger and co-workers[65] pointed out that in A356 alloys, a 0.01% increase in Mg results in an increase of yield strength of about 6.9 N mm^{-2}. In A357 alloys, the increase is only half as much, see Figure 2.2.2. Recently Jaquet et al.[66] reported that the level of the yield strength is determined by the combined contribution of the yield strength of pure aluminium, the solid-solution hardening by the Mg and the other elements in the solution in the matrix.

2-2-1-3 IRON

In aluminum of commercial purity, there are a number of naturally occurring impurities which can be removed at great cost. Iron is probably the most important of these elements because it forms intermetallic compounds which seriously impair the ductility of the alloy. Although several different iron-rich particles form in aluminum-silicon alloys, the reduced ductility and toughness are usually associated with the formation of the plate-shaped $FeSiAl_5$ particles often referred to as the β phase[49].

Gustafsson et al. presented their[67] and previous[68-70] results for the structure and composition of experimentally observed intermetallic phases (β, α, π) in A356 alloy, their composition is recorded in Table 2.2.2. Both β and π phases are present in the as cast condition of the alloys. The β phase ($FeSiAl_5$) formed as large platelets (see figure 2.2.3) and π phase often nucleated on the platelets. The α phase generally has a dendritic morphology which appears as 𝒦 chinese script 𝒦; this phase formed (instead of β phase particles) as result of the addition of Cr during solidification. They also presented size measurements made on α and β phases. As shown in Figure 2.2.4 the mean measured

particle lengths varied significantly with solidification rate. It can be seen that the particle length is also dependent upon the Fe and Cr content of the alloys, it is increased with decreasing solidification rate and increasing Fe content. For equivalent Fe contents the mean particle lengths for α and β were similar, but the standard deviation of the measurement was considerably greater for β.

Vorren et al.[56] have measured the maximum length of β phase as a function of secondary dendrite arm spacing and iron content for a Al-7%Si-0.3%Mg alloy as shown in Figure 2.2.5. At constant Fe content, there is a critical value of DAS or cooling rate at which there is a marked change in slope. This change indicates a variation in the formation mechanism or growth rate of β plate. It is evident that this transition depends on the iron content. The T6 heat treatment[67] results in the dissolution of this phase and the uniform fine scale precipitation of β' (Mg_2 Si) in both dendrite and eutectic Al.

The effect of Fe on the mechanical properties of Al-Si alloys has been studied by many authors[71-81]. Bonsack[71] says that Fe is probably the most undesirable impurity in binary Al-Si alloys. With Fe contents over 0.5% Al-Fe silicide is present as large needles which, up to about 0.8%Fe, increase strength and hardness but slightly reduce ductility. Above 0.8%Fe, the strength and elongation drop rapidly.

Grand[72] studied the influence of Fe on Al-Si and Al-Si-Cu alloys test bars cast in sand and in shell moulds. His results show that increasing Fe from 0.5 to 1.2 in Al-13%Si alloy dramatically reduces the mechanical properties, particularly the elongation. However, an increase from 0.17 to 0.6%Fe in Al-7%Si-Mg alloys has no effect on the tensile strength but markedly reduces elongation.

At room temperature Badia[73] found that the tensile strength and elongation of Al-11.5%Si-5%Ni alloy are drastically reduced when the Fe content is increased from 0.1

to 1.3%, while the yield strength is unaffected and the hardness increased. However, at 315 ^{0}C, tensile and yield strengths are appreciably increased by iron. Elongation is reduced by Fe addition up to 0.3% and then remains constant.

Archer and Kempf[10] reported that increasing the Fe content up to about 0.5 to 0.75% raises the tensile strength of the sand-cast test bars of Al-Si alloys containing 11.38 to 13.86%Si. Beyond 0.75%Fe additions reduce tensile strength. However, at all concentrations, Fe drastically reduces elongation.

Alfaro et al.[75] determined the influence of Fe on the properties of 10 alloys containing from 11.8 to 12.35%Si. They found that tensile strength, elastic limit and hardness were increased, whereas elongation was reduced by 10 to 50% when the Fe content was increased from 0.16 to 0.82%. Hajas[76] found that iron contents up to 0.2% in Al-10%Si-Mg improve the tensile strength and elongation and slightly increase the hardness. Drouzy and Jacob[77] found that the influence of Fe varies with Mg content, (0.07 and 0.45%) in Al-10%Si-4%Cu diecasting alloy, but the tensile strength rises to a maximum at about 0.25 to 1%Fe.

Moroigana et al.[78] studied the influence of Fe from 0.3to 2% on the properties of Al-11.5%Si-2.5%Cu alloy and they found the tensile strength increased up to 0.55%Fe and then decreased sharply up to 1%Fe and then less rapidly thereafter. Many authors[67,79-82] reported that the ductility of Al-Si alloys reduced as Fe content increases.

The effect of iron on the as-cast and T6 properties of an Al-7%Si-0.23%Mg-0.13%Ti-0.005%Na alloy is shown in Figure 2.2.6.[50] It is seen that Fe contents up to 0.5% enhance UTS and YS marginally. At levels greater than 0.5%Fe, UTS is reduced. However, even small amounts of Fe have a strong detrimental effect on elongation and impact strength[48].

2-2-1-4 IRON NEUTRALIZERS.

The most common addition to neutralize the effect of iron has been Mn and, to a lesser extent, Co, Be, and Cr[83]. According to Mondolfo[49], Mn transforms coarse $FeSiAl_5$ (ß) needles to a finely dispersed constituent, $(FeMn)_3Si_2Al_{15}$, exhibiting a chinese script type structure, which is less harmful to ductility. When the total Mn and Fe content in the alloy is greater than 0.8%, $(FeMn)_3Si_2Al_{15}$ forms as a primary constituent in the shape of hexagonal globules. These globules reduce machinability[48]. The ASTM specification indicates that in order to suppress the harmful influence of Fe in the sand casting, Mn content should be greater than one half of the iron content.

The role of iron neutralizers is the removal of undesirable ß plates by promoting the formation of another iron compound having a different morphology and is perhaps best illustrated by the study of Gustafsson et al.[67] on the effect of Cr additions. They found that Cr additions have a similar effect to that which is well established for additions of Mn to casting alloys of this type. By removing the harmful ß intermetallic phase and replacing it with a chinese script phase, the tensile ductility and fracture toughness were improved.

The modification of Al-Si alloy by Sr may be the more promising approach to reduce the effect of the harmful iron compound. It has been reported that the formation of large brittle iron intermetallic phases can be suppressed in a well modified alloy[65]. Recently, Granger et al.[65] have shown that in Be-free and Be-containing A357.0 alloys, the composition and the amount of iron-bearing phases are appreciably different. The Fe bearing phase, $Al_{10}Mg_4Si_4Fe$ form in Be-free alloys. Consequently, the Mg available for precipitation is reduced. Therefore, the strength decreases.

2-2-1-5 GRAIN REFINEMENT

It is very desirable to obtain Al castings with a fine and homogeneous structure to improve their mechanical properties and surface finish. This is commonly achieved by adding a grain refiner into the Al melt before casting. The effectiveness of various grain refining elements has been studied and it was found that Ti, Ta, Zr, Sc, W and B are the most effective grain refiners for Al and its alloys[85]. However, Ti is the most powerful and least expensive one. It has an unique grain refining efficiency which can be greatly enhanced by the addition of a very small amount of B.The advantages of grain refining are several and include:

1) A smaller amount and a fine dispersion of porosity in the cast product,[86-87] especially in alloys with a long freezing range. Grain refining will also reduce the amount of porosity found in an alloy containing a small to moderate amount of gas.[87] The overall effect is to improve the mechanical properties,[88-89] especially fatigue resistance, since fatigue failure in aluminum alloys is intergranular.[90]

2) Greater resistance to hot tearing.

3) Improved feeding of complex castings.

4) Elimination of columnar grains. In the absence of a grain refiner, the melt is undercooled by about 4 to 5 ^{0}C before spontaneous nucleation occurs.[91] This relatively large undercooling favours the growth of columnar grains. The undercooling in grain refined melts is generally less 1 ^{0}C.

The most common technique to accomplish grain refinement in the casting is through the addition of Al-Ti and Al-Ti-B ~master~ alloys, which provide large quantities of boride and aluminide inoculants. In Al-Ti type master alloys, $TiAl_3$ particles which are

introduced by master alloy act as the nucleating agents[48]. Both Al-Ti and Al-Ti-B master alloys typically contain as many as 50 million particles per cubic centimetre. The grain refining effect of particles has been attributed to the following peritectic reaction in the Al-Ti phase diagram:

$$Al(liquid) + TiAl_3 \rightarrow Al(solid with Ti \in solid solution)$$

The addition of B to Al-Ti master alloys improves the effectiveness of the grain refiner and significantly reduces the fading effect.[88-91] It appears that boron, that is the borides of Ti and Al, are better inoculants than Ti alone. Until recently, the Ti to B ratio in commercially used master alloys varied from 5:1 to about 50:1. Recently, a new grain refiner has been developed for hypoeutectic Al-Si alloys. The new master alloy has a Ti to B ratio of 1:1, Al-3%Ti-3%B.[92] This master alloy has been found to produce excellent grain refinement in 356, 319, and 308 casting alloys. The nucleating agent in the Al-3%Ti-3%B is a mixed boride, $(Al,Ti)B_2$, while in other grain refiners such as Al-5%Ti and Al-5%Ti-1%B, $TiAl_3$ and/or TiB_2 are the nucleants.

Alloying elements may also influence the grain refining process. The Si content of the alloy plays a major role in determining the efficiency of the grain refiner. B-rich grain refiners are not effective at low Si contents, but are extremely powerful grain refiners when 5 to 7% Si is present.[92] It has also been observed that Mg improves the grain refining response in hypoeutectic alloys, while Cu, Fe, Ni, Zn, and Mn do not seem to have any appreciable effect in foundry alloys.[93]

2-2-1-6 MODIFICATION OF EUTECTIC PHASE.

The mechanical properties of a casting are affected appreciably by the morphology of the Si in the eutectic. At low cooling rates, Si is present as coarse, acicular needles

(flake) in the unmodified state. These flakes act as crack initiators and consequently the material fractures in the brittle mode. In order to improve the mechanical properties Na or Sr are added to the alloy to modify the eutectic structure. Modification with Na or Sr changes the morphology of Si to the fine fibrous form.

The microstructural and property change due to strontium modification are comparable to those achieved with sodium. Both elements depressed the eutectic temperature, convert the flake to a fibrous eutectic morphology, a refinement of the eutectic. But the disadvantages of employing sodium for modification are well known, the major one being its rapid loss from the melt by volatization and oxidation. On the other hand, strontium added in a master alloy, which is a ternary Al-Si-Sr alloy containing various amounts of Si + Sr, gives almost 100% recovery on bath addition without fuming or burning. The rate of loss of strontium during holding is an order of magnitude lower than for sodium and occurs without the formation of a thick oxide skin.[94]

Hess[95] studied strontium as a modifying agent for hypoeutectic Al-Si alloys and reported that strontium modification effects a significant increase in the mechanical properties of Al-Si alloy sand and permanent mould castings. Closset and Gruzleski[70], have used the quality index to study the mechanical properties of Sr-modified A356.0 melts under several different conditions. Sand moulds were used to produce the specimens which were treated by the T6 heat treatment. Figure 2.2.7 shows the quality index* as a function of Sr concentrations. Modification with Sr increases the quality index and optimum additions for this casting are around 0.015%. Also, a coarse intermetallic phase Al_4SrSi_2 was observed in the microstructure which no doubt was a major contributor to a decrease in the quality index at high Sr concentrations found in these experiments. Their results also show that increases in quality index are mainly because of the increase in ductility resulting from modification.

* $Q = UTS + 150 \log.(\%el.)$

Fat-Halla[96] has studied fracture in a modified Al-7%Si-0.3%Mg. His results shows the fracture mode changes from intergranular to transgranular due to modification. The fracture surface exhibits the dimple like pattern characteristic a ductile fracture. Consequently, modified alloys possess higher ductility than unmodified alloys.

2-2-1-7 THE REFINEMENT OF THE EUTECTIC PHASE BY ANTIMONY.

Antimony has been used to refine the morphology of the eutectic phase, and to enhance the mechanical properties of Al-Si alloys. Telli and Kisakurek[97] have presented hardness measurements, tensile properties, and structural features of directionally solidified Al-Si eutectic alloy with and without Sb. They reported that hardness and tensile properties, i.e. ultimate tensile strength and 0.2%proof stress, show a similar dependence on growth velocity and Si phase interflake spacing. They concluded that the relationships between interflake spacing, growth velocity, temperature gradient, and concentration of Sb are such that a single relationship exists between the mechanical properties and interflake spacing. This relationship is of Hall-Petch type and it was suggested that it can be used to describe the mechanical properties in the presence and absence of Sb and independently of the Sb concentration and temperature gradient in the liquid. This implies that Sb increases the mechanical properties of the eutectic only by structural refinement. Recently, Ourdjini et al.[98] reported that the hardness-interflake spacing relationship does not follow the Hall-Petch type, and there is a slightly increased hardness of the alloy refined with Sb which is attributed to a slight solid solution hardening of Al phase.

Borgeaud[99] found that chill cast Al-10%Si alloy and Al-11%Si alloy treated with 0.2%Sb exhibited UTS values of 180.3-191.7 N mm^{-2} and elongation of 10-13%. Venkateswaran et al.[100] reported that addition of antimony to the eutectic Al-Si alloy causes a lamellar type of structure. Further, the modification effect has been shown to be more pronounced in the case of gravity-diecasting compared to sand casting. The effect

of antimony on the eutectic temperature has been reported by Venkateswaran[100]. They show that the eutectic freezing temperature is lowered to 564 ^{0}C, whereas the primary solidification temperature remains unaltered.

Closset[101] used A356.0 alloy to study the Sr-modification in the presence of antimony. He shows that antimony dilution is an effective method to allow Sr-modification. Sb dilution from 0.08% to 0.03% combined with Sr additions to levels between 0.013% and 0.017% produces a fibrous structure. This method seems to be more economical than the technique consisting of adding an excess of modifier. Gradual strontium and antimony losses denote certainly the formation and segregation of intermetallic compounds.

Tuttle et al.[102] reported that a drop of 45% occurs in the elongation as the Sb content increases from 0.0 to 0.06% and an increase to 6.5% elongation occurs as the Sb content increases from 0.06-0.2%Sb and this is due to change in morphology of the eutectic in the modified A356.2 casting alloy. Sb changes it from a fully modified (0.0%Sb) to acicular (0.06%Sb), to fine (moderate) lamellar (0.26%Sb). Also they reported that fluidity decreases drastically from 0.0%Sb to 0.14%Sb and then increases again gradually until it reaches a value equal to that of the original fully modified structure.

2-2-2 THE POROSITY FORMATION.

Probably the greatest problem associated with modification of Al-Si casting alloys is the fact that modified casting are often more porous than their unmodified counterparts. This effect may offset any advantage in improved mechanical properties which is gained by modification as well as leading to reduced pressure tightness in castings which are required to be leak-tight.[103]

The origin of porosity during solidification is usually attributed to rejection of gas

f· ·m solution and/or the inability of liquid to feed through solid + liquid regions to compensate for the volume shrinkage that accompanies the phase change. Neglecting pore formation due to entrapped air which is a consequence of bad casting design and practice, the ease of pore formation can be described by the equation,

$$P_g + P_s > P_{atm.} + P_h + P_{s-l} \qquad (2\text{-}21)$$

where P_g is the equilibrium pressure of dissolved gases in the liquid,

P_s is the pressure drop due to shrinkage,

$P_{atm.}$ is the pressure of the atmosphere over the system,

P_h is the pressure due to the metallostatic head and

P_{s-l} is the pressure due to surface tension at the pore-liquid interface.

The parameters P_h and $P_{atm.}$ are constant for a given casting design. The dissolved gas pressure, P_g, is a major driving force in microporosity formation. If an aluminium melt contains excessive amounts of dissolved gas, particularly hydrogen, the decrease in solubility on solidification can be sufficient to cause pore formation and gas porosity. It has been shown that modification with strontium can increase both pore size and volume.[104] However, the gas content of a melt can be reduced by degassing and held to a predetermined level before casting.

Shrinkage porosity pressure, P_s, which is directly related to the ease of the interdendritic feeding is not as easy to control. Contraction during solidification leads to microshrinkage particularly in interdendritic areas. Often gas and microshrinkage porosity occur simultaneously. The remaining parameter, P_{s-l}, is the surface tension effect. Modifiers are known to reduce surface tension and hence, promote pore formation. However, the relative effects of strontium and sodium have not been reported. Argo and Gruzleski[105] measured microshrinkage quantitatively with a Tatur mould for unmodified

and strontium treated aluminum-silicon alloys at a constant gas pressure. Bars were sand cast with a graphite chill and the porosity distribution was examined in both alloys. Modification increased microshrinkage as a percentage of the total shrinkage from 7.27 to 9.7% and decreased the pipe volume by 44%. Modifying agents decrease the eutectic temperature and, hence, extend the freezing range and the length of the mushy zone, increasing both feeding distance and difficulty. The decrease in pipe volume is evidence of an increase in feeding difficulty. Radiographs of the sand cast bars showed that microshrinkage was located mainly in one area in unmodified bars but was distributed more widely in the modified bars. These observations led to the picture of microshrinkage formation in hypoeutectic alloys depicted in Figure 2.2.8. The shorter freezing range of unmodified alloys means a shorter interdendritic feeding distance. Easier feeding concentrates microshrinkage into the last areas to solidify. The eutectic liquid in these areas solidifies with a flake morphology at a non-isothermal interface. Small pockets of eutectic become trapped behind this advancing, irregular interface to produce fine porosity concentrated in the last areas to solidify. Good feeding practice can locate these areas into the feeder promoting casting soundness. Feeding is more difficult in the modified alloy with a possibility of the formation of larger isolated pockets of eutectic liquid between dendrite arms. This results in widely dispersed, isolated solidification cells which can solidify with an isothermal, regular interface. Thus pores in modified alloys are likely to be larger and more dispersed.

Gruzleski[103] has reported Tatur mould measurements for sodium modified Al-Si alloys. The microshrinkage percentage of the total shrinkage was found to increase from 7.27 to 14.7%. These measurements were made on A356 alloy at constant hydrogen concentration. Consequently these measurements show sodium modified alloys to be more porous and do not offer any evidence for strontium modified alloys being more prone to microshrinkage porosity.

Denton and Spittle[106] have reported that the regular interface of the modified alloy may develop a scalloped interface at slow cooling rates and that this may occur under different solidification conditions in sodium and strontium modified alloys. Deep liquid channels were observed to extend back to the mould wall creating areas of microshrinkage.

It should not be concluded from the results of Ago and Gruzleski[3] that Sr modification is undesirable. Modification has a beneficial influence on the quality of the casting in most cases. Porosity can be caused by a number of factors and in practice, there are many ways to eliminate undesired porosity. These steps include:

1. Reduction of gas content by proper degassing techniques.
2. Grain refinement will help to break up and eliminate the microporosity.
3. Proper mould design will shift undesirable shrinkage into the riser.[48]

2-2-3 HEAT TREATMENT OF CAST Al-Si-Mg ALLOYS.

Castings of Al-Si-Mg alloys can be heat treated to obtain an optimum combination of strength and ductility. The heat treatment consists of solutionizing at temperatures close to the eutectic temperature, quenching, and a combination of natural and artificial aging.[107] Several different heat treatment tempers have been developed for Al-Si-Mg alloys. Sinfield et al.[55] have studied the effect of various treatments on mechanical properties of grain refined and Na-modified Al-7%Si alloys containing 0.25 to 0.45%Mg. Their results show a full T6 treatment produces higher strengths because of greater amounts of fine Mg_2Si precipitates formed during aging (see Figure 2.2.9). The T6 (in some cases T7) treatment gives the optimum balance of strength and ductility and is most commonly

employed with aluminium alloy castings.

2-2-3-1 THE SOLUTION TREATMENT.

The solution treatment of the casting produces the following effects.

I Dissolves Mg_2Si particles.

Heat treatable aluminium alloys display appreciable solid solubility of the precipitating Mg_2Si phase at the solidus temperature. Solubility decreases with temperature and the second phase precipitates out as coarse particles. This decrease in solubility is a prerequisite to a significant response to heat treatment.[48] The solubility of Mg and Si in the Al-rich phase decreases with temperature as can be seen from Figure 2.2.10.

The solution temperature should be as close as possible to the eutectic temperature to obtain a maximum concentration of Mg and Si particles in solid solution. To avoid any damage to the mechanical properties the solution temperature should be controlled and not allowed to exceeded the melting point. In most cases, the 356 and 357 type alloys are solutionized at 540 ± 5 ^{0}C. At this temperature, about 0.6% Mg can be placed in solution see Figure 2.2.10.

II Homogenization.

The solution treatment homogenizes the cast structure and minimizes segregation of alloying elements in the casting.[107] The time required for homogenization is determined by solution temperature and by dendrite arm spacing. In the as-cast sample of 356 alloy silicon contents are lowest in the centre of dendrite, since this formed first at relatively high temperatures. The Mg content in dendrite increases from centre to edge, but

only slightly. Closset et al.[108] found that homogenization was essentially complete within 30 min at 550 ^{0}C. No differences in the rate of homogenization between modified and unmodified samples were observed.

III Changes in eutectic Si morphology.

Under thermal modification the Si particles are broken down into smaller fragments and are gradually spheroidized. Prolonged solution treatment leads to coarsening of the particles. Both spheroidization and coarsening are surface area energy driven, i.e. the system tries to reduce excess surface area to the minimum possible. In alloys modified by Sr, a high degree of spheroidization occurs after only 12 hr. of solution treatment, while in unmodified alloys, even after 12 hr. coarse needles of Si are observed.[48] Rhine et al.[109] reported that rapid spheroidization occurs during solutionizing at 540 ^{0}C in the modified alloys. The rate of spheroidization and coarsening increases with solution temperature.[110] Zhu et al.[111] propose that changes in Si morphology occur in two stages;

a) Dissolution separation,

b) Spheroidization.

In the first stage, Si is separated into segments at corners or thin growth steps but they retain their flake morphology. In the second, the broken segments spheroidize and the aspect ratio decreases.

2-2-3-2 QUENCHING.

Following solutionizing the castings are usually quenched in water for the purpose of suppressing the formation of equilibrium Mg_2Si phase during cooling and retaining the maximum amount in solution to form a supersaturated solid solution at low temperature.[48] A rapid quench will ensure that all Mg_2Si is retained in solid solution and the highest

strength attainable is obtained with fast quench rates. Residual stress and distortion are introduced into the casting at high quench rates. This is why the quench rate cannot be increased indefinitely. Tsukuda et al.[112] found in an A356 alloy that impact strength, elongation and UTS vary inversely with water temperature and with quench delay. The higher elongation and greater impact strength were found with rapid quenching (lower water temperature) see Figure 2.2.11.

2-2-3-3 PREAGING.

Maintaining quenched samples at a temperature below the final artificial aging temperature for extended periods is termed preaging. This temperature may be equal to,above, or below room temperature. Quadt et al.[113] show that YS and UTS decrease with preaging time while elongation increases and they suggest a room temperature aging of 24 hr. for a balanced combination of mechanical properties. Ghate et al.[114] have shown that the effect of preaging is a decrease in UTS and YS and is more pronounced at higher Mg contents. Also, the effect of preaging is considerably reduced when trace elements such as In, Sn, Cd or Cu are present in the casting.

2-2-3-4 TEMPERATURE AGING.

The purpose of this treatment is to precipitate out of solution the constituents which were dissolved during solutionizing. Al-Si-Mg alloys follow the characteristic precipitation sequence:[49]

$$\alpha \text{ — GP Zone — } \beta' \text{ — } \beta$$

Precipitation starts with the formation of spherical GP zones, these zones elongate in the [100] matrix direction and assume a needle shape; the needles grow to become rods

and eventually platelets. The β' is a semi-coherent phase. The final equilibrium phase nucleates on β'. Gustafsson et al.[57] indicated that fine scale precipitation of $\beta'(Mg_2Si)$ occurs during aging for all solidification rates. The aging temperature and time are two variables that can be used to control the properties of the heat treated part. Chamberlain et al.[115] found in A356 alloy cast in both sand and permanent molds, UTS, YS increase with temperature while elongation decreases. Tsukuda et al.[112] found UTS, YS, and hardness increase with aging temperature and time while impact strength and elongation decrease. Higher strengths are obtained by increasing Mg or Fe content at the expense of ductility and impact strength.

2-2-4 CASTING PROCESS.

At an early stage in design and before proceeding to the detailed determination of shape, the casting process, the alloy and, if possible, a general outline of the proposed manufacturing method needs to be established. One of the first considerations is whether the product is made by casting, die casting or some other specialised process. The main processes and the principal factors influencing selection are listed in Table 2.2.3.[110] The casting may be in one mould or a single casting may be broken down into smaller units to be subsequently fabricated by welding, bolting or other mechanical means. Aluminum alloys are one of the few alloys that can be cast by all processes used in the casting of metals.

2-2-4-1 DIE CASTING.

Die castings are made by injection of molten metal into metal moulds under substantial pressure. Rapid injection is due to the high pressure and rapid solidification under high pressure is due to the use of metal moulds; these combine to produce a dense, fine-grained surface structure. Consequently excellent wear and fatigue properties can be

achieved. Porosity may exist as a result of air entrapment and shrinkage. Die castings are not easily welded or heat treated because of entrapped gases.[117]

2-2-4-2 PERMANENT MOULD CASTING.

Permanent mould castings are typically larger than die castings and are gravity-fed. The pouring rate is relatively low but the metal mould produces rapid solidification. Permanent mould castings exhibit excellent mechanical properties which can be enhanced by heat treatment. Castings are generally sound.

2-2-4-3 SAND CASTING.

In sand casting, the mould is formed around a pattern by ramming sand, mixed with the proper bonding agent, onto the pattern. Then the pattern is removed, leaving a cavity in the shape of the casting to be made. The main advantages of sand casting are versatility (wide variety of alloys, shapes and sizes can be sand cast), and the low cost of minimum equipment required. Among its disadvantages are low dimensional accuracy and poor surface finish as well as low strength as a result of low cooling.rate.

2-2-4-4 SHELL MOULD CASTING.

In shell mould casting, the molten metal is poured into a shell of resin - bonded sand and 10 to 20 mm thick-much thinner than the massive moulds commonly used in sand foundries. Surface finish and dimensional accuracy for alloys produced in this mould are similar to these produced in a sand mould but with slightly higher cooling rates.

2-2-4-5 INVESTMENT CASTING.

Investment casting of aluminum most commonly employs plaster moulds and expendable patterns of wax or other fusible materials. A plaster slurry is "invested" around patterns for several castings and the patterns are melted out as the plaster is baked. Investment casting produces dimensional accuracy and a good surface finish. Some internal porosity is usually present. Because of porosity and slow solidification, mechanical properties are low.

2-2-4-6 CENTRIFUGAL CASTING.

Centrifuging is another method of forcing metal into a mould. Steel, baked sand, plaster, cast iron, or graphite moulds and cores are used for centrifugal casting of aluminum. Metal dies or moulds provide rapid chilling, resulting in a level of soundness and mechanical properties comparable or superior to that of gravity-poured permanent mould castings.

TABLE 2.2.1.

Alloy	Si	Fe	Cu	Mn	Mg	Zn	Ti	Total others	Ni	Zn
336.0	11-13	1.2m	0.5-1.5	0.35m	1.3m	0.35m	0.25m	0.15m		
354	8.6-9.5	0.2m	1.6-2	0.1m	0.4-0.6	0.1m	0.2m	0.15m		
355.0	4.5-5.5	0.6m	1-1.5	0.5m	=	0.25m	0.05m	Cr.2 =		
C355.0	=	0.2m	1-1.5	0.1m	=	0.1m	0.2m	0.15		
356.0	6-7.5	0.6m	0.25m	0.35m	0.2-0.45	0.35m	0.25	=		
A357.0	=	0.2m	0.2m	0.1	=	0.1m	0.2m	=		
357.0	6.5-7.5	0.15m	0.05m	0.03m	0.45-0.6	0.05m	0.2m	=		
A357.0	=	0.2m	0.2m	0.1m	0.4-0.7	0.1m	0.1-0.2	0.2		
359.0	8.5-9.5	0.2m	0.2m	0.1m	0.5-0.7	0.1	0.2	Sn		
360.0	9.0-10.0	0.2m	0.6m	0.35m	0.4-0.6	0.5m	---	0.25m	0.5m	0.5m
A360.0	=	1.3m	=	=	=	=	---	0.15m	=	=
380.0	7.5-9.5	2.0m	3-4	0.5m	0.1m	3.0m	---	0.35	=	3.0m
A380.0	=	1.3m	=	=	=	=	---	=	=	=
383.0	9.5-11.5	=	2-3	=	=	=	---	0.15m	0.3m	=
384.0	10.5-12	=	3-4.5	=	=	=	---	0.35m	0.5m	=
A384.0	=	=	=	=	=	1.0m	---	=	=	1.0m
390.0	16-18	=	4-5	0.1m	0.4-0.65	0.1m	0.2m	---	---	0.1m
A390.0	=	0.5m	=	=	=	=	0.2m	---	---	=
413.0	11-13	2.0m	1.0m	0.35m	0.1m	0.5m	---	0.15m	0.5m	0.5m
A413.0	=	1.3m	=	=	=	=	---	0.15m	=	=
443.0	4.5-6.0	0.8m	0.6m	0.5m	0.05m	=	---	---	---	=
A443.0	=	=	0.3m	=	=	=	0.25m	---	---	=
B443.0	=	=	0.15m	0.35m	=	0.35m	=	---	---	0.35m
C443.0	=	2.0m	0.6m	=	0.1m	=	0.15m	---	0.5m	---

Where m is maximum

TABLE 2.2.2. Structure and composition of experimentally observed intermetallic phases (Wt Pct)

Phase	Mg	Si	Cr	Fe	(Cr+Fe)/Si	Reference
β $FeSiAl_5$	---	12-15	---	20-30	2.2	Mondolfo
	---	13.8-14.9	---	26.7-27.3	1.9	Pratt
	---	15.8-18.9	---	23.5-25.8	1.4	Obinata
	---	17	---	29	1.7	Closset
	---	18-19	---	16-25	1.2	Gustafsson
	---	17	---	24	1.4	=
π $FeMg_3Si_6Al_8$	15.6	33.8	---	12.1	0.3	Mondolfo
	13	28	---	10	0.3	Closset
	13-16	25-28	---	8-9	0.3	Gustafsson
α $(Cr,Fe)_4Si_4Al_{13}$	---	6-8	---	27-35	4.2	Mondolfo
	---	10-11	8-9	16-19	2.2	Gustafsson

TABLE 2.2.3. **Process selection.**

Casting Processes	Factors in Process Selection
1. Sand casting 2. Gravity die or permanent mould casting 3. Pressure die casting 4. Shell moulded casting 5. Investment casting (permanent and expendable pattern techniques) 6. Centrifugal casting	1. Suitability for shape and size of product 2. Suitability for alloy 3. Accuracy and surface finish 4. Quantity requirements and overall cost of production

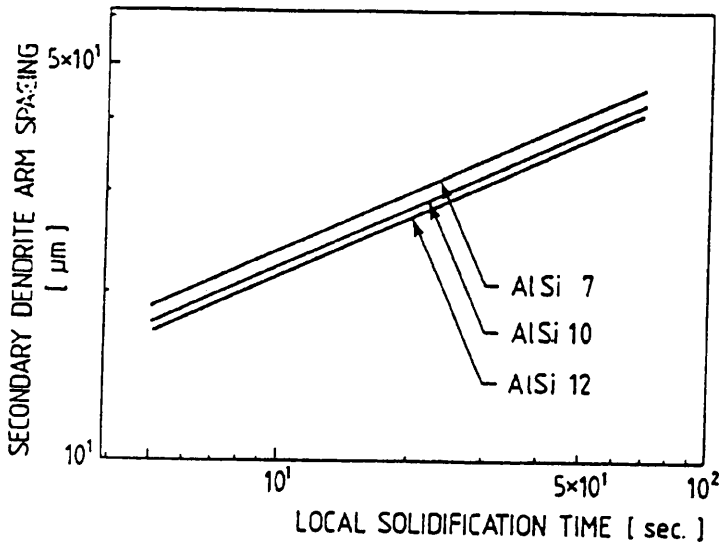

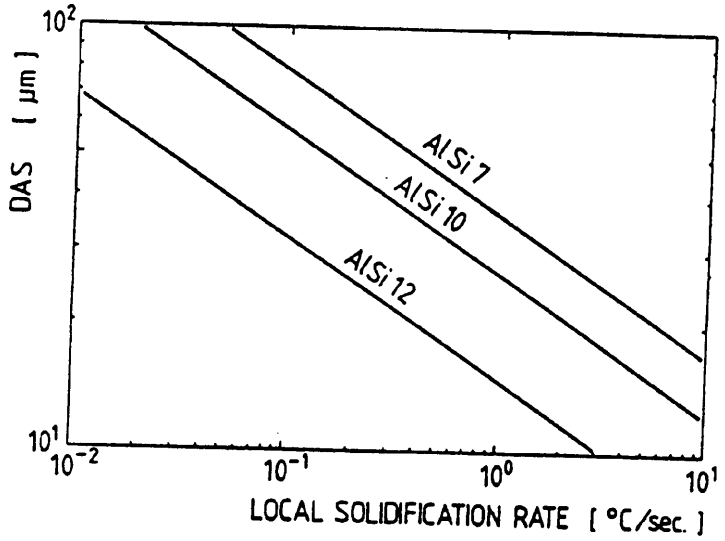

Figure 2.2.1. a) Secondary dendrite arm spacing versus local solidification time for binary AlSi7, AlSi10, and AlSi12 alloys,

b) Secondary dendrite arm spacing versus solidification rate for binary AlSi7, AlSi10, and AlSi12 alloys.[56]

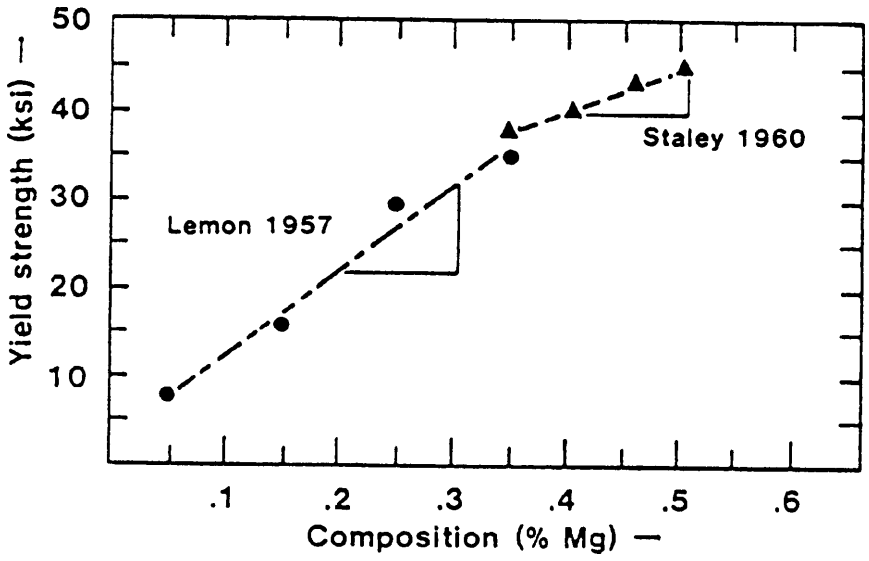

Figure 2.2.2. Effect of Mg on T6 yield strength in Al-7%Si alloys.[65]

Figure 2.2.3. ß ($FeSiAl_5$) phase in the as-cast LM25 alloy.

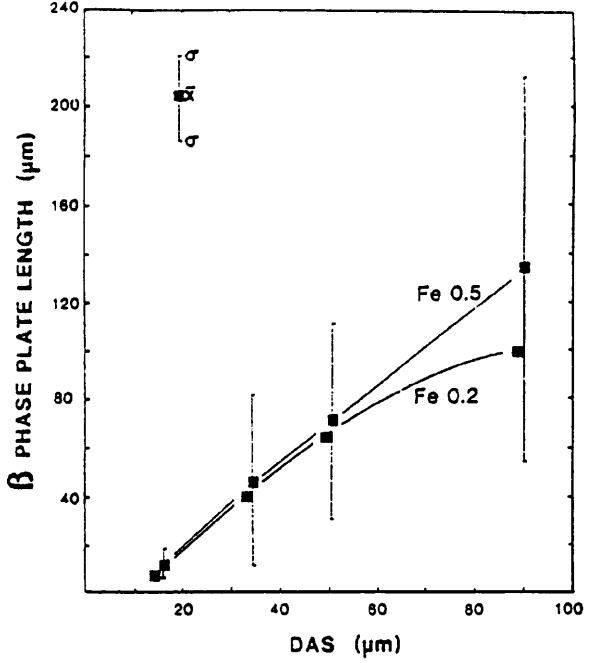

(a)

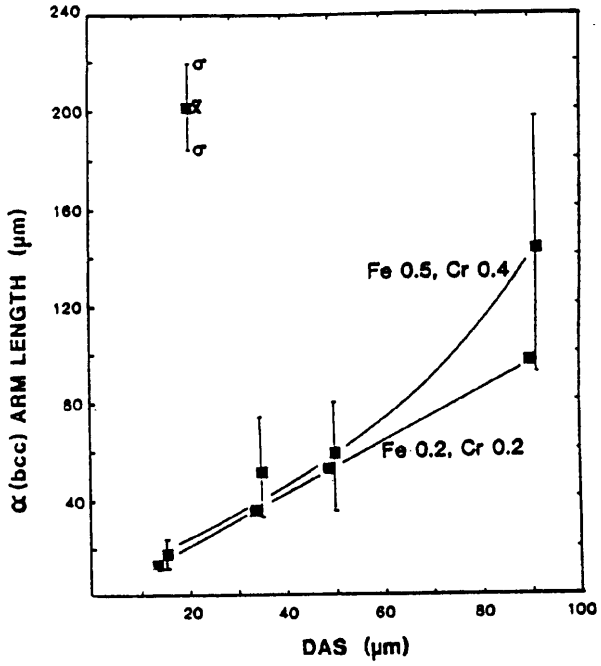

(b)

Figure 2.2.4. Length measurements of (ß&α) intermetallics in A356 alloy as function of dendrite arm spacing, a) ß intermetallic, b) α intermetallic.[67]

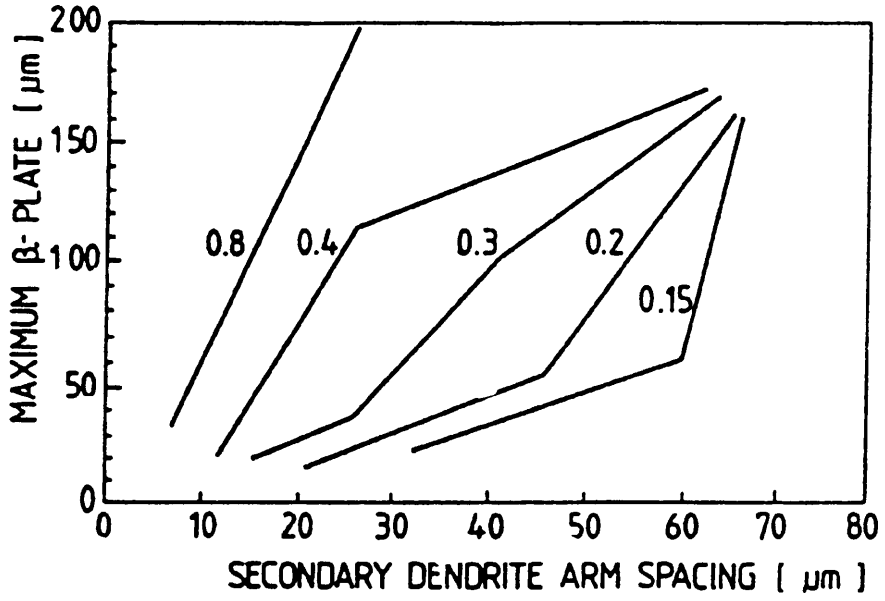

Figure 2.2.5. Maximum observed length of β plates versus secondary dendrite arm spacing for AlSi7Mg0.3 containing various amount of iron.[56]

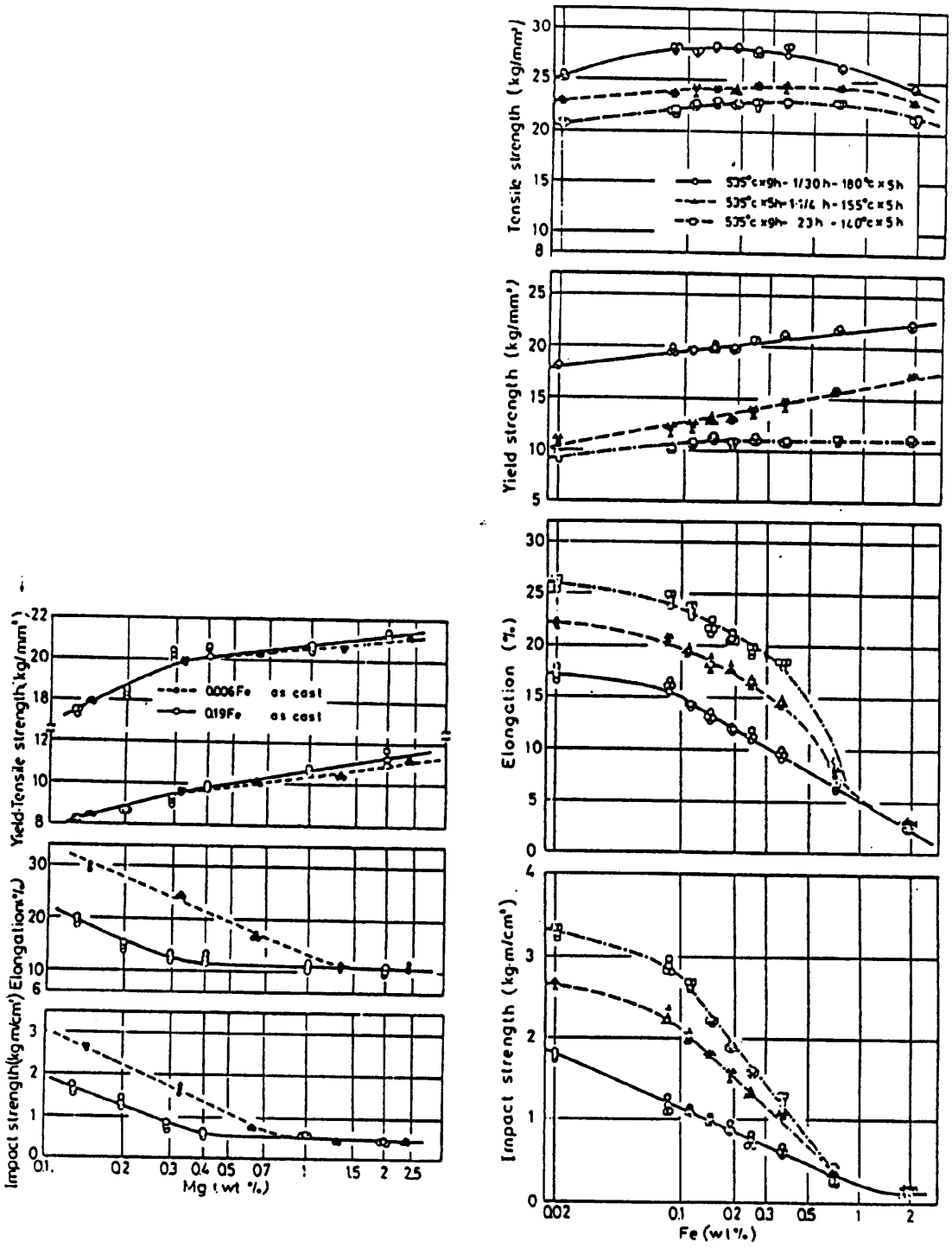

Figure 2.2.6. Effect of Fe on the mechanical properties of permanent mold cast Al-7%Si-0.23%Mg-0.13%Ti-0.005%Na alloy.

a) As-cast condition,

b) T6 condition.(50)

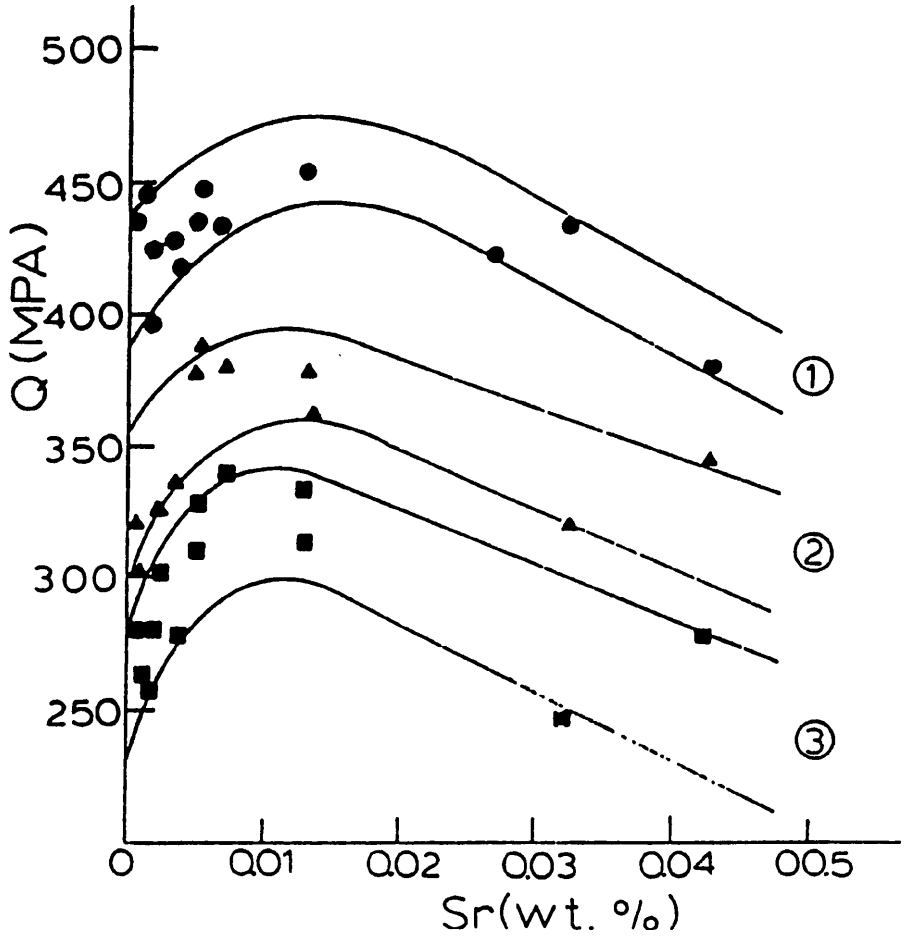

Figure 2.2.7. Variation of quality index Q in relation to strontium content for three different cooling rates. Band 1--cooling rate 1.5 $^{0}C\ sec^{-1}$ 2--cooling rate 0.5 $^{0}C\ sec^{-1}$ 3--cooling rate 0.08 $^{0}C\ sec^{-1}$.[70]

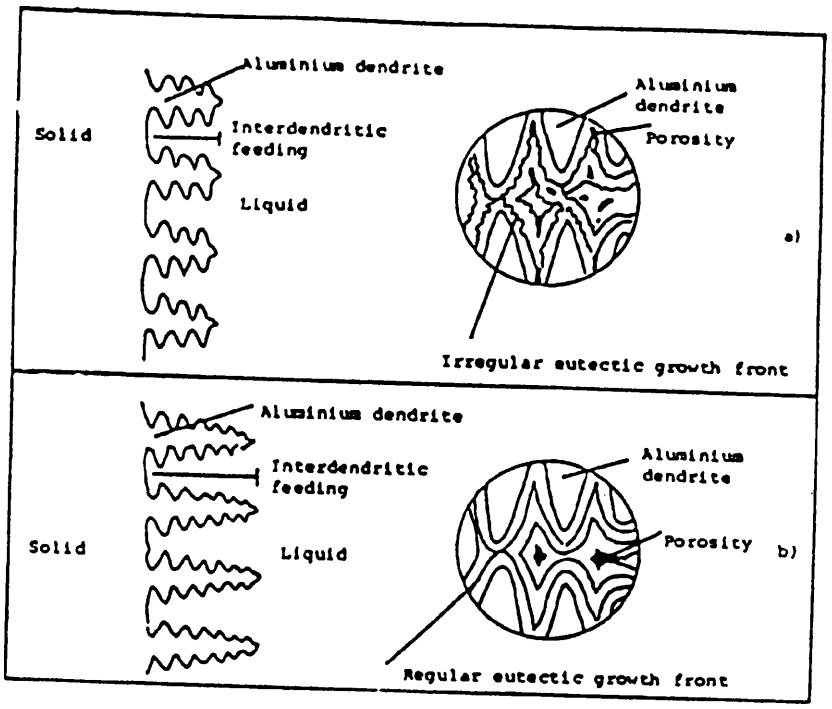

Figure 2.2.8. The different modes of microshrinkage porosity in unmodified and modified hypoeutectic alloys.[121]

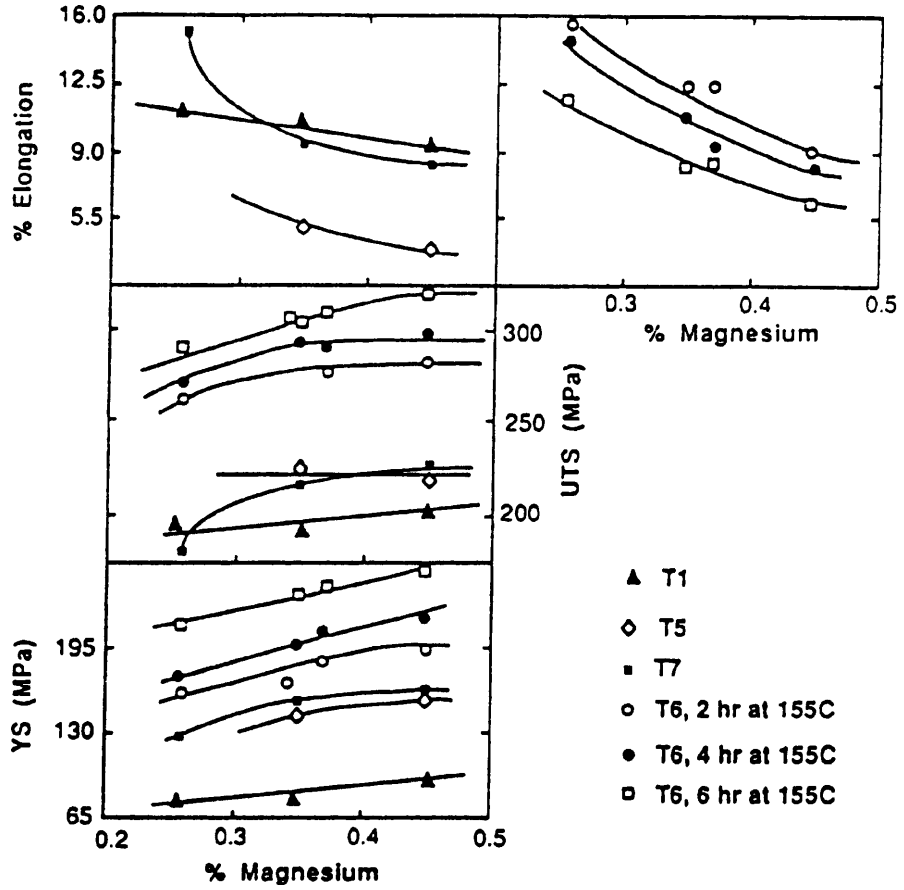

Figure 2.2.9. Mechanical properties of Al-7%Si-Mg alloys subjected to different heat treatments.(55)

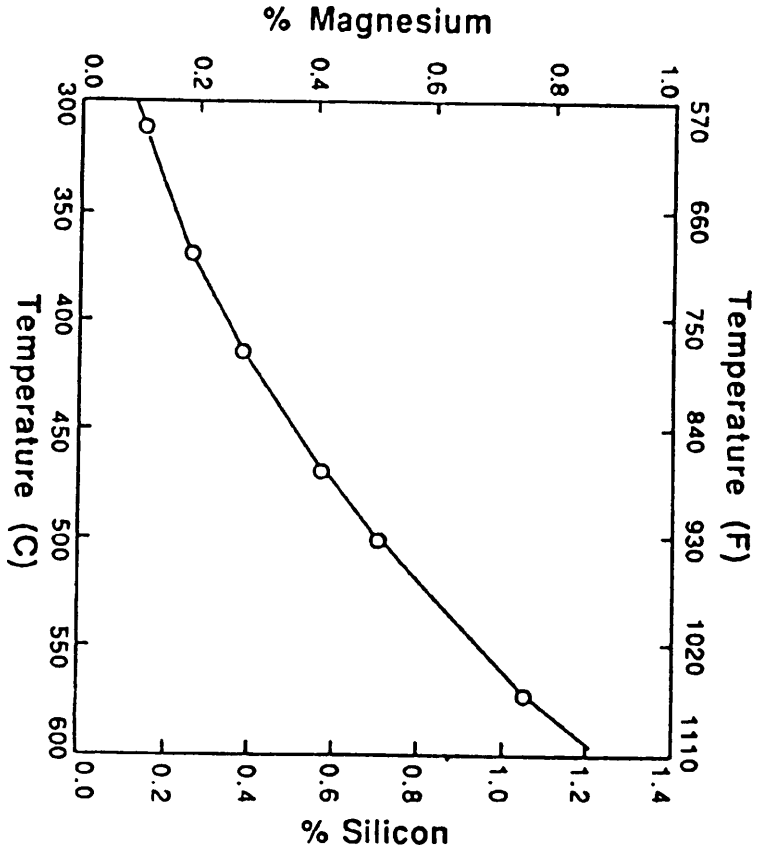

Figure 2.2.10. Equilibrium solubility of Mg and Si in solid aluminum when both Mg_2Si and Si are present.[48]

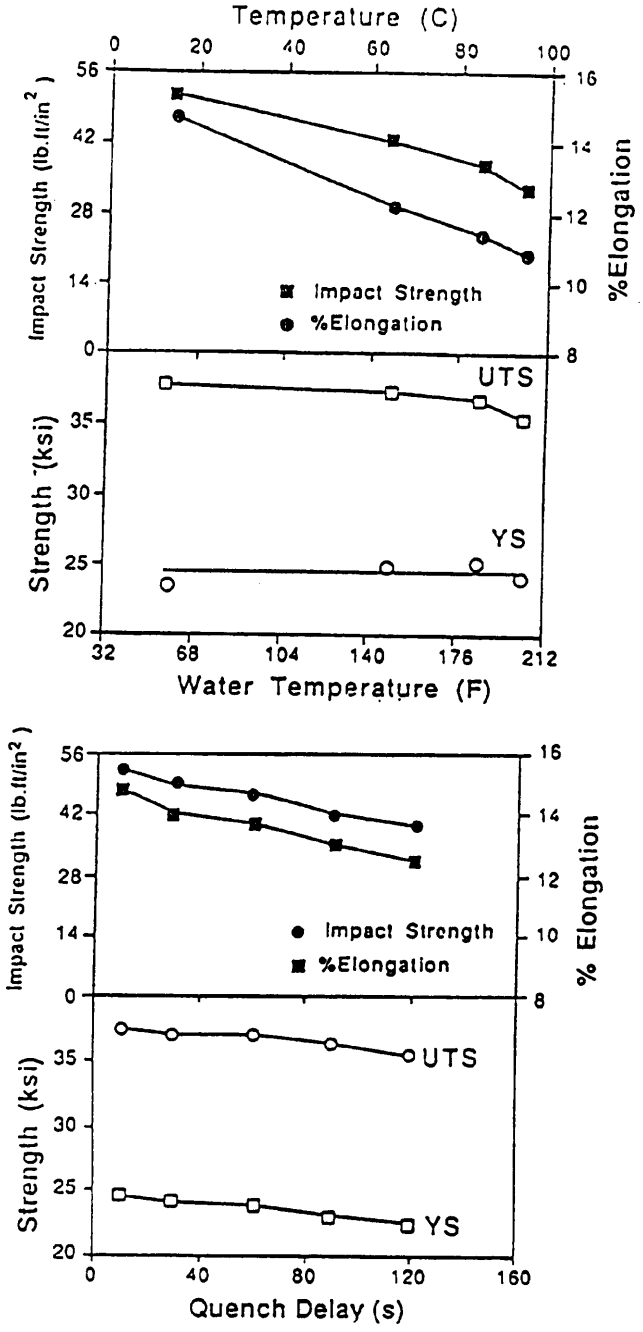

Figure 2.2.11. a) **Effect of water temperature at quench on the mechanical properties of A356 alloy.**

b) **Effect of quench delay on the mechanical properties of A356 alloy solution treated at 520 ^{0}C for 5 hr and aged at 155 ^{0}C for 4.5 hr.**[112]

CHAPTER THREE

EXPERIMENTAL WORK

CHAPTER THREE

EXPERIMENTAL WORK

3-1 ALLOY PREPARATION.

3-1-1 PURE ALLOY

It has been shown conclusively that the presence of even small quantities of impurities can have a profound effect on the morphology of eutectic alloys under certain solidification conditions. The aluminium ingots, silicon lumps and strontium used in the preparation of Al-12.7%Si-0.2%Sr and Al-7.8%Si-0.04%Sr alloys were therefore all of 99.99% purity.

The alloys were prepared by melting the appropriate amounts of aluminium and silicon under an argon gas atmosphere in a high purity graphite crucible, using a H. F. induction furnace. In order to get homogeneity of the melt a graphite rod was used to stir the melt before casting into a high purity graphite mould 13x10x220 mm.

To get a fully modified alloy a calculated amount of pure strontium was added into the melt and then stirred to ensure a uniform melt. The melt was then held at about 750 ^{0}C for 10 minutes before casting into the mould. The mould (boat) was kept in another resistance furnace to keep it at about 650 ^{0}C for about 15 minutes.

3-1-2 LM25 ALLOY

All specimens were made from virgin LM25 ingots of analysed composition,

%Si	%Mg	%Cu	%Fe	%Mn	%Ni	%Pb	%Sn	%Ti
7.84	0.45	0.04	0.33	0.18	0.02	0.02	0.01	0.02

The required quantity of alloy was melted in a graphite crucible in a H.F. induction furnace

under a protective argon atmosphere. The melt was degassed with argon for 15 minutes at 750 °C and then cast into one of three moulds shown in Figure 3.1 depending on the subsequent solidification process. Any addition to the LM25 alloy was made in the same way as for the modified eutectic alloy.

3-1-3 SPECIMEN TUBE FILLING

The specimens used in the Bridgman directional solidification apparatus were prepared by filling the specimen tube as described below. Alumina tubes (6mm OD and 3mm ID) were used to make a specimen. They were preheated for 10 minutes at about 650 ^{0}C, then filled with the molten alloy, whether eutectic or LM25 (with or without addition) by suction. The needle valve was used to regulate flow (connected to a rotary pump). Filling of the tube was achieved by controlling the melt temperature, suction power and cold water circulating in a holder which held the specimen at the top. Bridgman directional solidification apparatus was used to produced all specimens which solidified with a high temperature gradient. The apparatus is shown in Figure 3.1c and was described in detail by Javidi.[118]

3-2 APPARATUS FOR UNIDIRECTIONAL SOLIDIFICATION OF ALLOYS

Figure 3.1a shows the alloy in the form of a bar approximately 13x10x190 mm contained in a high purity graphite boat, which is open at one end. The aim is to produce unidirectional solidification; this means that the solid/liquid interface must be normal to the growth direction.

This was achieved by using an open ended high purity graphite boat to contain the alloy and placing a copper water chill in direct contact with the alloy at the open end of the boat. The whole boat chill assembly was contained in a quartz tube of 30 mm internal diameter. Oxygen-free nitrogen was passed through the quartz tube to prevent any oxidation.

3-3 THERMAL VALVE TECHNIQUE.

The thermal valve furnace illustrated in Figure 3.2, consists of two pairs of gradient wound heating coils. The furnace, constructed in two halves, was hinged along one side; this enables the boat and chill assemble to be positioned correctly in relation to the furnace windings. Each half of the furnace contained two split furnace tubes 120 mm long, each of which has four internal channels 3 mm wide running its whole length.

The upper windings were each connected in series with the windings directly below. Each pair of coils was controlled independently by a Eurotherm temperature controller, using a T_1--T_2 thermocouple placed at the hot spot of the upper coil. The temperature of each pair of coils was adjusted so that the S/L interface was stabilised approximately 20 mm from the chill and the desired growth velocity and temperature gradient in the liquid were obtained by feeding a linearly varying d.c. voltage into the temperature of each pair of coils. These linearly varying voltages were provided by Eurotherm programmers and if an increasing e.m.f. was fed in series with the e.m.f. generated by the control thermocouple, the S/L interface was propagated into the liquid. It was found that the e.m.f. for the Eurotherm which controlled the cold furnace is approximately double that required for the hot furnace. The theory of the thermal valve technique was developed by Tiller and Rutter and was described in detail by Glenister.[119]

3-4 TEMPERATURE MEASUREMENT

Three thermocouples were set in the specimen so that they were normal to the direction of heat flow and parallel to the solid/liquid interface; They were inserted into the melt from the bottom of the boat with 20 mm distance between each thermocouple. The molten alloy will cover the bead of the thermocouple giving a good thermocouple response.

The 0.315mm diameter T_1--T_2 thermocouple were made by spark welding and were

insulated with twin 4mm external diameter alumina sheaths. The output from these thermocouples during solidification was fed into a multichannel, programmable Rikadenki recorder which records a measurement every second. This data was used to plot cooling curves from which the total solidification time at each thermocouple position and the average temperature gradient in the liquid, G and the growth velocity, V between the thermocouple positions were calculated.

3-5 GROWTH VELOCITY AND TEMPERATURE GRADIENT MEASUREMENTS

It has been shown that it is possible to measure the growth velocity and temperature gradient in the liquid by unidirectionally solidifying specimens and allowing the interface to move past two fine thermocouple a known distance apart. For this technique to be successful the thermocouple must measure the true interface temperature and it must be possible to calculate accurately the growth velocity and temperature gradient i.e. the exact time when the S/L interface passes the two thermocouples must be known.If the time interval between the interface passing the thermocouples is t, the growth velocity is given by;

$$Growthvelocity(V)=\frac{d}{t} \qquad (3\text{-}1)$$

where d is a distance between the two thermocouples.

The time can be defined by the change in the slope of the time-temperature trace of the thermocouple. The change in the trace indicates that the S/L interface has just passed the thermocouple. This change of slope needs to be sharp to obtain accurate results.

The temperature gradient was measured by taking the difference in the temperature of the first and second thermocouple when the S/L interface position is at the first thermocouple position, then dividing by the distance separating these two thermocouples,

$$Temperature gradient (G) = \frac{T_2 - T_1}{d} \qquad (3\text{-}2)$$

Figure 3.3 shows how the growth velocity and temperature gradient are calculated.

3-6 EXPERIMENTAL PROCEDURE FOR CASTING USING THE SAND MOULD

3-6-1 SAND MOULD

Initially, greensand moulds were used for making the castings. However, these preliminary castings contained significant gas porosity. Most of this porosity was due to a metal/mould interaction, as H_2 gas was generated from moisture in the mould. Consequently, dry sodium silicate sand/CO_2 moulds were employed to reduce the gas porosity since sodium silicate sand hardened with gas contains negligible moisture. This sand mould is similar to that described by Radhakrishna and Seshan.[122] The melt was poured into a dried mould of height 220 mm and diameter 25 or 50 mm. Steel plates of thickness 13 or 25 mm were used at the base of the mould as shown in Figure 3.1b to promote directional solidification. Four fine T_1-T_2 thermocouples were positioned along the mould axis at 20 mm intervals. The output from these thermocouples during solidification was fed into the recorder.

3-6-2 MELTING AND CASTING

LM25 was melted in a graphite crucible using a H.F. induction furnace. The melt was taken to 750 ^{0}C, then the additions of Sr, Tibal or Sb were made separately. The melt was degassed for 15 minutes using argon gas. The melt was poured from 750 ^{0}C into the prepared mould. 25mm and 50mm diameter and 220mm long bars were cast. Exothermic powder was sprinkled onto the top of the mould to delay its freezing and allow feeding. During solidification cooling curves were recorded as shown in Figure 3.4. From these curves

the total solidification time can be calculated by using the equation;

$$Total\,Solidification\,Time(t_f) = t_2 - t_1 \qquad (3\text{-}3)$$

3-7 MICROSTRUCTURAL EXAMINATION

Sections from the position of the thermocouple and from both of the fracture surfaces from each bar were mounted and polished. No etching was necessary for microscopical examination. Each microstructure was photographed and dendrite arm spacing measurements were made from these photographs for each sample and the mean DAS calculated.

The fracture surface was examined using SEM to analysis the type of fracture and to monitor any porosity in the sample. The SEM was also used to make a full analysis of the intermetallic compounds. The polished surface was carbon coated for this examination.

3-8 DENDRITE ARM SPACING MEASUREMENTS

To calculate the secondary dendrite arm spacing, a line of known length was drawn on the micrograph as shown in Figure 3.5a. The number of dendrite arms intercepting this line was counted. If the number was N then;

$$D.A.S. = \frac{L}{NxM} \qquad (3\text{-}4)$$

where L is a length of the line and M is a magnification.

3-9 FLAKE AND FIBRE SPACING MEASUREMENTS

Flake and fibre spacing measurements were carried out on transverse sections of the specimens, produced in the thermal valve furnace and Bridgman directional solidification apparatus. The line intercept method was adopted to measure flake spacing on selected areas of the micrograph. A line (D) was drawn in a selected area to intercept N flakes; then the flake spacing was found by;

$$\lambda = \frac{1}{M} * \frac{L}{N-1} \qquad (3\text{-}5)$$

Each value of spacing was measured from the average of twenty individual measurements.

The specimens were modified by addition of Strontium (Sr) to give a fibre Si structure. The fibre spacing was estimated on a micrograph of known magnification, M, by counting the number of fibres, N, within a known area, A. The average spacing λ is then found as follows;

$$\lambda = \frac{1}{M} * \sqrt{\frac{A}{N}} \qquad (3\text{-}6)$$

The two methods used to measure flake and fibre spacing are illustrated in Figures 3.5b and 3.5c.

3-10 MECHANICAL PROPERTIES.

3-10-1 SPECIMEN MACHINING AND TENSILE TESTING.

Round tensile specimens conforming to BS4A4 of dimensions (5.6 mm x 30 mm gauge length) were used. No threads were machined on the gripped ends of the tensile specimens.

Tensile tests were carried out on a 100 KN hydraulic Instron 4500 universal testing machine with a constant beam travel speed of 1 mm min^{-1}. The machine was connected to a standard Instron (x-y) plotter. The diameter of each tensile specimen was measured at different points along the gauge length of the specimen using a micrometer and the average diameter and the cross-sectional area were calculated. The specimen was placed in the testing machine and an extensometer (25 mm) attached to its gauge length. A load-extension curve was plotted and was used to determine the ultimate tensile strength (UTS), 0.2% proof stress and the elongation to fracture was calculated by measuring the initial (l_0) and final (l_f) gauge length and using the equation;

$$\%elongation = \frac{l_o - l_f}{l_o} x100 \qquad (3\text{-}7)$$

All tests were carried out at room temperature

3-10-2 HARDNESS MEASUREMENTS

Vickers hardness tests were made on all specimens using the Vickers hardness testing machine with a diamond square-based pyramid. In this test, the two diagonal lengths of the square impression were measured by means of a microscope which had a variable slit built into the eyepiece. The width of the slit was adjusted so that its edges coincided with the corners of the impression.

The diagonal length of the impression was then obtained from a small instrument attached to the slit. The average of the two diagonal lengths was determined and was then converted to Vickers pyramid hardness number by reference to tables provided. The load used in these tests was 2 kg. Five hardness measurements were carried out on each specimen, then the average hardness value of the specimen was calculated.

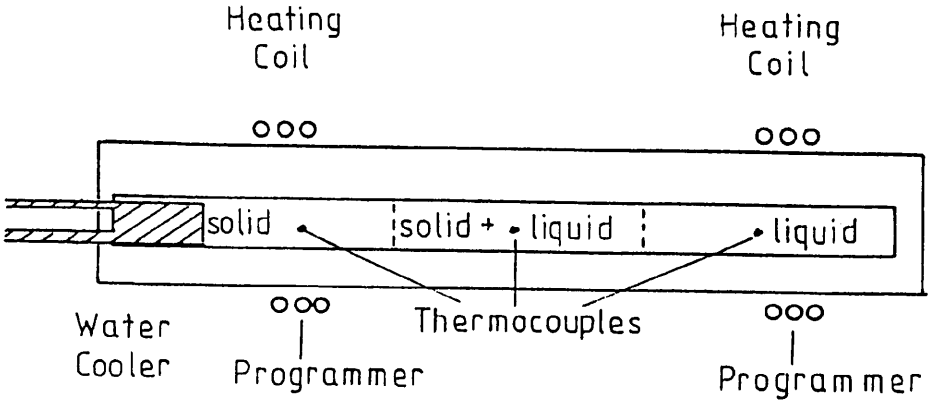

-a-

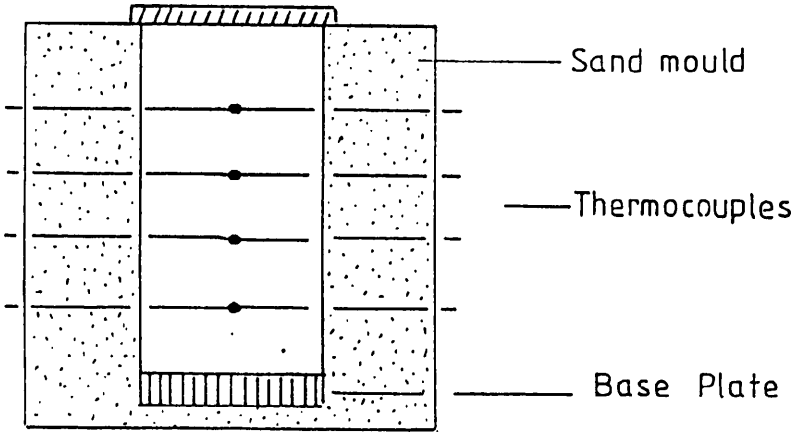

Figure 3.1. **a) the thermal valve furnace.**

b) the sand mould,

c) the Bridgman furnace.

-b-

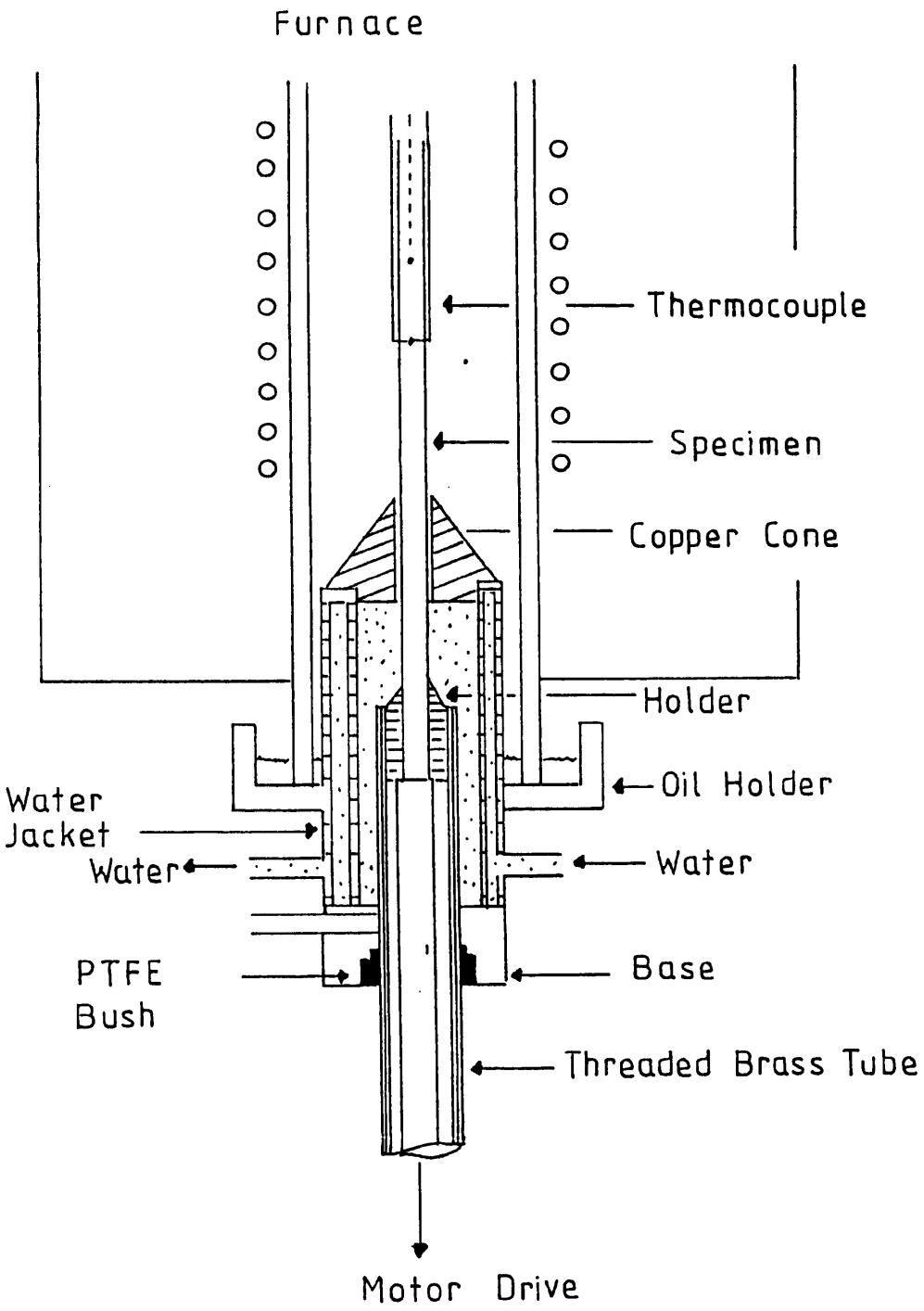
Furnace
Thermocouple
Specimen
Copper Cone
Holder
Oil Holder
Water
Jacket
Water
Water
PTFE
Bush
Base
Threaded Brass Tube
Motor Drive

Figure 3.2. Photograph of the thermal valve furnace.

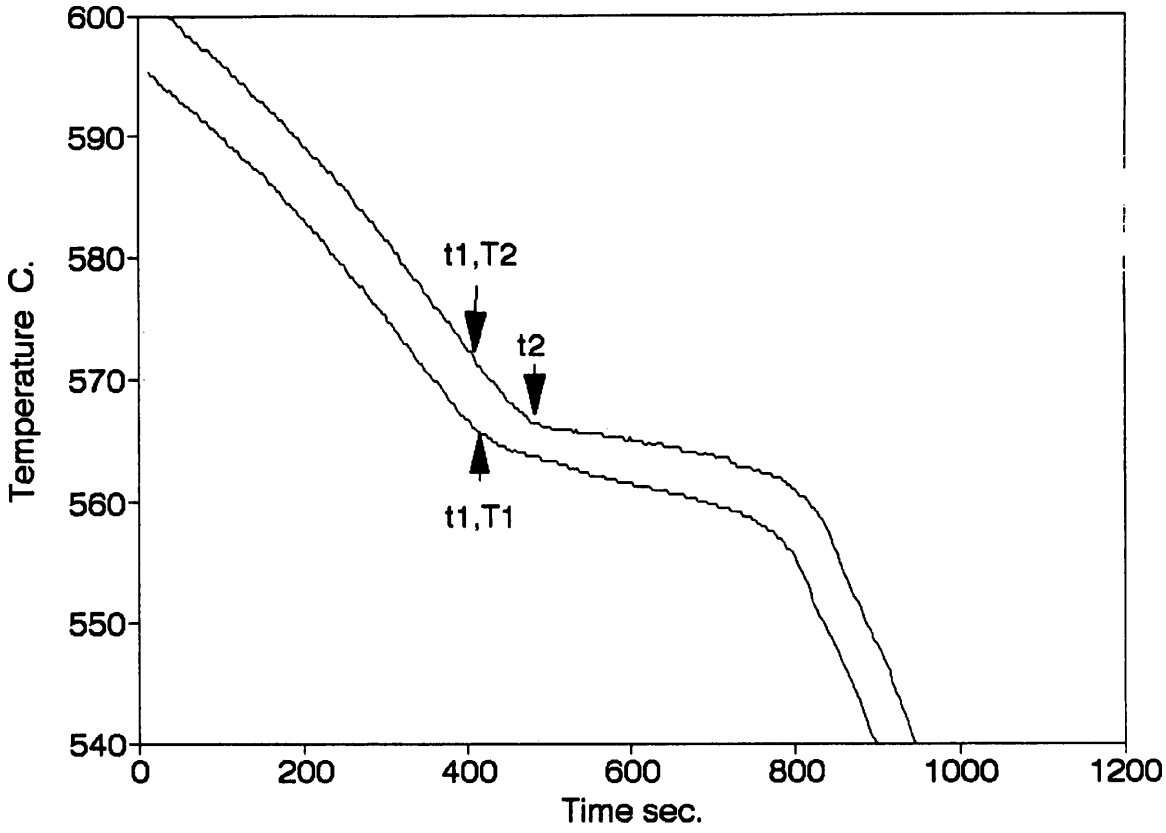

Figure 3.3. Cooling curve of the eutectic alloy.

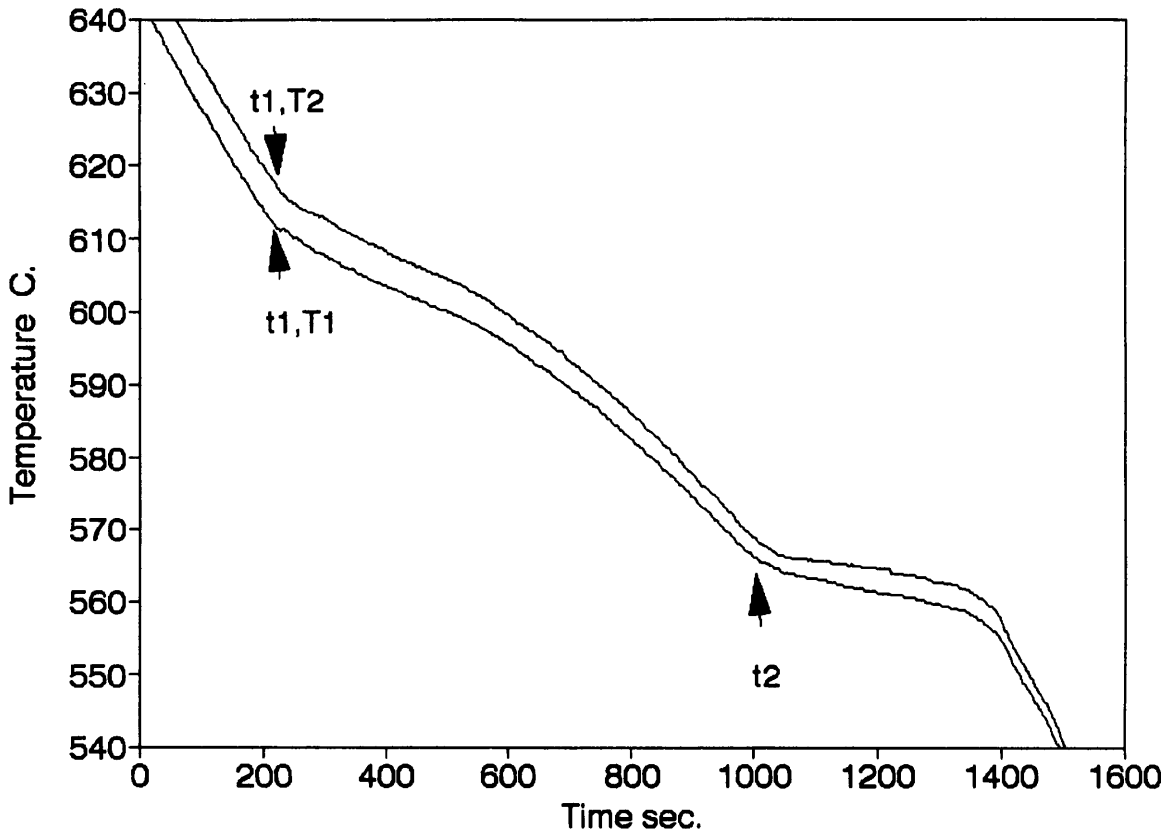

Figure 3.4. Cooling curve for LM25 alloy.

A

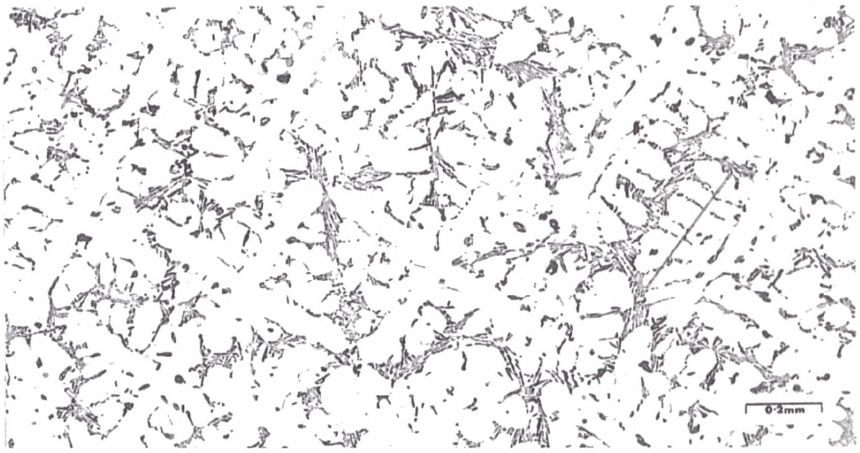

B

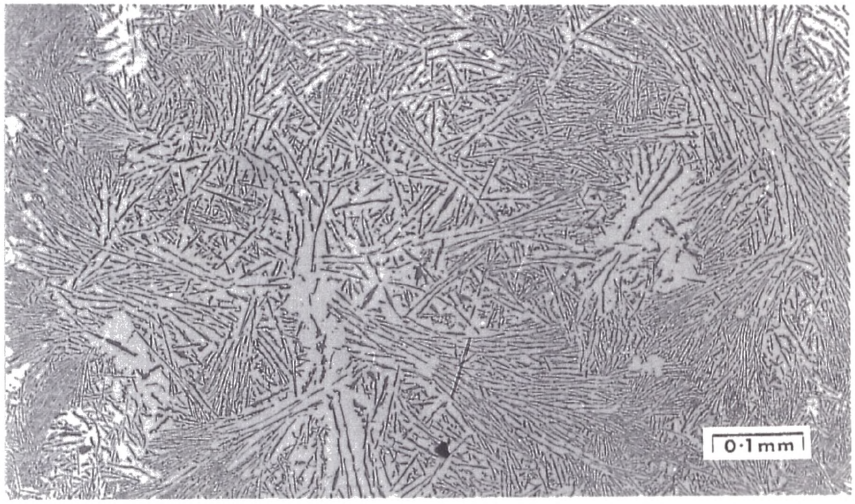

C

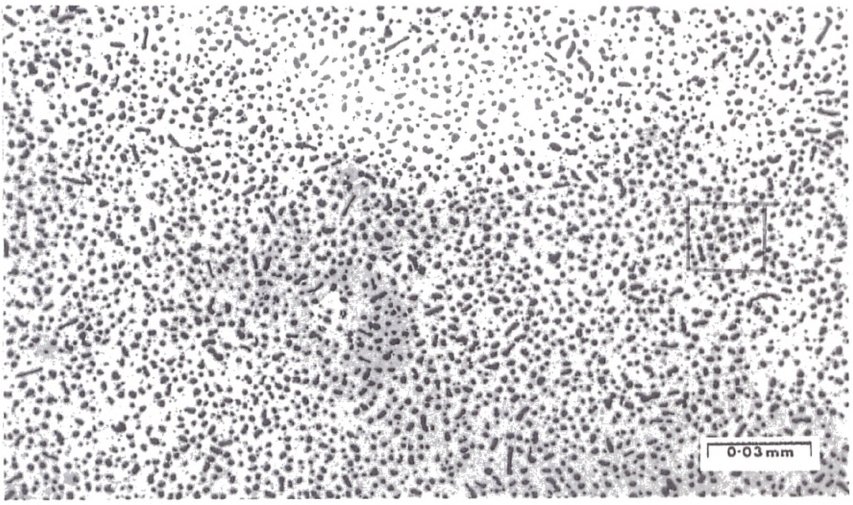

Figure 3.5 The micrographs show how the DAS in the LM25 alloy and interflake and fibre spacing in unmodified Al-12.7%Si and Sr modified Al-12.7%Si eutectic alloys were measured.

a) DAS

b) Interflake spacing.

c) Fibre spacing.

CHAPTER FOUR

EXPERIMENTAL RESULTS AND DISCUSSION. – 1

CHAPTER FOUR

4-1 SOLIDIFICATION CHARACTERISTICS OF STRONTIUM MODIFIED Al-Si EUTECTIC ALLOY.

4-1-1 PREVIOUS WORK.

A small ingot[120-121] has been used to solidify eutectic Al-Si alloy untreated and treated with Sr. It has been shown that different solidification behaviour of strontium modified eutectic alloy is obtained at a cooling rate 7 °C min^{-1}. In the untreated alloy the solidification occurs from the mould wall inwards in a radial direction at a very irregular interface as described by Argo and Gruzleski.[106] In the Sr modified eutectic there is a low density of nucleation sites on the mould wall and the grains grow slowly in a hemispherical fashion from the nucleation centres.

Lateral growth along the mould wall eventually leads to the joining of grains when growth continues in a radial direction but with a scalloped interface. The scalloped interface leaves behind deep liquid channels which can leave a liquid trapped completely by solid. Therefore microporosity can be formed in these parts of the sample.

4-1-2 PRESENT WORK.

Thermal valve and Bridgman furnaces were used to solidified strontium modified alloys of eutectic composition in order to define the influence of growth velocity and temperature gradient on microstructural features.

Figure 4.1-4.4 details the microstructure characteristics of strontium modified eutectic alloys solidified under steady state conditions with growth velocities in the range 10 to 200 μm sec^{-1} and temperature gradient in the liquid between 1.8 and 75 °C cm^{-1} (see Table 4.1). As the G/V ratio decreases constitutional undercooling increases and the eutectic interface becomes more unstable.

At high G/V ratios the interface is near isothermal and regular as shown in Figure 4.5a, and this ratio will produce columnar growth and the structure associated with these ratios is shown Figures 4.1 and 4.6a. As G/V decreases the interface becomes cellular and the growth becomes broken columnar. The structure associated with this type of growth can be called discontinuous columnar (see Figure 4.6b). The cell boundaries are shallow and are easily fed so there is no microshrinkage associated with them. However, as G/V decreases further, the cell boundaries deepen and become inclined to the growth axis. The structure is shown in Figure 4.6c and is produced by equiaxed growth. The interface associated with this type of growth is scalloped as can be seen in Figure 4.5b. Also in this region primary dendrites of aluminium formed as shown in Figures 4.2 and 4.7a. These changes result in an increased difficulty in feeding and microshrinkage porosity formation.

Figure 4.3 shows the region when the liquid channels are formed and indicates that the liquid channels are always associated with equiaxed growth. At very low G/V ratios, eutectic grains nucleate ahead of the interface and microshrinkage voids can form in areas where grains meet. Areas of microshrinkage associated with liquid channels are shown in Figure 4.7b.

TABLE.4.1 The characteristic of the growth of the Al-12.7Si-0.2%Sr alloy solidified in the thermal valve and Bridgman furnaces.

Columnar Growth		Discont. Columnar Growth		Equiaxed Growth	
G $x10^4$ °C μm^{-1}	V $\mu m\ sec^{-1}$	G $x10^4$ °C μm^{-1}	V $\mu m\ sec^{-1}$	G $x10^4$ °C μm^{-1}	V $\mu m\ sec^{-1}$
75	12.15	10.2	20.8	3	20
75	27	14	83	1.8	19.4
75	54	16	83	2.1	77
75	86.15	18	83	5.1	120
75	115	5.6	20.1	5.5	186
75	144	8.5	105	5.5	53
40	12.15	9.5	105	2.5	40
40	27				
40	54				
38	115				
20	18				
17	18				
16	22.9				
18.12	37.12				
15	22.9				
16	22.9				

TABLE.4.1 (Continued)

Free Liquid Channels		Liquid Channels	
G $x10^4$ °C μm^{-1}	V $\mu m\ sec^{-1}$	G $x10^4$ °C μm^{-1}	V $\mu m\ sec^{-1}$
75	12.15	10.2	20.8
75	27	14	16
75	54	14	83
75	86.15	18.12	37.12
40	12.15	3	20
40	54	8.5	105
40	27	9.5	105
16	22.9	18	83.3
14	83	16	83.3
16	22.9	2.5	40
20	18	2.1	77
17	18	1.8	19.4
		5.1	120
		5.5	186
		5.5	53
		38	115
		75	115
		75	144

TABLE.4.1 (Continued)

Eutectic Phase		Al-Primary + Eutectic Phases	
G $x10^4$ °C μm^{-1}	V $\mu m\ sec^{-1}$	G $x10^4$ °C μm^{-1}	V $\mu m\ sec^{-1}$
75	12.15	14	83
75	27	3	20
75	54	1.8	19.4
75	86.15	2.1	77
75	115	5.1	120
40	54	8.5	105
40	27	9.5	105
40	12.15	18	83.3
14	16	16	83.3
16	22.9	38	115
20	18	75	144
17	18		
15	22.9		
18.12	37.12		
5.6	20.1		
10.2	20.8		

TABLE.4.1 (Continued)

Free Nucleation Ahead of Solid/Liquid Interface		Nucleation Ahead of Solid/Liquid Interface	
G $x10^4$ °C μm^{-1}	V $\mu m\ sec^{-1}$	G $x10^4$ °C μm^{-1}	V $\mu m\ sec^{-1}$
75	12.15	1.8	19.4
75	27	3	20
75	54	2.5	40
75	86.15	2.1	77
75	115		
40	54		
40	27		
40	12.15		
14	16		
16	22.9		
20	18		
17	18		
15	22.9		
18.12	37.12		
5.6	20.1		
10.2	20.8		
5.1	120		
5.5	186		
5.5	53		
14	83		
18	83.3		
16	83.3		
9.5	105		
8.5	105		

TABLE.4.1 (Continued)

Free Porosity		Porosity Existence	
G $x10^4$ °C μm^{-1}	V $\mu m\ sec^{-1}$	G $x10^4$ °C μm^{-1}	V $\mu m\ sec^{-1}$
75	12.15	1.8	19.4
75	27	3	20
75	54	2.1	77
75	86.15	2.5	40
75	115	5.1	120
40	54	5.5	186
40	27	5.5	53
40	12.15	8.5	105
14	16	9.5	105
16	22.9		
20	18		
17	18		
15	22.9		
18.12	37.12		
5.6	20.1		
10.2	20.8		
14	83		
18	83.3		
16	83.3		

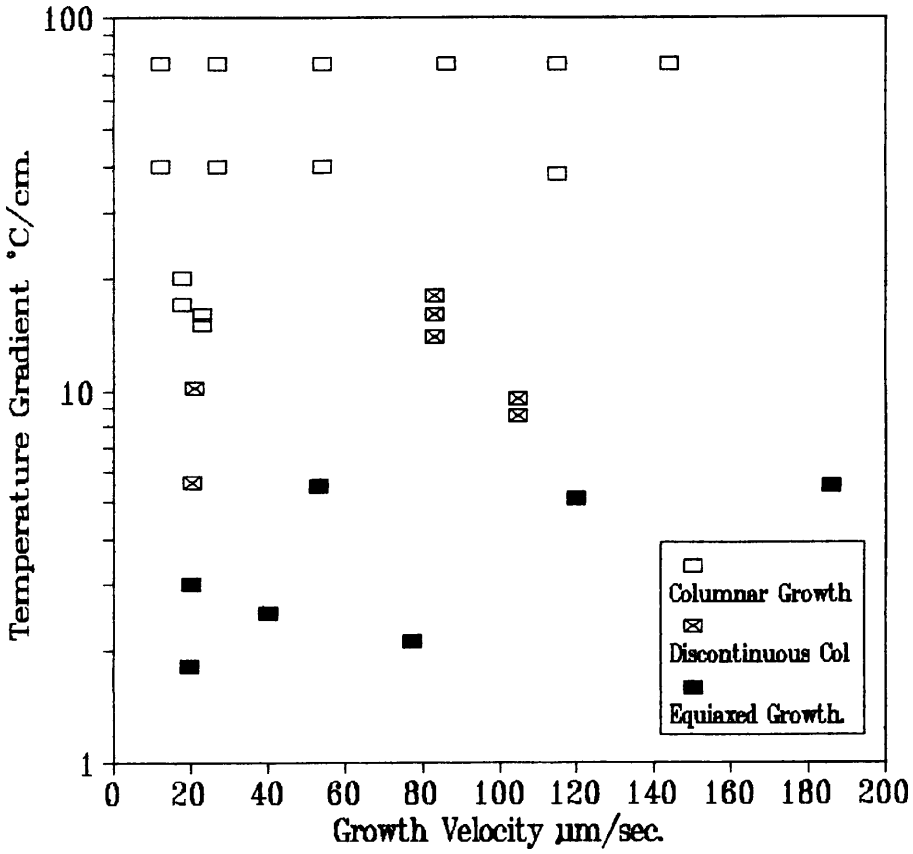

Figure 4.1 The growth structural features of strontium modified eutectic alloys as a function of growth velocity and temperature gradient in the liquid.

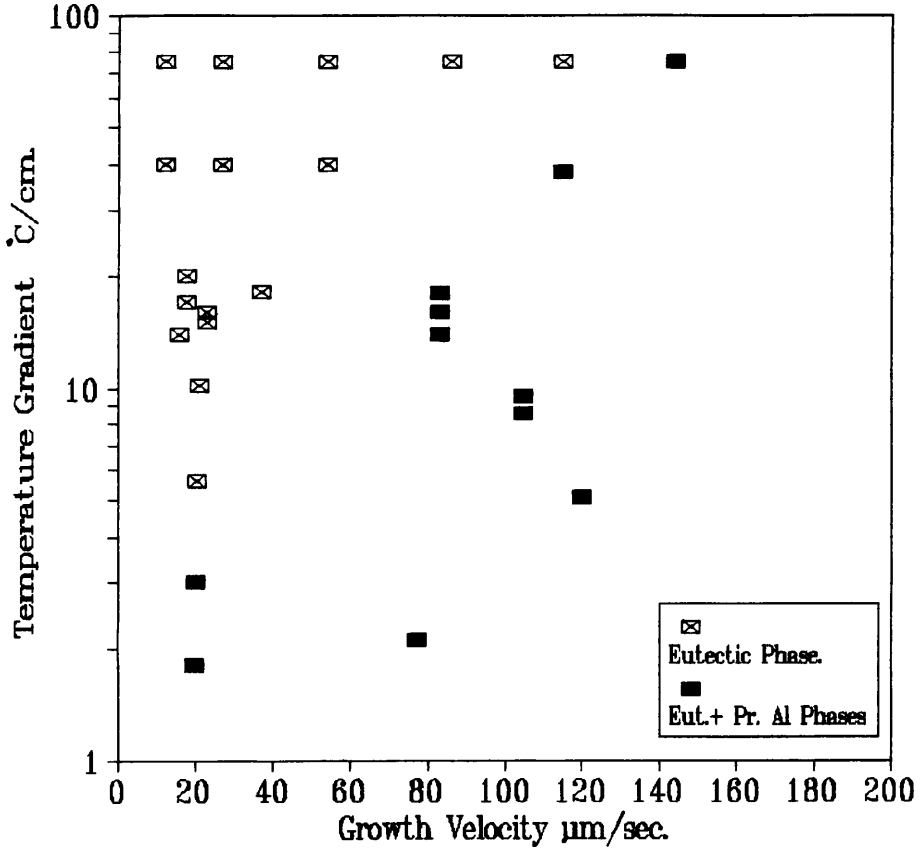

Figure 4.2 The occurrence of primary aluminium dendrites in strontium modified eutectic alloys as a function of growth velocity and temperature gradient in the liquid.

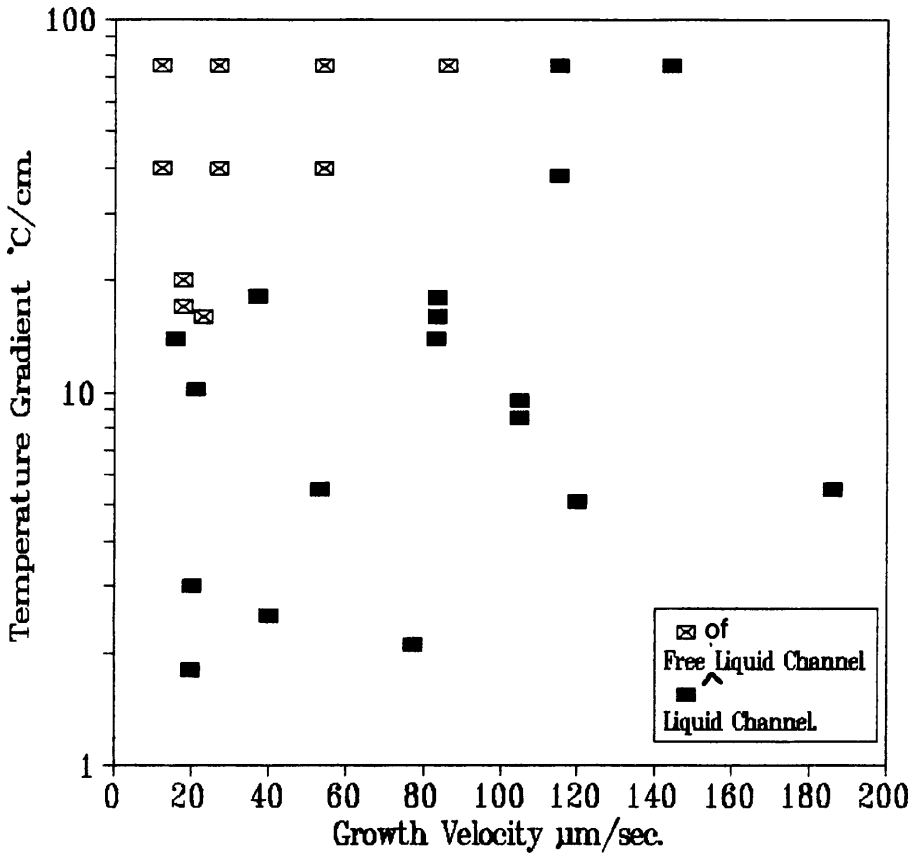

Figure 4.3 The occurrence of liquid channels in strontium modified eutectic alloys as a function of growth velocity and temperature gradient in the liquid.

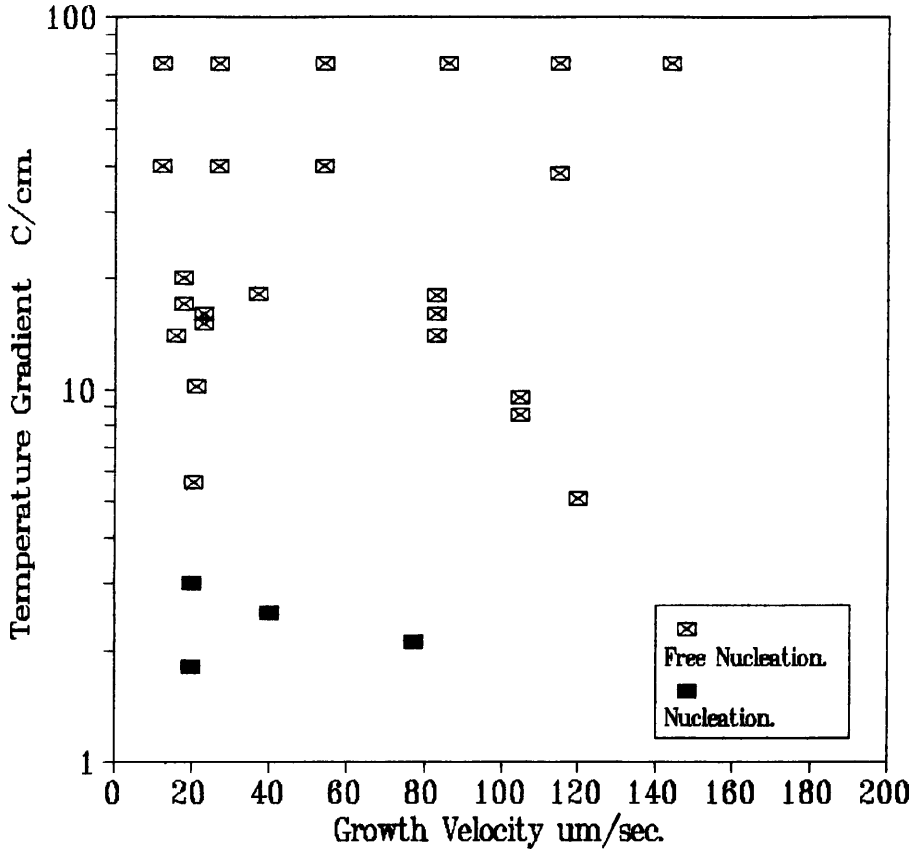

Figure 4.4 The nucleation of eutectic grain ahead of the interface in strontium modified eutectic alloys as a function of growth velocity and temperature gradient in the liquid.

A

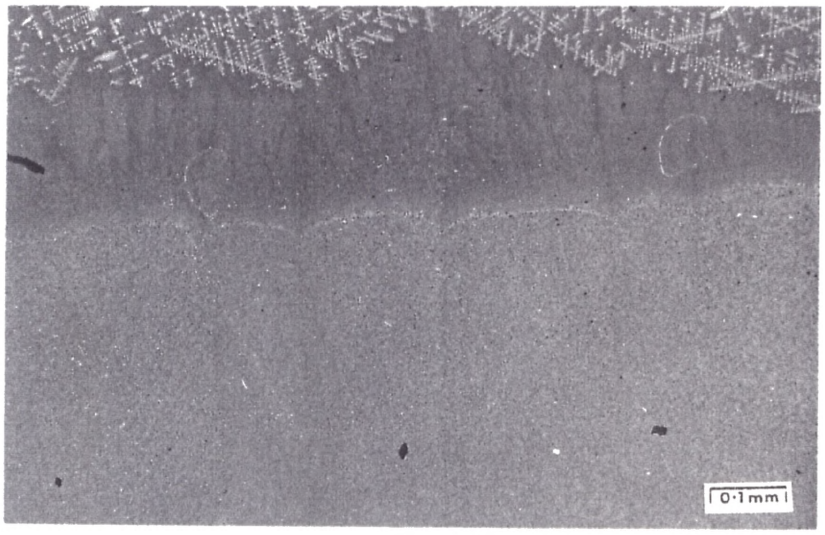

B

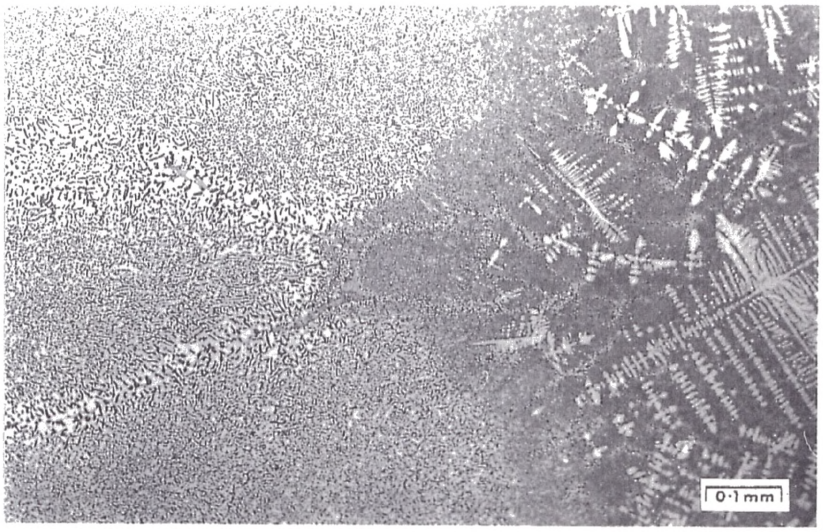

Figure 4.5. Eutectic solid/liquid interfaces revealed by quenching during directional solidification,

a) G = 75 °C cm^{-1}, V = 54 µm sec^{-1}

b) G = 5.6 °C cm^{-1}, V = 20.1 µm sec^{-1}.

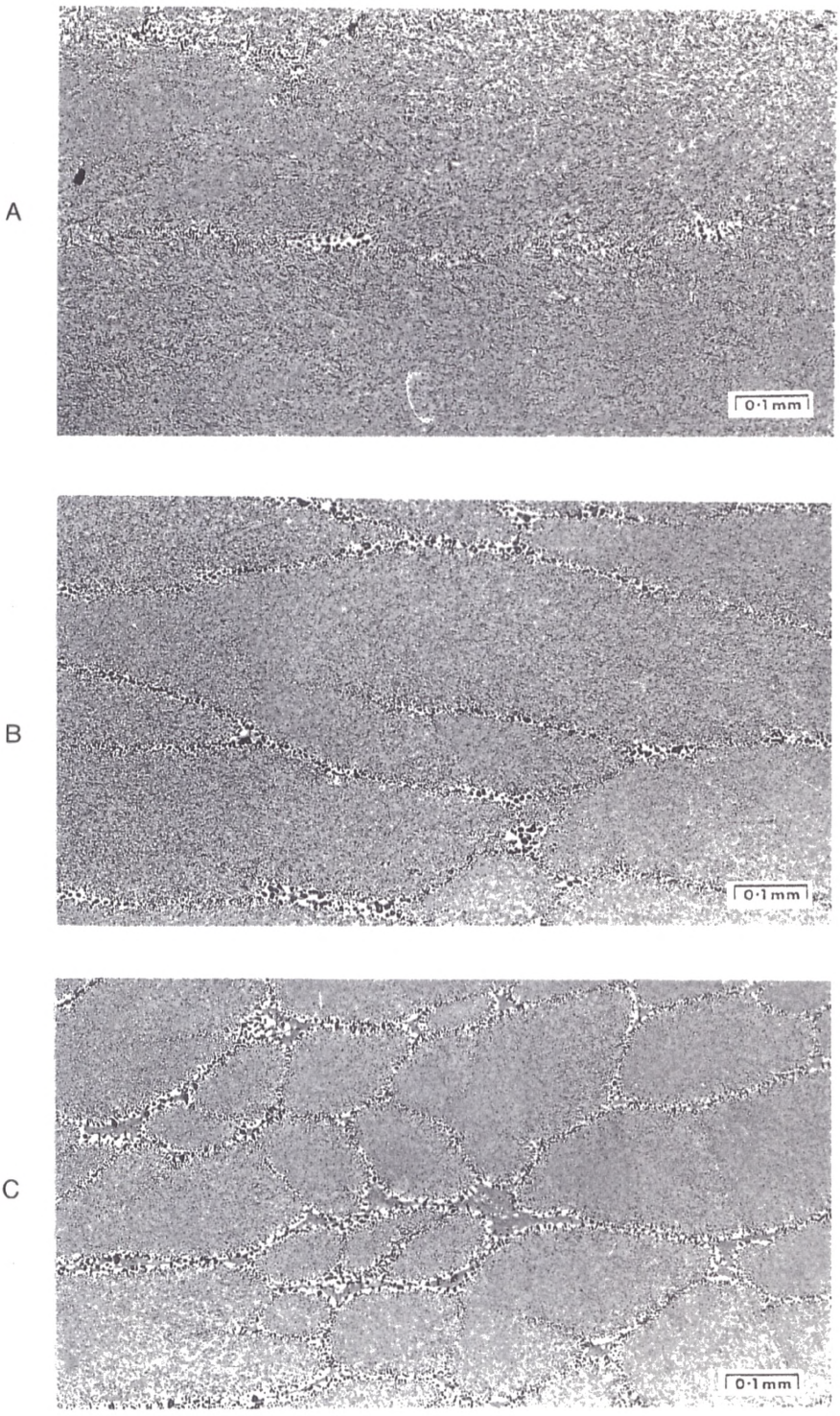

Figure 4.6. Longitudinal section of strontium modified eutectic alloys shows the different type of structure; a) Columnar b) Discontinuous columnar c) Equiaxed structure.

A

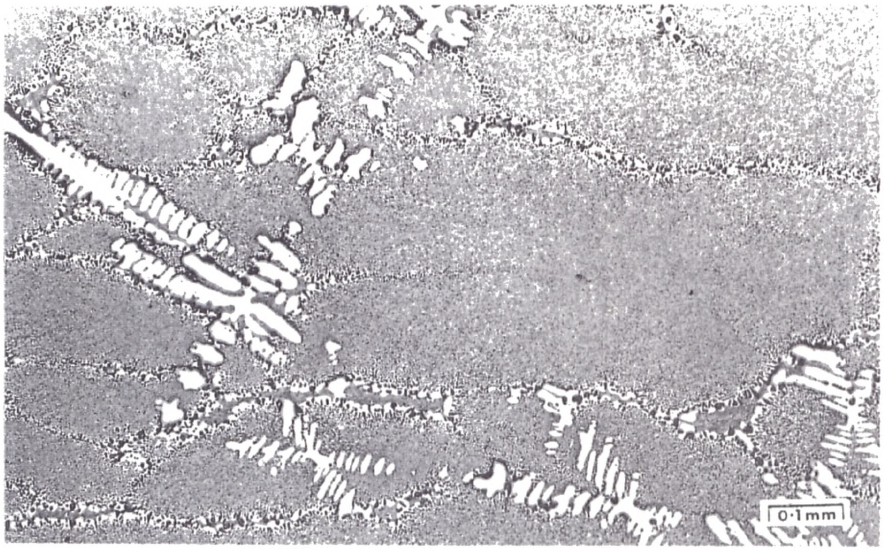

B

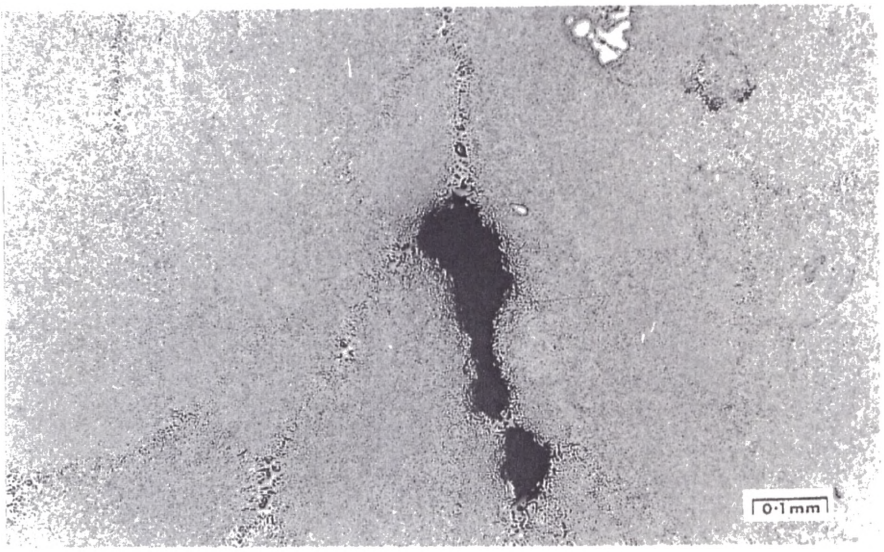

Figure 4.7 Longitudinal section of strontium modified eutectic alloys shows

a) Liquid channels and Al primary phase in alloy solidified with G = 2.5 °C cm^{-1} and V 40 µm sec^{-1}

b) Porosity in the liquid channel G = 3 °C cm^{-1}.

CHAPTER -FIVE-

EXPERIMENTAL RESULTS AND DISCUSSION -2

CHAPTER -FIVE-

MICROSTRUCTURE-SOLIDIFICATION PARAMETER RELATIONSHIPS

Steady state directional solidification studies are described for untreated and treated commercial purity LM25 alloys. This chapter will concentrated in the coarsening of the secondary dendrite arm spacing related with solidification conditions and a different types of treatment to the LM25 alloy. Also the interflake spacing measurements related with growth velocity will be presented for the hypoeutectic and eutectic alloys.

5-1 PRELIMINARY EXPERIMENTS.

A series of LM25 alloys with and without additions were solidified in CO_2 hardened sand moulds using either a 13 or 25mm thick chill plate at the bottom of the mould. Mould diameters were 25 and 50mm. Cooling curves were recorded from four thermocouples placed at measured distances from the chill plate. The solidification time was calculated from these curves. The results obtained for untreated LM25 alloys are shown in Figure 5.1, and recorded in Table 5.1. The square points were obtained with mould of diameter 25mm and the triangular ones with mould of diameter 50mm. A chill plate thickness of 13mm was used for all castings.

The two full lines in Figure 5.1 are the limits of the band of results obtained by Radhakrishna and Seshan[122]. Measurements made at shorter times by Jaquet and Hotz[66] are also shown in Figure 5.1. The difference in the results between the square and triangular points and the scatter observed by the previous authors is due to the dependence of the secondary dendrite arm spacing (DAS) on both temperature gradient and growth velocity. Higher temperature gradients and higher growth velocities result in shorter solidification times and lower DAS However, the experimental arrangement used in the preliminary studies adds to the scatter in the results because both the temperature gradient and the growth velocity fall as the solidification front moves away from the plate. The width of the band may be such as to mask

improvements in properties due to the treatment of the melt. Consequently, it was decided to use a thermal valve solidification technique. The advantage of this method is that the temperature gradient and growth velocity remain constant during solidification and specimens are nearly free of porosity. Porosity was frequently observed in the samples solidified in the sand.

It can be seen that the results for LM25 are within the band suggested by Radhakrishna and Seshan. They lie towards the top of the band because the temperature gradient was very low with the mould diameters used. The temperature gradient in the mould which has a diameter of 50mm is approximately three times greater than that for the mould of 25mm diameter and the DAS of these specimens is lower.

5-2 THERMAL VALVE STUDIES.

A systematic study of the dependence of DAS (λ_f) on the parameters total solidification time, temperature gradient and growth velocity has been carried out. A second specimen has been solidified without a thermocouple to provide tensile test pieces. The occurrence of porosity and intermetallic compounds was monitored in each series of specimens.

5-2-1 LM25 (NO ADDITIONS)

The results presented in Table 5.2, show the total solidification time (t_f), temperature gradient, growth velocity and DAS for untreated LM25 alloys. They are shown by the filled squares in Figure 5.1. The DAS and t_f plotted on a logarithmic scale show a linear relationship. With increasing total solidification time, DAS becomes coarser and vice versa. They lie in the centre of the band for the previous results (see Figure 5.1). If plotted on a DAS vs log t_f graph they can be shown to satisfy the equation;

$$\lambda_f = 23.89 + 48.27\log(t_f) \qquad (5\text{-}1)$$

The results in Table 5.2 with the results obtained using the Bridgman furnace and recorded in Table 5.3 are shown graphically in Figure 5.2, these results display less scatter than those in Figure 5.1 (sand mould) supporting the suggestion that a changing G and V leads to scatter in the results. The results in Figure 5.2 can be fitted to the equation given by:

$$\lambda_f = 10.27 \pm 0.55 t^{0.3 \pm 0.01} \qquad (5\text{-}2)$$

In the previous studies most of the authors[41,45,66,123] chose equation (5-2) to express the relationship between DAS and t_f, but Radhakrishna[122] chose the first one and a good agreement is obtained. The equation describing the Radhakrishna and Seshan[122] results is;

$$\lambda_f = 24.30 + 45.07\log(t_f) \qquad (5\text{-}3)$$

Equation (5-2) is almost the same as the equation found by Jaquet and Hotz[66] for Al7SiMg. Their relationship was;

$$\lambda_f = 9.4 t_f^{0.31} \qquad (5\text{-}4)$$

Flemings[123] work was concerned with Al-4.5%Cu alloy and by combining his results with others[124-127], he concluded that the important solidification parameter affecting final DAS is local solidification time and he used a power function to described his and other findings as shown by;

$$\lambda_f = 7.5 t_f^{0.39} \quad (5\text{-}5)$$

It can be seen that both the power and the constant in the above equation are different than in the present results and may be is due to different materials. Young[41] used Al-4.4%Cu alloy to study the coarsening in the DAS, and he found the value of the power in equation (5-2) is equal to 0.31, which is close to the value found in the present work. A Roosz[45] et al used Al-Cu alloys to investigate the coarsening of dendrite arm spacing and they[45] developed an equation which contains two parameters, the solidification time and composition of the alloy (C_0) given by;

$$\lambda_f = 19.7 C_o^{-0.4} t_f^{0.33} \quad (5\text{-}6)$$

To illustrate the influence of temperature gradient (G) and growth velocity (V) upon the secondary arm spacing DAS, Figure 5.3 shows the data obtained from the LM25 alloy grown using the thermal valve and Bridgman furnaces. It can be seen that the DAS is inversely related with G; therefore, increasing both G and V results in a finer DAS (see Figure 5.4). Also increasing the growth velocity decreases the distance between the Al-tip and eutectic interface and as these materials solidified in the steady state, therefore the growth velocity is equal to;

$$V = \frac{X_m}{t_f} \quad (5\text{-}7)$$

where X_m is the distance between the Al-tip and eutectic interface. However the time t_f that the dendrite spends in the solid/liquid region will reduce. Therefore with higher growth velocity the DAS is reduced, due to the refining the initial spacing and reduction in the time t_f. Many workers [41,45,46,123] reported that the alloy grown at a faster rate has smaller secondary arm spacing. Gu Genda[128] et al. concluded that increasing the velocity V reduces the time t_f or the time the alloy exists between the liquidus and solidus temperature. This reduces the chance of the

joining of the arms.

It is clear that we may express the relationship between G and V with DAS through the empirical equation;

$$\lambda_f = k(G*V)^{-a} \qquad (5\text{-}8)$$

where k and a are all constants. This procedure has been carried out on the data from Table 5.2 and 5.3, for LM25 alloy. Figure 5.5 shows Log.(DAS) plotted against Log.(G*V), showing the variation of the DAS, with the cooling rate (G*V). Thus DAS is increased as the cooling rate decreases. The equation of the best fit line is given by:

$$\lambda_f = 31.93(G*V)^{-0.25} \qquad (5\text{-}9)$$

The third part of the study was concerned with the coarsening of the initial dendritic skeleton during solidification. Dendrite arm spacing measurements were made as a function of distance behind the primary dendrite arm tips on the specimens quenched during directional solidification. The results are recorded in Table 5.4. Measurements were made over 10 arms and the distance behind the interface was measured from the centre of the 10 arms. A typical longitudinal microstructure showing a quenched interface is shown in Figure 5.6. The coarsening of the secondary arms behind the primary arm tips is evident. Figure 5.7 shows the change in DAS with distance behind the primary arm tips. This Figure shows that the initial secondary arm spacing close to the tip depends on the solidification conditions. It decreases as the temperature gradient is increased at constant velocity and as the velocity is increased at constant temperature gradient. The initial spacing in Figure 5.7 decreases in specimen order A,B,C,D. Dendrite modelling[40] predicts that the ratio of primary dendrite tip radius to the initial secondary arm spacing is constant over a wide range of solidification conditions. Consequently, as the tip radius

depends on the tip growth temperature, the initial secondary arm spacing is predicted to decrease as the tip growth temperature decreases (undercooling increases). Dendrite growth theory also predicts the dendrite tip undercooling to vary with G and V according to the equation;

$$\Delta T=\frac{GD}{V}+K*V^{0.5} \qquad (5\text{-}10)$$

This equation is shown in Figure 5.8 where it can be seen that the sequence of specimens in decreasing tip growth temperature is A,B,C,D. This sequence is the same as that given above showing that the initial DAS, λ_o, decreases as the primary dendrite tip growth temperature decreases. Figure 5.8 also suggests that at higher growth velocities the primary tip growth temperature is determined mainly by the growth velocity.

Several models have been proposed for coarsening as illustrated in Figure 5.9. In model[42] I two coarse, identical arm are separated by a finer arm. This arm reduces its thickness by lateral dissolution and shrinks back as the other two arms increase their radius slightly during coarsening. In the second model[129] a neck forms at the root of an arm. With increasing time further remelting occurs at the neck with freezing at areas of lower curvature until the arm becomes disconnected from the main dendrite and gradually spheroidises. Model[43] III considers that a finer dendrite arm between two coarser arms of equal radii gradually shrinks back at constant radius by dissolution at its tip as the radii of the coarser arms increase slightly . Model IV is a coalescence coarsening model proposed by Chien[40] and Young[41]. If different solute concentrations exist at arm roots and tips solute diffusion will occur towards the tips with solid being deposited at the roots. With time the liquid channel between the arms is removed by solidification from the roots to the tips. A second coalescence model, model V, has been proposed recently[128]. Adjacent arms first swell and join at their mid points. This coalescence extends to the tips and roots with time. The driving force for this process is a reduction in the total surface energy of the system. These models are not considered to be mutually exclusive. This

was found to be the case in the present study. Figure 5.10 shows evidence of the operation of the several of the models described above.

Roosz[46] has used the equation;

$$\lambda^3=\lambda_0^3+\int_0^t B.M(T(t))dt \qquad (5\text{-}11)$$

where

$$M(T(t))=\frac{[D_L(T).T.\sigma]}{m_L(T)[1-k(t)].\Delta H.\rho.C_L(T)}$$

and B is a numerical constant (33) related to the geometry of the dendrites, to describe the coarsening behaviour during steady state directional solidification. The numerical analysis of equation (5-11) described by Roosz[46] has been applied to the present system using the constants listed in Table 5.5. However, because of the uncertainty in the diffusion coefficient term it has been assumed to be constant at the value given in Table 5.5 over the freezing range. The results of the analysis are shown in Figure 5.11. The initial dendrite arm spacing was assumed to be zero. Good agreement with experimental measurements is observed. This is particularly true for specimen D confirming that the initial dendrite spacing under these solidification conditions is small. The slope of the calculated relationship for fraction solidified values of between 0.1 and 0.5. The deviation between the two relationships increases continuously as the distance behind the dendrite tips decreases. This is due to a higher value of the initial dendrite arm spacing for specimens A,B and C as discussed above.

When uncertainty exists concerning the value of the system parameters required to perform the numerical analysis coarsening behaviour can be analyzed using an average coarsening parameter, M and the equation;

$$\lambda = (\lambda_o + B.\bar{M}.t)^{0.33} \qquad (5\text{-}12)$$

In steady state directional solidification t and t_f can be expressed in the form $t = X/V$ and $t_f = X_m/V$ where X is the distance behind the interface and X_m is the distance between the dendrite tips and the eutectic interface. Both can be measured from the microstructure of quenched specimens. Measurements made in the present study are recorded in Table 5.4. Roosz[10] has demonstrated that the magnitude of λ_o does not influence the final dendrite arm spacing significantly. Consequently, the average coarsening parameter can be calculated from the relationship;

$$\lambda_f = \left[\frac{B.\bar{M}.X_m}{V}\right]^{0.33} \qquad (5\text{-}13)$$

This relationship is shown in Figure 5.11 from which a value of 22.46 ($\mu m\ sec^{-1}$) is calculated for M assuming that B is 33. The measurements for DAS as a function of distance behind the interface for different G and V values are recorded in Table 5.4 and shown on a logarithmic plot in Figure 5.12. The relationship

$$\lambda^3 = \frac{B.\bar{M}.X}{V} \qquad (5\text{-}14)$$

is shown by the filled circles in Figure 5.12 for each specimen. Good agreement with the numerical analysis is observed for all the specimens indicating that the average coarsening parameter can be used to describe coarsening behaviour. Equations (5-12) and 13 can be used to calculate λ_o values for the different solidification conditions. Calculated values are shown in Table 5.6. These calculations confirm that the initial dendrite spacing in specimen D is small and that the sequence of decreasing λ_o is A,B,C,D. This is the same sequence as that predicted using the dendrite growth model. Roosz showed that the effect of increasing the initial λ_o/λ_f ratio on

the coarsening kinetics of Al-4.4%Cu alloys solidified with G = 24 ^{0}C cm^{-1} and V = 50 μm sec^{-1} was to decrease the average slope of the λ vs X relationship from a value of 0.31 for $\lambda_o/\lambda_f = 0$ to 0.08 for a ratio of 0.5. The present measurements are for different values of G and V but a similar behaviour is evident from Table 5.6.

5-2-2 THE MELT TREATMENT FOR LM25 ALLOY.

5-2-2-1 LM25-0.04%Sr and LM25-0.2%Sb alloys.

An addition of either 0.04%Sr or 0.2%Sb was made to the LM25 alloy in this study. Measurements made with the thermal valve furnace are recorded in Table 5.7 and those with the Bridgman furnace in Table 5.8. The variation of the final dendrite arm spacing, DAS, with the total solidification time, t_f, is shown in Figure 5.13. The dashed line in the Figure defines measurements for LM25 alloy. The variation of spacing with solidification time can be represented by equations;

For LM25 $\lambda_f = 10.27 \pm 0.55 t_f^{0.30 \pm 0.01}$ (5-2)

LM25 –0.04%Sr $\lambda_f = 9.35 \pm 0.45 t_f^{0.30 \pm 0.01}$ (5-15)

LM25 –0.2%Sb $\lambda_f = 8.44 \pm 0.40 t_f^{0.30 \pm 0.01}$ (5-16)

These results show that there is a refinement of the dendrite arm spacing when Sr or Sb are added to LM25. The refining effect is greater with the 0.2%Sb addition. This is evident from the microstructure in Figure 5.14 which are for the same solidification conditions (V = 54 μm sec^{-1}, G = 82 x10^{-4} °C μm^{-1}). As stated in the previous section the larger arms tend to grow at the expense of smaller arms driven by surface energy considerations. The general form of the equation describing secondary arm coarsening is;

$$\lambda_f^3=\lambda_o^3+Kt \qquad (5\text{-}17)$$

where K is a constant. Coarsening behaviour during directional solidification was examined in the previous study using a numerical procedure described by Roosz[10]. It was also shown in the previous section that an adequate analysis could be performed using an average coarsening parameter, M and the equation (5-12). The average coarsening parameter can be calculated from the equation (5-13). This relationship is shown in Figure 5.15 for untreated, Sr and Sb treated LM25 alloys. Values of M calculated using equation (5-13) with B = 33 are 22.46, 20.80 and 15.22 μm sec^{-1} for untreated, Sr and Sb treated alloys, respectively. The decreasing order of average coarsening parameter is the same as that of the total solidification time for constant solidification conditions. This order is, in turn , the same as that of decreasing X_m values as can be see from Table 5.8. It is possible to make some deductions concerning the effect of Sr and Sb additions on the growth temperature of the primary phase dendrite tips using known values of the eutectic growth for the eutectic growth temperature for the solidification conditions used in the present study. These measurements are shown in Table 5.9. Comparing the untreated and Sr treated LM25 alloys at a temperature gradient of 82 °C cm^{-1}, it can be seen that the eutectic growth temperature of the Sr treated alloy is much lower for both growth velocities. As the X_m value for the Sr treated alloy is less than that of the untreated alloy for both velocities, the dendrite tip growth temperature of the Sr treated alloy must be less than that of the untreated alloy. Exactly the same reasoning can be applied for the measurements at the lower temperature gradient of 12 °C cm^{-1}. The same conclusion is drawn when comparing the measurements for the Sb treated alloy solidified under a temperature gradient of 82 °C cm^{-1}. Unfortunately, it is not possible to calculate the dendrite growth temperatures because the temperature gradients recorded in Table 5.9 were measured ahead of the dendritic interface and will decrease from the dendritic interface to the eutectic interface. A decrease of approximately 50% has been reported for the Al-6%Si alloy[130]. This uncertainty in the magnitude of the temperature gradient makes it impossible to make deductions concerning the relative growth temperature of the dendrite tips of Sr and Sb treated alloys. However, the above reasoning provides strong evidence for believing that the

addition of Sr and Sb to LM25 leads to growth of the primary phase at a lower temperature than in the untreated alloy for the solidification conditions used in the present study. This may be due to an influence of Sr and Sb on the solid-liquid interfacial free energy or due to the generation of constitutional undercooling. However, the latter is unlikely with a temperature gradient of 82 °C cm^{-1}. A lower initial dendrite arm spacing, λ_o, might be anticipated if the dendrites grow at a lower temperature. The experimental measurements of spacing as a function of distance behind the dendritic interface are recorded in Table 5.10 and shown in Figures 5.16 and 5.17 for the three LM25 alloys for growth velocities of 54 and 300 μm °C cm^{-1}. These measurements follow equation (5-12). Also shown in the two Figures is equation (5-13). It can be seen in Figure 5.17 that the deviation between the two relationships is minimal indicating that λ_o is very small.

The deviation in Figure 5.16 is greater suggesting larger λ_o values. The difference in the λ_o values of LM25 for two solidification conditions has been discussed before where the higher λ_o value was shown to be associated with a higher growth temperature of the dendrite tip. Equations (5-12) and (5-13) can be used to estimate values for λ_o. The results are shown in Table 5.11. It is evident from this Table that the addition of Sr and Sb results in a lowering of the λ_o value compared to the untreated alloy for both solidification conditions. These findings provide further evidence in support of the earlier conclusion that the addition of Sr and Sb reduces the growth temperature of the dendrite tips. Once again calculation of the λ_o values is not sufficiently accurate to be able to comment on the relative effects of Sr and Sb.

5-2-2-2 LM25 ALLOYS TREATED WITH TiBAL.

The preliminary measurements of DAS as a function of growth velocity are recorded in Table 5.12 and compared to similar measurements for the untreated alloy in Figure 5.18. There is a refinement of the DAS of the untreated LM25 alloy compared with the high purity alloy (Al-7.5%Si-0.45%Mg) for the same solidification conditions. The scatter in the relationships is due to a dependence of DAS on the temperature gradient in the liquid. The refinement is also evident

by comparing Figures 5.19a and 5.19b. The variation of final dendrite arm spacing with solidification time is shown in Figure 5.20 for the untreated alloy and the alloy treated with 2%(3/1 TiBAL). The measurements for the TiBAL treated alloy are recorded in Table 5.13 and 5.14. Table 5.14 shows that, as noted previously, the final dendrite arm spacing is dependent on temperature gradient and growth velocity. The microstructural studies showed that there was a progressive reduction in the grain size with the specimen sequence pure, untreated and (3/1) TiBAL treated alloy. However, the temperature gradient used in the directional solidification experiments was sufficiently high to retain a columnar structure. The reduction in grain size was accompanied by a refinement of the DAS. This is evident from Figures 5.19a, 5.19b and 5.19c. The TiBAL treatment refined the structure as indicated by the relationship;

$$\lambda_f=[9.40\pm0.45]t^{0.30\pm0.01} \qquad (5\text{-}18)$$

compared with

$$\lambda_f=[10.27\pm0.55]t^{0.30\pm0.01} \qquad (5\text{-}2)$$

for the untreated LM25 alloy.

Several models have been proposed for coarsening and each relates K (equation 5-17) to system parameters. For example, Feurer and Wunderlin[44] have presented a model for an alloy of concentration C_o which exceeds the solubility limit and derive the equation;

$$\lambda_f^3.G.V=A^3\ln\left(\frac{C_{EU}}{C_o}\right) \qquad (5\text{-}19)$$

where $A = \phi[D\tau/(1-k)]^{(1/3)}$, with $\phi = 5.5$. C_{EU} is the eutectic composition and k, D and τ are the solute partition coefficient, solute diffusivity in the liquid and the ratio of solid-liqui interfacial

energy to entropy of fusion, respectively.

Measurements made on specimens solidified in the Bridgman furnace after TiBAL treatment and without treatment are expressed in the form of equation (5-19) in Figure 5.21. The value of ϕ calculated using the parameters in Table 5.15 is 4.0 for the untreated alloy. This is close to the theoretical value of 5.5. The value calculated for the TiBAL treated alloy is 3.54. This suggests that the TiBAL treatment influences the coarsening action. A slight reduction in the interfacial energy or in the diffusion coefficient due to the presence of Ti would cause the reduction in the ϕ value.

Measurements made in the this way on alloys treated with 2%(3/1 TiBAL and solidified in the Bridgman furnace are recorded in Table 5.13. The magnitude of λ_o does not influence the λ_f value significantly. Consequently, the average coarsening parameter can be measured from equation (5-13). The relationship between X_m and λ_f is shown in Figure 5.22 from which a value of 20.80 $\mu m\ sec^{-1}$ is calculated for M assuming that B is 33. This value of M is slightly less than that measured for the untreated alloy (22.46 $\mu m\ sec^{-1}$) indicating that the TiBAL treatment has influenced the coarsening process. The relationship

$$\lambda^3 = B.\overline{M}.\frac{X}{V} \qquad (5\text{-}14)$$

is shown in Figure 5.23 by the filled circles for the two growth velocities used in these experiments. The open circles represent the present experimental measurements in the form of equation (5-12). These two relationships can be used to calculate values for λ_o which are given in Table 5.16 with those calculated in the previous section for the untreated LM25 alloy. Dendrite growth theory predicts that the ratio of primary dendrite tip radius to the initial secondary dendrite arm spacing is constant over a wide range of solidification conditions. As the tip radius depends on the tip temperature, so the initial secondary dendrite arm spacing is predicted to decrease as

the dendrite growth temperature decreases. Table 5.16 shows that the initial secondary arm spacing is reduced for each growth condition in the TiBAL treated LM25 alloy. This suggests that the primary dendrite tip temperature is reduced in the presence of TiBAL. In addition, Table 5.16 shows that the X_m value is reduced for each growth condition for the TiBAL treated alloy. A comparison of Figures 5.19b and 5.19c shows that the flake Si eutectic morphology is retained in the TiBAL treated alloy but it is refined. This refinement has been noted previously[132] and is an indirect effect. As can be seen from Figures 5.19b and 5.19c, the presence of the grain refiner has created more primary phase islands and although the volume of the interdendritic liquid is the same the size of the interdendritic pockets is smaller. This effectively promotes a more rapid cooling that generates a finer eutectic spacing. This finer eutectic will grow at a slightly lower eutectic temperature. However, as the Xm value of the treated alloy is reduced, this must mean that the dendrite tip growth temperature in the treated alloy is lower. These observations suggest that when 2% of (3/1) TiBAL is added to the commercial Al-7%Si-0.45%Mg alloy, solidification under the conditions used in the present study results in a decrease in the columnar grain size and a refinement in the secondary dendrite arm spacing that results from an increase in the primary dendrite tip undercooling and a reduction in the extent of coarsening of the secondary dendrite arms during solidification.

Studies of the grain refinement of foundry alloys have shown that the Si and Mg present have a significant effect on the grain refining action. Sigworth and Guzowski[131] suggest that the Si interferes with the grain refining action of Ti and promotes that of B. As a result of these observations it has been suggested and verified that a (3/3) TiBAL grain refiner is more efficient for Al-Si casting alloys. A similar conclusion can be drawn from the results of a study by Apelian and Cheng.[132] Tφndel and Arnberg[133] have also shown that Si influences the grain refining action. Measurements made on an Al-10%Si alloy treated with increasing amounts of (5/1) TiBAL showed that the grain size decreased as the amount of Ti increased. Simultaneously, the dendrite growth temperature first increased up to a Ti concentration of 0.05%, then decreased and for Ti additions in excess of 0.15% increased. These changes are shown in Figure 5.24. They are

considered to be consistent with a shift of the peritectic composition in the Al-Ti system to lower Ti levels in the presence of Si.

Against this background further measurements were made using a (3/3) TiBAL grain refiner. LM25 alloys were treated with 1,2 and 3% of grain refiner and directionally solidified in the Bridgman furnace at a velocity of 54 μm sec^{-1} under a temperature gradient of 82 °C cm^{-1}. Measurements made on quenched alloys are recorded in Table 5.17. Figures 5.19c and 5.19d show that there is a further refinement of the DAS under constant solidification conditions when 2% of (3/3) TiBAL is added instead of 2% (3/1) TiBAL. Figure 5.25 shows how the DAS varies with distance behind the dendrite interface. The relationship shown by the full circles is that given by;

$$\lambda^3 = 19.22 B \frac{X}{V} \qquad (5\text{-}20)$$

The use of only one solidification condition in this part of the study precludes the use of equation (5-13) to calculate a value of M for (3/3) TiBAL addition. However, the points recorded in Figure 5.22 suggest that the value of M is slightly less than that for the (3/1) TiBAL treatment. Indeed, a value of 19.22 for M gives the best fit to the experimental points measured for higher values of X in Figure 5.25. The other points in this Figure are for the different (3/3) TiBAL treatments. The λ_o values shown in Table 5.17 are calculated from Figure 5.25 using the procedure described earlier. It can be seen that the additional refinement is associated with a reduction in the λ_o value and a reduction in the X_m value. This suggests that the DAS refinement is accompanied by a reduction in the dendrite tip growth temperature and a reduction in the rate of coarsening. Increasing the amount of (3/3) TiBAL added from 1 to 3%, corresponding with a change in Ti content from 0.05 to 0.11%, causes a reduction in columnar grain size and a refinement of the secondary dendrite arm spacing. This is accompanied by a reduction in λ_o as shown in Table 5.17. This may be interpreted as a decrease in the dendrite tip growth temperature. This is in agreement with the observations made by Tφndel and Arnberg[133] and

shown in Figure 5.24.

Finally, the last part of the work was concerned with treatment of LM25 done in collaboration with Dogan[134], studies were conducted for a double treatment of 2%(3/1) TiBAL and 0.04%Sr on the DAS of LM25 alloy solidified under different conditions in the thermal valve and Bridgman furnaces. The measurements made in these studies are recorded in Table 5.18 and 5.19. The variation of DAS with growth velocity of alloys solidified in the thermal valve furnace is shown in Figure 5.18. A refinement of the DAS compared to the alloy treated with TiBAL only is evident. This is also evident by comparing the microstructure in Figure 5.19c and 5.19e. The variation of DAS with the total solidification time is shown in Figure 5.20. This leads to the relationship;

$$\lambda_f=[9.03\pm0.30]t_f^{0.30\pm0.01} \qquad (5\text{-}21)$$

The refinement of the final secondary arm spacing is evident when this equation is compared with equation (5-2),(5-15) and (5-18). Figure 5.22 shows the variation of λ_o with X_m/V from which a value of 17.06 is calculated for the average coarsening parameter M. The variation of DAS with distance behind the quenched interface is shown in Figure 5.26. Using equation (5-12) and (5-14) shown in this Figure, the values of λ_o shown in Table 5.20 were calculated. This Table also records measured values of λ_o for untreated, (3/1) TiBAL treated, and 0.04%Sr treated alloys. The λ_o value for the alloy given the double treatment is lower. The same is true of the measured X_m value. These observations show that the double treatment results in the greatest refinement of DAS.

5-3 INTERFLAKE SPACING MEASUREMENTS.

Interflake spacing measurements were made on LM25, Al-7.5%Si-0.45%Mg and Al-12.7%Si alloys directionally solidified in the thermal valve furnace. The results are given in Table 5.21 and

plotted in Figure 5.27. The relationship between interflake spacing and growth velocity are described by equation of the form;

$$\lambda = bV^{-n} \qquad (5\text{-}22)$$

where b and n are constant,

It can be seen from Figure 5.27 that all the points belong to different alloys can be fitted by just one equation given by;

$$\lambda = 41.4V^{-0.38} \qquad (5\text{-}23)$$

Interflake spacing in the Al-12.7%Si alloy has been reported on several occasions[135-137] in the literature. All the measurements have been described in terms of the equation 5-22, with values of n varying from 0.33 to 0.50. The different microstructure models[138-139] of the eutectic reaction also predict a value of n in this range.

5-4 INTERMETALLIC MEASUREMENTS.

The length of the intermetallic (β) measurements were made on LM25 alloy are recorded in Table 5.22 and is plotted against the growth velocity in Figure 5.28a and against the DAS in Figure 5.28b with previous results[67]. There is a good agreement between the present results and the previous ones[67] when the D.A.S., exceeded 70 μm (see Figure 5.28b), but the present curve lies below the curves found by Gustafasson[16] when the D.A.S. is less than 70 μm. The relationship between the length of the intermetallic and growth velocity is described by an equation of the form;

$$Length of(\beta) Intermetallic = 700.7V^{-0.51} \qquad (5\text{-}24)$$

TABLE 5.1. Measurements made with sand mould for LM25 alloy.

Mould Diameter mm	DAS µm	Solidification Time sec.
25	46.64	81.6
	51.46	97.8
	56.22	105.6
	57.90	112.8
	64.23	134.4
50	46.91	136.8
	51.97	166.8
	63.15	282.6
	68.29	304.2

TABLE 5.2. Measurements made with the thermal valve furnace for LM25 alloy.

Temperature Gradient $x10^4\ ^0C\ \mu m^{-1}$	Growth Velocity $\mu m\ sec^{-1}$	Solidification Time sec	DAS μm
10.7	70.0	534	65.68
19.0	78.0	414	62.00
13.0	37.7	840	81.9
3.00	57.5	834	71.9
11.0	151.5	240	56.3
5.00	188.8	240	51.3
7.50	60.6	920	73.0
18.0	56.3	390	69.6
12.0	83.3	438	60.4
5.30	48.8	830	81.9
15.0	46.3	606	67.5
10.0	68.0	612	68.8
6.00	256.0	186	46.87

TABLE 5.3. Measurements made with thermal valve and Bridgman furnace for LM25 alloy.

G $x10^4$ °C μm^{-1}	V $\mu m\ sec^{-1}$	DAS μm	Distance Behind Interface μm	Time sec
82	54	45.40	6900	127.7
82	300	25.66	5100	17.00
12	54	73.03	36000	654.5
12	111	56.50	31900	287.3

TABLE 5.4. DAS measurements of LM25 alloys solidified in the thermal valve and Bridgman furnace.

$G = 12 \times 10^{-4}\ ^0C\ \mu m^{-1}$ $V = 54\ \mu m\ sec^{-1}$		$G = 12 \times 10^{-4}\ ^0C\ \mu m^{-1}$ $V = 111\ \mu m\ sec^{-1}$	
Distance Behind Interface μm	D.A.S μm	Distance Behind Interface μm	D.A.S μm
200	27.3	200	23.1
1000	35.8	1000	27.9
1800	40.1	2200	33.0
2600	43.5	7500	39.9
5400	50.2	10800	44.3
6200	51.6	15600	48.6
11400	58.9	20500	53.0
16400	67.3	26000	53.6
33600	73.0	31900	56.5
37400	73.0		
$G = 82 \times 10^{-4}\ ^0C\ \mu m^{-1}$ $V = 54\ \mu m\ sec^{-1}$		$G = 82 \times 10^{-4}\ ^0C\ \mu m^{-1}$ $V = 300\ \mu m\ sec^{-1}$	
90	18.2	170	7.8
420	21.2	530	10.7
720	23.6	560	12.0
1120	25.7	930	14.0
2640	33.3	1340	15.5
4300	37.3	1770	16.3
6460	43.4	2700	18.9
7370	44.9	3660	21.9
8050	45.1	4490	23.4
		4910	25.3
		5340	25.7
		8000	26.5

TABLE 5.5. System parameters used in the numerical calculations.

σ	surface energy	0.44 J m^{-2}
ρ	density	2.46 x 10^3 Kg m^{-3}
ΔH	latent heat of solidification	389 x10^3 KJ Kg^{-1}
m_L	liquidus slope	8.3 °C wt%$^{-1}$
k	partition coefficient	0.119
B	geometric factor	33
C_o	average concentration of alloy	7.1 %Si
C_E	eutectic composition	12.6 %Si
T_L	liquidus temperature	613.5 °C
T_E	eutectic temperature	577 °C
D_L	diffusion coefficient	5 x10^{-9} m^2 sec^{-1}

TABLE 5.6. Initial dendrite arm spacing measurements for LM25 alloy.

Specimen	Initial Spacing µm	Average Slope	λ_o/λ_f Ratio
A	24.78	0.18	0.37
B	23.7	0.19	0.42
C	17.05	0.18	0.37
D	3.00	0.31	0.07

TABLE 5.7. Measurements made with the thermal valve furnace.

Temperature Gradient $x10^{+4}$ ^0C μm^{-1}	Growth Velocity $\mu m\ sec^{-1}$	Solidification Time sec	DAS μm
LM25-0.04%Sr alloy.			
11.0	133	300	56.3
11.0	128	360	50.9
4.00	291	360	55.0
7.50	158	402	56.44
11.5	190	222	49.1
5.10	333	216	47.51
12.0	67	438	62.8
7.50	115	462	59.7
10.5	64	702	61.35
6.80	88	696	68.3
5.00	57	1128	77.07
17.0	77	330	57.7
12.5	107	342	57.3
13.0	81	426	56.7
9.00	115	426	49.83
4.20	88	888	72.24
7.50	67	948	74.23
7.00	87	732	66.77
6.00	83	696	66.17
LM25-0.2%Sb alloy.			
8.0	73	474	60.5
7.0	97	510	58.9
4.0	192	504	59.6
		516	61.2
3.6	389	347	51.3
15.0	106	347	50.9
		391	52.0

TABLE 5.8. Measurements made with thermal valve and Bridgman furnace.

Type of Alloy	G $x10^{+4}$ °C μm^{-1}	V $\mu m\ sec^{-1}$	DAS μm	Distance Behind Interface cm	Time sec
LM25-0.04%Sr	12	54	67.50	3.46	629.1
	82	54	41.37	0.65	120.3
	82	300	23.10	0.47	15.66
LM25-0.2%Sb	82	54	35.3	0.508	94.07
	82	300	18.8	0.442	18.73

TABLE 5.9. Eutectic interface growth undercoolings.

G $x10^{+4}$ °C μm^{-1}	V $\mu m\ sec^{-1}$	Undercooling Al-Si °C	Undercooling Al-Si-Sr °C	Undercooling Al-Si-Sb °C
82	54	2.0	11.0	7.5
82	300	7.0	18.0	16.0
12	54	6.0	11.0	

TABLE 5.10. DAS Measurements of alloys solidified in the Bridgman furnace.

LM25-0.2%Sr $G = 82 \times 10^{-4}\ ^{0}C\ \mu m^{-1}$ $V = 54\ \mu m\ sec^{-1}$		LM25-0.2%Sb $G = 82 \times 10^{-4}\ ^{0}C\ \mu m^{-1}$ $V = 54\ \mu m\ sec^{-1}$	
Distance Behind interface µm	DAS µm	Distance Behind interface µm	DAS µm
90	13.88	30	12.71
180	14.124	240	16.95
670	23.54	570	21.18
1250	24.71	650	21.18
2350	30.01	1260	26.48
3640	35.32	1650	28.24
4600	37.3	2750	32.3
5850	40.05	3600	33.9
6010	41	4620	34.88
6990	41.54	5100	35.3
8840	41.31	5460	35.3

TABLE 5.10 Continued.

Distance Behind interface μm	DAS μm	Distance Behind interface μm	DAS μm
$G = 82 \times 10^{-4}\ ^{0}C\ \mu m^{-1}$ $V = 300\ \mu m\ sec^{-1}$		$G = 82 \times 10^{-4}\ ^{0}C\ \mu m^{-1}$ $V = 300\ \mu m\ sec^{-1}$	
130	5.34	21	5.33
350	8.91	74	5.77
510	9.7	298	8.52
780	11.88	447	10.6
1120	13.5	852	11.8
1540	15.27	1172	13.3
2280	17.12	1599	13.8
2580	18.8	1833	14.2
3280	20.2	2771	15.9
4170	22.3	3784	17.7
4380	23	4264	18.4
4860	23.39	5330	18.8
5190	23.42	6044	18.85
6700	23.5		

TABLE 5.11 Initial dendrite spacing calculations.

Specimen	Temperature Gradient $x10^4$ °C μm^{-1}	Growth Velocity $\mu m\ sec^{-1}$	Final Spacing μm	Initial Spacing μm
LM25	82	54	45.40	17.05
LM25 + Sr	82	54	41.40	10.52
LM25 + Sb	82	54	35.30	12.85
LM25	82	300	25.70	3.00
LM25 + Sr	82	300	23.10	1.20
LM25 + Sb	82	300	18.80	1.70

TABLE 5.12. The variation of DAS with growth velocity of high purity Al-7.5%Si-0.45%Mg alloys solidified in the thermal valve furnace. Temperature gradient < $15 x10^{-4}$ °C μm^{-1}.

DAS μm	Growth Velocity $\mu m\ sec^{-1}$
72.9	180.7
55.1	332.5
83.8	117.2
88.2	97.4
54.6	337.8
96.2	61.6

TABLE 5.13. DAS measurements of LM25 alloys treated with 2wt.%TiBAL and solidified in the thermal valve furnace.

Temperature Gradient $x10^4$ °C μm^{-1}	Growth Velocity $\mu m\ sec^{-1}$	Solidification Time sec	DAS μm
12	49.75	624	69.00
8	74.00	690	69.10
4	114.9	876	66.90
12	80.00	444	63.20
9	101.1	450	59.40
11	151.5	264	53.13
7.5	208.3	270	48.70
10	166.0	252	48.94
5	333.0	258	52.30
15	62.00	432	62.85
11	83.33	438	61.65
11	196.4	198	45.20
6	200.0	198	48.80
13.5	83.30	390	54.42
8	133.3	390	60.43
4	70.00	1140	74.59
8	47.59	1134	77.70
13.5	77.5	426	55.15
9	86.20	480	59.99
4	104.0	916	68.90

TABLE 5.14. DAS measurements of LM25 alloys treated with 2wt.%TiBAL(3/1) and solidified in the Bridgman furnace.

Growth Velocity μm sec^{-1}	Temperature Gradient $x10^4$ °C μm^{-1}	Distance Behind Interface μm	Solidification Time sec	DAS μm
54	82	6760	125.1	42.6
300	82	5060	16.86	22.8
54	12	34500	627.3	68.92

LM25-2%TiBAL G = 82 $x10^{-4}$ ^{0}C μm^{-1} V = 54 μm sec-1		LM25-2%TiBAL G = 82 $x10^{-4}$ ^{0}C μm^{-1} V = 300 μm sec-1		LM25-2%TiBAL G = 12 $x10^{-4}$ ^{0}C μm^{-1} V = 54 μm sec-1	
Distance Behind Interface μm	DAS μm	Distance Behind Interface μm	DAS μm	Distance Behind Interface μm	DAS μm
120	11.80	30	5.32	100	27.20
450	17.73	110	6.65	300	40.80
700	21.00	230	8.68	850	48.80
1110	23.60	380	10.64	1060	54.20
2200	28.80	630	11.19	3770	68.90
3400	33.39	1120	13.01	4130	68.90
3950	36.51	1820	16.20	20000	62.80
4780	38.55	2570	17.50	25000	65.40
6920	42.60	3250	19.50	29300	67.90
8900	42.68	4380	21.90	36000	68.90
		5170	22.68		
		6230	22.82		

TABLE 5.15. System Parameters.

Distribution coefficient	K	0.119 K.wt%$^{-1}$
Diffusion	D	5x10^{-9} m^2 se:$^{-1}$
Gibbs-Thompson parameter	τ	1.8x10^{-7} K.m

TABLE 5.16. Calculated λ values and measured values for untreated and (3/1) TiBAL treated LM25 alloys.

Solidification Condition		Untreated Alloy		TiBAL Treated Alloy	
G x10^4 °C µm^{-1}	V µm sec^{-1}	λ_o µm	X_m µm	λ_o µm	X_m µm
12	54	27.78	36000	25.60	34500
82	54	17.05	6900	11.58	6760
82	300	3.00	5100	2.85	5060

TABLE 5.17. DAS measurements of LM25 alloys treated with 1, 2 and 3wt% (3/3) TiBAL and directionally solidified with G = 82 °C cm^{-1} and V = 54 µm sec^{-1} in the Bridgman furnace.

Treatment	DAS µm	Solidification Time sec	λ_o µm	X_m µm
1wt% TiBAL	41.6	122.7	16.2	6630
2wt% TiBAL	40.7	115.2	10.3	6220
3wt% TiBAL	40.1	106.1	4.5	5730

1%TiBAL G = 82 x10^{-4} °C μm^{-1} V = 54 µm sec^{-1}		2%TiBAL G = 82 x10^{-4} °C μm^{-1} V = 54 µm sec^{-1}		3%TiBAL G = 82 x10^{-4} °C μm^{-1} V = 54 µm sec^{-1}	
Distance Behind Interface µm	DAS µm	Distance Behind Interface µm	DAS µm	Distance Behind Interface µm	DAS µm
68	17.18	136	13.88	111	11.11
272	20.45	266	18.51	488	15.80
797	19.48	711	22.22	1222	24.64
1636	22.72	955	23.8	2155	29.62
2818	31.25	2933	25.92	4111	33.33
3840	35.71	4400	36.03	5288	38.88
5613	38.96	5266	38.88	5730	40.10
6600	41.6	6220	40.70		

TABLE 5.18. DAS measurements of LM25 alloys treated with 2wt% (3/1) TiBAL and 0.04%Sr and in the thermal valve furnace.

Temperature Gradient $x10^4$ °C μm^{-1}	Growth Velocity $\mu m\ sec^{-1}$	Solidification Time sec.	DAS μm
9.3	101.9	340.6	50.9
7.5	166.7	378.2	53.0
13.3	42.6	740.0	68.8
15.0	40.3	866.4	64.8
17.3	17.3	1450.0	74.8
24.0	9.9	1251.0	74.4
12.5	79.4	390.0	61.1
16.9	39.1	634.2	64.6

TABLE 5.19. DAS measurements of LM25 alloys treated with 2wt% (3/1) TiBAL and 0.04%Sr and directionally solidified in the Bridgman furnace.

G $x10^4$ °C μm^{-1}	V $\mu m\ sec^{-1}$	DAS μm	Solidification Time sec	λ_o μm	X_m μm
82	54	40.0	116.0	7.7	6265
82	300	19.8	17.1	1.0	4600
32	54	54.4	318.5	18.2	17200

TABLE 5.19. Continued (D.B.I. Distance Behind Interface).

$G = 82 \times 10^{-4}$ °C µm^{-1} V = 54 µm sec^{-1}		$G = 82 \times 10^{-4}$ °C µm^{-1} V = 300 µm sec^{-1}		$G = 32 \times 10^{-4}$ °C µm^{-1} V = 54 µm sec^{-1}	
D.B.I. µm	DAS µm	D.B.I. µm	DAS µm	D.B.I. µm	DAS µm
40	10.0	42	4.7	54	18.6
150	12.5	100	5.6	100	19.9
390	16.7	150	6.2	633	22.4
960	20.0	310	7.1	1000	23.2
1060	25.0	440	10.3	4100	32.7
1140	25.0	700	10.9	5347	37.6
2170	25.4	800	11.2	6122	37.0
2300	30.0	1300	13.4	8776	42.0
2820	31.4	1600	14.8	11429	44.8
3640	33.3	1900	16.0	13592	49.7
4380	34.0	2800	16.8	15592	51.0
4480	35.0	3600	16.9	15700	53.1
5200	40.0	4200	18.5	17200	54.4
5620	40.0	5000	19.8		
6290	40.2	8900	20.5		

TABLE 5.20. Calculated λ_o values for differently treated LM25 alloys.

Solidification Condition	Untreated λ_o μm	3/1 TiBAL Treated λ_o μm	0.04%Sr Treated λ_o μm	3/1 Tibal-0.04%Sr Treated λ_o μm
G=82 V=54	17.05	11.58	10.52	7.70
G=82 V=300	3.00	2.85	1.20	1.00
G=12 V=54	27.78	25.60	---	---

TABLE 5.21 Interflake spacing measurements of Al-12.7%Si, Al-7.5%Si-0.45%Mg and LM25 alloys solidified in the thermal valve furnace.

Al-12.7%Si		Al-7.5%Si-0.45%Mg		LM25	
λ μm	V μm sec^{-1}	λ μm	V μm sec^{-1}	λ μm	V μm sec^{-1}
4.550	312.2	5.58	180.72	6.20	140.26
5.160	221.5	4.48	332.51	8.75	49.66
6.487	118.9	6.521	117.23	4.96	239.85
5.920	153.3	4.278	377.81	5.90	159.34
5.906	152.3	6.971	97.36	7.15	94.42
5.314	207.6	8.223	61.55		

TABLE 5.22 Intermetallic length measurements of LM25 alloys solidified in the thermal valve furnace.

V $\mu m\ sec^{-1}$	DAS μm	I.L.(β) μm	V $\mu m\ sec^{-1}$	DAS μm	I.L.(β) μm
56.3	69.6	90.64	68.0	68.8	87.46
104.1	60.4	68.34	188.8	51.3	52.73
57.5	71.9	89.75	70.7	65.7	81.07
48.8	81.9	101.81			

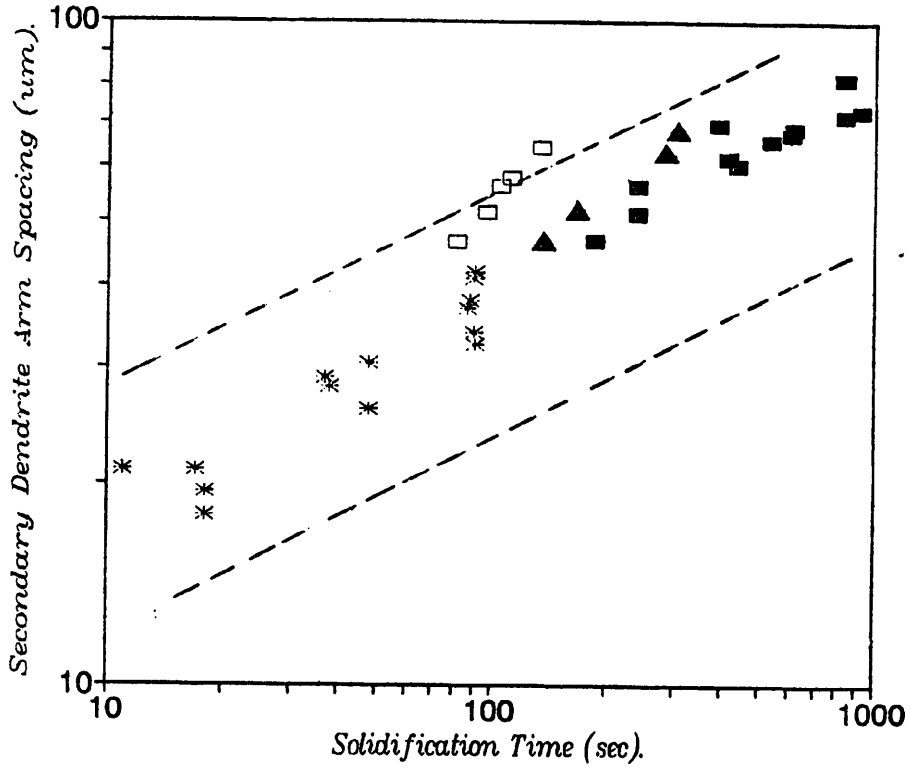

Figure 5.1. Variation of the secondary dendrite arm spacing, DAS with total solidification time, t_f using the thermal valve furnace and sand mould.

* measurements from ref.66.

---- limits of measurements from ref.122.

□ present measurements, low temperature gradient.

▲ present measurements, higher temperature gradient.

■ present measurements using thermal valve furnace.

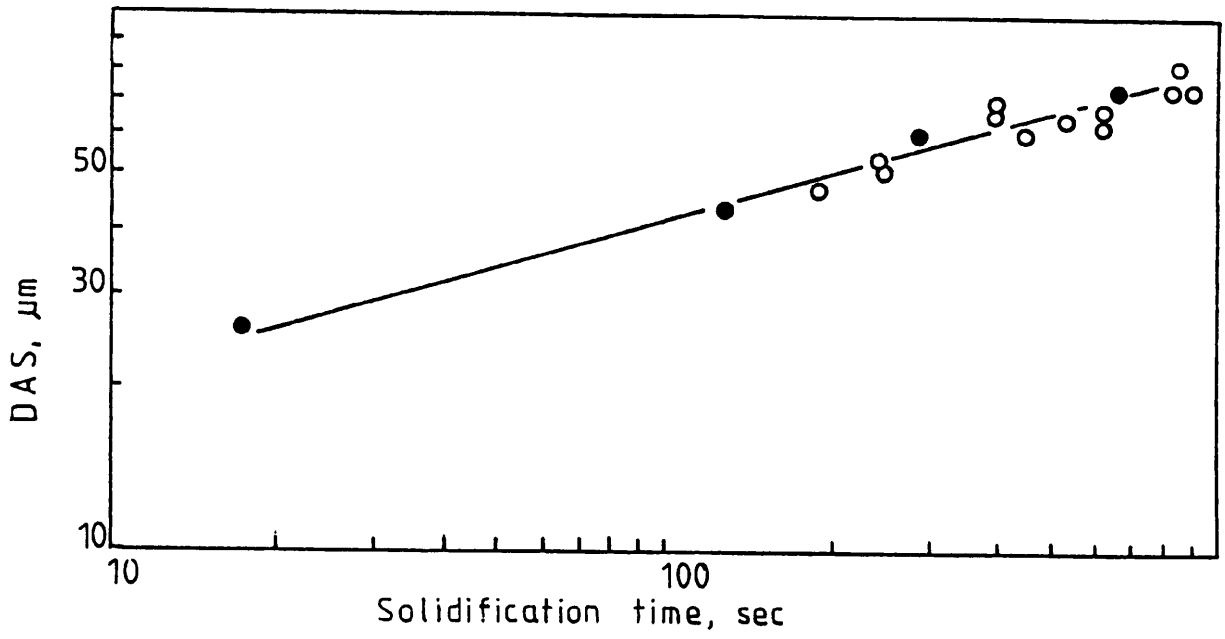

Figure 5.2. Variation of DAS with total solidification time

0 thermal valve furnace

● Bridgman furnace.

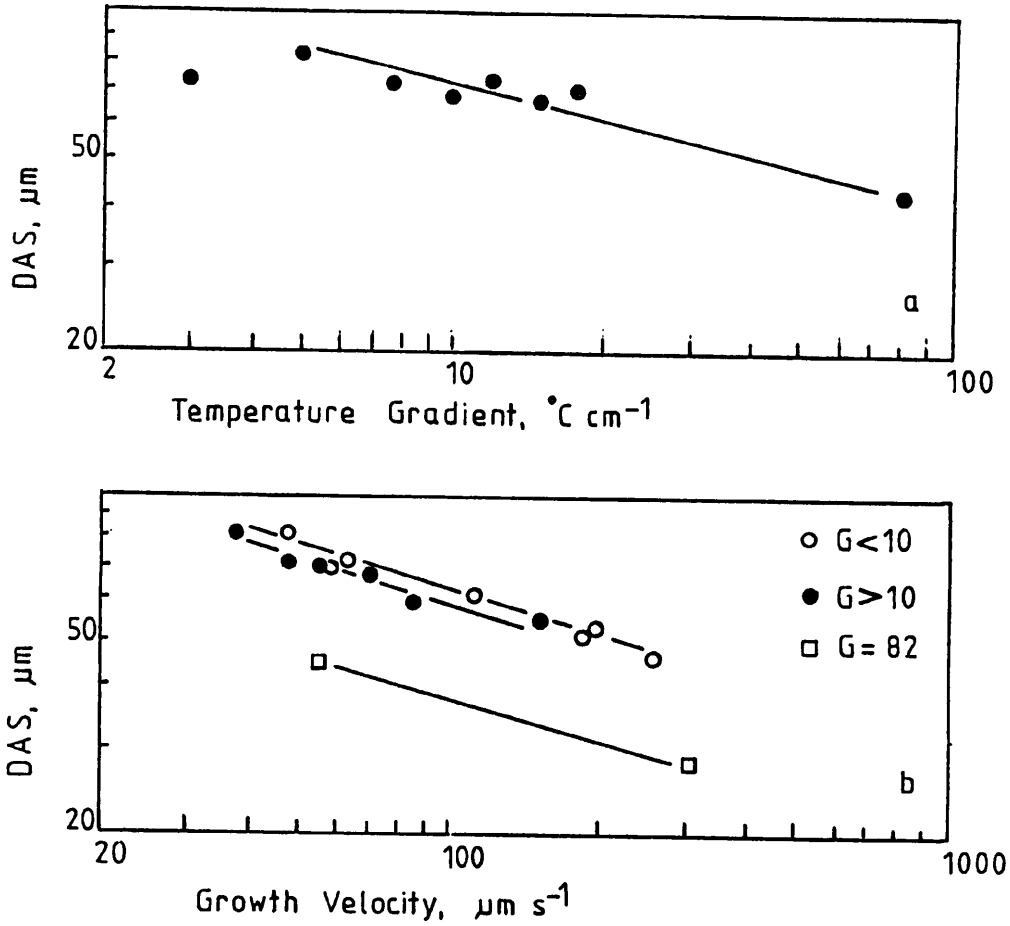

Figure 5.3. a) Variation of DAS with temperature gradient for alloys solidified with velocities between 40 and 80 μm sec^{-1}.

b) Variation of DAS with growth velocity for alloys solidified with different temperature gradients.

A

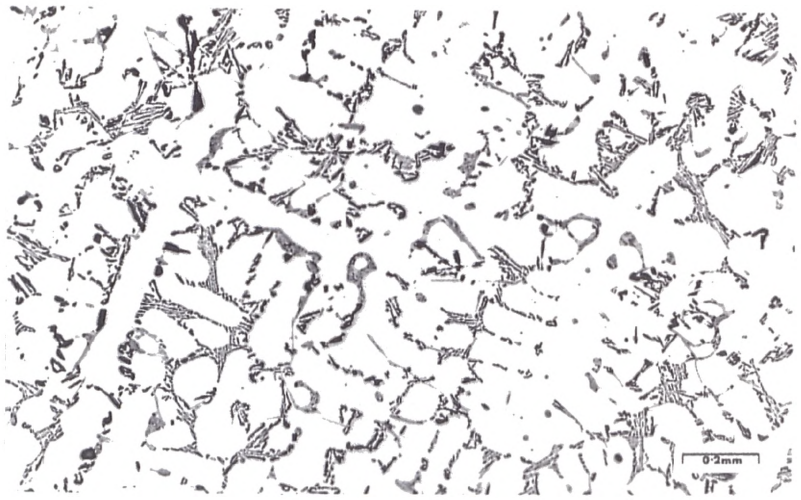

B

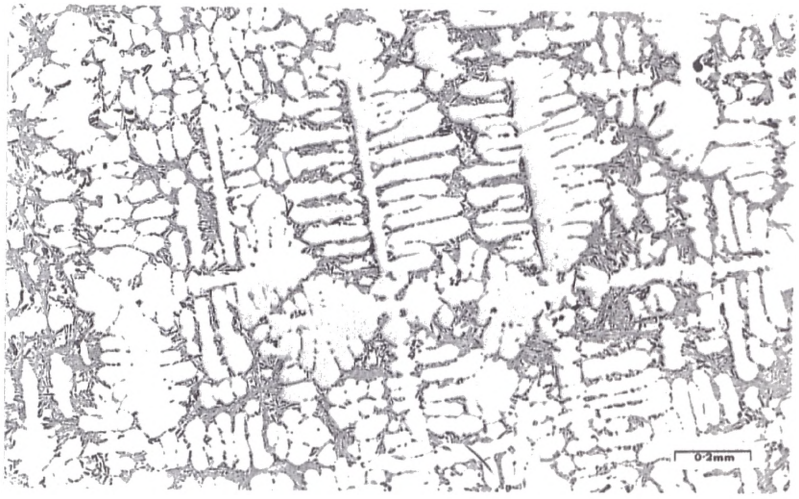

Figure 5.4. Microstructure of LM25 alloy solidified with different solidification conditions.

a) t_f = 870 sec, G = 5.3 °C cm^{-1}, V = 43.85 µm sec^{-1}.

b) t_f = 240 sec, G = 11 °C cm^{-1}, V = 151.5 µm sec^{-1}.

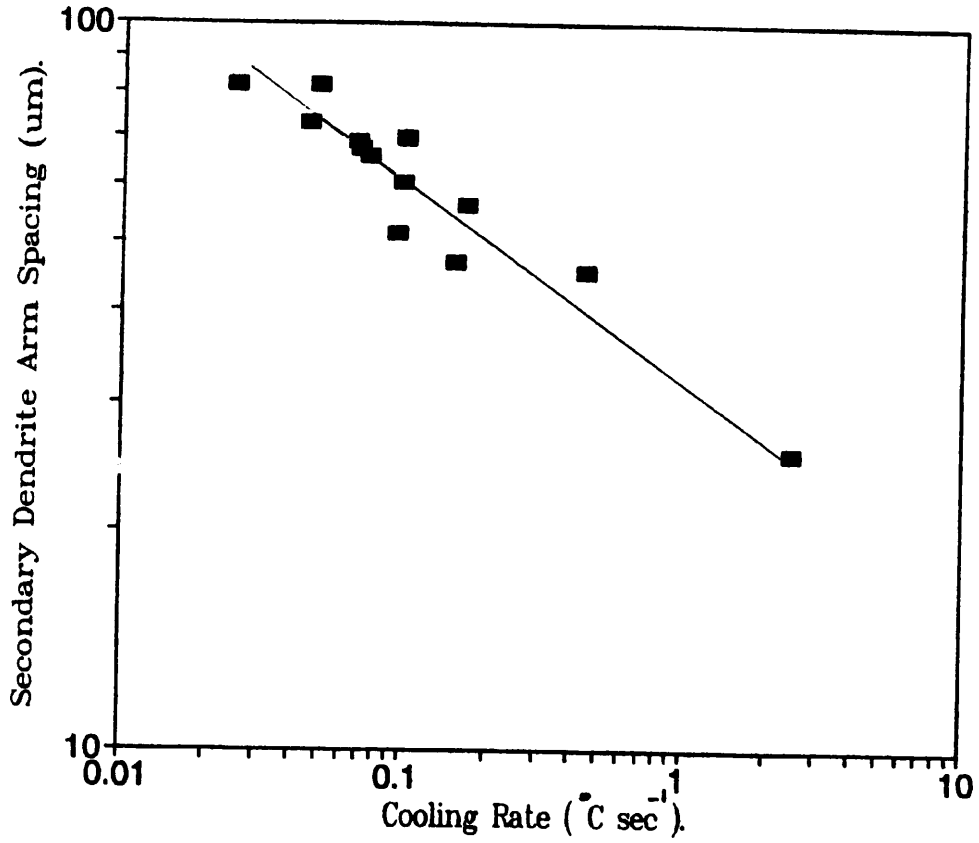

Figure 5.5. Variation of DAS with cooling rate,(GxV) for LM25 alloy.

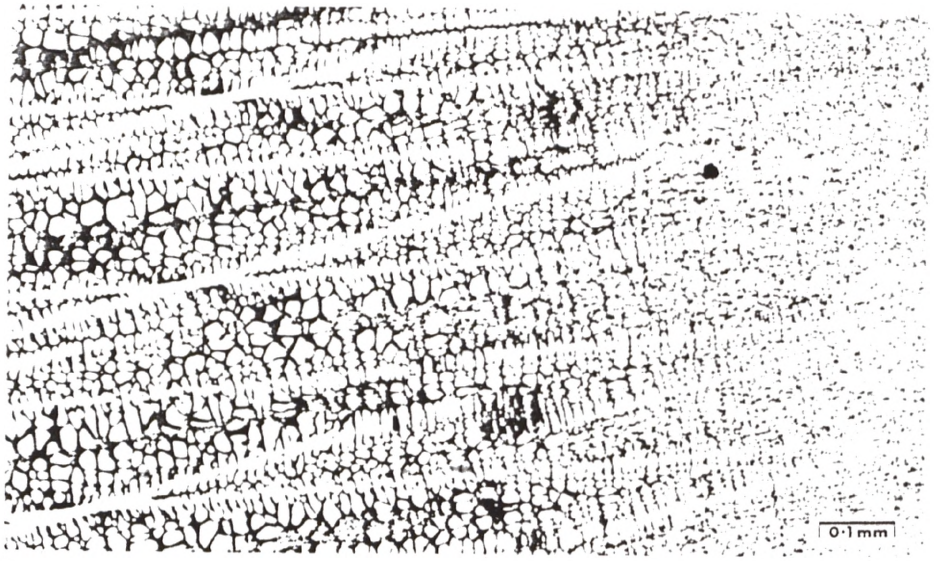

Figure 5.6. Longitudinal section of an alloy solidified with G = 82 °C cm^{-1} and V = 300 μm sec^{-1} showing the dendrite growth front and coarsening of the dendrites.

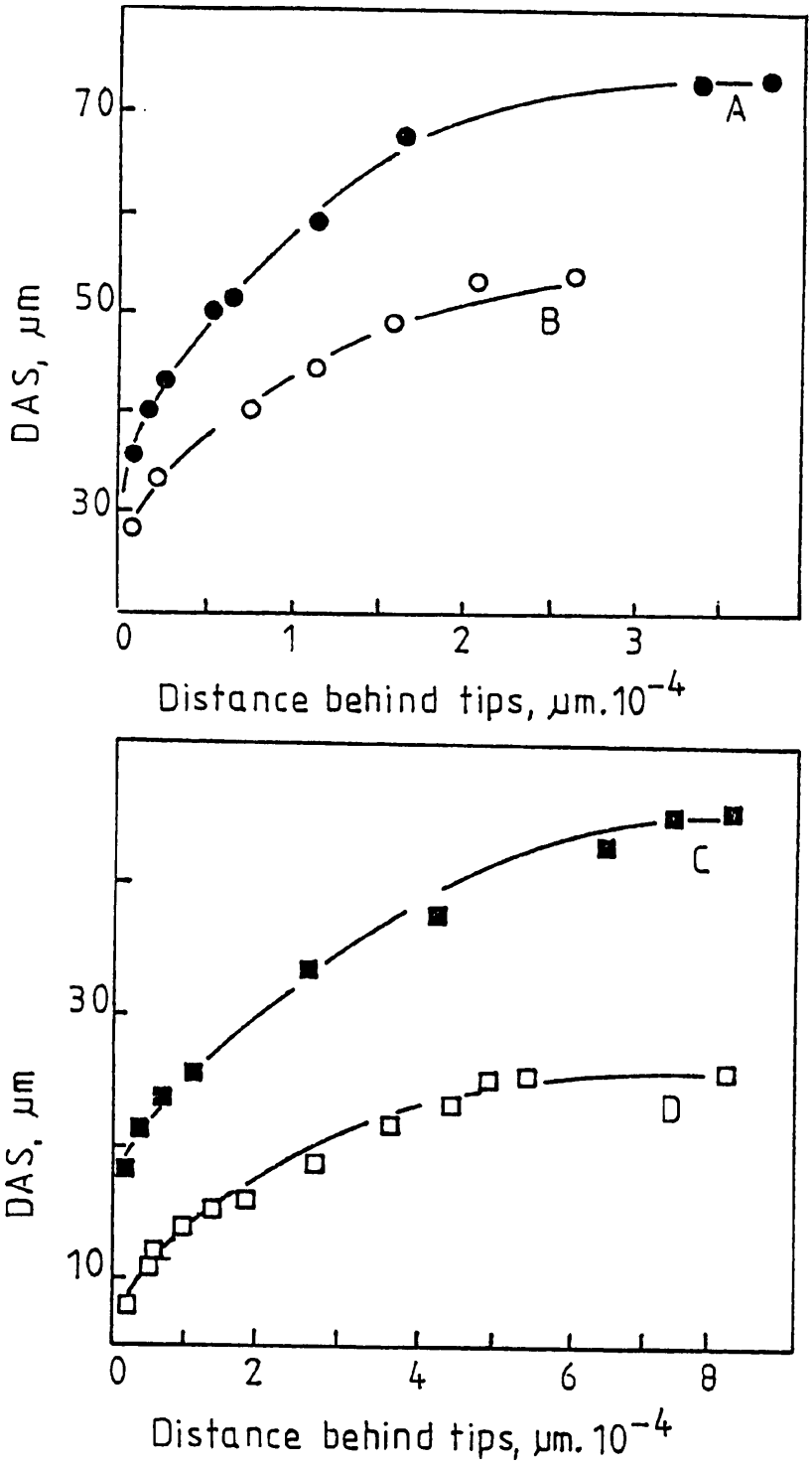

Figure 5.7. **Variation of DAS with distance behind the dendrite tips.**

A **G = 12 °C cm^{-1} V = 54 μm sec^{-1}.**

B **G = 12 °C cm^{-1} V = 111 μm sec^{-1}.**

C **G = 82 °C cm^{-1} V = 54 μm sec^{-1}.**

D **G = 82 °C cm^{-1} V = 300 μm sec^{-1}.**

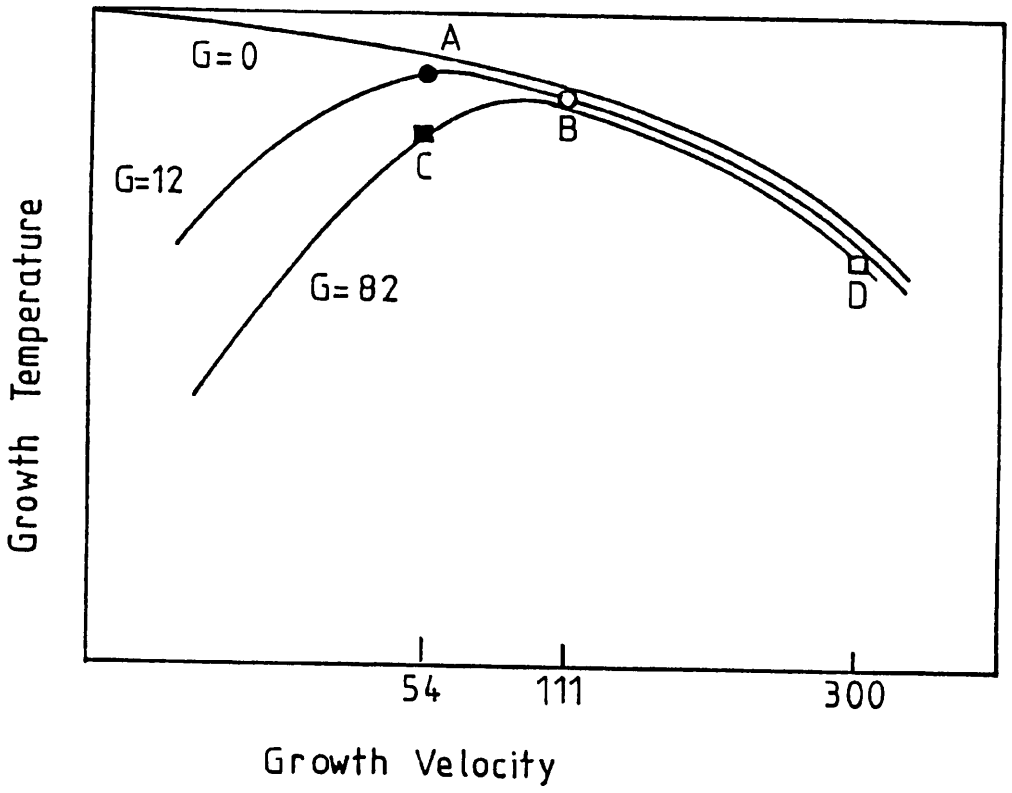

Figure 5.8. Schematic representation of the variation of dendrite tip growth temperature with growth velocity for different temperature gradients.

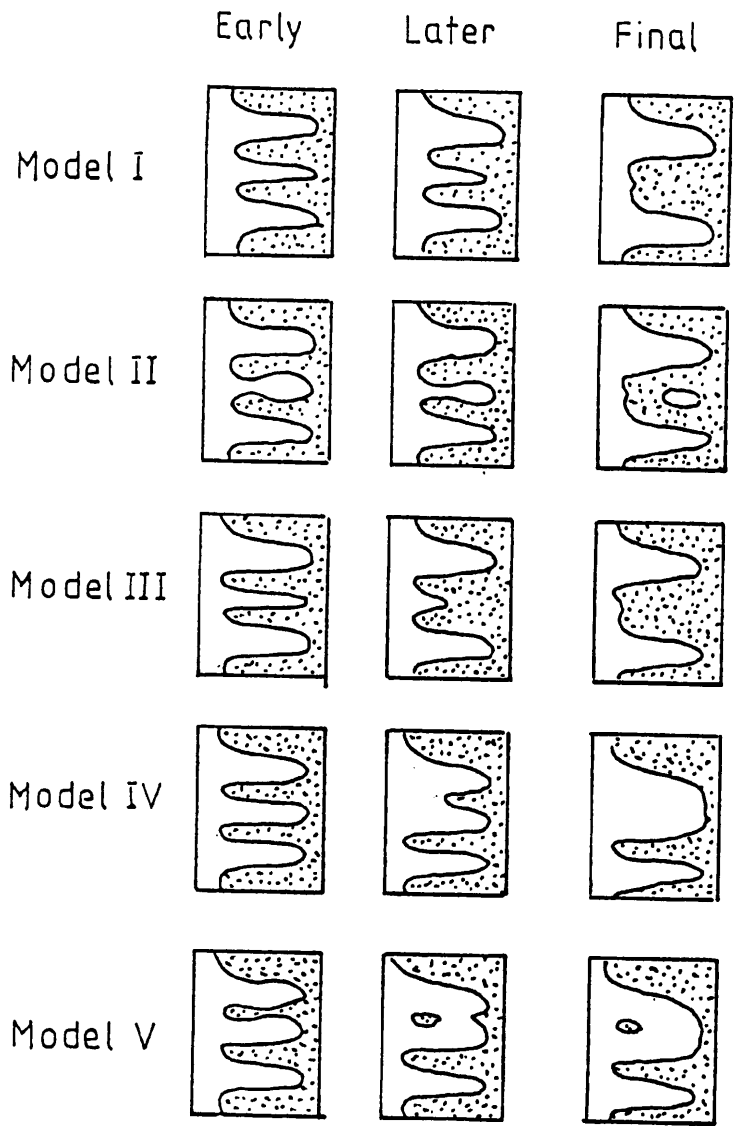

Figure 5.9. **Models suggested for coarsening.**

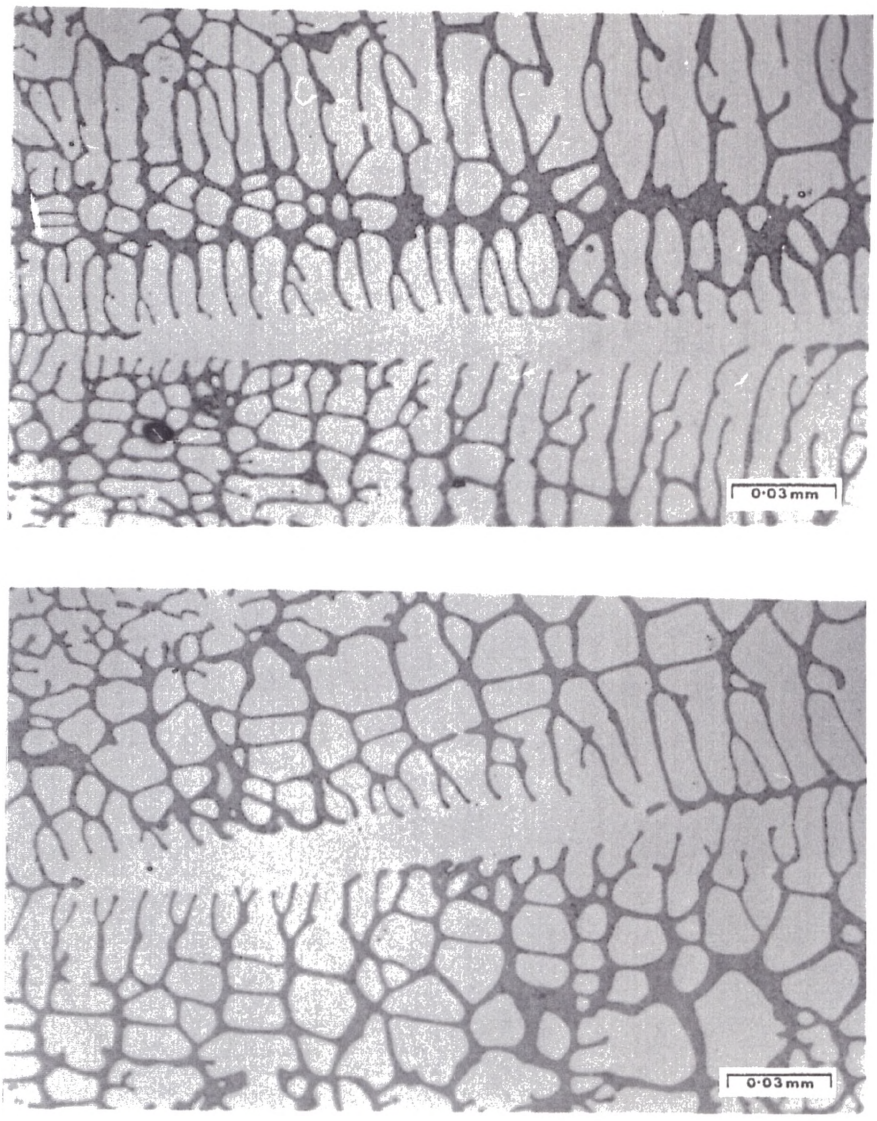

Figure 5.10. Longitudinal section of an alloy solidified with G = 82 °C c^{-1} and v = 300 μm sec^{-1} showing evidence of the operation of different coarsening mechanisms.

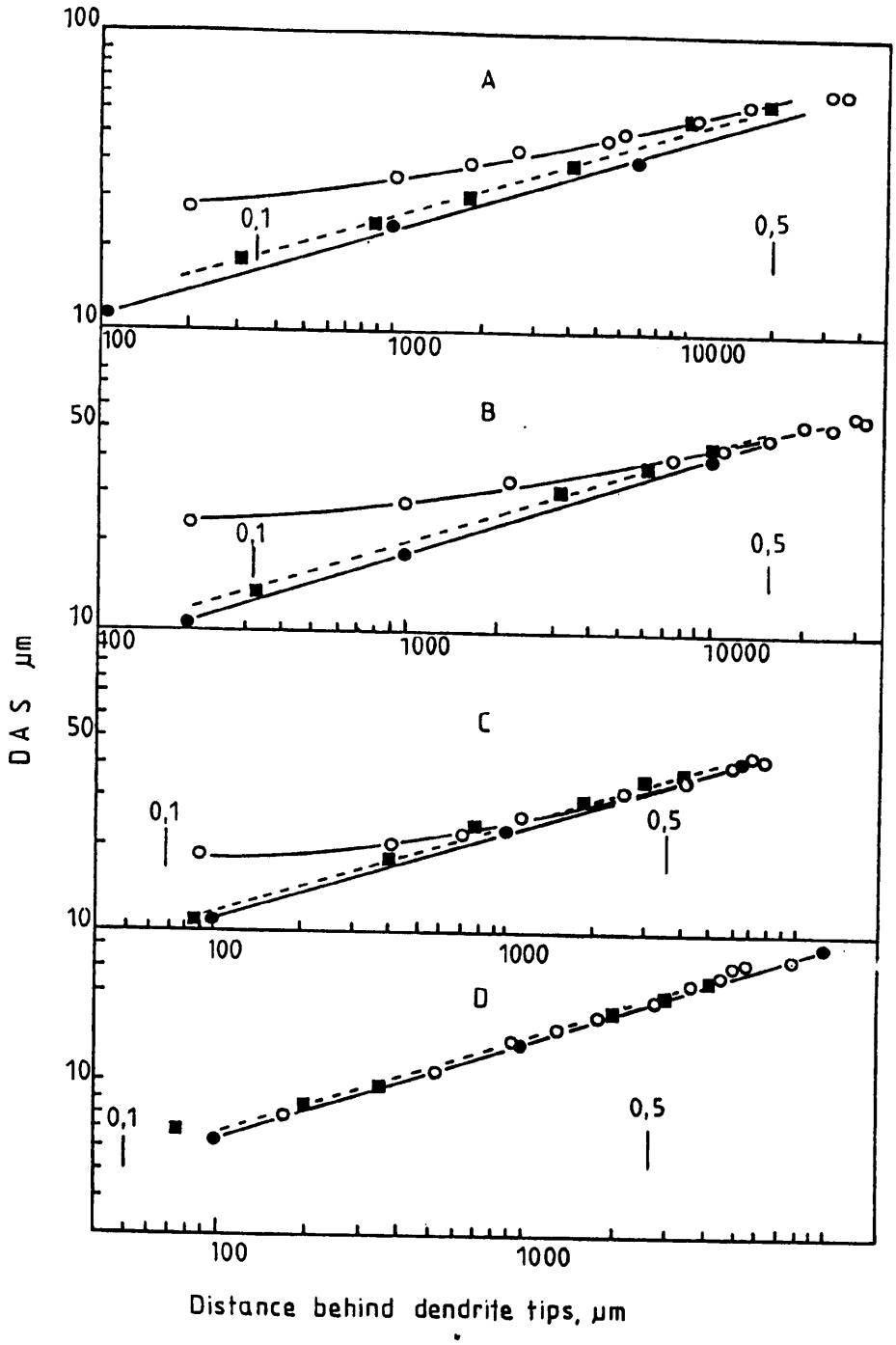

Figure 5.11. The variation of DAS with distance behind the dendrite tip for specimens A,B,C, and D.

0 experimental measurements.

● calculated using an average coarsening parameter and assuming $\lambda_o = 0$.

■ calculated using a numerical analysis.

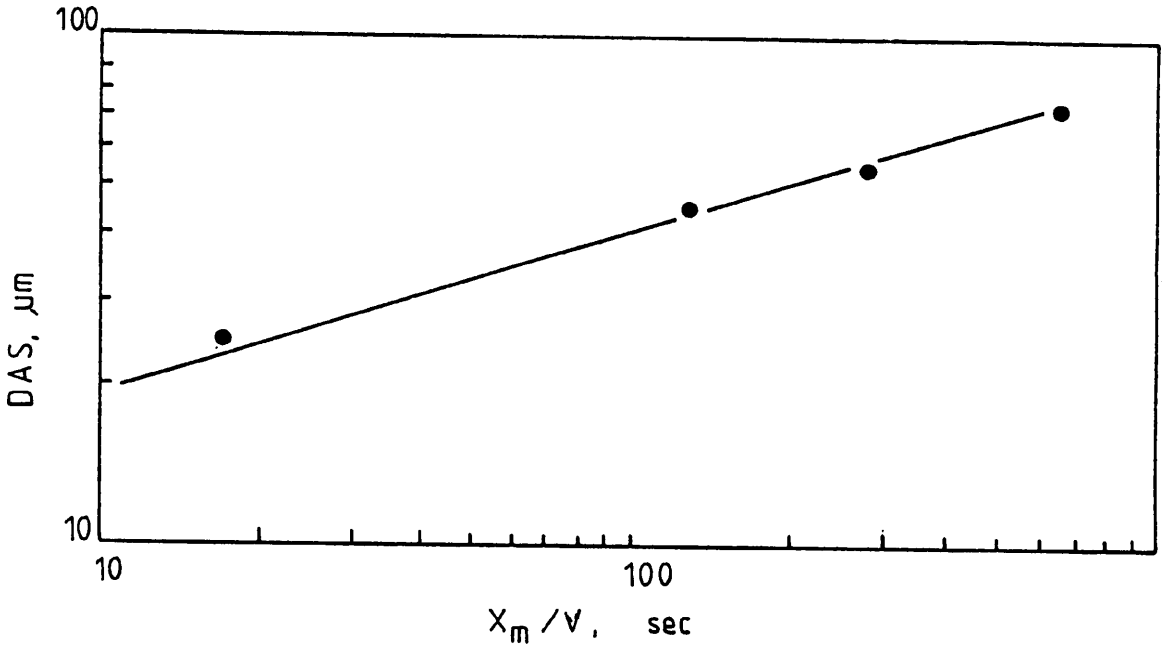

Figure 5.12. The variation of DAS with distance between the dendrite and eutectic interface, X_m and assuming $\lambda_o = 0$.

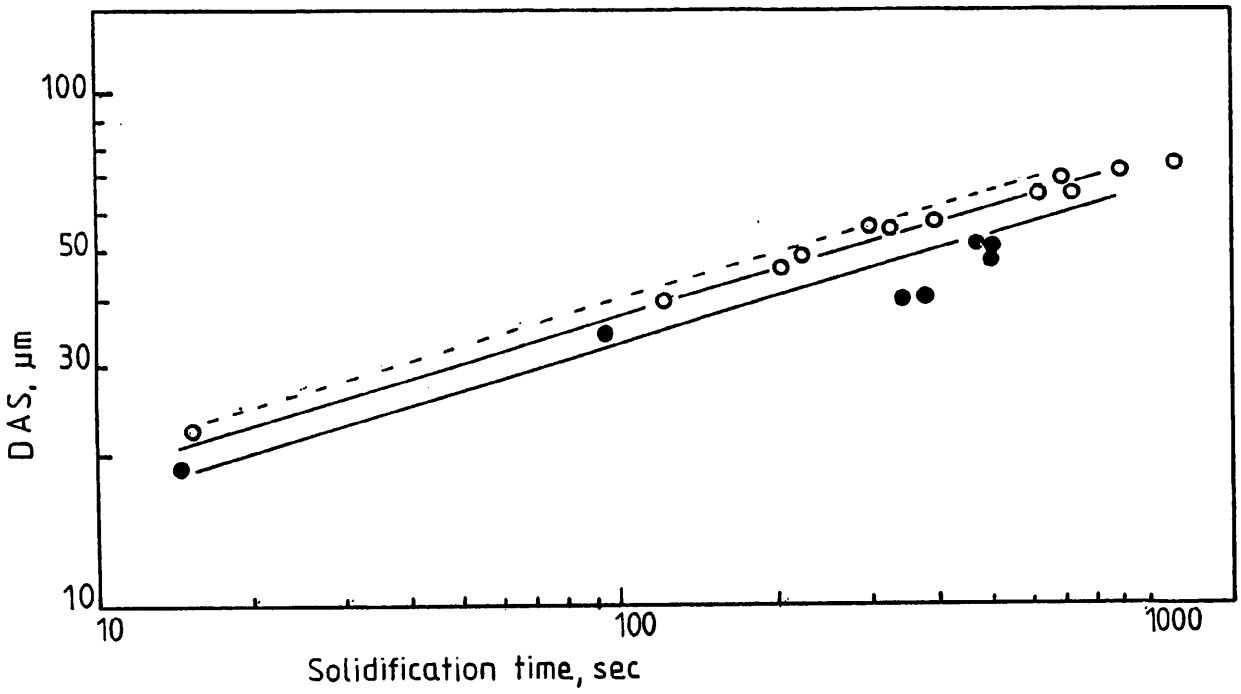

Figure 5.13. The variation of final DAS with total solidification time.

--- LM25, O LM25 + 0.04%Sr, ● LM25 + 0.2%Sb.

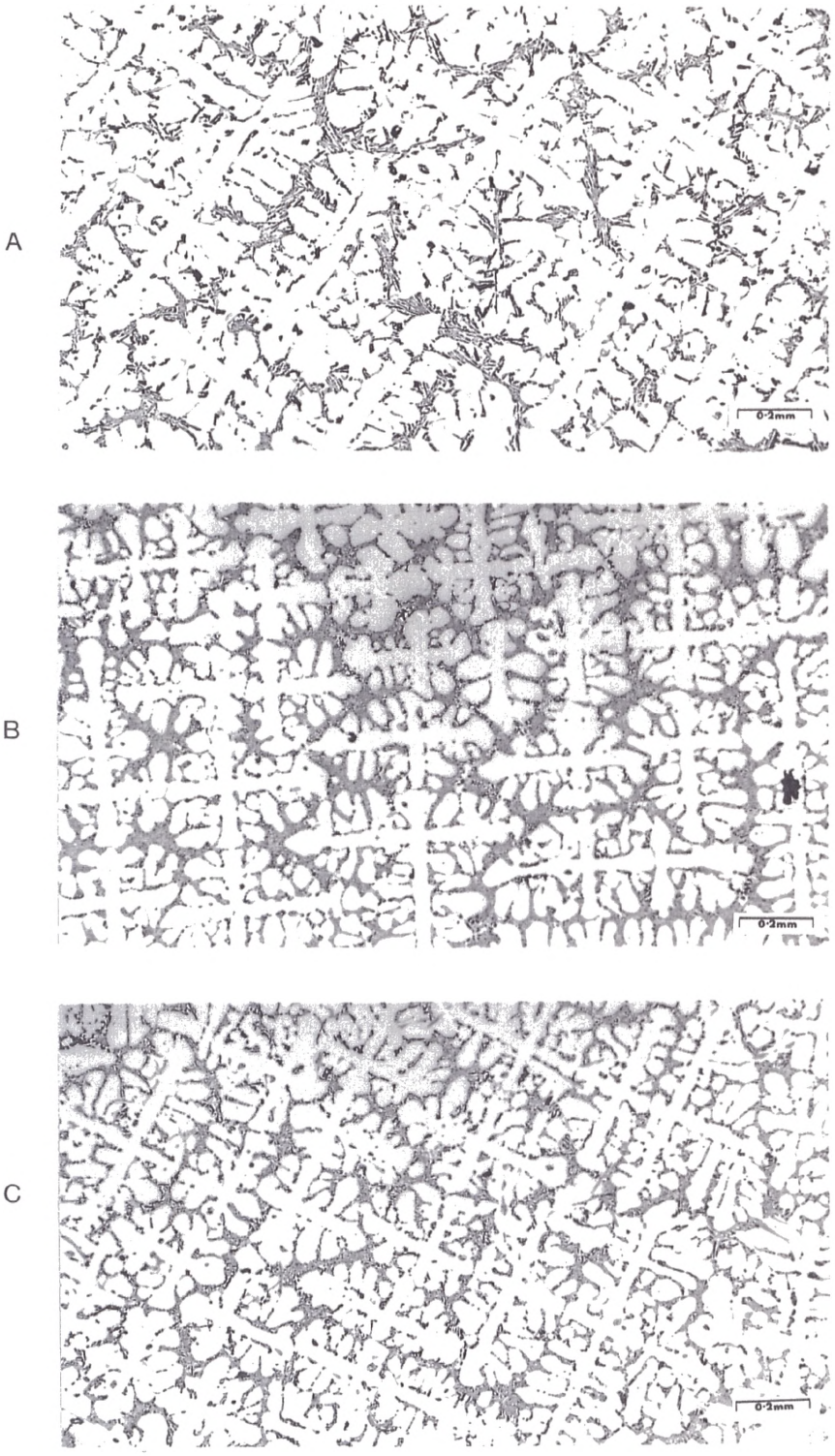

Figure 5.14. The microstructure at constant solidification condition of

a) LM25 b) LM25 + 0.04%Sr c) LM25 + 0.2%Sb.

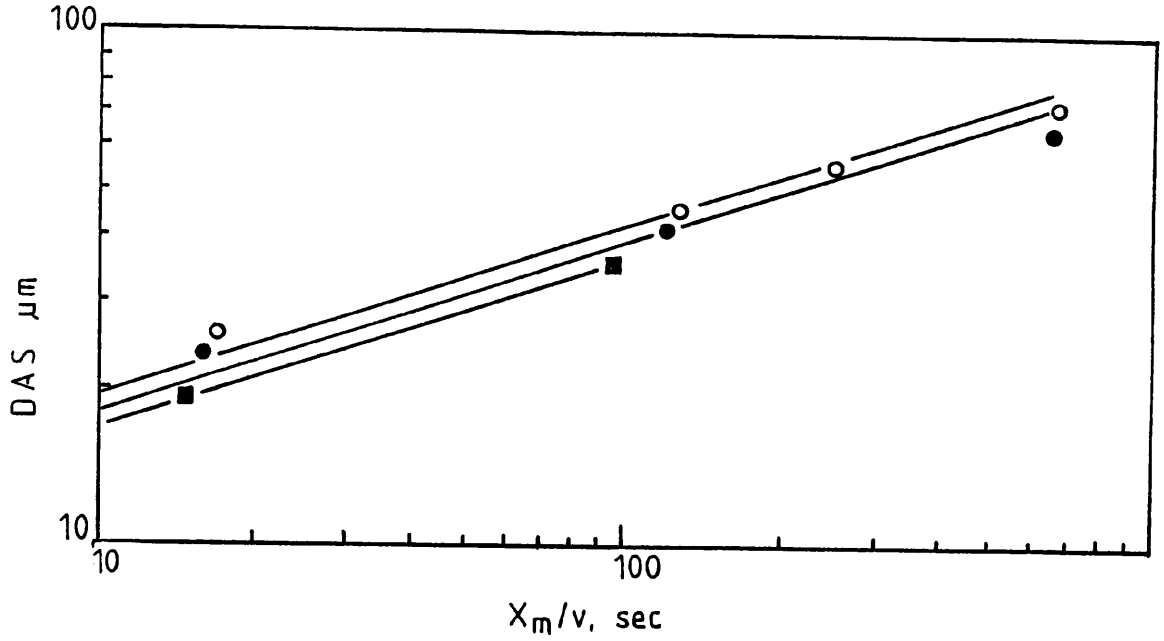

Figure 5.15. The variation of DAS with distance between the dendrite and eutectic interface, X_m.

O LM25,

● LM25 + 0.04%Sr,

■ LM25 + 0.2%Sb.

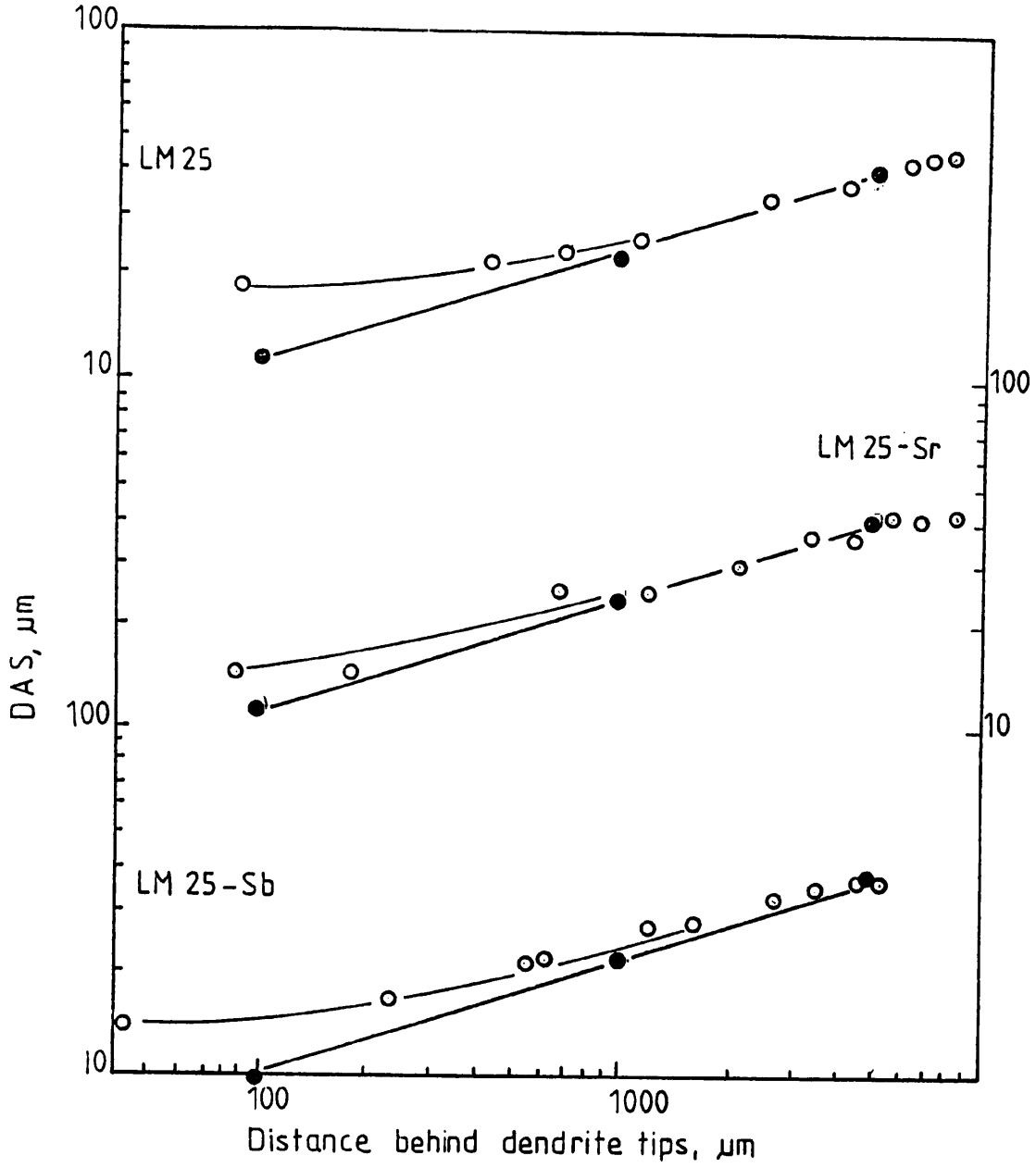

Figure 5.16. Variation of DAS with distance behind tip for G = 82 °C cm^{-1}, V = 54 μm sec^{-1}

0 experimental measurements

● calculated using the average coarsening parameter and assuming $\lambda_o = 0.5$.

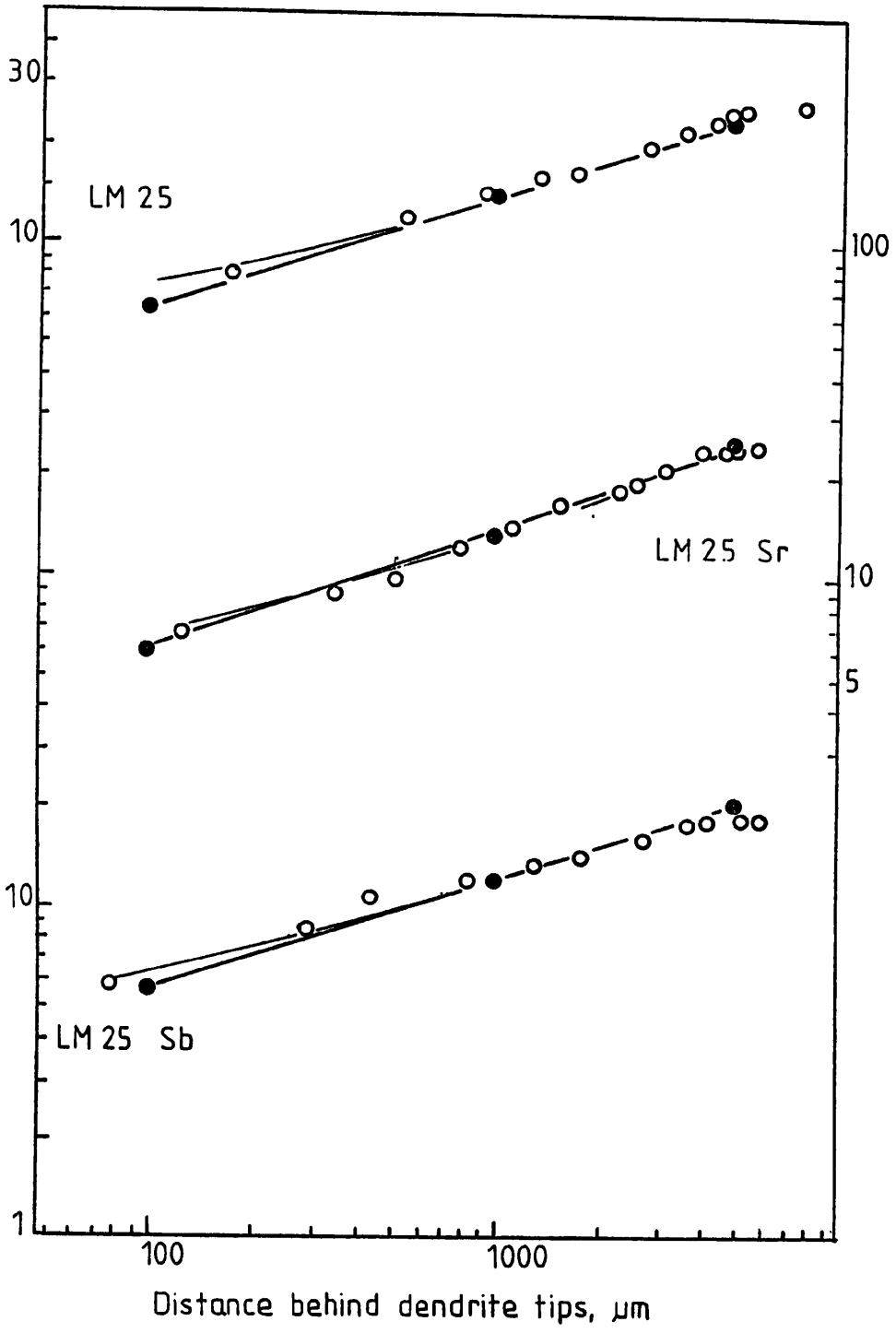

Figure 5.17. Variation of DAS with distance behind tip for G = 82 °C cm^{-1}, V = 300 μm sec^{-1}

0 experimental measurements

● calculated using the average coarsening parameter and assuming $\lambda_o = 0.0$.

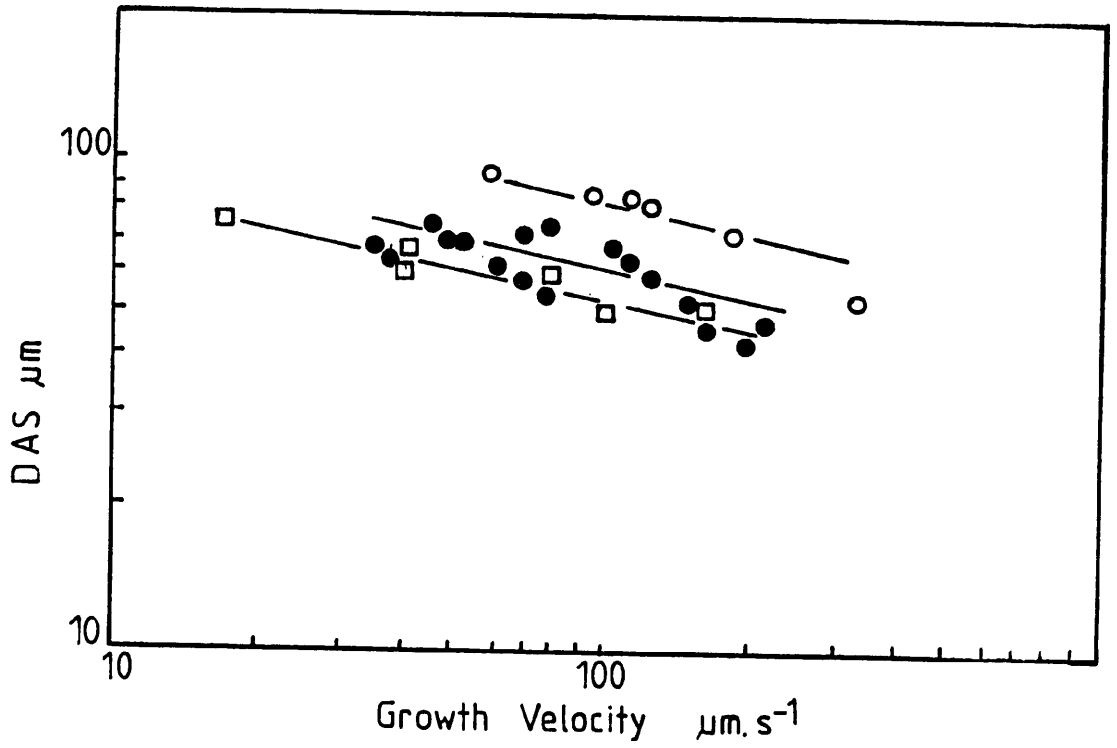

Figure 5.18. The variation of secondary dendrite arm spacing, DAS, with growth velocity of alloys solidified in the thermal valve furnace.

o pure Al-Si-Mg alloys

● untreated LM25 alloys

□ LM25 alloys treated with 2wt% (3/1) TiBAL and 0.04wt%Sr.

A

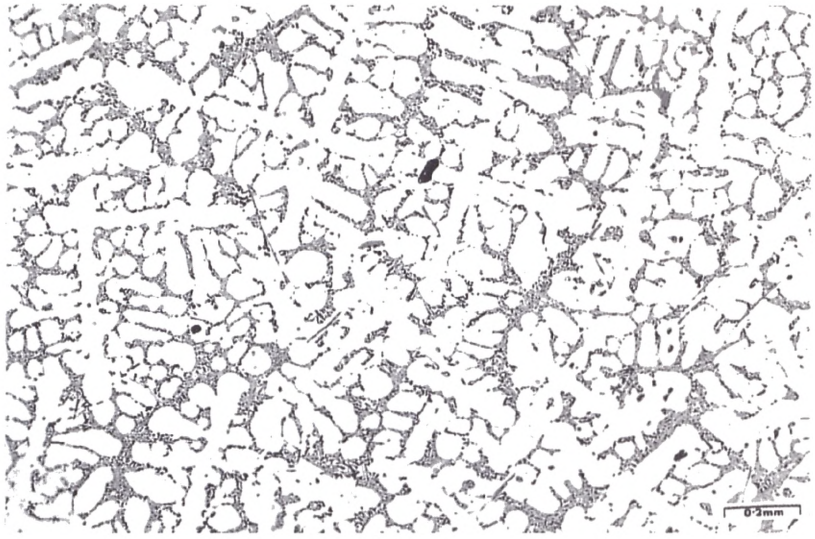

B

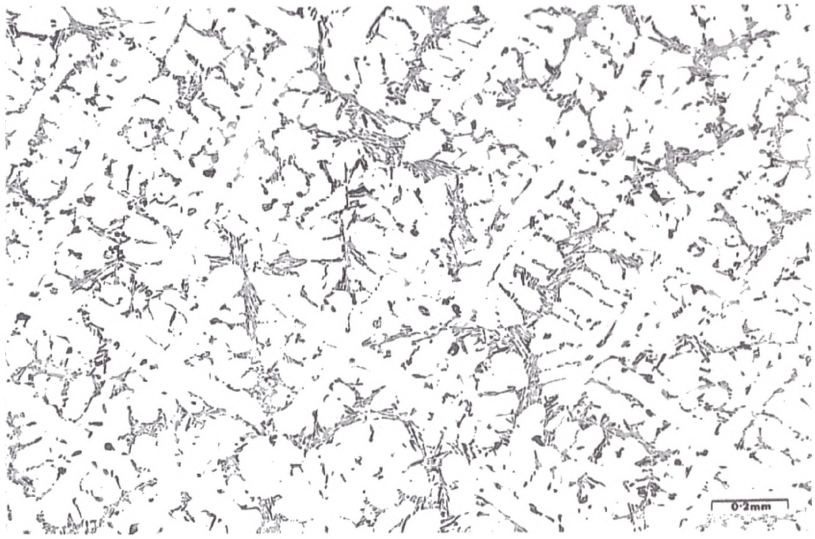

Figure 5.19. Microstructure of transverse sections of alloy directionally solidified with G = 82 $^{o}C\ cm^{-1}$ and V = 54 μm sec^{-1}.

a) pure Al-7.5%Si-0.45%Mg alloy

b) untreated LM25 alloy

c) LM25 alloy treated with 2wt% 3/1 TiBAL

d) LM25 alloy treated with 2wt% 3/3 TiBAL

e) LM25 alloy treated with 2wt% 3/1 TiBAL and 0.04wt% Sr.

C

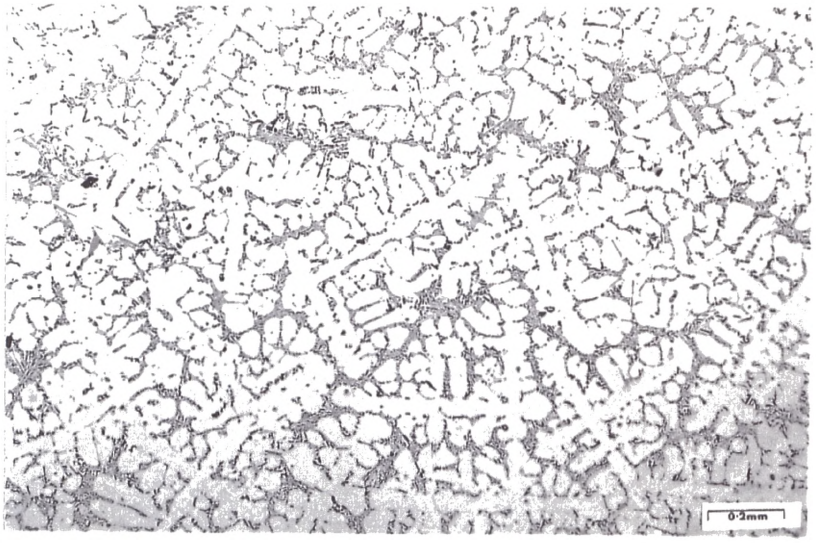

D

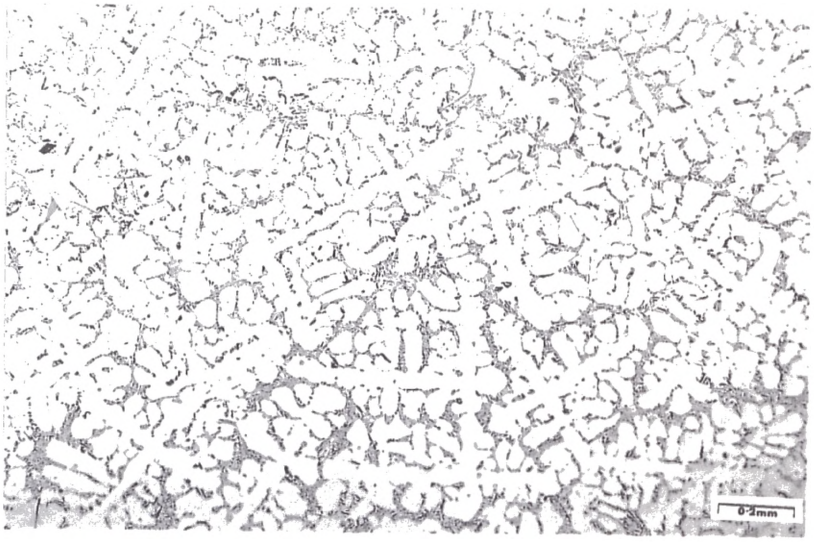

E

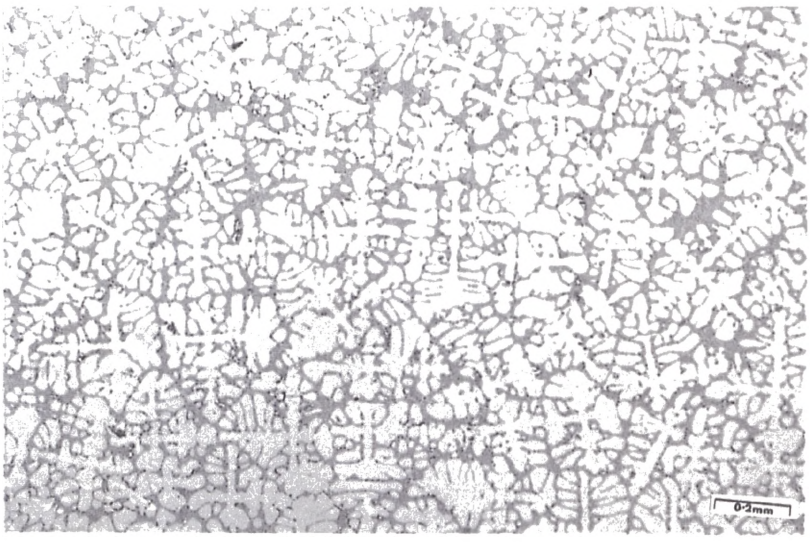

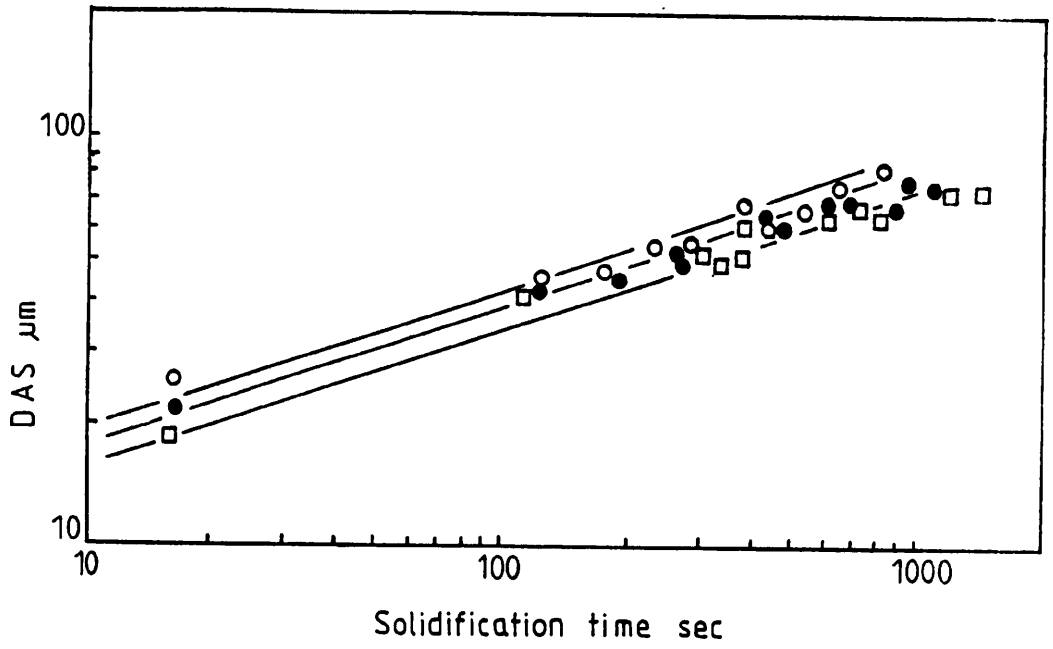

Figure 5.20. Variation of DAS with total solidification time for

- ○ untreated LM25 alloy
- ● LM25 alloy treated with 2wt% 3/1 TiBAL
- ■ LM25 alloy treated with 2wt% 3/1 TiBAL and 0.045wt% Sr.

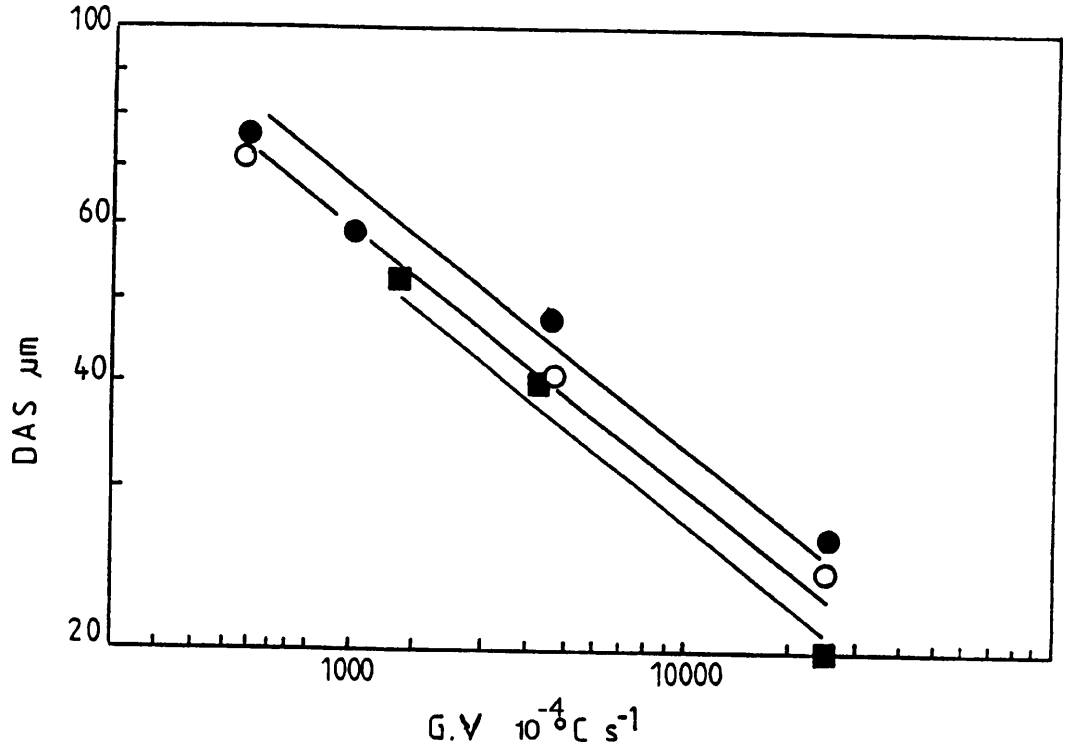

Figure 5.21. Variation of DAS with the product G.V for

- ○ untreated LM25 alloy
- ● LM25 treated with 2wt% 3/1 TiBAL
- ■ LM25 treated with 2wt% 3/1 TiBAL and 0.04wt%Sr.

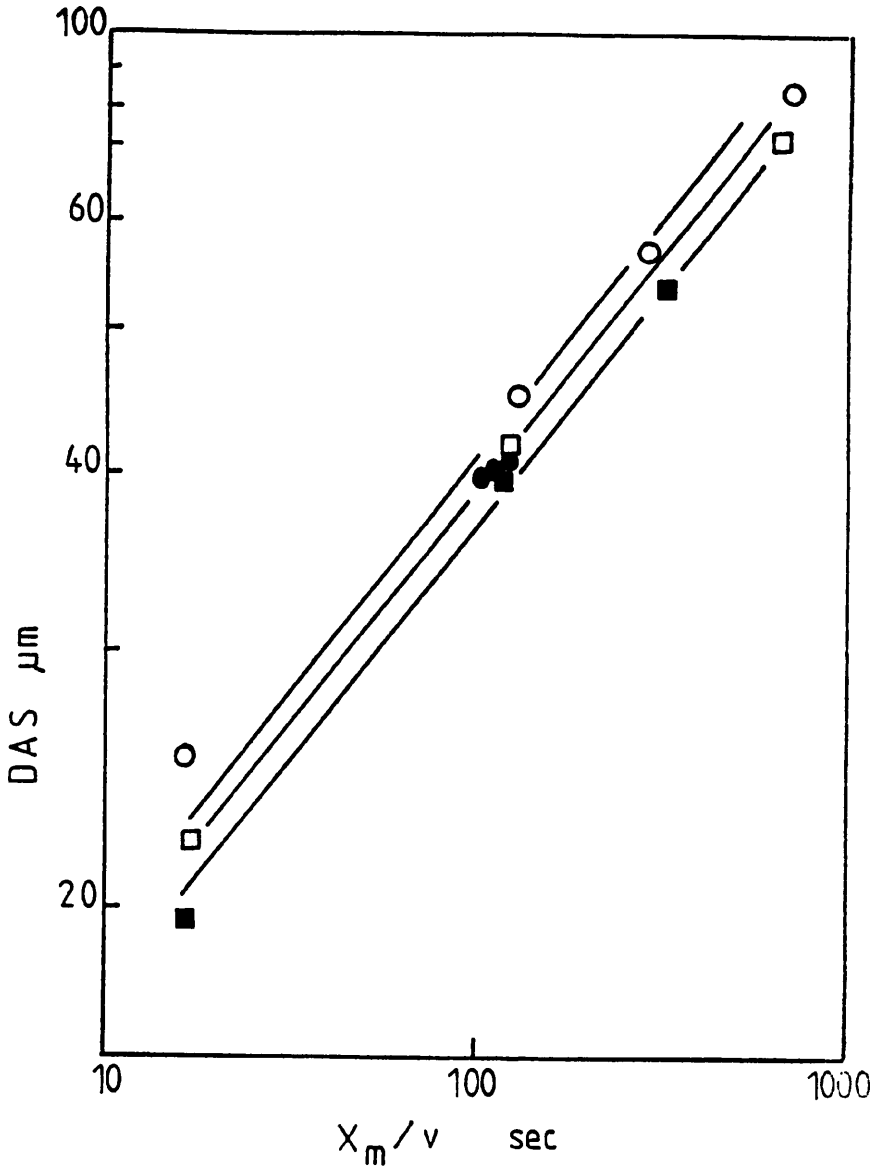

Figure 5.22. Variation of DAS with the X_m/V for

- ○ untreated LM25 alloy
- □ LM25 treated with 2wt% 3/1 TiBAL
- ● LM25 treated with 2wt% 3/3 TiBAL and 0.04wt%Sr.
- ■ LM25 treated with 2wt% 3/1 TiBAL and 0.04wt%Sr.

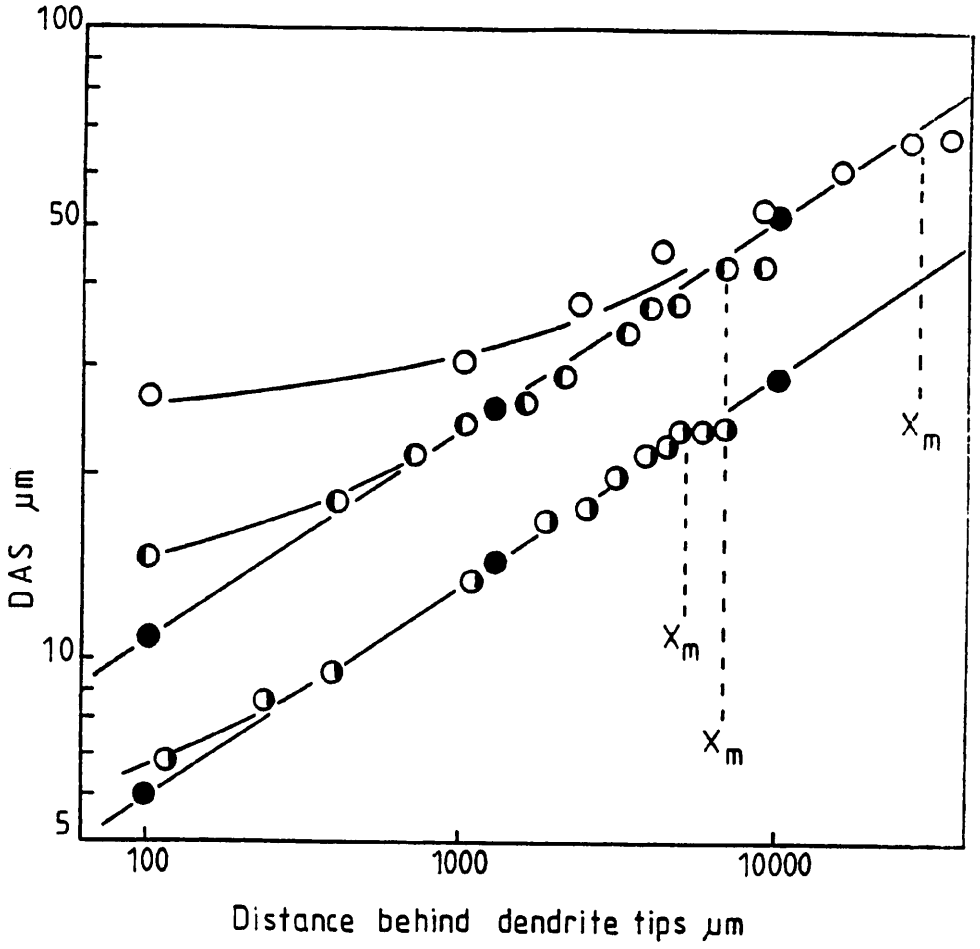

Figure 5.23. Variation of DAS with distance behind dendrite tip for directionally solidified LM25 alloys treated with 2wt% (3/1) TiBAL for the solidification conditions

O	G = 12 °C cm^{-1}	V = 54 μm sec^{-1}
◐	G = 82 °C cm^{-1}	V = 54 μm sec^{-1}
◑	G = 82 °C cm^{-1}	V = 300 μm sec^{-1}

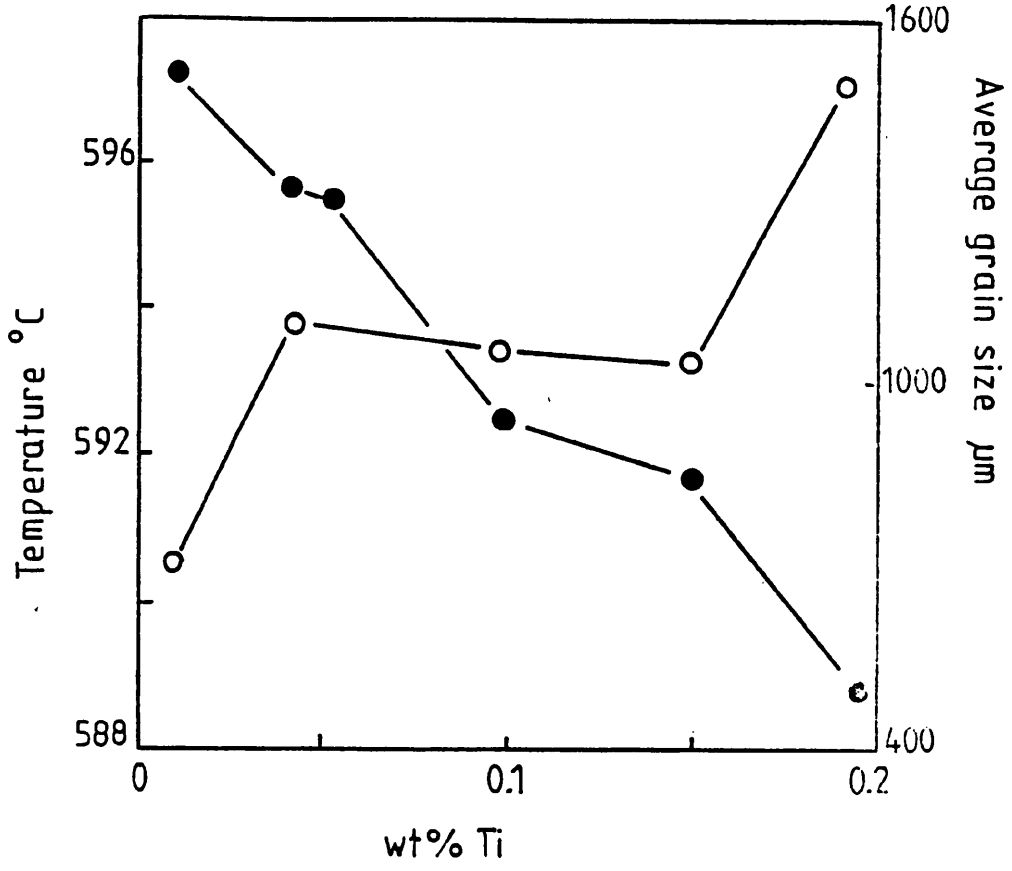

Figure 5.24. The variation of growth temperature and grain size with amount of Ti added when an Al-10wt%Si alloy is treated with 5/1 TIBAL

● grain size

O growth temperature.[133]

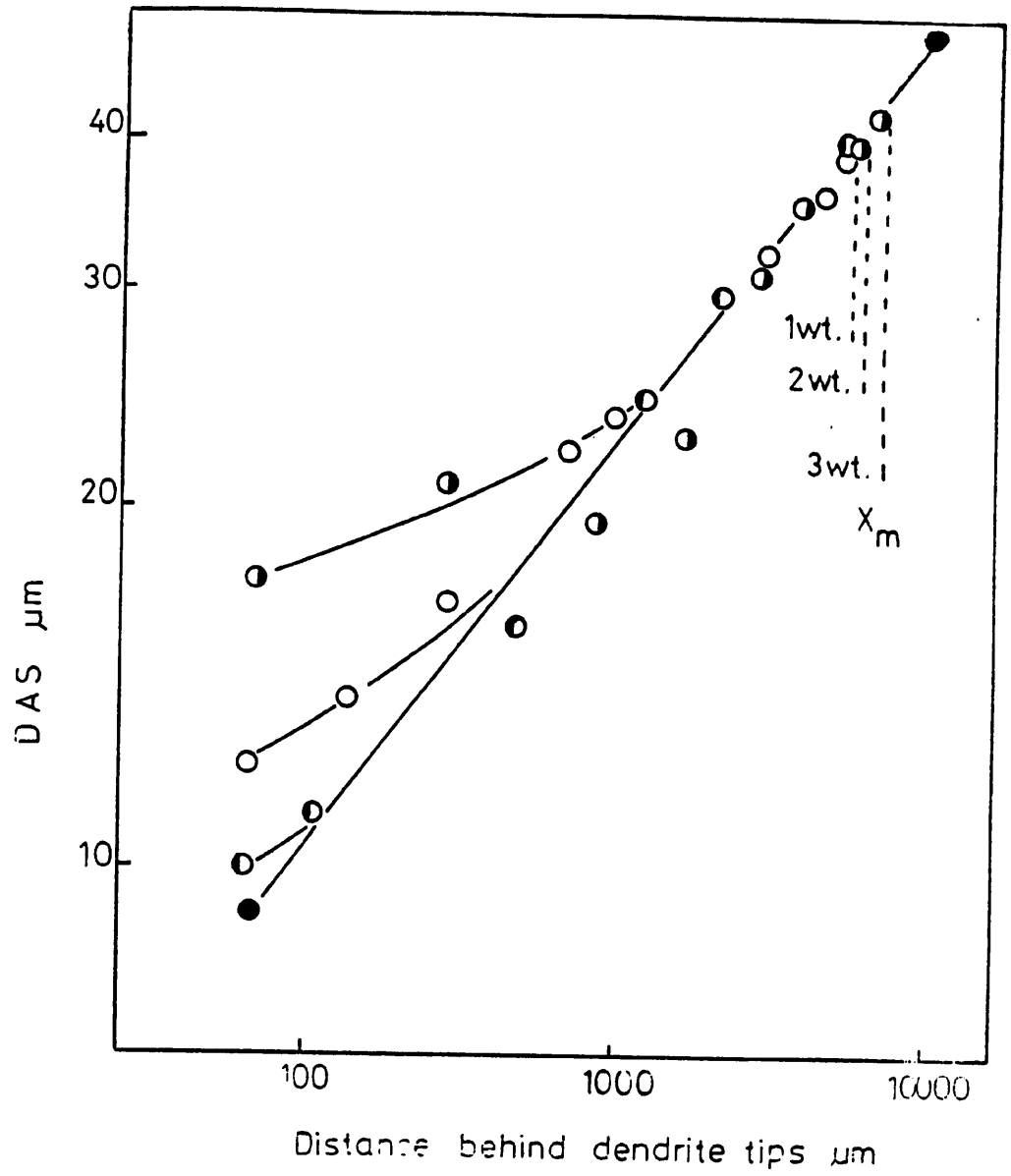

Figure 5.25. **Variation of DAS with distance behind dendrite tip for directionally solidified LM25 alloys G = 82 °C cm^{-1} V = 54 μm sec^{-1}**

- ◑ 1wt% 3/3 TiBAL
- ○ 2wt% 3/3 TiBAL
- ◐ 3wt% 3/3 TiBAL

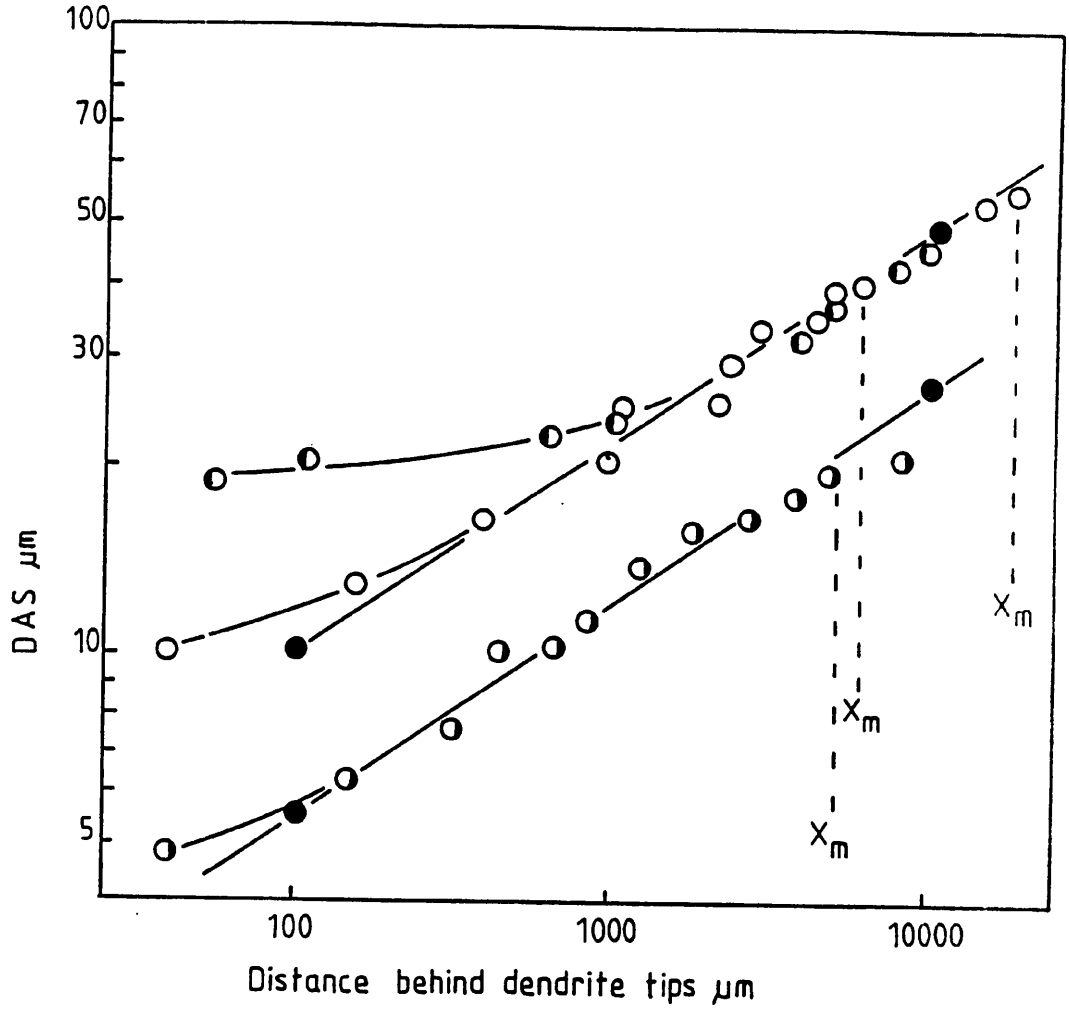

Figure 5.26. Variation of DAS with distance behind dendrite tip for directionally solidified LM25 alloys treated with 2wt% 3/1 TiBAL and 0.04%Sr for the solidification conditions

- ● G = 32 °C cm^{-1} V = 54 μm sec^{-1}
- ○ G = 82 °C cm^{-1} V = 54 μm sec^{-1}
- ◐ G = 82 °C cm^{-1} V = 300 μm sec^{-1}

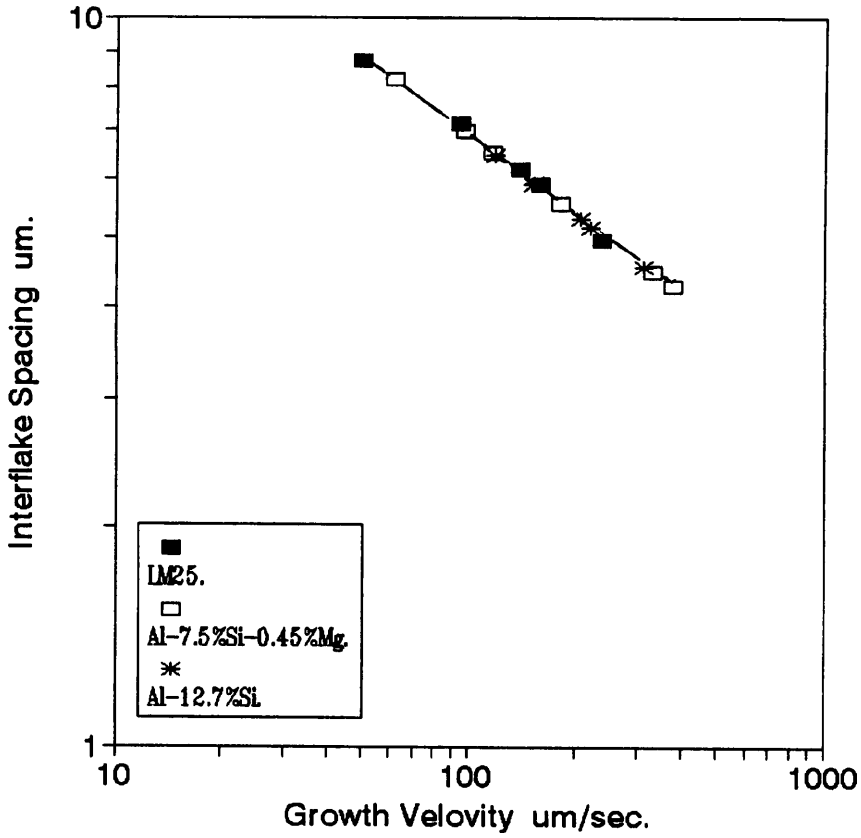

Figure 5.27 Variation of the interflake spacing with growth velocity for different alloys.

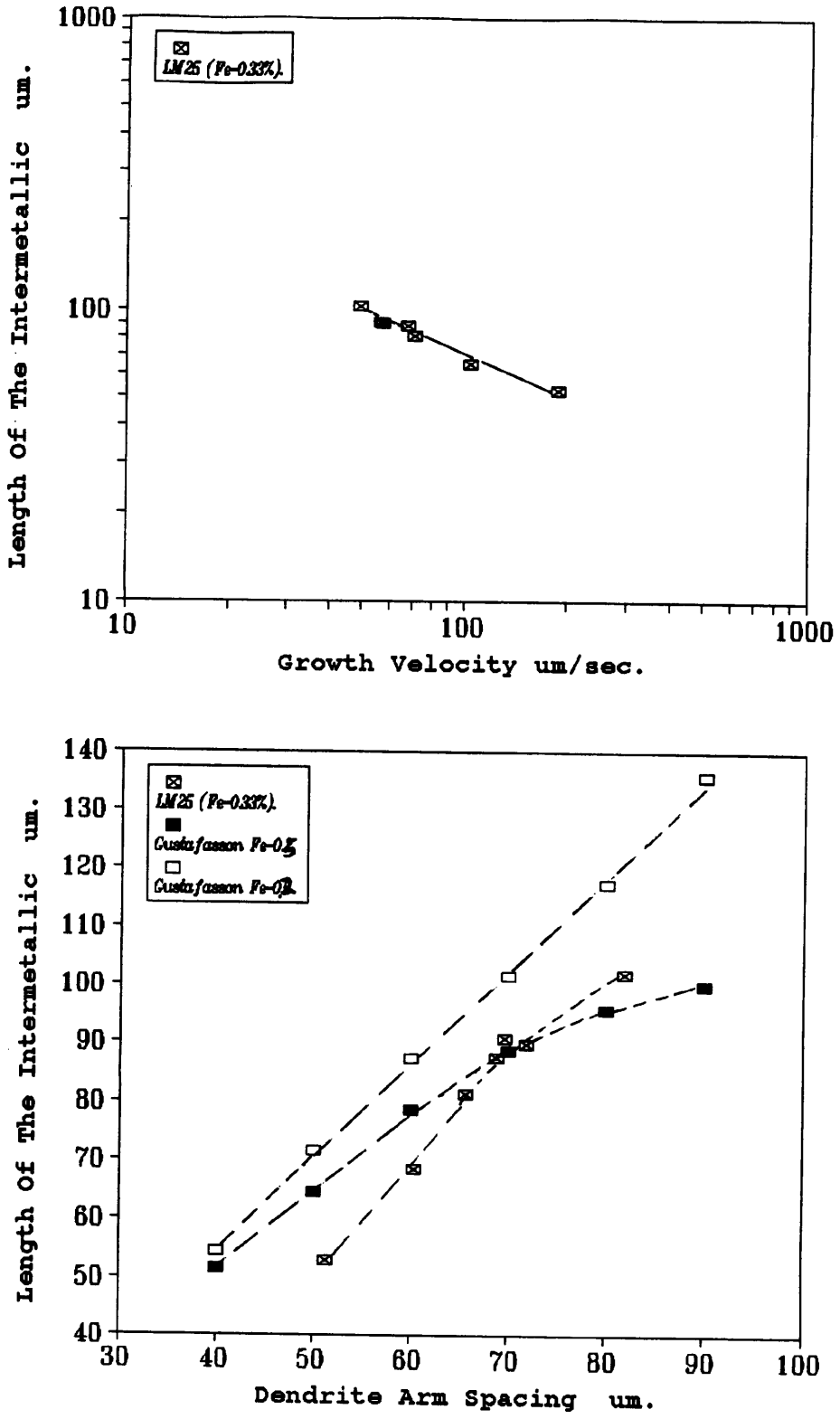

Figure 5.28. Variation of length of the intermetallic with (a) growth velocity (b) D.A.S. in the LM25 alloy.

CHAPTER SIX

EXPERIMENTAL RESULTS AND DISCUSSIONS – 3

CHAPTER SIX

MECHANICAL PROPERTIES-SOLIDIFICATION PARAMETER RELATIONSHIPS

6-1 INTRODUCTION.

The influence of various melt treatments on one of the triangular relationships, that between microstructure and the solidification conditions was examined in the previous chapter. In the present chapter, the other two relationships, namely those between mechanical properties and microstructure and between mechanical properties and solidification conditions are explored and the influence of the same melt treatments examined.

It is well established that the mechanical properties of LM25, through alloy composition and control of processing variables are sensitive to the nature, scale and morphology of several microstructural features. The analysed composition of the LM25 ingots used in the present study was;

7.79%Si, 0.42%Mg, 0.16%Mn, 0.33%Fe, 0.04%Cu, 0.02%Zn, 0.02%Ti Pb, Sn, Cr, Ni < 0.02%.

The Mg has relatively little effect on the as-cast properties[140-141] but increases the strength after heat treatment[48,64]. Fe forms intermetallic compounds and Mn is added to limit the detrimental effect of the compounds on ductility. The significant microstructural features in LM25 are the primary Al dendrites, the eutectic Si phase, inclusions particularly the Fe containing β phase and porosity. In the present study, the alloy is considered as a composite consisting of 0.67 vol% of ductile primary phase and 0.33 vol% of interdendritic, brittle constituent consisting of Al phase, Si eutectic phase, intermetallic compounds and porosity. An attempt is made to evaluate quantitatively the contribution of each of the above microstructural features to the mechanical properties by analysing experimental data in terms of a simple composite model using the rule of mixtures, that is;

$$P_{LM25} = V_{P.D.} * P_{P.D.} + V_{Si} * P_{Si} + V_{I.C.} * P_{I.C.} + V_P * P_P \qquad (6\text{-}1)$$

where P is the measured property, V is the volume fraction of the microstructural constituent and P.D. refers to primary dendrites, Si to the Al-Si eutectic, I.C. to intermetallic compounds and P to porosity. Very little porosity was present in the areas of directionally solidified samples used for preparing tensile samples and, consequently, this contribution was sufficiently small to be ignored. Porosity was present in the preliminary studies using a sand mould and a significant influence of porosity on mechanical properties was observed. Further information on the effect of porosity is described in the section on hipping experiments.

LM25 alloys are used in practice in the as-cast and heat treated condition. Properties were measured in the as-cast condition in the present studies. Various mechanical properties are of significance depending upon the service condition. In the present study 0.2% proof stress, UTS and elongation to fracture have been measured. The quality index Q has also been used to asses the overall mechanical properties of the alloy.

6-2 PURE LM25 ALLOYS.

In order to measure the contribution of each microstructural constituent to the properties of commercial LM25, initial studies were made on a pure LM25 alloy, which did not contain Fe. This was made by melting pure Al, Si and Mg to produce an Al-7.5%Si-0.45%Mg alloy which was considered to be a base for the commercial LM25 alloy. The microstructure of this alloy consists of Al primary phase and unmodified flake eutectic. The mechanical properties of this alloy are recorded in Table 6.1. A typical microstructure is shown in Figure 6.1. The mechanical properties of the unmodified Al-12.7%Si alloy are shown in Table 6.2.

The variation of UTS with growth velocity is shown in Figure 6.2 for the Al-Mg-Si alloy and the eutectic 12.7 wt%Si flake eutectic alloy. These relationships show that the measured UTS

of both alloys increases as the growth velocity increases and this increase may be described by an equation of the form;

$$\sigma_{UTS}=\sigma_o+KV^n \qquad (6\text{-}2)$$

with σ_o = 36.74, K = 38.57 and n = 0.16 for the pure Al-Mg-Si alloy

σ_o = 3.23, K = 83.48 and n = 0.12 for the eutectic alloy.

where [σ_{UTS} (N mm^{-2}), V (μm sec^{-1})]

Assuming that a rule of mixture law can be used to describe the individual contributions of the two microstructural phases, the contribution of the primary Al dendrites to the alloy UTS and its variation with growth velocity may be calculated from the equation;

$$\sigma_{UTS}=0.67\sigma_{P.D.}+0.33\sigma_{Si} \qquad (6\text{-}3)$$

The results of this calculation are shown in Figure 6.2 and this contribution can be described by the equation;

$$\sigma_{P.D.}=\sigma_o+KV^n \qquad (6\text{-}4)$$

where σ_o = 20.58, K = 42.89 and n = 0.14.

where [$\sigma_{P.D.}$ (N mm^{-2}), V (μm sec^{-1})]

The contributions to the Al-Mg-Si alloy UTS, namely 0.67 $\sigma_{P.D.}$ and 0.33 σ_{Si} are shown as function of growth velocity in Figure 6.3. As expected, it can be seen from this figure that the primary Al phase, the reinforcing phase in the composite makes the greater contribution to the alloy UTS.

The increase in strength due to an increased solidification velocity or cooling rate is often

related to the associated microstructural refinements. The dependence of DAS and interflake spacing on growth velocity in the pure Al-Mg-Si alloy is shown in Figure 6.4. These relationships are described by equations of the form;

$$DAS = KV^{-m} \qquad \text{for Al-Mg-Si alloy} \qquad (6\text{-}5)$$

$$\lambda = KV^{-m} \qquad \text{for eutectic} \qquad (6\text{-}6)$$

with K = 419.07 and m = 0.34 for dendrites

K = 41.40 and m = 0.38 for eutectic.

where [DAS, λ (μm), V (μm sec^{-1})]

Using equations (6-5) and (6-6) the UTS contributions can be related to the respective spacings through the equations;

$$\sigma_{UTS} = \sigma_o + K * DAS^{-0.48} \qquad (6\text{-}7)$$

$$\sigma_{Si} = \sigma_o + K\lambda^{-0.50} \qquad (6\text{-}8)$$

$$\sigma_{P.D.} = \sigma_o + K * DAS^{-0.40} \qquad (6\text{-}9)$$

Figure 6.5 shows that equations (6-7) to (6-9) suggested that the UTS-interflake spacing of the unmodified eutectic follows a Hall-Petch relationship. The same conclusion is drawn from the UTS-DAS relationship for the alloy. The equation describing the behaviour of the contribution from the dendrites shows a slightly lower power value (0.40).

When the 0.2% proof stress of the pure alloy is plotted against velocity a different

behaviour is observed. The relationship is shown in Figure 6.6 to which may be fitted the relationship;

$$\sigma_{0.2}=\sigma_o+KV^n \qquad (6\text{-}10)$$

with σ_o = 18.13 K = 41.80 and n = 0.06

where [$\sigma_{0.2}$ (N mm^{-2}), V (μm sec^{-1})]

This indicates that the proof stress shows a much smaller dependence on the growth velocity. Where the proof stress is plotted against DAS, the relationship in Figure 6.7 is described by;

$$\sigma_{0.2}=\sigma_o+K*DAS^m \qquad (6\text{-}11)$$

with σ_o = 11.08 K = 171.89 and m = -0.24

where [$\sigma_{0.2}$ (N mm^{-2}), DAS (μm)]

The variation of %elongation with DAS is shown in Figure 6.8 and the variation of Q, quality index, with DAS in Figure 6.9.

In conclusion, the measurements made in the pure alloy show that the UTS, 0.2% proof stress , elongation and quality index, Q, decrease as the DAS of the alloy increases. A rule of mixtures analysis has been used to show that approximately 60% of the strength of the alloy is derived from the contribution of the primary dendrite network. The UTS-DAS relationship is of the Hall-Petch type, whereas the 0.2% proof strength-DAS relationship is not.

6-3 COMMERCIAL PURITY LM25 ALLOYS.

The measurements described above were used as a basis for studying the mechanical property-structure relationships in commercial purity LM25 alloy. Preliminary measurements were

made using the CO_2 hardened sand mould used in the studies of Radhakrishna and Seshan[122]. These measurements are shown in Table 6.3. However, these samples were known to solidify with a varying temperature gradient and growth velocity and were found to contain some porosity. As evident in Figure 6.10 this results in inferior mechanical properties. Therefore, samples were solidified in the thermal valve furnace where greater control could be exercised over growth velocity and temperature gradient during solidification and the samples contained much less porosity. The mechanical property measurements made in this way are recorded in Table 6.4. A comparison of Table 6.1 and 6.4 shows the commercial purity LM25 alloy is stronger but less ductile than the pure Al-Mg-Si alloy. Two factors may contribute to this difference in properties. These are solid solution strengthening due to the presence of Fe and Mn and the presence of brittle intermetallic compounds. The reactions that occur during the solidification of the commercial purity LM25 at the cooling rates employed in this study (0.1 to 0.4 $^0C\ sec^{-1}$) are;

1)	Development of the dendritic network commencing	at 614 ^0C
2a)	Liquid $\rightarrow$ Al + $Al_{15}(Mn,Fe)_3Si_2$	at 594 ^0C
2b)	Liquid $\rightarrow$ Al + Al_5FeSi + $Al_{15}(Mn,Fe)_3Si$	at 594 ^0C
3)	Liquid $\rightarrow$ Al + Si + Al_5FeSi	at 575 ^0C
4)	Liquid $\rightarrow$ Al + Si + Mg_2Si	at 555 ^0C

The intermetallic compounds are detrimental to mechanical properties if they are needle shaped. This is the natural morphology of the β (AlFeSi) compound. In practice, Mn is added when the $Al_{15}(Mn,Fe)_3Si$ compound forms which displays a less damaging chinese script structure. Alternatively superheating of the melt changes the crystallization mode to a chinese script form. This treatment was not employed in the present study. The amount of Mn present was insufficient to prevent the formation of the needle shaped β compound. Also the $Al_{15}(Mn,Fe)_3Si$ compound was present in a needle shaped morphology. Needles of AlSiFeMn compound are shown in Figure 6.11. Microprobe analysis showed that they have an approximate composition by weight of 45.1 ± 4.7 %Al, 29.47 ± 4.6 %Si, 19.5 ± 1.1 %Fe and 5.6 ± 0.7 %Mn. It has

been reported[50,55] that Fe contents up to 0.5%Fe enhance UTS and 0.2% proof stress marginally and at levels in excess of 0.5% reduce UTS. Small amounts of Fe are known to have a strong detrimental effect on elongation.[50,142]

The variation of UTS with growth velocity for the LM25 alloy is shown in Figure 6.2. The increased strength of the alloy is evident from this figure. The dependence of UTS is similar to that of the Al-Mg-Si alloy and can be represented by the equation;

$$\sigma_{UTS}=\sigma_o+KV^n \qquad (6\text{-}12)$$

with σ_o = 39.13 K = 43.43 and n = 0.22

where [σ_{UTS} (N mm^{-2}), V (μm sec^{-1})]

Assuming that a rule of mixtures law can be used to describe the individual contributions of the microstructural phases, the total contribution of the intermetallic compound and the solid solution hardening of the Al phases may be estimated using the equation;

$$\sigma_{UTS}=0.67*\sigma_{P.D.}+0.33*\sigma_{Si}+\sigma_{I.C.} \qquad (6\text{-}13)$$

Figure 6.4 shows the variation of DAS with growth velocity for the pure Al-Mg-Si alloy and for the commercial purity LM25 alloy. It is evident that there is a refinement of DAS in the commercial alloy, probably due to the residual Ti content. If the dendrites are assumed to be the same constitution as in Al-Mg-Si, this refinement must be taken into account in calculating the $\sigma_{P.D.}$ contribution. Figure 6.4 also shows that there is very little difference in the eutectic spacing - growth velocity relationship in the two alloys. Consequently, the eutectic contribution may be considered to be the same in the two alloys. Incorporating this information into equation (6-13) leads to the contribution to the LM25 UTS shown in Figure 6.12. Also included in this figure are the contributions calculated to the UTS for the pure Al-Mg-Si alloy. This figure stress that the

extra strength of the commercial alloy is derived from an increased contribution from the dendrite refinement, a contribution due to solid solution hardening and a contribution from the intermetallic compounds. It is likely that the solid solution strengthing contribution is independent of growth velocity. If this is true, Figure 6.2 shows that the intermetallic compound (AlSiFeMn) makes a contribution that increases significantly with increasing growth velocity as shown in Figure 6.2. This Figure shows that this contribution can be described by an equation of the form;

$$\sigma_{I.C.}=\sigma_o+KV^n \qquad (6\text{-}14)$$

with σ_o =-10.50 K =4.43 and n = 0.46

where [$\sigma_{I.C.}$ (N mm^{-2}), V (μm sec^{-1})]

The increase in strength due to the various contributions may be related to the corresponding structural refinements. The length of the intermetallic needles in the LM25 alloy is plotted as a function of growth velocity in Figure 6.4. The relationship obeys the equation;

$$L_{I.C.}=700*V^{-0.51} \qquad (6\text{-}15)$$

where [$L_{I.C.}$ (μm), V (μm sec^{-1})]

Figure 6.13 shows that good agreement exists between the present and previous measurements[67] when the DAS exceeds 70 μm but the present relationship lies below the relationship found by Gustafasson[67] when the DAS is less that 70 μm. This figure shows that the UTS contribution calculated for the intermetallic compound increases as the needle length decreases. The dependence of the alloy UTS on DAS is shown in Figure 6.10 and, as with the Al-Mg-Si alloy, the relationship is of the Hall Petch form;

$$\sigma_{UTS} = \sigma_o + K * DAS^{-m} \qquad (6\text{-}17)$$

with σ_o = -2.29 K = 1312.8 and m = +0.51

where [σ_{UTS} (N mm^{-2}), DAS (μm)]

The eutectic contribution has been considered to be the same in the two alloys and is shown in Figure 6.5. This figure also shows that, as for the Al-Mg-Si alloy, the equation observing the contribution from the dendrites as a function of their DAS has a slightly lower power function(0.4).

The variation of 0.2% proof stress with growth velocity is shown in Figure 6.6. Again, in common with the Al-Mg-Si alloy, the measured values fit a relationship of the form of equation (6-10) with n = 0.06. Again, in common with the Al-Mg-Si alloy, the proof stress-DAS relationship does not obey a Hall Petch relationship. The proof strength is higher in the LM25 alloy due to additional contributions from DAS refinement, solid solution hardening and the presence of intermetallic compounds.

The variation of % elongation with DAS is shown in Figure 6.8 and the variation of the quality index Q with DAS in Figure 6.9. There is a significant reduction in the % elongation in the presence of intermetallic compounds indicating their significant effect on ductility. This is reflected in the lower values of the quality index. Both properties show a slight increase with growth velocity and structural refinement.

The measurements described hitherto for pure Al-Mg-Si and LM25 alloys suggest that there is a dependence of properties on growth velocity and structure refinement. The relationship between UTS and DAS for both alloys display a Hall-Petch type of behaviour but the 0.2% proof stress does not show this type of relationship and the effect of structural refinement (DAS) is not as great on the proof stress.

These same features are evident in the results presented by Radhakrishna and Seshan[122] although their alloys are in heat treated condition. The variation of proof stress, UTS and % elongation with DAS for their LM25 alloy is drawn in Figure 6.14. When the average of their measurements is plotted against DAS it is found that the following equations are followed;

$$\sigma_{UTS}=\sigma_o+K*DAS^{-0.50} \qquad (6\text{-}17)$$

and

$$\sigma_{0.2}=\sigma_o+K*DAS^{-0.22} \qquad (6\text{-}18)$$

where [σ_{UTS}, $\sigma_{0.2}$ (N mm^{-2}), DAS (μm)]

A further feature of this same study is the strong effect of temperature gradient in the liquid on mechanical properties. For LM25 in the unmodified condition, Radhakrishna and Seshan[122] show that as their average temperature gradient increases from 10 to 82 °C cm^{-1} there is an increase in UTS from 235.2 to 362.6 N mm^{-2} or a 54% increase. This improvement in strength is likely to occur from improved contributions from the dendritic and eutectic structures because of their refinement. Selecting a growth velocity of 224 μm sec^{-1} increasing the temperature gradient from 10 to 82 ^{0}C cm^{-1}; reduces the DAS from 48 to 28 μm from Figure 6.15. From Figure 6.10, the increase in the UTS dendrite contribution is approximately 20 N mm^{-2}. The increased temperature gradient also refines the eutectic flake spacing. Previous measurements have shown that this refinement is from 5 to 2.5 μm. The increase in the eutectic contribution to the UTS from this refinement is estimated to be 15 N mm^{-2} from Figure 6.4. Consequently, the rule of mixtures approach suggests that the increase in UTS due to these two microstructural refinements is 35 N mm^{-2}. Figure 6.12 suggests that there is a further increase in UTS due to refinement of the intermetallic compounds of 20 N mm^{-2}. This suggests that the total increase is 55 N mm^{-2}. As the UTS measured for a temperature gradient of 10 ^{0}C cm^{-1} and a growth velocity of 224 μm sec^{-1} is 177 N mm^{-2}, the improvement is 31 %. This improvement

is smaller than that found by Radhakrishna and Seshan[122] but it must be remembered that their measurements are for heat treated specimens. The results show the importance of temperature gradient during solidification on promoting strength both in the as-cast state and the heat treated condition.

A better understanding of the variation of mechanical properties with alloy type and solidification conditions is possible if the microstructural features of deformation and fracture are known. LM25, Al-Mg-Si and eutectic specimens were deformed to various degrees and then the samples were sectioned and polished to observe the microstructural features. The observations made are consistent with the following picture of microstructural changes during deformation. During the initial straining fracture of the eutectic Si phase and intermetallic compounds occurs at several locations once the strain has exceeded that corresponding to the yield point. Most of the fractures occur across the transverse axis of the particles unless the longitudinal axis of the particle is orientated parallel to the final crack growth direction as shown in Figure 6.16a. Further straining results in localized plastic deformation in the Al phase of the eutectic region around the fractured particles eventually causing small cracks connecting two or more particles this is illustrated in Figure 6.16b. No interfacial cracking was observed (Si or intermetallic). On further straining microcracks join neighbouring microcracks in the same eutectic region to initiate a primary crack or join a propagating crack as shown in Figure 6.16c. The crack propagation path follows eutectic regions between the dendrite arms. The primary phase dendrite arms act as barriers to the crack propagation. The proeutectic Al phase regions along the crack path do not always fracture fully until the primary crack has propagated through neighbouring eutectic regions. Figure 6.17 shows typical fracture paths in the three alloys studied.

These and other similar studies[143-145] give valuable information concerning the microstructural aspects of mechanical deformation in Al-Si based casting alloys. They[143-145] show that failure in a ductile mode is influenced by;

1) Initiation of cracks in Si and other compound particles

2) Growth of cracks into cavities

3) Propagation of voids through the Al matrix.

It is to be expected that the size, shape (aspect ratio) and distribution of Si and other particles will play a significant part in the fracture process. All of these particle features can be influenced by modification, cooling rate and heat treatment.

The mechanical properties described for pure Al-Mg-Si and commercial purity alloys show that the presence of large aspect ratio Fe compound particles have a strong influence on elongation to fracture and a small but positive influence on strength. The second and third stages are more related to the nature and dispersion of the matrix phase. The growth of the particle cracks into voids involves failure of the matrix between the particles. This will be influenced by the nature of the matrix which may be changed by heat treatment and the amount of matrix between the particles which, in turn, will be influenced by the solidification conditions and heat treatment. The pro eutectic Al phase is fracture resistant forcing the fracture path to follow interdendritic regions. Therefore one might anticipate that dendrite arm spacing may also influence the mechanical properties. Although the as-cast matrix structure is fracture resistant it has low strength; consequently, heat treatment will promote better overall properties. Indeed, the more successful attempts to improve the fracture resistance of these alloys may be those designed to isolating eutectic regions in the microstructure so that cracks must propagate through more of the fracture resistant proeutectic Al.

6-4 INFLUENCE OF MODIFICATION ON THE MECHANICAL PROPERTIES OF LM25 ALLOYS.

The mechanical properties of a pure Al-Si alloy and the commercial alloy treated with 0.04%Sr and the commercial alloy treated with 0.2%Sr are given in Table 6.5. Comparing the

results in this table with those for the untreated alloys in Table 6.4 shows that the addition of 0.04%Sr improves the mechanical strength but results in a greater improvement in the elongation to fracture. The addition of 0.2%Sr results in a decrease in all mechanical properties. The results are shown as a function of DAS in Figure 6.18. This Figure shows that the overall behaviour of the treated alloy is similar to that of the untreated alloy with respect to solidification conditions and structure refinement. The variation of UTS with DAS can be described by the equations;

for the LM25 + 0.04%Sr alloy

$$\sigma_{UTS}=\sigma_o+K*DAS^{-m} \qquad (6\text{-}19)$$

with σ_o = 2.31 K = 1494.15 and m = 0.51

and for the LM25 + 0.2%Sr alloy

$$\sigma_{UTS}=\sigma_o+K*DAS^{-m} \qquad (6\text{-}20)$$

with σ_o = 0.03 K = 1049.66 and m = 0.50

where [σ (N mm^{-2}), DAS (μm)]

The addition of Sr has little effect on the nature of the primary Al phase and as shown in the previous chapter refines the DAS by approximately 10%. This refinement is also shown in Figure 6.15. The major influence of the addition of Sr is on the size, shape and distribution of the eutectic Si phase. The presence of Sr changes the Si morphology from a co zonal twinned flake structure to a multi twinned, microfaceted fibrous structure. There is also a significant refinement of the structure. The consequence of this structural change is to influence the initial cracking behaviour so as to yield on increase in strength and a significant increase in elongation. The latter is particularly evident in the case of the pure Al-Si alloy. The increase is still significant in the commercial alloy but is moderated by the presence of the intermetallic compounds. Figure 6.19 illustrates the microstructural features of fracture in the these alloys. Cracking in the pure alloy occurs in the eutectic Si fibres. The stress/strain conditions for cracking are likely to be

different than in the case of the eutectic flake Si particles of the unmodified alloy. The joining of microcracks will differ in the modified alloy as the dimensions of the fibres are much smaller than the dimensions of flakes. These differences in the initial stages of the fracture behaviour make a more significant contribution to the improved mechanical properties than the small refinement in the dendrite arm spacing. Intermetallic compound needles were observed in the commercial purity LM25 alloy and their presence will reduce the effectiveness of the change in morphology of the eutectic Si phase. As a consequence there is a much smaller improvement in the properties of the commercial alloy. Over modification with 0.2%Sr resulted in the appearance of large faceted Al_4SrSi_2 compound. This compound is shown in Figure 6.20. Analysis showed it to have a composition by weight of 28.1±0.41 %Al, 46.62±1.77%Si, 25.76±1.78%Sr. The presence of the Fe and Sr compounds in the overmodified commercial alloy produces a reduction in elongation and strength. Figure 6.15 shows that increasing the temperature gradient from 10 $^0C\ cm^{-1}$ to 82 $^0C\ cm^{-1}$ produces a significant reduction in DAS in the alloy treated with 0.04%Sr. There is a significant increase in strength and elongation accompanying this refinement but Figure 6.18 indicates that the improvement in properties is not as great as that achieved by modification.

6-6 INFLUENCE OF GRAIN REFINEMENT WITH 2wt% 3/1 TiBAL ON THE MECHANICAL PROPERTIES OF LM25 ALLOYS.

Mechanical property measurements made on the LM25 alloy treated with 2% (3/1) TiBAL are given in Table 6. The variation of UTS and elongation with DAS is shown in Figure 6.21 together with the same relationships for the untreated alloy. The variation of both UTS and elongation with DAS is similar for the untreated and treated alloy. The variation of UTS with DAS follows the equation;

$$\sigma_{UTS}=\sigma_o+K*DAS^{-m} \qquad (6\text{-}21)$$

with σ_o = 4.66 K = 1188.65 and m = 0.48

where [σ_{UTS} (N mm^{-2}), DAS (μm)]

The addition of the grain refining agent to the commercial LM25 alloy refines the DAS slightly and has a very small refining effect on the interflake spacing. Figure 6.15b shows that the DAS refining effect is similar to that in Sr modified alloys. Table 6.7 compares the UTS and elongation values at a constant growth velocity of 63 μm sec^{-1}. This table shows that there is only a small improvement in mechanical properties after grain refining. The only significant microstructural change is the refinement of the dendrite arm spacing. Consequently the improvement in properties is mainly due to the refinement of DAS. For example, selecting a growth velocity of 63 μm sec^{-1}, the refinement in DAS can be measured from Figure 6.15b. Using Figure 6.21 and the UTS-DAS relationship for the LM25 alloy gives an increase of 4 N mm^{-2} for the DAS refinement. The value shown in Table 6.7 is 8 N mm^{-2}. The 4 N mm^{-2} value does not take into account any strengthening due to solid solution effects or the slight refinement of the eutectic. The same calculation for the increase in elongation accounts for all the increase shown in Table 6.7. Thus it is reasonable to concluded that the slight improvement in properties is due to the refinement of the DAS and eutectic spacing. Table 6.7 shows that there is a much greater improvement in the UTS and elongation after modification with Sr. As the refinement of DAS is similar in the two treatments, it is reasonable to concluded that the improvement in mechanical properties on modification derives from the change of eutectic Si morphology and the significant refinement in eutectic spacing. Once again Figure 6.15b shows that there is greater refinement of DAS if a high temperature gradient is present in the liquid during solidification. There should also be an improvement in the mechanical properties.

6-6 INFLUENCE OF ANTIMONY ADDITIONS ON THE MECHANICAL PROPERTIES OF LM25 ALLOYS.

Mechanical property measurements made on LM25 alloys treated 0.2%Sb are given in Table 6.8. The variation of UTS and elongation with DAS is shown in Figure 6.22 with the

relationships for untreated and Sr treated LM25 alloys. The variation of UTS and elongation with DAS is similar to that of the other alloys examined. The variation of UTS with DAS can be described by the equation;

$$\sigma_{UTS}=\sigma_o+K*DAS^{-m} \qquad (3\text{-}22)$$

with σ_o = 2.57 K = 1351.13 and m = 0.51

where [σ_{UTS} (N mm^{-2}), DAS (μm)]

Antimony treatment of the melt is the treatment used in many European foundries. It has the benefit of improving castability and soundness of the product. However, as Figure 6.22 shows, the improvement in mechanical properties is not as great as with treatment with 0.04% Sr. As shown in the previous chapter and in Figure 6.15b there is a much greater DAS refinement with Sb treated alloys. It is well established that Sb does not change the Si eutectic phase morphology. It refines the Si eutectic flake structure. Again, selecting a growth velocity of 63 μm sec^{-1} the refinement in DAS can be measured from Figure 6.15b. Using Figure 6.22 and the UTS-DAS relationship for the LM25 alloy gives an increase of 9 N mm^{-2} for the DAS refinement. The value shown in Table 6.7 is 17.6 N mm^{-2}. There will be contributions to the increase in strength from a solid solution hardening effect and the refinement of the eutectic structure. However, the above calculation shows that the improvement in mechanical properties due to the DAS refinement is much greater in Sb treated alloys and makes a significant contribution to the improvement in properties.

6-7 HARDNESS MECHANICAL PROPERTY RELATIONSHIPS.

There have been several attempts to use hardness as a measure of mechanical strength. In particular, Telli and Kisakurek[97] have proposed that there exists a universal Hall-Petch type of relationship between hardness and spacing for the Al-Si eutectic and that the 0.2% proof stress and UTS show similar relationships to spacing. Consequently, hardness can be used as a measure of both the 0.2% proof stress and the UTS. They also suggest that however the

spacing is controlled, by addition of Sb or by control over temperature gradient, the universal relationship is obeyed.

Measurements described in the previous sections have shown that whilst UTS does show a Hall-Petch type of dependence on DAS, the 0.2% proof stress does not. In order to investigate this further and to reexamine the conclusion drawn by Telli and Kisakurek mechanical property measurements and hardness measurements were made on Al-12.7%Si and Al-12.7%Si-0.2%Sb alloys solidified using thermal valve furnace. The results are shown in Table 6.9. These results are shown in Figure 6.23 together with the UTS results shown in Table 6.2. The hardness measurements for Al-12.7%Si alloys solidified at a low temperature gradient (10 ^{0}C cm^{-1}) can be described by the equation;

$$H=H_o+K*\lambda^{-a} \qquad (6\text{-}23)$$

with a = 0.22. This finding agrees well with other measurements made on alloys solidified at different temperature gradients[98]. The measurements for Al-12.7%Si-0.2%Sb can be described by equation (6-23) with a slightly higher value of H_o. The present and previous measurements show that the hardness depends on the temperature gradient as shown in Figure 6.23 as the temperature gradient increases, the hardness increases in both alloys.

The variation of hardness with interflake spacing differs from that suggested by Telli and Kisakurek who found a = 0.5. This difference may be due to the λ-V relationship used by Telli and Kisakurek to convert growth velocity to interflake spacing which differs from that measured by all other researchers. Measurements of the variation of 0.2% proof stress and UTS with interflake spacing in Figure 6.23 show that, as found for alloys in the earlier sections, only the proof stress shows a similar variation with spacing as hardness. Consequently, it is suggested that hardness can be used to predict the proof stress. The universal relationship suggested by Telli and Kisakurek for Sb treated and Sb free alloys is not confirmed. Both hardness and proof stress are slightly greater for Sb treated alloys at the same spacing. This is probably due to solid solution hardening by the Sb addition. The factor for converting hardness to proof stress (units of kg mm-2

β) is 0.11 compared to a value of 0.13 observed by Justi and Bragg.

6-8 COMMERCIAL LM25 ALLOYS TREATED BY THE HIPPING PROCESS.

The mechanical properties of a commercial LM25 alloy solidified in the thermal valve furnace and subjected to the HIPPING process (at 540 ^{0}C, 67 N mm^{-2} for 1 hour), are given in Table 6.10. Comparing the morphologic features of the silicon particles before and after HIPPING as shown in Figure 6.24, the eutectic silicon morphologies of HIPPED materials have been changed, due to the thermal treatment of the HIPPING process. The flake silicon became globular after HIPPING. The possible reason of this structure coarsening and spheroidizing is the dissolution of the silicon occurring at corners of high energy and at thin steps and branches of the structure[146]. Also this figure shows the morphology of the compound needles β intermetallic is chinese script, which can reduce the harmful effect of the needle shape on the mechanical properties.

The variation of the mechanical properties with DAS is shown in Figure 6.25 for the HIPPED and non-HIPPED LM25 alloys. The UTS and proof stress for the HIPPED materials only show a slight improvement due to the HIPPING process, since these samples are solidified in the thermal valve furnace which it can produce a specimen with low porosity content. The elongation of these sample has improved by almost 30% and this can be attributed to removal of the porosity and change in the morphology of both silicon particles and intermetallic compounds. It can be seen from Figure 6.25 that the dendrite arm spacing after HIPPING has increased, this may be due to the high temperature used in the HIPPING process (540 °C).

From the optical metallography on the deformed HIPPED LM25 alloy, it was observed that extensive cracking of the silicon particles and intermetallic compounds occurred in the samples see Figure 6.27. Apparently, the fracture behaviour for the HIPPED sample is similar to that found in the non-HIPPED samples.

TABLE 6.1 Mechanical property measurements of Al-7.5%Si-0.45%Mg alloy solidified in the thermal valve furnace.

D.A.S. μm	λ μm	V μm sec^{-1}	%Elong.	0.2%P.S. N mm^{-2}	UTS N mm^{-2}	Q. N mm^{-2}
72.88	5.58	180.72	13.74	74.9	133.2	303.89
55.05	4.48	332.51	16.27	73.6	130.17	311.87
83.77	6.521	117.23	15.03	73.1	123.62	300.15
96.02	8.223	61.550	15.53	71.2	113.53	292.20
54.68	4.278	377.81	16.61	75.2	133.27	316.44
88.20	6.971	97.361	14.07	69.66	118.37	290.61

TABLE 6.2 Mechanical property measurements of Al-12.7%Si alloy solidified in the thermal valve furnace.

λ μm	V μm sec^{-1}	%Elong.	0.2%P.S. N mm^{-2}	UTS N mm^{-2}	Q N mm^{-2}
4.55	312.2	9.330	---	180.70	326.20
5.16	221.5	10.14	73.73	156.00	306.90
6.48	118.9	6.700	67.49	142.80	266.70
5.92	153.3	7.750	69.80	147.70	281.10
5.91	152.3	9.158	70.79	147.46	291.73
5.31	207.6	10.93	72.97	157.22	313.01

TABLE 6.3 Mechanical property measurements of commercial purity LM25 solidified in the sand mould.

Chill Thickness mm	D.A.S μm	U.T.S. N mm^{-2}	%Elong.	Q N mm^{-2}
13	38.83	132.8	1.9	176
13	42.91	125.9	1.5	152
25	41.56	132.1	1.9	172
25	49.39	126.4	1.5	152

TABLE 6.4 Mechanical property measurements of commercial purity LM25 solidified in the thermal value furnace.

D.A.S. μm	V μm sec^{-1}	λ μm	%Elong.	0.2%P.S. N mm^{-2}	UTS N mm^{-2}	Q N mm^{-2}
55.44	140.26	6.20	4.50	91.2	166.70	266.11
74.50	49.66	8.75	3.50	83.2	143.70	225.30
47.59	239.85	4.96	4.79	97.3	187.40	289.45
52.86	159.34	5.90	4.59	---	178.10	277.70
62.04	94.42	7.15	4.62	---	152.51	252.26
64.00	84.21	---	4.73	---	157.38	258.61
49.73	178.76	---	5.39	91.0	176.86	286.59
64.28	84.52	---	4.62	88.3	152.51	253.26
55.3	141.20	---	4.77	---	165.67	267.44
49.93	180.31	---	4.74	---	185.66	287.03
52.89	159.90	---	4.59	93.3	178.13	277.27

TABLE 6.5 Mechanical properties of the pure Al-7.5%Si and commercial purity LM25 alloy treated with Sr and solidified in the thermal valve furnace.

Type of Alloy	DAS μm	0.2%P.S N mm^{-2}	%Elongation	UTS N mm^{-2}	Q N mm^{-2}
LM25-0.04%Sr	60.00	98.6	7.50	188.4	319.6
	74.70	91.2	6.17	175.7	294.2
	75.34	98.4	5.90	171.2	286.6
	79.84	83.6	5.60	154.0	266.2
PURE Al-Si-0.04%Sr	42.95		23.18	129.0	333.7
	53.90		24.41	119.5	327.6
	56.66		24.13	114.8	322.1
	82.12		19.80	107.6	302.1
LM25-0.2%Sr	64.97		3.00	136.8	208.2
	52.63		3.70	149.1	234.3
	70.59		3.35	123.8	202.3
	68.90		3.71	122.4	207.8
	48.57		3.71	148.1	233.5

TABLE 6.6 Mechanical property measurements made on LM25 alloys treated with 2% 3/1 TiBAL and solidified in the thermal valve furnace.

DAS μm	%Elongation	UTS N mm^{-2}	Q N mm^{-2}
70.24	4.27	160.0	254.50
80.04	3.98	149.0	239.11
67.50	4.5	167.2	265.19
56.14	4.9	171.6	275.19

TABLE 6.7 UTS and elongation of LM25, LM25-0.04%Sr, LM25-0.2%Sb and LM25-2%TiBAL(3/1) at a constant growth velocity of 63 μm sec^{-1} and a low temperature gradient in the melt.

Alloy	UTS (N mm^{-2})	Elongation
LM25	146.2	4.02
LM25-0.04%Sr	177.8	6.45
LM25-2%TiBAL	154.2	4.25
LM25-0.2%Sb	163.8	5.82

TABLE 6.8 Mechanical property measurements made on LM25 alloys treated with 0.2% Sb and solidified in the thermal valve furnace.

DAS μm	%Elongation	UTS N mm^{-2}	Q N mm^{-2}
37.4	6.76	216.3	340.8
37.8	6.60	223.2	346.1
50.31	6.24	186.1	305.3
31.87	7.50	242.7	373.9
44.96	6.62	190.5	313.6
45.92	5.88	195.2	310.6

TABLE 6.9 Mechanical properties measurements for Al-12.7%Si and Al-12.7%Si-0.2 %Sb alloys solidified in the thermal valve furnace.

Type of Alloy	λ µm	Hardness	%Elong.	0.2%P.S. N mm^{-2}	UTS N mm^{-2}	Q N mm^{-2}
Al-12.7% Si O.18% Sb	5.920	59.1	9.220	77.97	142.00	286.77
	7.814	56.3	7.800	66.24	135.63	269.44
	5.000	62.9	13.97	81.13	163.89	335.67
Al-12.7% Si	5.906	58.62		70.97		
	5.314	62.10		72.95		
	5.920	57.75		69.80		
	6.487	57.95		67.49		
	5.160	60.8		73.73		

TABLE 6.10 Mechanical property measurements made on HIPPED LM25 alloys and solidified in the thermal valve furnace.

DAS µm	%Elongation	UTS N mm^{-2}	Q N mm^{-2}
62.9	7.50	154.5	285.7
72.52	6.46	142.6	264.2
78.3	7.62	144.9	276.2
113.6	5.93	138.1	254.1

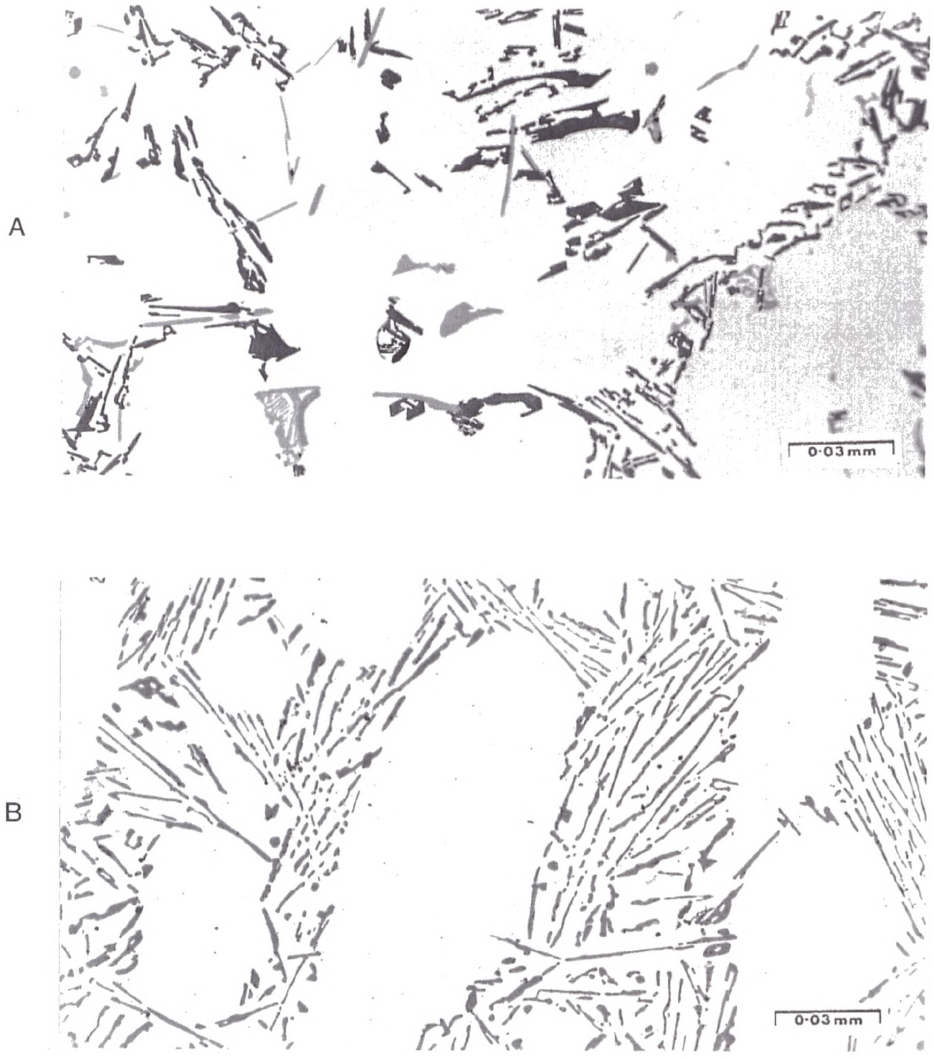

Figure 6.1 Microstructures obtained in a) LM25 alloy b) Al-7.5%Si-0.45%Mg alloy

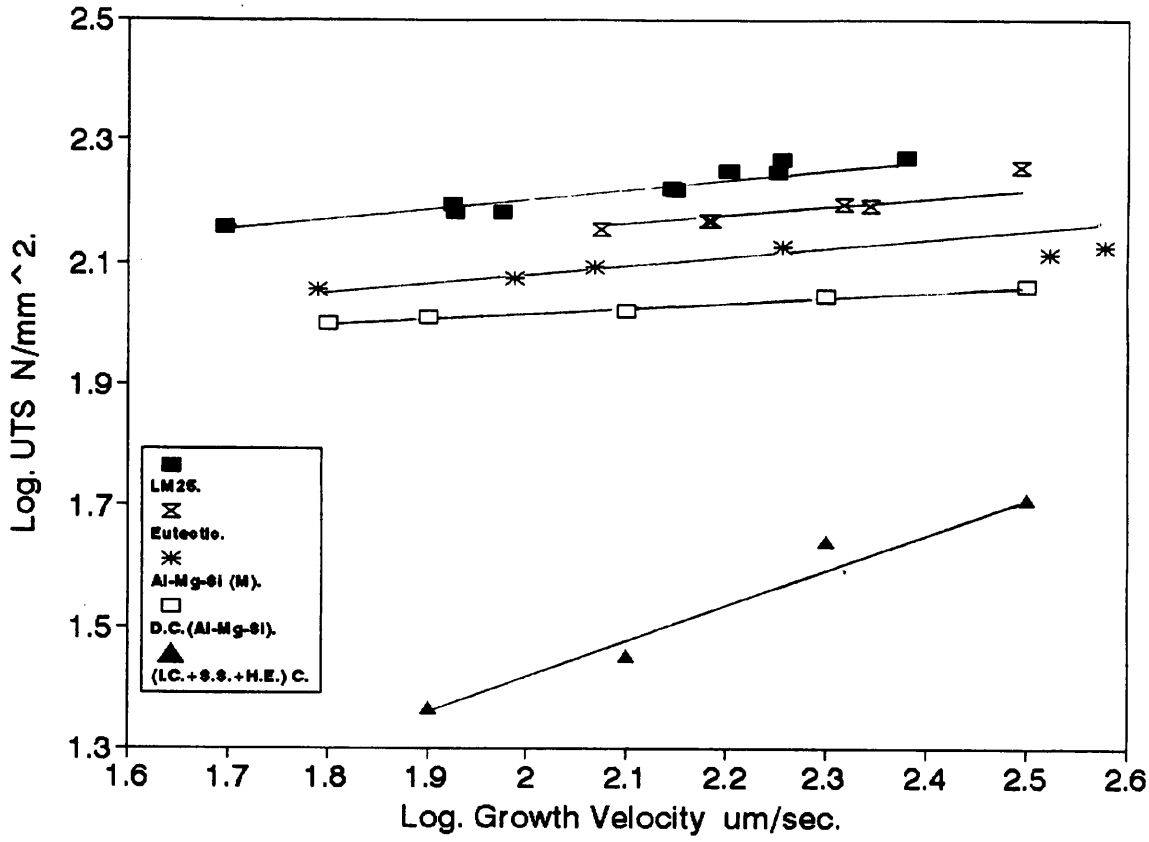

Figure. 6.2 Variation of the UTS with growth velocity for LM25, Al-12.7%Si, Al-7.5%Si-0.45%Mg, dendrite contribution (Al-Mg-Si) and the contribution of the intermetallic, solid solution and hardening effect (I.C. + S.S. + H.E.).

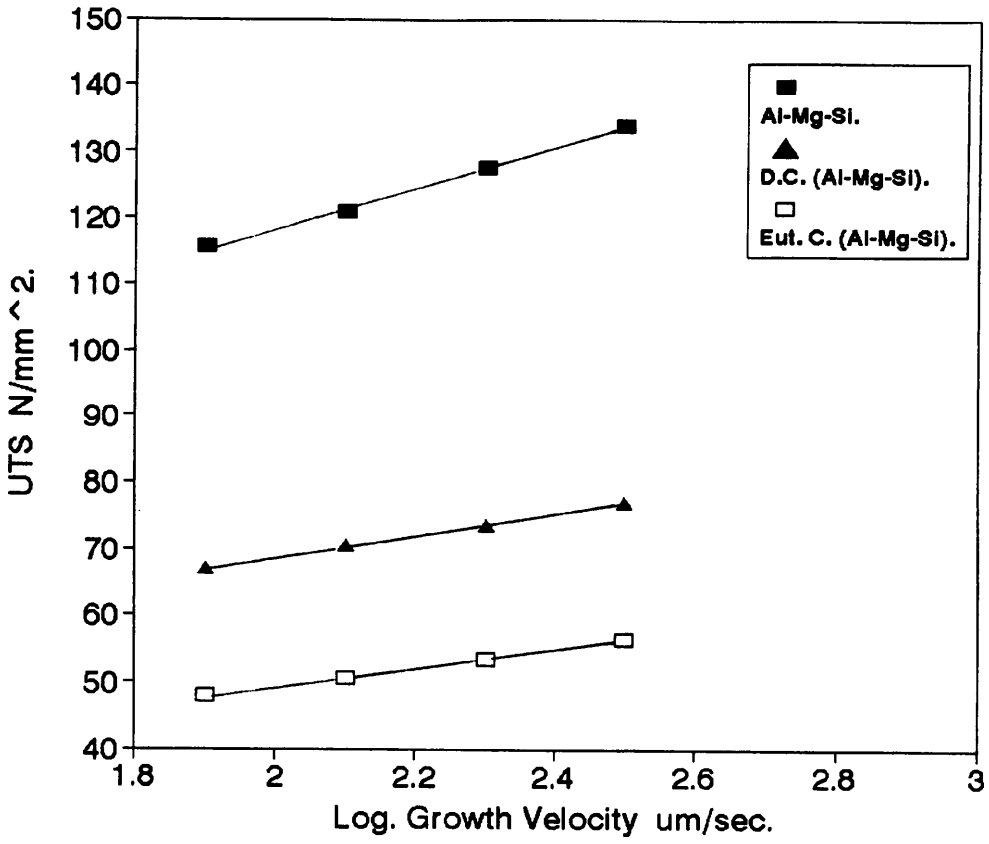

Figure. 6.3 Variation of the UTS with growth velocity for Al-7.5%Si-0.45%Mg, calculated contributions from dendrites and eutectic in an Al-Mg-Si alloy.

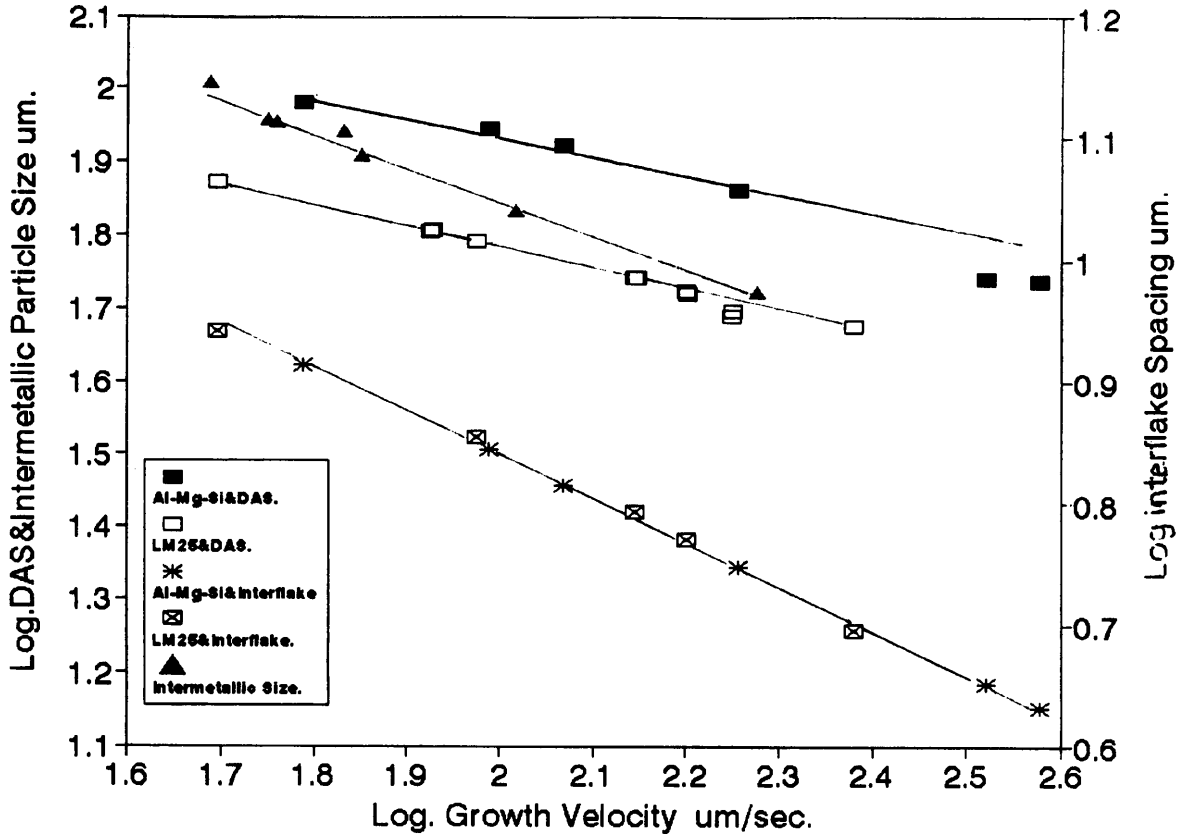

Figure. 6.4 Variation of the DAS, the intermetallic particles size (B) and interflake spacing with growth velocity for Al-7.5%Si-0.45%Mg and LM25 alloys.

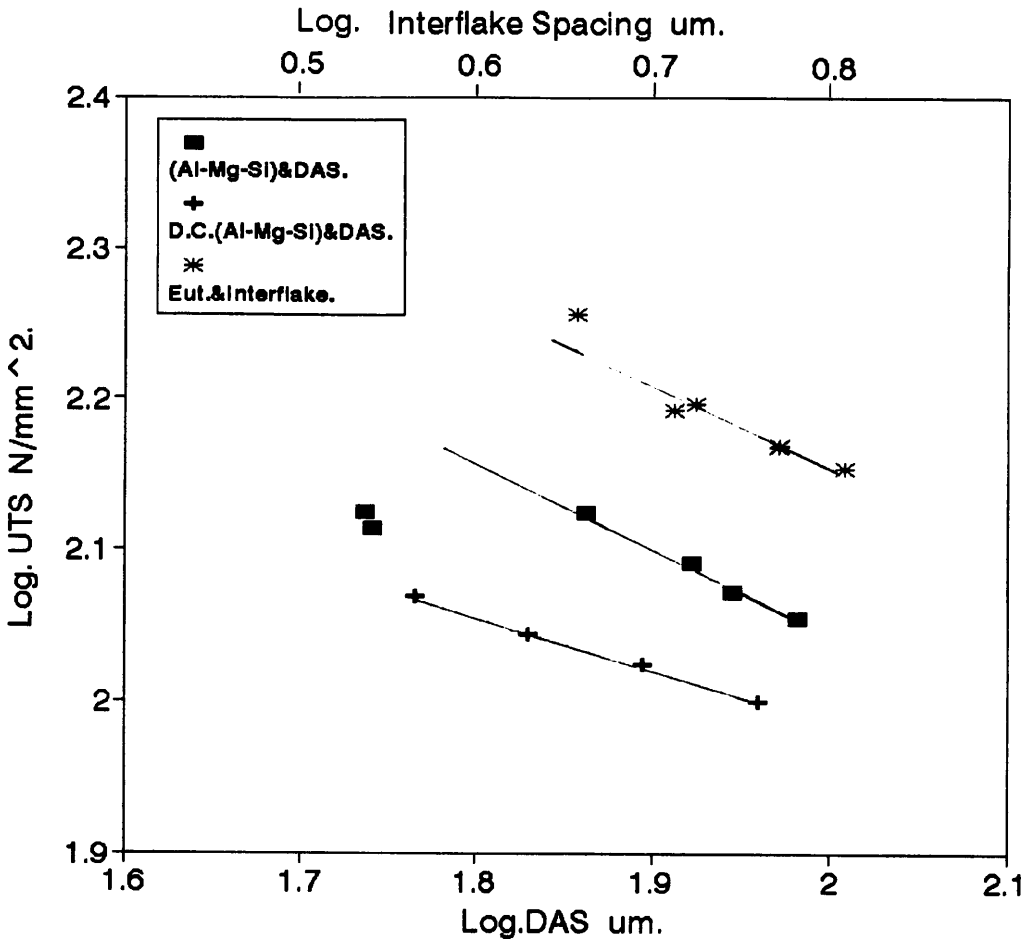

Figure. 6.5 Variation of the UTS with DAS and interflake spacing for Al-7.5%Si-0.45%Mg, Al-12.7%Si and calculated contribution from dendrites in an Al-Mg-Si alloy.

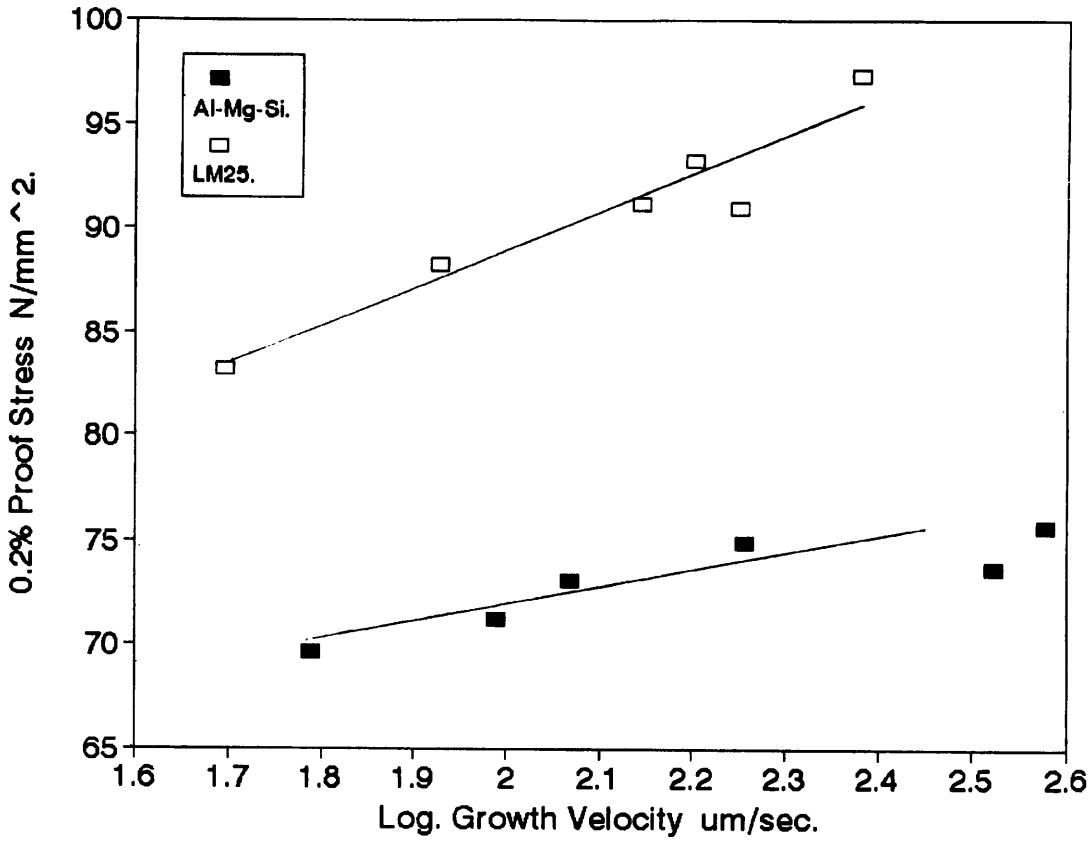

Figure. 6.6 Variation of the 0.2% proof stress with growth velocity for Al-7.5%Si-0.45%Mg and LM25 alloys.

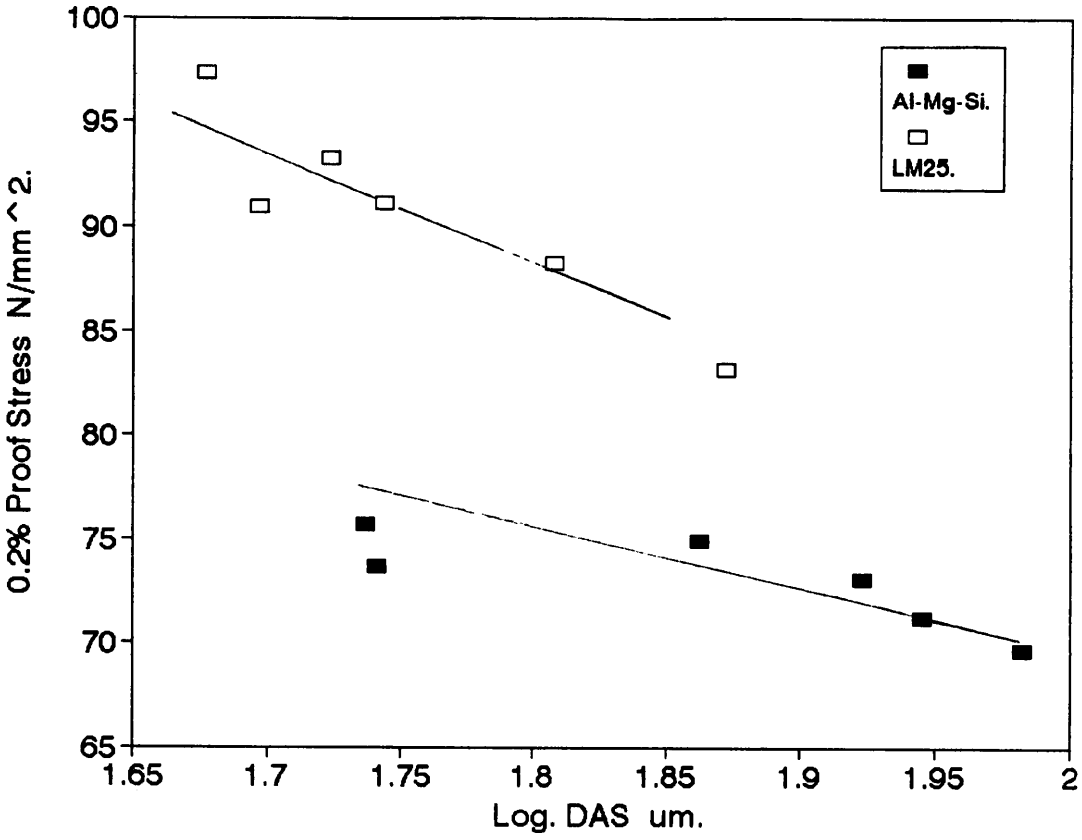

Figure. 6.7 Variation of the 0.2% proof stress with DAS for Al-7.5%Si-0.45%Mg and LM25 alloys.

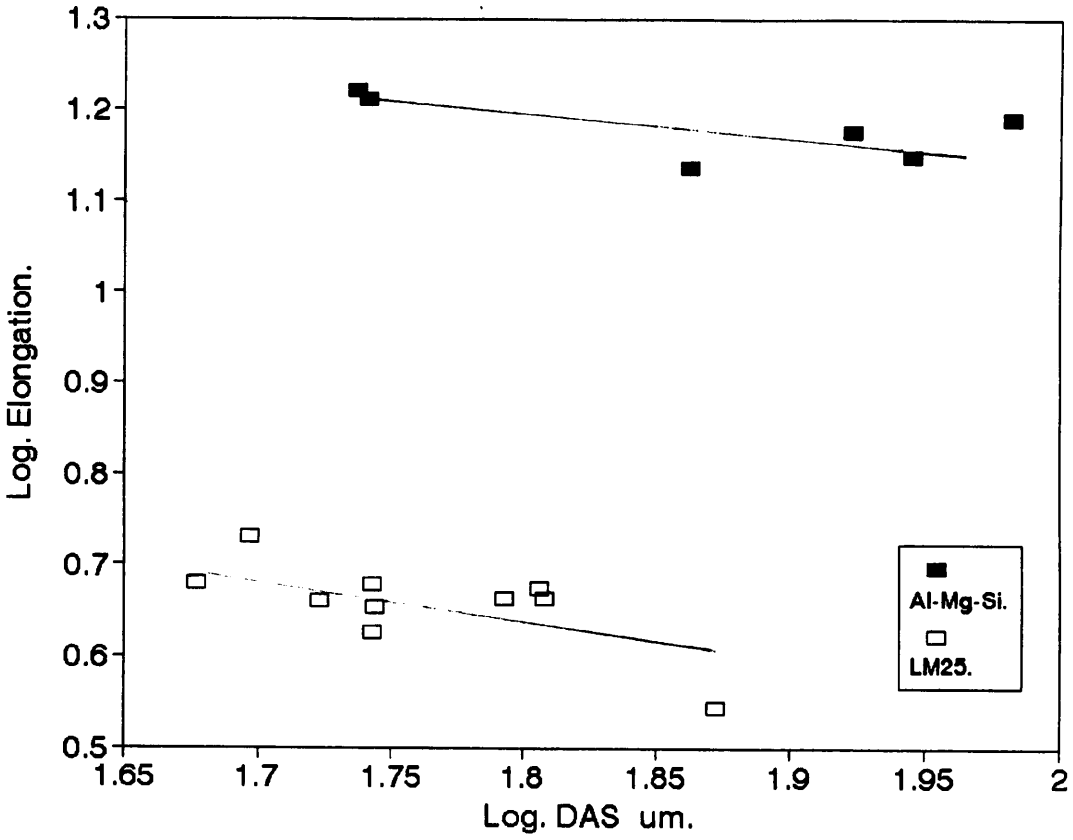

Figure. 6.8 Variation of the elongation with DAS for Al-7.5%Si-0.45%Mg and LM25 alloys.

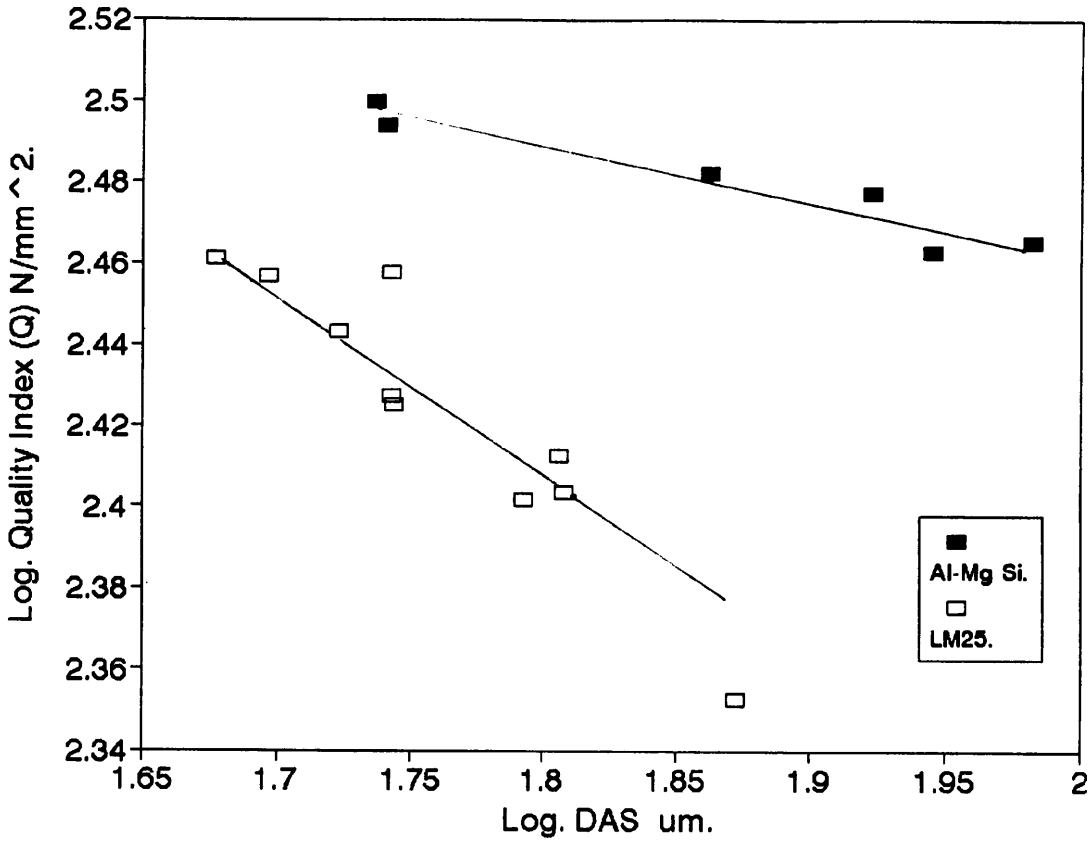

Figure. 6.9 Variation of the quality index (Q) with DAS for Al-7.5%Si-0.45%Mg and LM25 alloys.

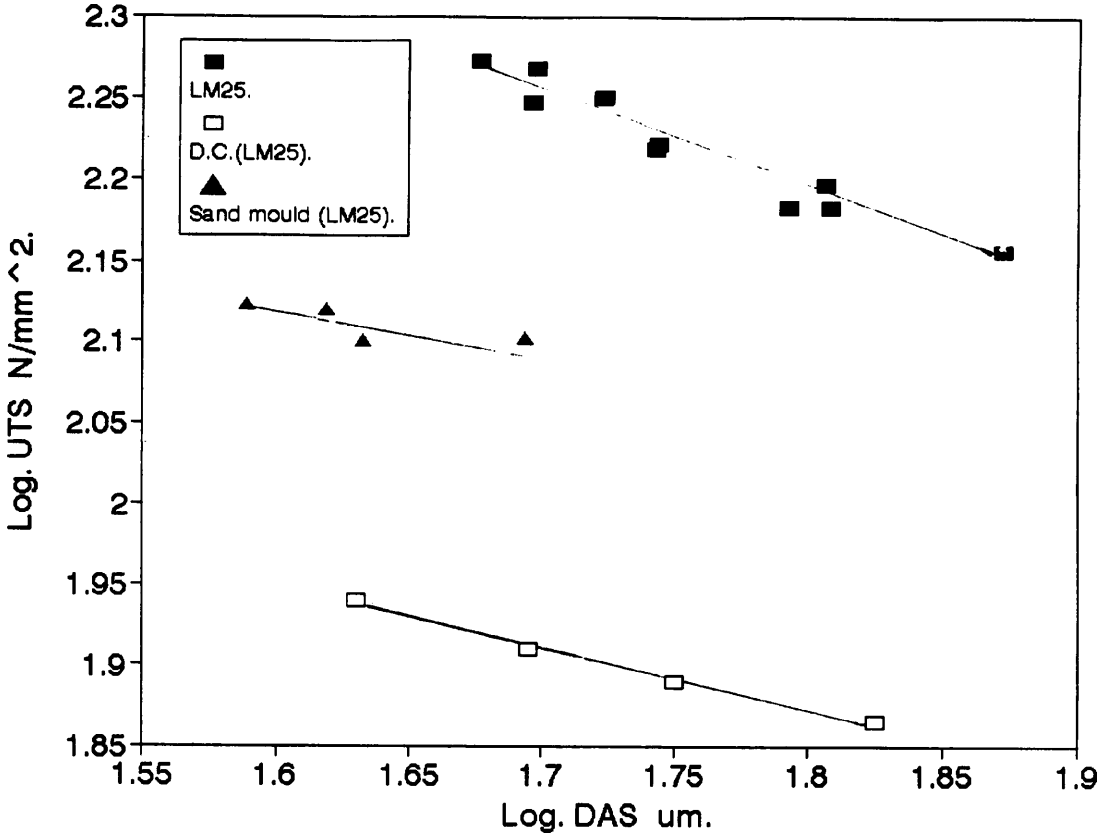

Figure. 6.10 Variation of the UTS with DAS for LM25 alloy solidified in the thermal valve furnace, LM25 alloy solidified in the sand mould and the calculated contribution for the dendrites in the LM25 alloys.

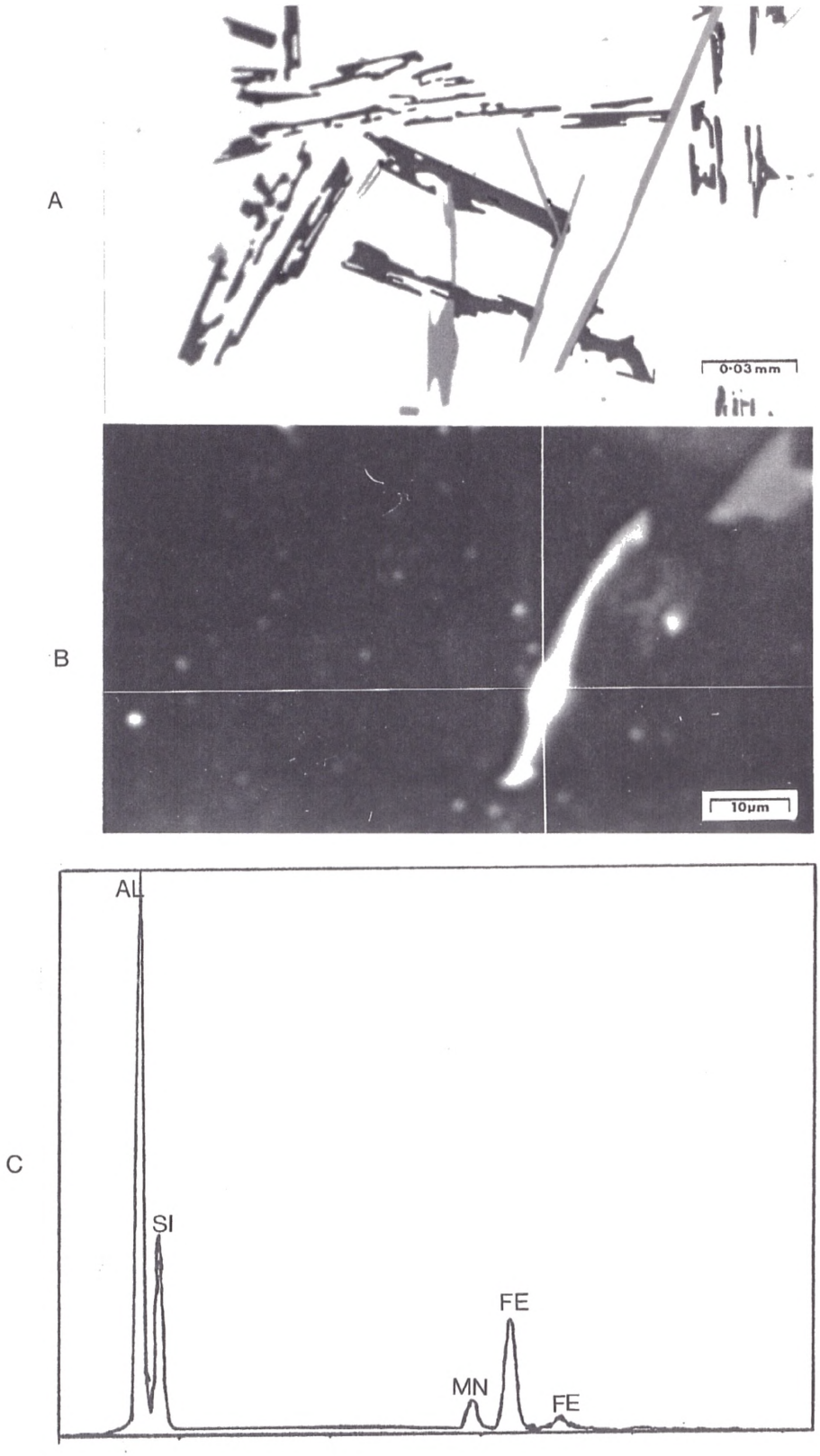

Figure. 6.11 Intermetallic phase ß (AlSiFeMn) in LM25 alloy,

a) Optical micrograph b) S.E.M. c) Analysis curve.

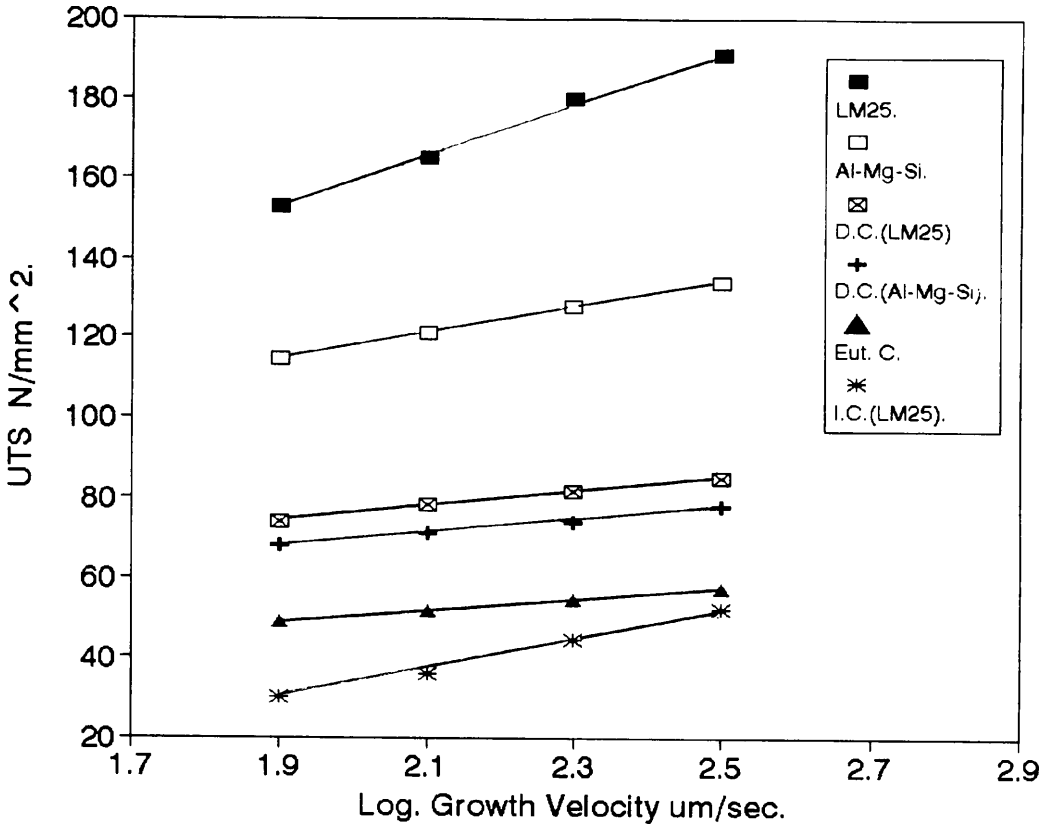

Figure. 6.12 Variation of the UTS with growth velocity for LM25, Al-Mg-Si, dendrites and eutectic contributions in LM25 and Al-Mg-Si and the contribution from intermetallic compounds. the dendrites in the LM25 alloys.

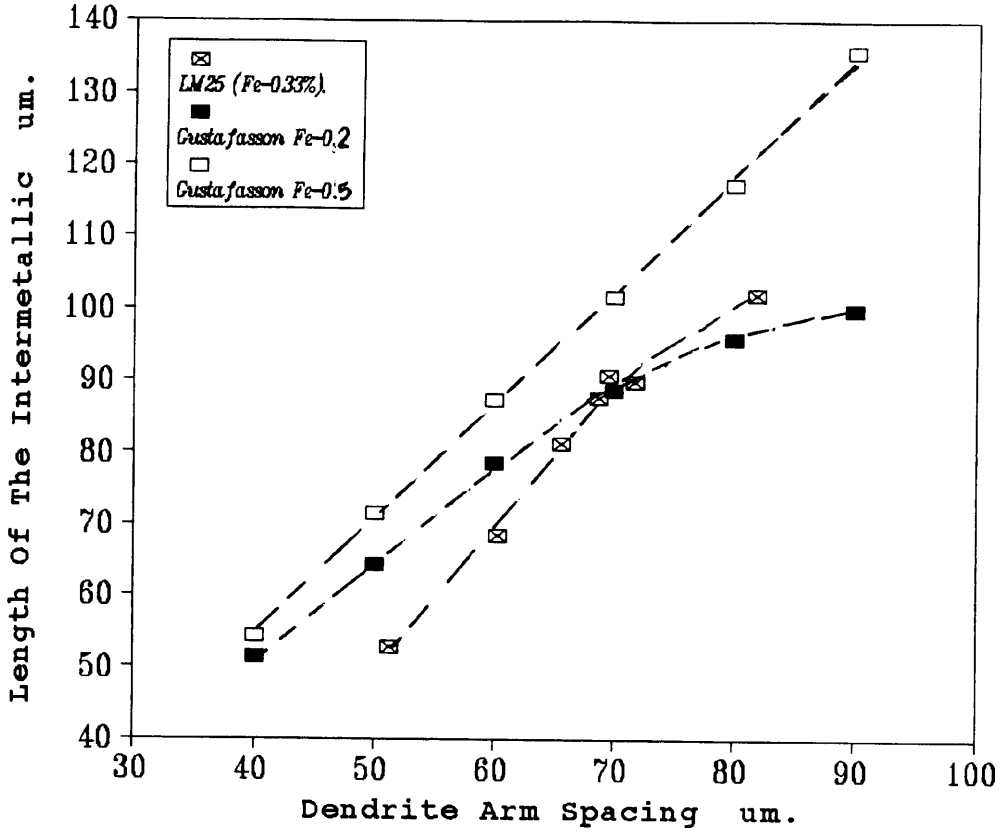

Figure. 6.13 Variation of the intermetallic particles size with DAS for LM25 solidified in the thermal valve furnace with previous results.[67]

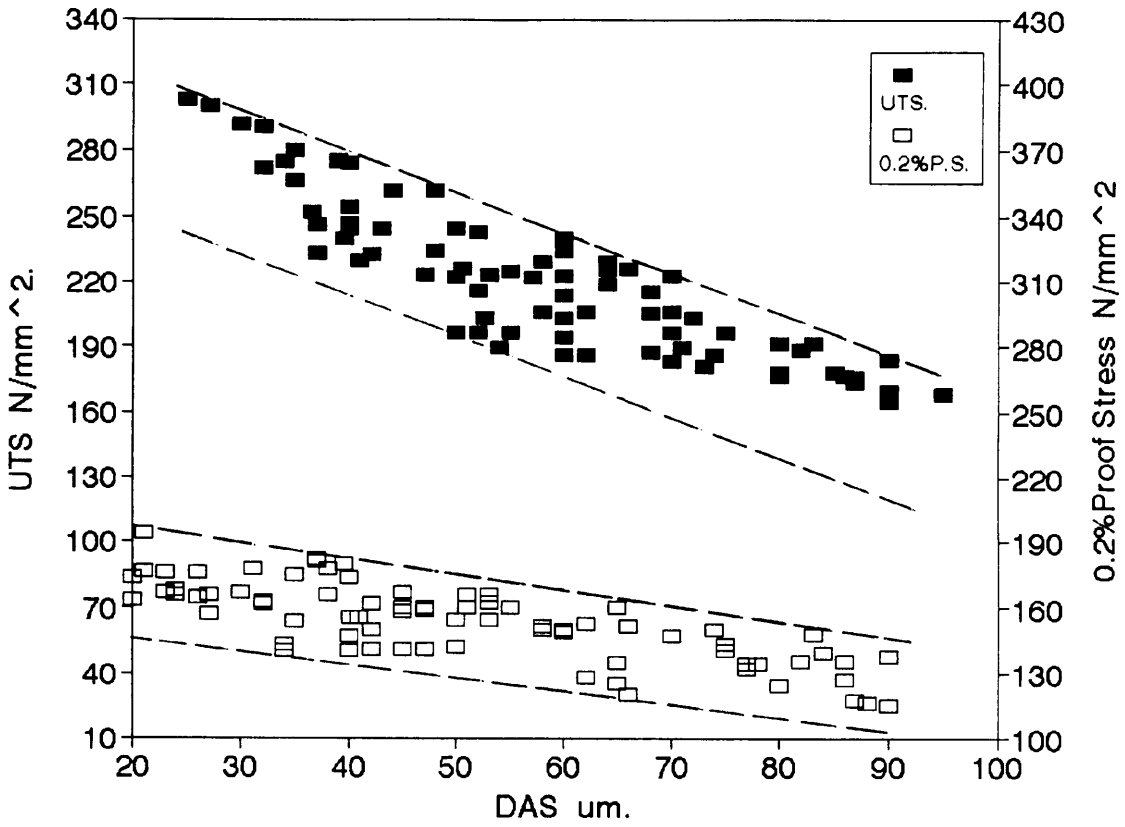

Figure. 6.14 Variation of the UTS, 0.2% proof stress and elongation with DAS for LM25 alloy alloy from previous results.[122]

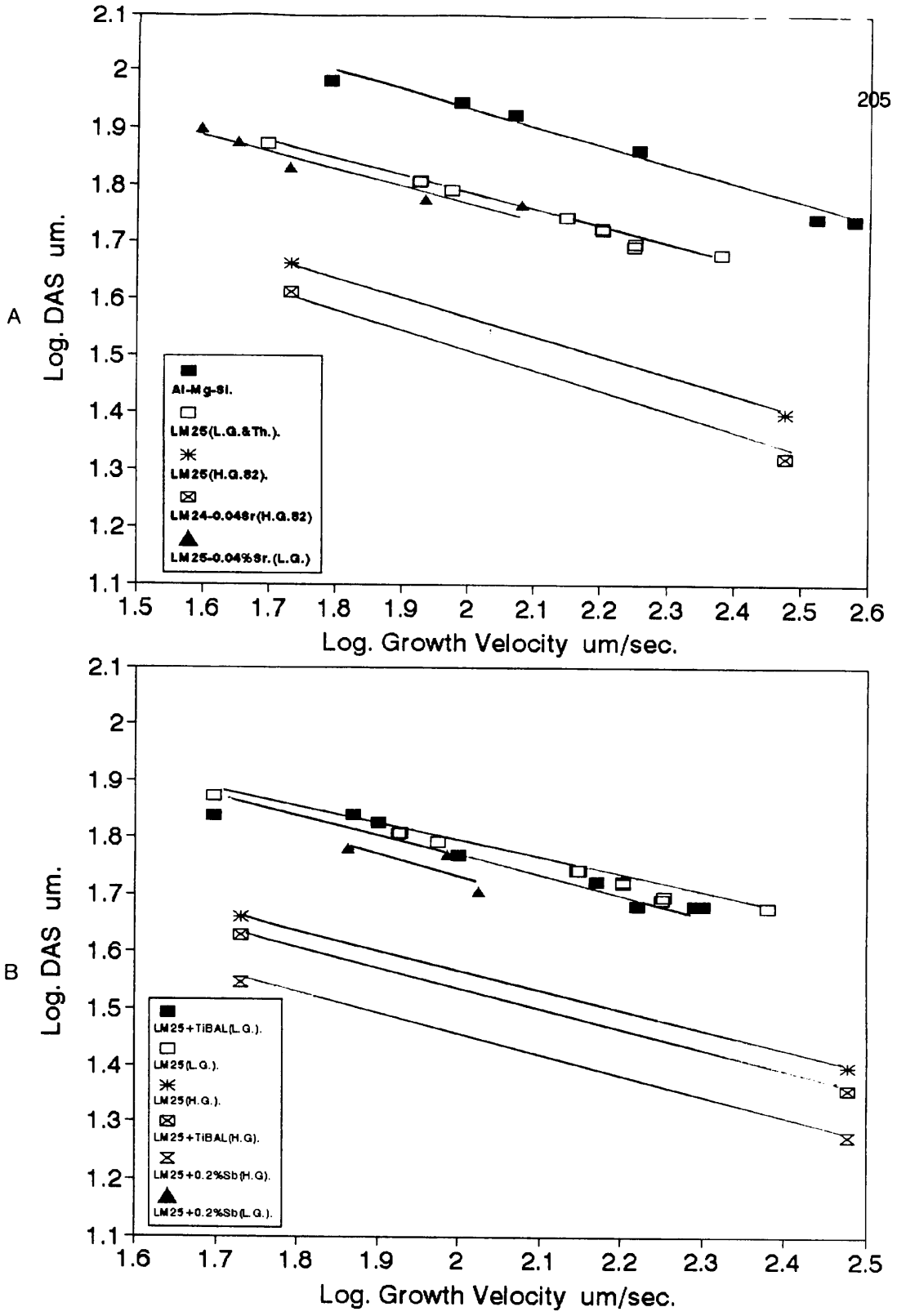

Figure. 6.15 Variation of the DAS with growth velocity for LM25, Al-Mg-Si and LM25-0.04%Sr alloys solidified in the thermal valve furnace and Bridgman furnace.

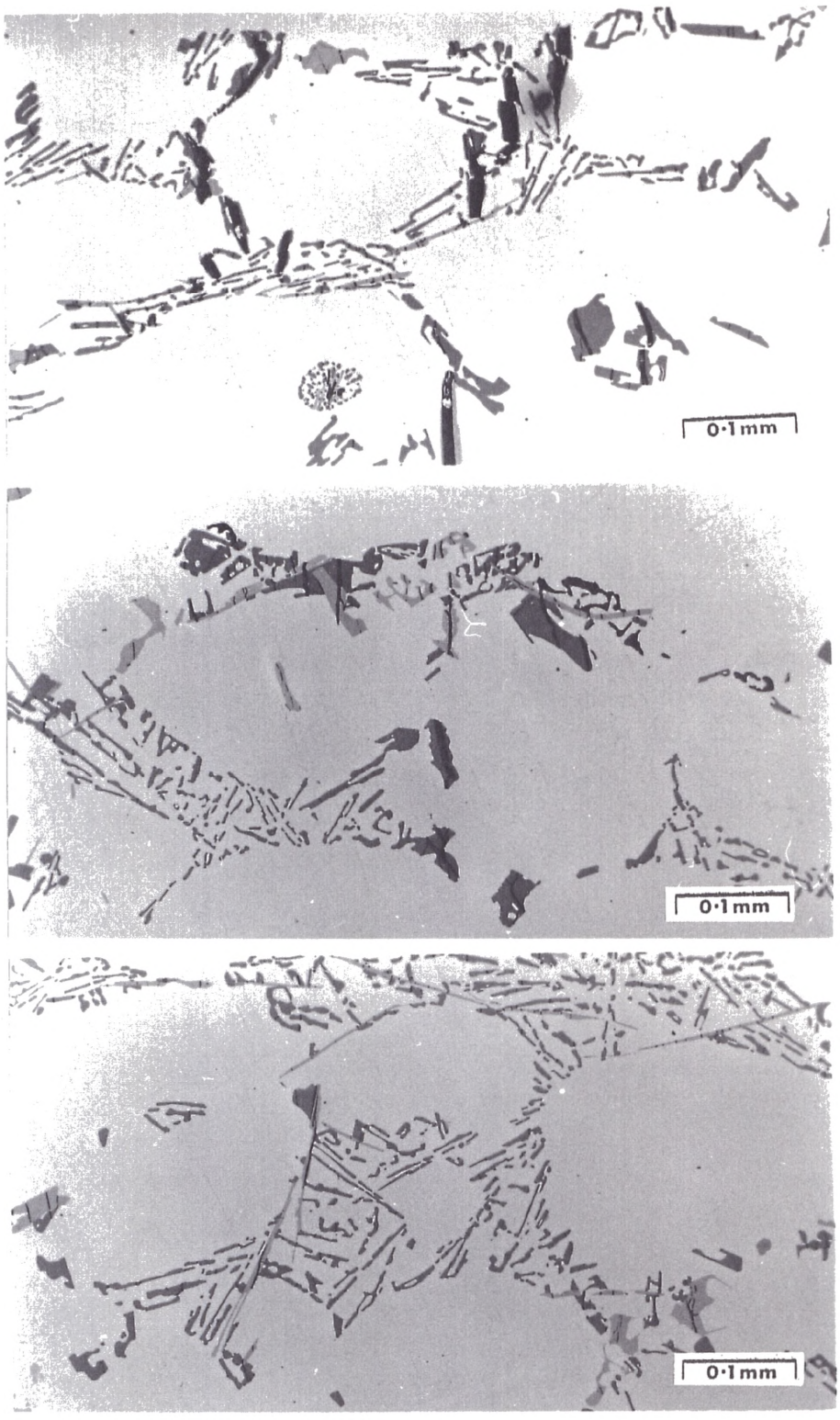

(a)

Figure. 6.16 Transverse section along a fracture surface shows cracks in the Si particles and intermetallic compounds in LM25 alloy. a) particle crack, b) voids and c) final crack.

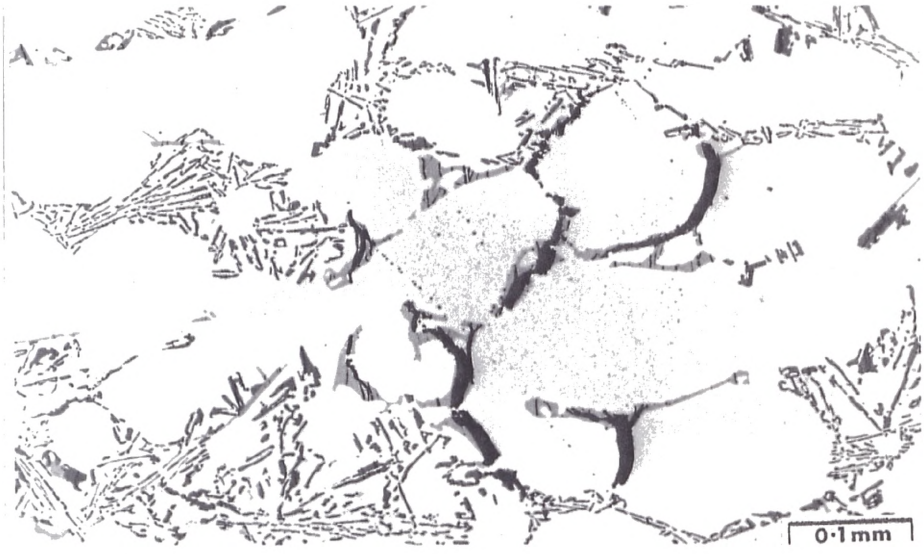

(b)

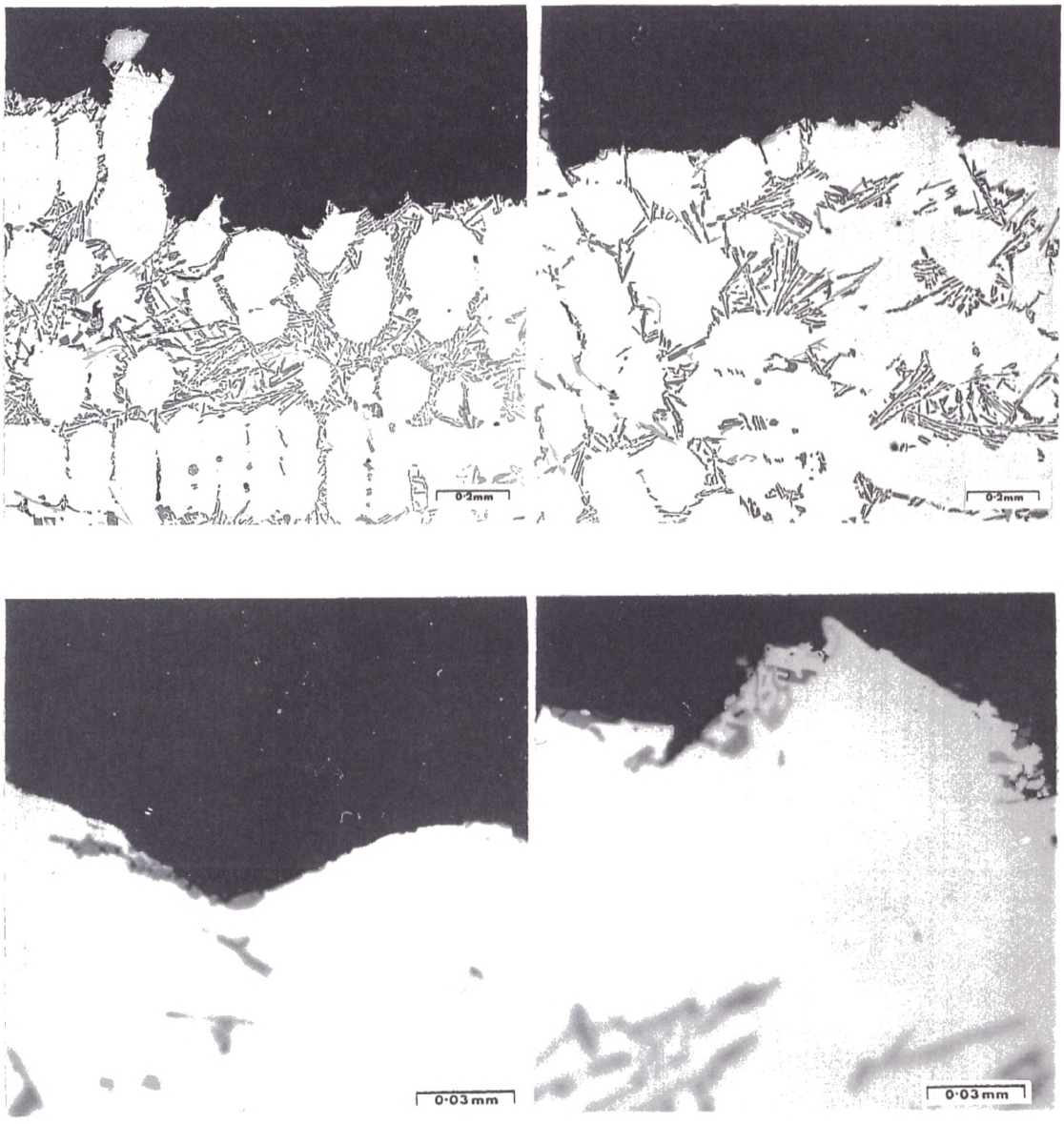

(c)

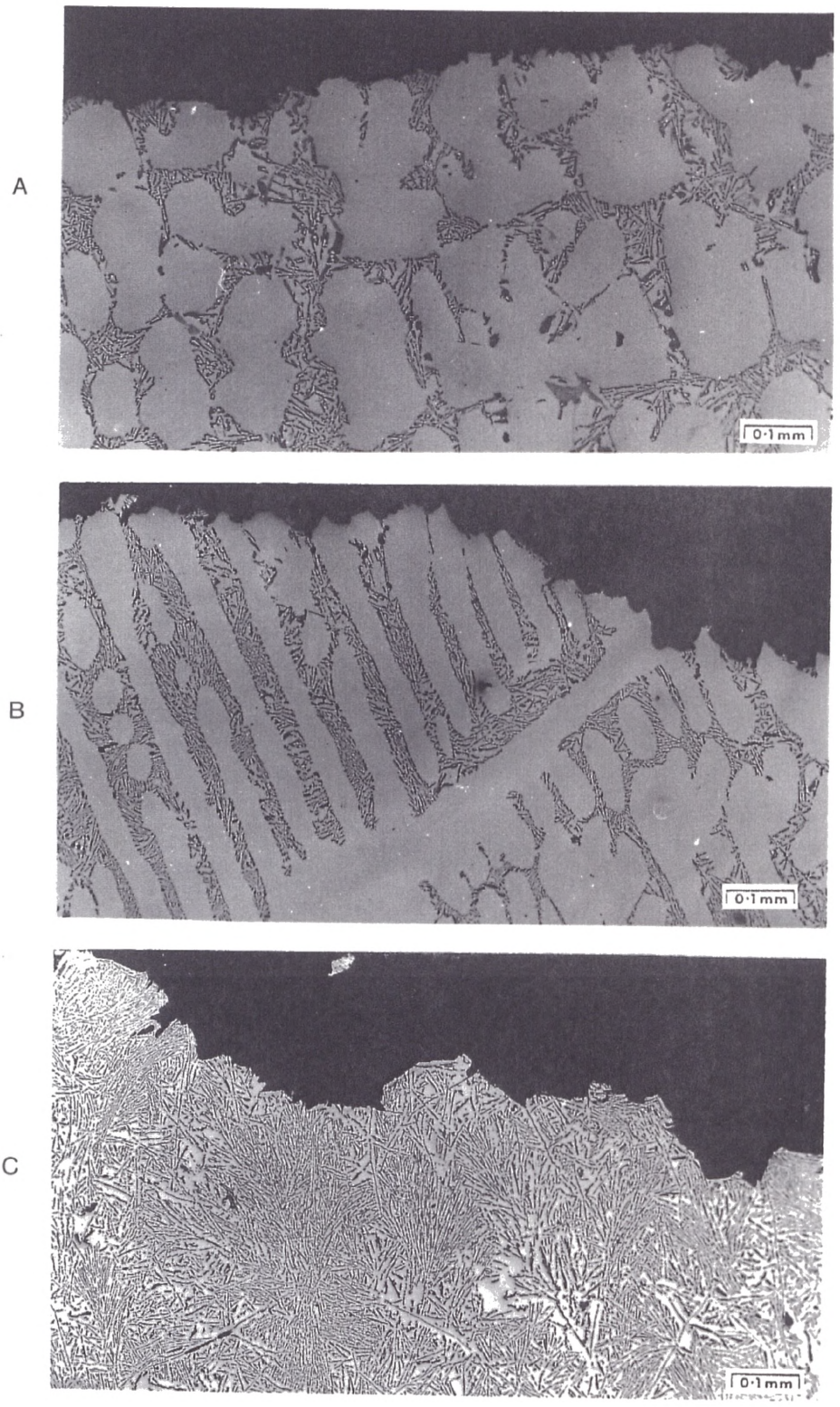

Figure. 6.17 Transverse section along a fracture surface in (a) LM25 (b) Al-7.5%Si-0.45%Mg (c) Al-12.7%Si.

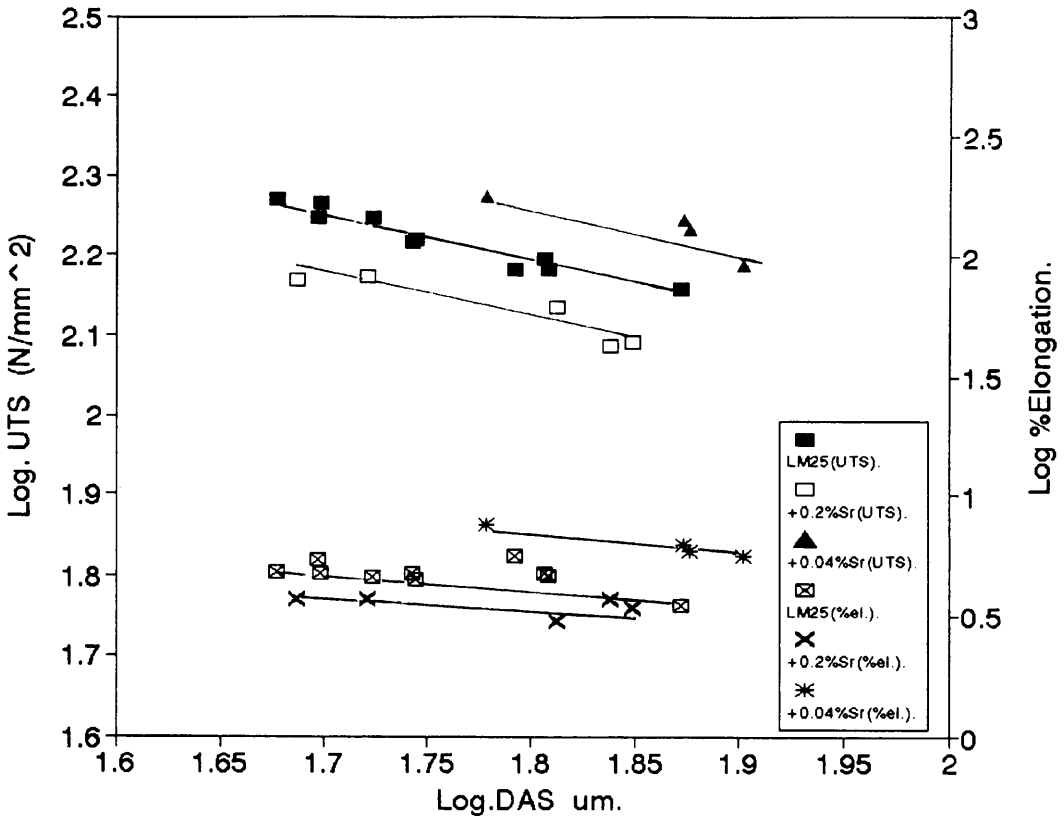

Figure. 6.18 Variation of the UTS and elongation with DAS for LM25 and Sr modified LM25 alloys solidified in the thermal valve furnace.

A

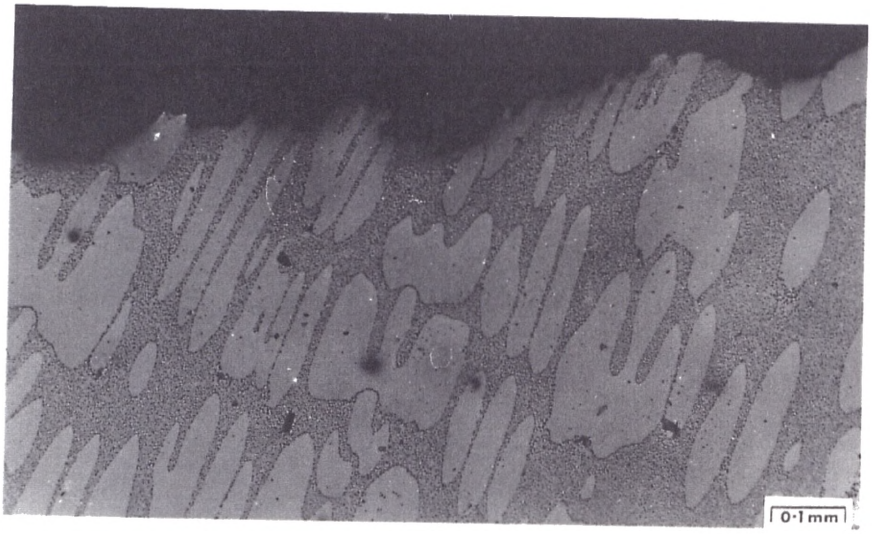

B

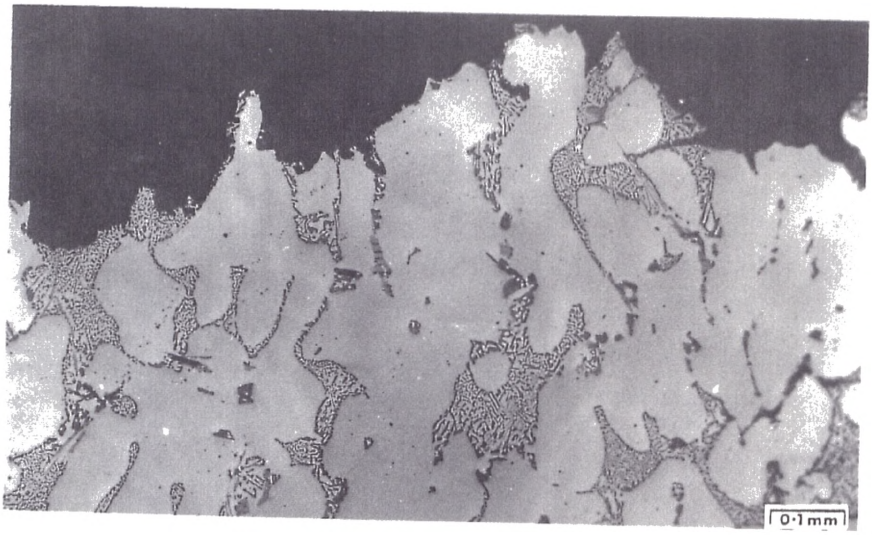

Figure. 6.19 Transverse section along a fracture surface in the a) Al-7.5%Si-0.04%Sr, b) LM25-0.04%Sr.

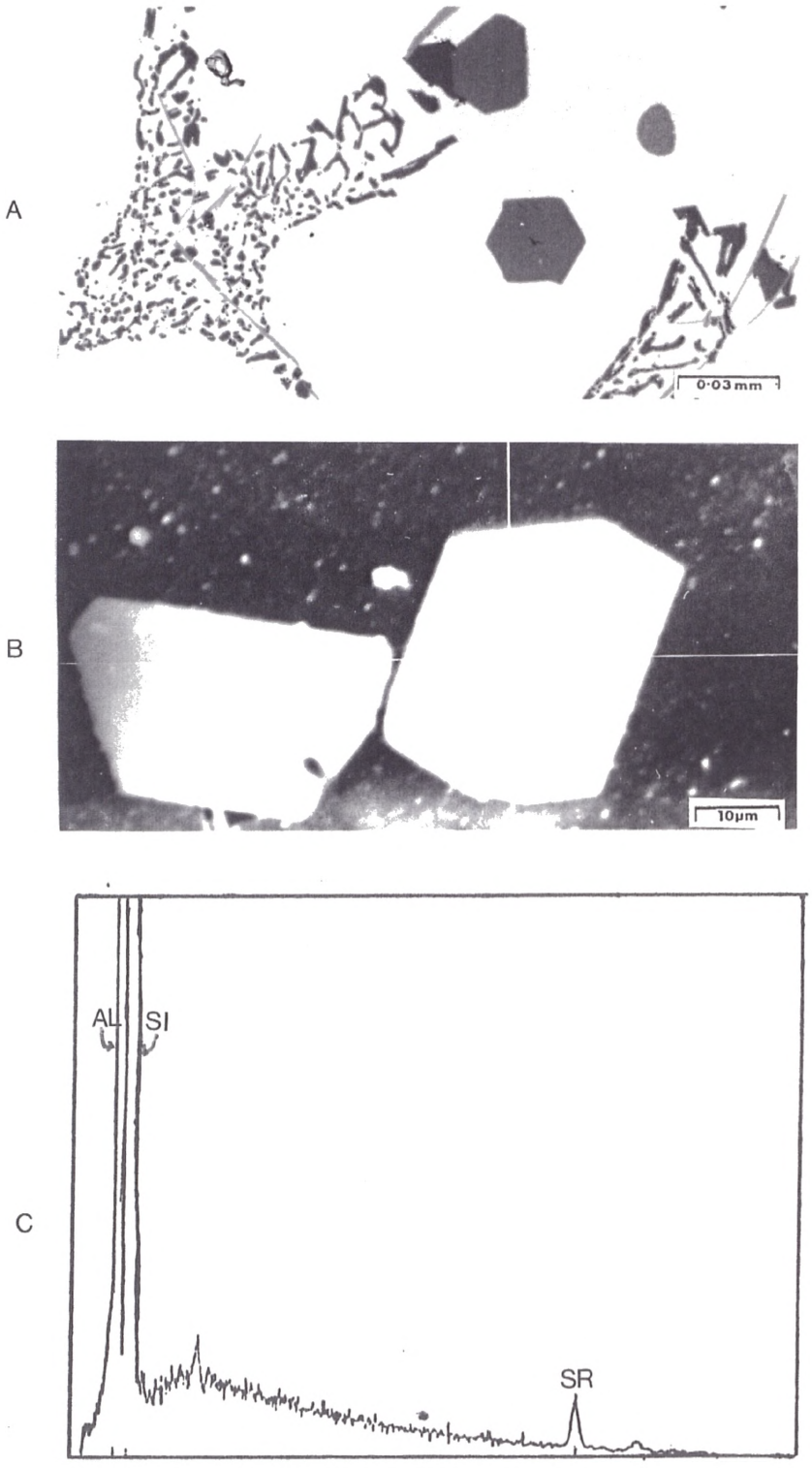

Figure. 6.20 Microstructure shows (AlSiSr) intermetallic compounds a) optic l, b) SEM and c) analysis curve.

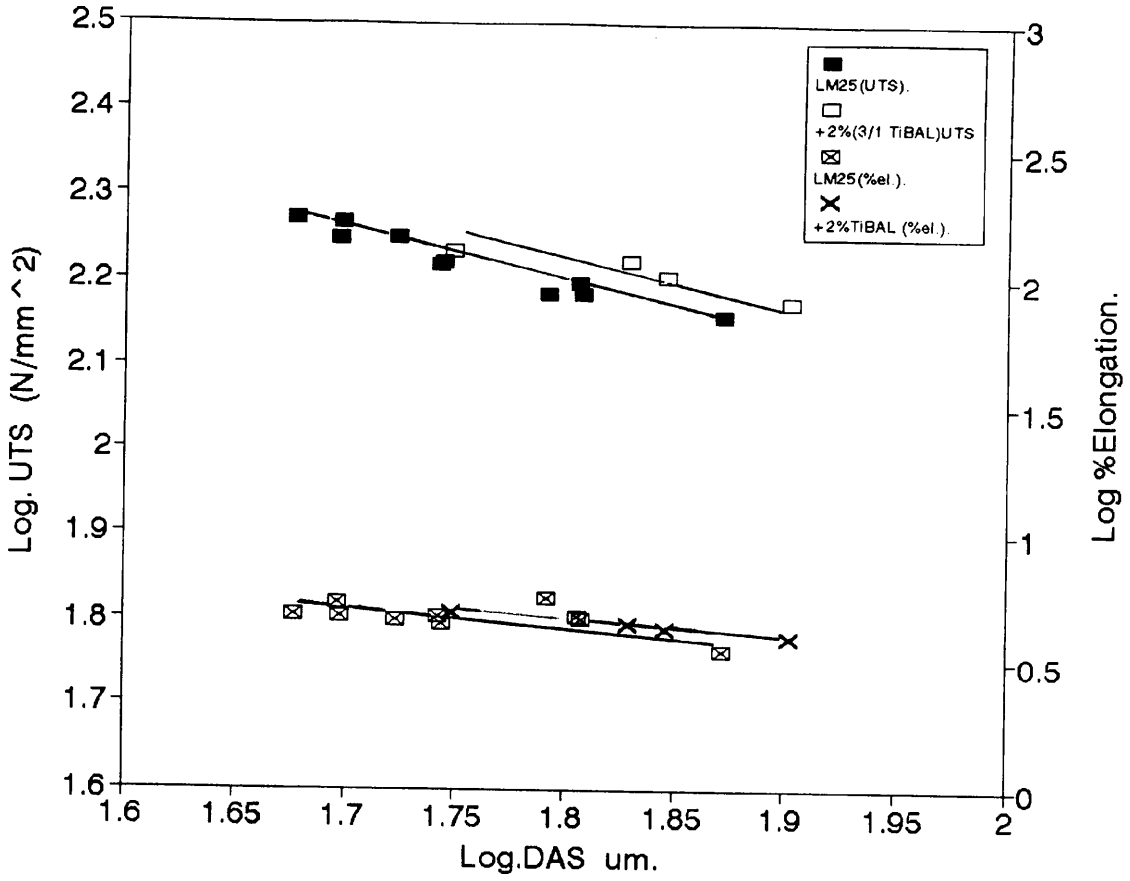

Figure. 6.21 Variation of the UTS and elongation with DAS for LM25 and LM25 treated by 2%TiBAL (3/1) alloys solidified in the thermal valve furnace.

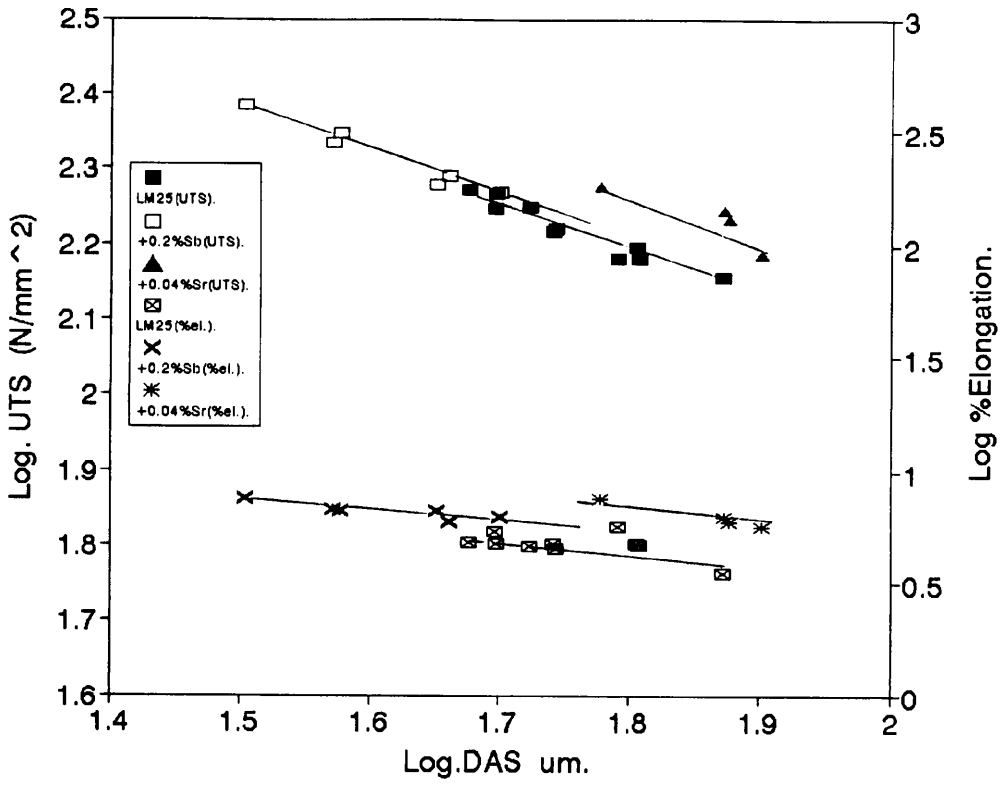

Figure. 6.22 Variation of the UTS and elongation with DAS for LM25, LM25 treated by 0.2%Sb and LM25-0.04%Sr alloys solidified in the thermal valve furnace.

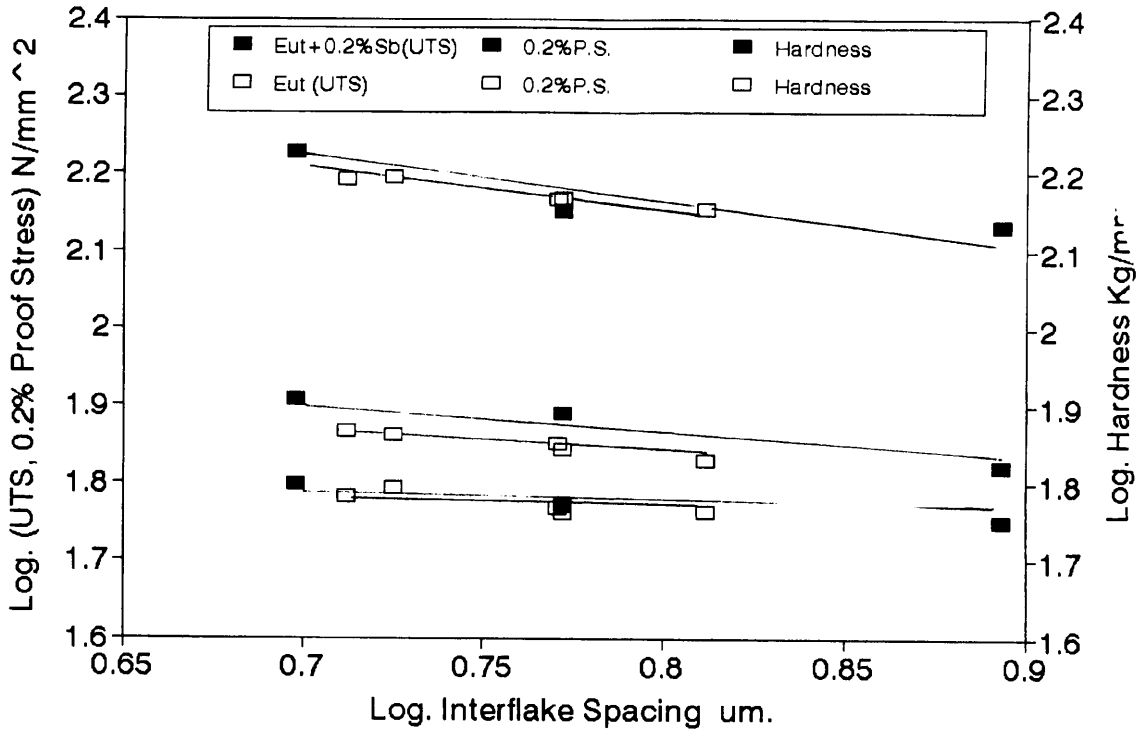

Figure. 6.23 Variation of the UTS, 0.2% proof stress and hardness with interflake spacing for Al-12.7%Si and Al-12.7%Si-0.2%Sb alloys solidified in the thermal valve furnace.

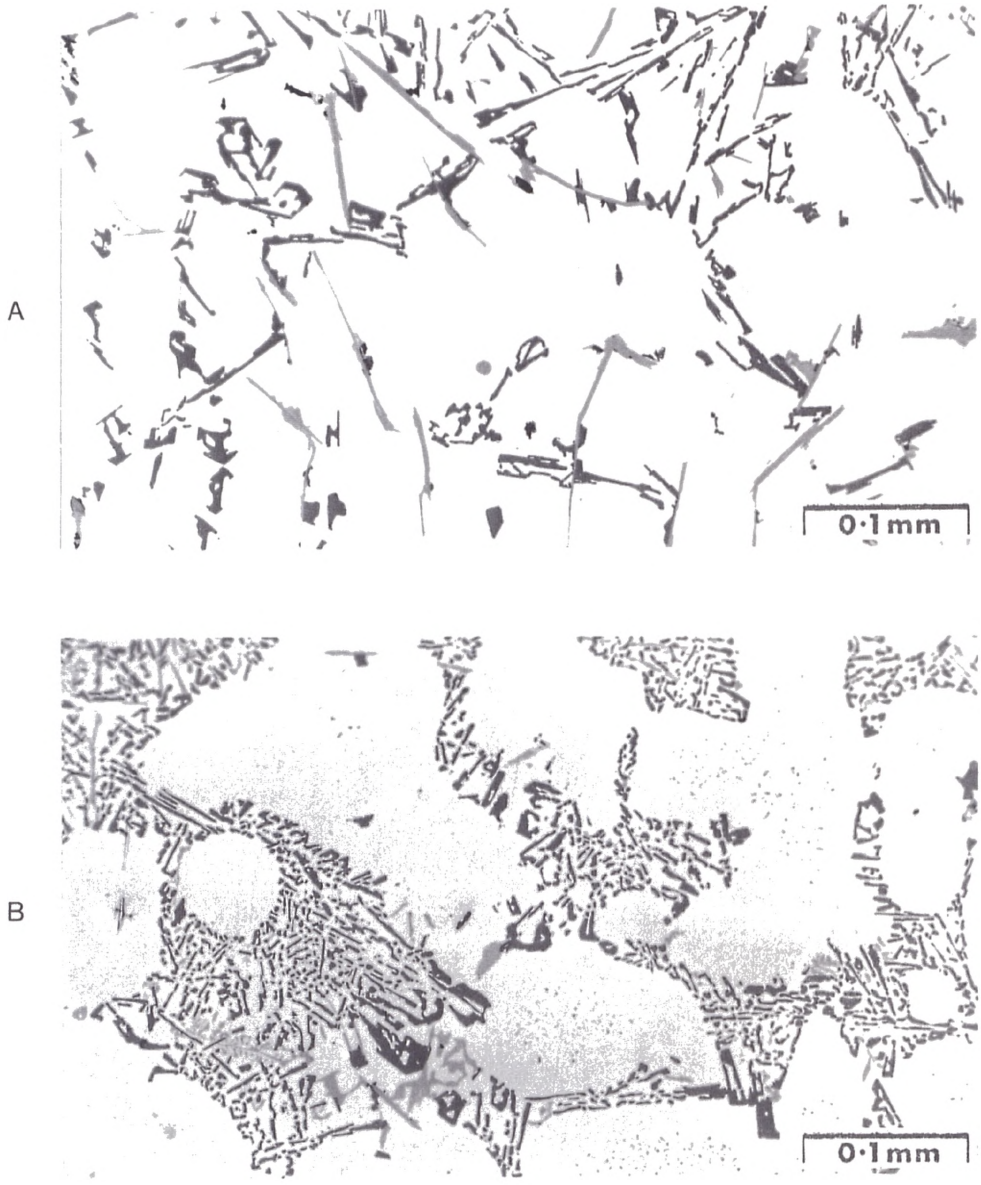

Figure. 6.24 Optical microstructure for a) non-HIPPED LM25 alloy, b) HIPPED LM25 alloy.

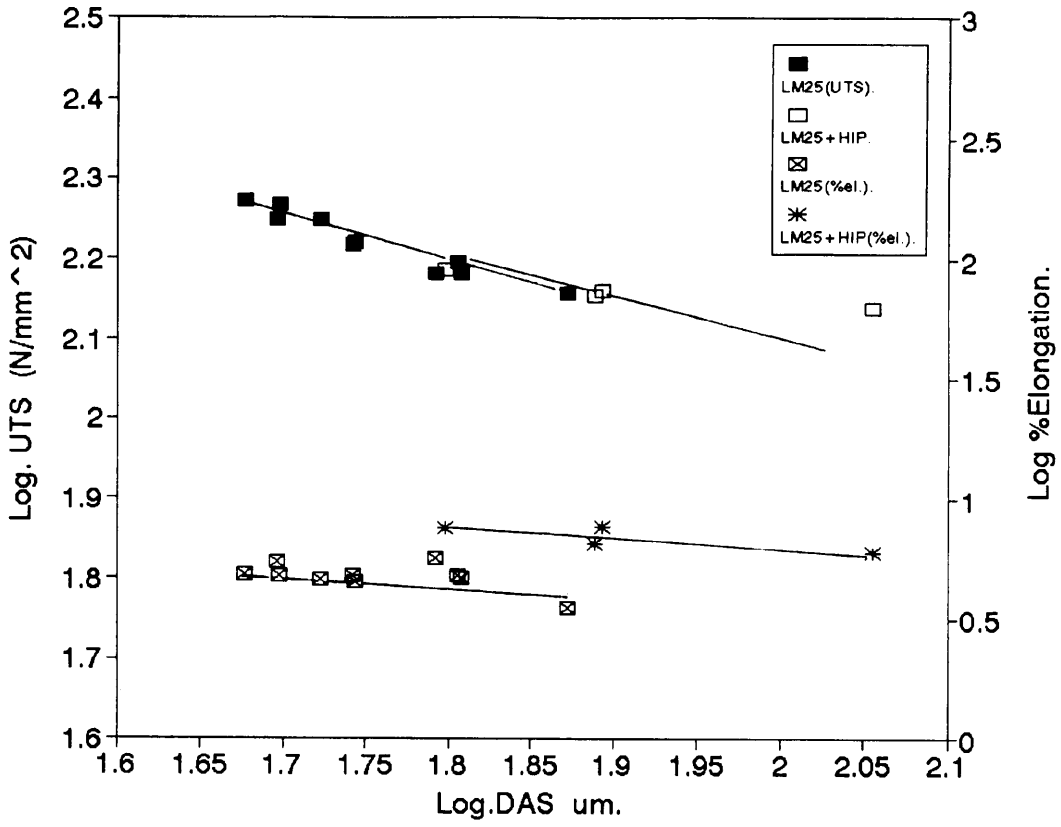

Figure. 6.25 Variation of the UTS with DAS for HIPPED and non-HIPPED LM25 alloys solidified in the thermal valve furnace.

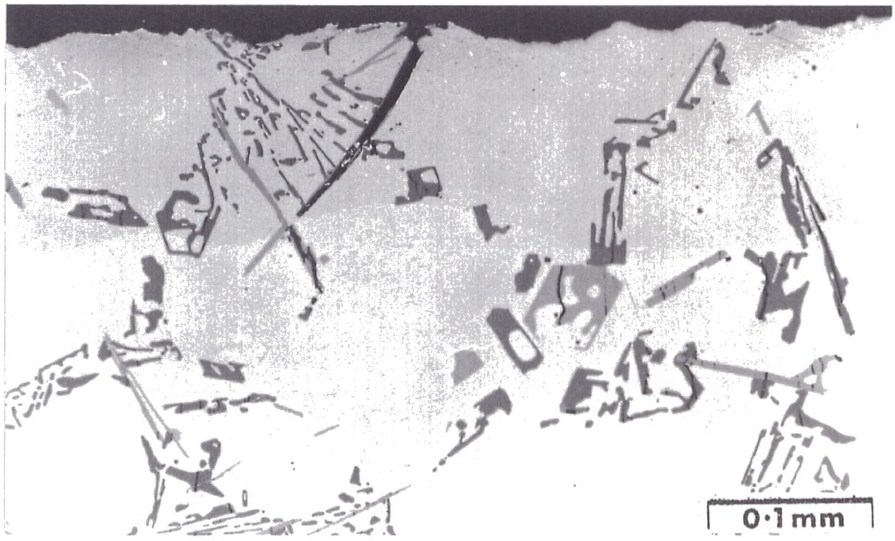

Figure. 6.26 Optical microstructure showing particles cracking in the HIPPED LM25 samples.

CHAPTER SEVEN

CONCLUSIONS

1) Directional solidification studies with strontium modified eutectic alloys identified the influence of solidification conditions on the development of the scalloped interface and associated porosity. Temperature gradient was shown to play an important role. This undesirable aspect of strontium modification can be overcome by ensuring that the temperature gradient in the liquid remains high during solidification. This can be achieved with suitable adjustments to running, gating, feeding and cooling systems.

2) Directional solidification studies have shown that during steady state solidification the final dendrite arm spacing in untreated LM25 alloys can be described by the equation;

$$\lambda_f=[10.27\pm0.55]t_f^{0.3\pm0.01}$$

Coarsening behaviour for solid fractions below 0.5 can be described by an average coarsening parameter of 22.46 μm sec^{-1} calculated from the linear relationship between $\log\lambda_f$ and $\log X_m/V$. The rate of increase of spacing during coarsening depends on the λ_o value. The average slope of the experimental $\log\lambda$ vs logt or log X/V relationship decreases as the ratio λ_o/λ_f increases.

3) In the present study evidence was found, that several ~~mechanism~~ coarsening mechanisms can operate simultaneously in one LM25 alloy and the mechanisms are considered not to be mutually exclusive.

4) Directional solidification studies have shown that the addition of 0.04%Sr and 0.2%Sb to commercial purity LM25 alloys refines the secondary dendrite arm spacing. The final dendrite arm spacing can be described by the equations;

for LM25-0.04%Sr

$$\lambda_f=[9.35\pm0.50]t_f^{0.30\pm0.01}$$

for LM25-0.2%Sb

$$\lambda_f=[8.44\pm0.45]t_f^{0.30\pm0.01}$$

The addition of Sr and Sb decreases the rate of coarsening as reflected in coarsening parameters of 20.8 and 15.22 μm sec^{-1} for Sr and Sb, respectively.

5) There is a refinement of DAS (λ_f) as well as a decrease in grain size when Al-7.5%Si-0.45%Mg alloys are grain refined with TiBAL. Treatment with 2wt% (3/1), 2wt% (3/3) TiBAL results in a progressive decrease in DAS for fixed solidification conditions. The DAS refinement can be expressed quantitatively for other than the (3/3) TiBAL treatment by the equation;

$$\lambda_f=[9.4\pm0.45]t_f^{0.30\pm0.01}$$

In all cases studied the DAS refinement was accompanied by a reduction in the dendrite tip growth temperature, indicated by a lower λ_o value and a reduced rate of coarsening. The average coarsening parameter, M, measured for (3/1) TiBAL and (3/3) TiBAL is 20.80 and 19.22, respectively.

6) The relationship between interflake spacing and growth velocity in the Al-7.5%Si-0.45%Mg, LM25 and Al-12.7%Si alloys found to follow one relation as given by the equation;

$$\lambda=41.4V^{0.38}$$

7) The measurements made in the pure alloy show that the UTS, 0.2% proof stress, elongation and quality index, Q, decrease as the DAS of the alloy increases. A rule of mixtures analysis has been used to show that approximately 60% of the strength of the alloy is derived from the contribution of the primary dendrite network. The UTS-DAS relationship is of the Hall-Petch type, whereas the 0.2% proof strength-DAS relationship is not.

8) A comparison between the measurements for the commercial purity LM25 alloy and pure Al-Mg-Si show that the LM25 is stronger but less ductile than the pure Al-Mg-Si alloy. This have been attributed to a refinement of the dendrite arm spacing, intermetallic compounds and to the solid solution strengthening by Mg. The shape and the aspect ratio of the intermetallic compound have a strong effect on the mechanical properties of the LM25 and this was related to solidification conditions.

9) The fracture in the LM25 alloys started by cracking of the Si particles and β intermetallic compounds after the strain exceeded that corresponding to the yield point, then the second step is growth of cracks into cavities (voids). The last step is the propagation of voids through the Al matrix.

10) The modification by 0.04%Sr improves the mechanical strength but results in a greater improvement in the elongation to fracture. Overmodification by 0.2%Sr results in a decrease in all mechanical properties. This has been attributed to formation of the (AlSiSr) intermetallic compounds.

11) The addition of the grain refining alloy, (3/1) TiBAL, to the commercial LM25 alloy improved the mechanical properties slightly due to the refinement of the DAS and eutectic spacing.

12) The measurements of the mechanical properties for LM25 treated by 0.2%Sb shows that the improvements in mechanical properties due to the DAS refinement is much greater than in other treated alloys and makes a significant contribution to the improvement in properties.

13) The present study has shown that a relationship exists between hardness and 0.2% proof stress and interflake spacing. It is of the same form, but slightly different, for Sb containing and Sb free Al-Si eutectic alloys. It is not of a Hall-Petch type.

14) The strength properties for LM25 alloys are slightly improved by HIPPING process but the elongation is improved by at least by 30%. This is due to the coarsening of the Si particles.

Reference

1. R. Elliott; Material Science and Engineering, Vol 65, pp 85, 1984.
2. F. E. Lamplough and L.T. Scott; Proc. Roy. Society, 90A, 600, 914.
3. F.L. Brady; J. Inst. of Metals, Vol. 28, pp 369, 1922.
4. A.M. Protevin; J. Inst. of Metals, Vol. 29, pp 239, 1923
5. E. Scheil; Z. Metallkunde, Vol 45, pp 298, 1954.
6. G.A. Chadwick; Progress in Materials Science, Vol 12, pp 97, 1963.
7. J.D. Hunt and K.A. Jackson; Trans. Metall. AIME., Vol 236, 1966.
8. K.A. Jackson; Liquid Metals and Solidification; A.S.M. Cleveland, Ohio, pp 174, 1958.
9. M.N. Croker, R.S. Fidler and R.W. Smith; Proc. Roy. Society, Vol 335A, pp 15, 1973
10. M.N. Croker, R.S. Fidler and R.W. Smith; J. Crystal Growth, Vol 11, pp 121, 1971.
11. M.N. Croker, M. Mcparlan, D. Baragar and R.W. Smith; J. Crystal Growth, Vol 29, pp 85, 1975.
12. M.N. Croker, D. Baragar and R.W. Smith; J. Crystal Growth, Vol 30, pp 198, 1975.
13. A.G.C. Gwyer and H.C. Philips; J. Inst. Metals, Vol 36, pp 283, 1926.
14. M.G. Day and A. Hellawell; Proc. Roy. Society, A305, pp 473, 1968.
15. M.G. Day and A. Hellawell; J. Inst. Metals, Vol 46, pp 377, 1967.
16. H.A.H. Steen and A. Hellawell; Acta Metallurgics, Vol 20, pp 363, 1972.
17. A. Hellawell; Progress in Materials Science, Vol 15, pp 1, 1970-73.
18. Shu-Zu-Lu and A. Hellawell; Metall. Trans., Vol 18A, pp 1721, 1987.
19. R.J. Brisly and D.J. Fray; Metall. Trans., Vol 14B, pp 435, 1983.
20. S.P. Clough, M.B. Hintz, Shu-Zu-Lu and A. Hellawell; Michigan Tech. Uni., Unpublished work, 1986.
21. H. Fredriksson, M. Hillert and N. Lange; J. Inst. Metals, Vol 101, pp 285, 1973.
22. C.E. Ransley and H. Neufeld; J. Inst. Metals, Vol 78, pp 25, 1950.
23. M.D. Hanna and A. Hellawell; Metall. Trans., Vol 15A, pp 595, 1984.
24. S.M.D. Glenister and R. Elliott; Metal Science, Vol 15, pp 181, 1981.

25. D.C. Jenkinson and L.M. Hogan; J. Crystal Growth, Vol 28, pp 171, 1975.

26. R.C. Plumb and J. Lewis; J. Inst. Metal., Vol 86, pp 393, 1958.

27. W.L. Davis and J.W. West; J. Inst. Metal., Vol 92, pp 175, 1963-64.

28. S. Ghosh and Kondic; Foundry Trade Journal, Vol 21, pp 435, 1958.

29. S. Ghosh and Kondic; Modern Casting, Vol 43, pp 17, 1963.

30. G.A. Chadwick in Liquids, Structure, Properties and Solids Interactions, T. J. Hughel, Ed. Am Elsevier, New York, 1965.

31. C.W. Haworth and E.P. Whelan; J. Aust. Inst. Met., Vol 10, pp 84, 1965.

32. M.F.X. Gigliotti Jr and G.A. Colligan; Metall. Trans., Vol 3, pp 933, 1972.

33. R. Elliott; Cast Metals, Vol 1, 1988.

34. Shu-Zu-Lu and A. Hellawell; J. Crystal Growth, Vol 73, pp 316, 1985.

35. M. Shamsuzzoha and L.M. Hogan; Phil. Mag. A54, 459, 1986.

36. O.A. Atasoy; Z. Metallkd, Vol 78, pp 177, 1987.

37. L. Clapham and R.W. Smith; Solidification Processing Inst. Of Metals London (1987), pp 479, 1988.

38. Shu-Zu-Lu and A. Hellawell; Solidification Processing Inst. Of Metals London (1987), pp 44, 1988.

39. M.C. Flemings, T.Z. Kattamis and B.P. Bardes; AFS Trans. 1991, 99, 501.

40. K.H. Chien, T.Z. Kattamis: Z.Metalk., 1970, 61, 475.

41. K. P. Young, and D. H. Kirkwood: Metall. Trans. A, 6:197 (1975).

42. T. Z. Kattamis, J. C. Couglin, M. C. Flemings : Trans. Met., 239, 1967, 1504.

43. M. Kahlweit; Scripta Metaall., 1968, 2, 251.

44. U. Feurer, and R. Wunderlin; Fachbericht DGM-FB-38/667/x Oberursel, 1977.

45. A. Roosz, E. Halder, H. E. Exner : Mat. Science and Tech., Vol.2. Nov. 1986, P1149.

46. A. Roosz : Cast Metals, Vol. 1, 1989.

47. MetalsHand Book, vol 2, fourth edition, American Society for Metals, 1988.

48. G. K. Sigworth, S. Shivkumar, and D. Apelian; AFS Transactions, paper 89-139, pp.811-823.

49. L.F. Mondolfo; Aluminium alloys: Structure & Properties, Butterworth's & Co. Lt 1976.

50. M. Tsukud, M. Harada, T. Suzuki, and S. Koike; Journal of Japan Institute of Light Metals, 28(3), pp.109-115, 1978.

51. R. Elliott; Proc. 2nd Int. Conf.on Molten Metal Processing, AFS, Orlando, 1989, paper 10.

52. A. Hellawell; Proc. 2nd Int. Conf. on Molten Metal Processing, AFS, Orlando, 1989, paper 9.

53. L.M. Hogan and M. Shamsuzzoha; Solidification processing, Int. Metals, 1987, 40.

54. E. N. Pan, H. S. Chiou, and G. J. Liao; AFS Transactions, 91-65.

55. R. Sinfield and D. A. Harris; Journal of Australian Inst. of Metals, 20(1), pp.44-47, 1975.

56. O. Vorren, J.E. Evensen, and T.B. Pedersen; AFS Transactions, 84-162, pp.459-466.

57. U. Feurer, and R. Wunderlin; Deutsche Gesellschaft Fur Metallkunde Ev DGm Fachbericht 38, 1978.

58. M.M. Haque, G.H. Bennett, and V. Kondic; Foundry Trade Journal, March 24, 1983,pp.387-390.

59. J.E. Gruzleski, and B. Closset; AFS, Inc., Illinois, 1990.

60. S. Bercovici; Paper presented at 45th Int. Foundry Gongress, 1978.

61. A.T. Joenoes, and J.E. Gruzleski; Cast Metals, Vol.4, 1991.

62. R. Dasgupta, C.C. Brown, and S. Marelc; AFS Transaction, 1989-34.

63. S. Murali, K.S. Roman, and K.S.S. Murthy; Cast Metals, Vol.4, 1991, pp.31-36.

64. W.A. Bailey; Foundry, pp.54-60,May 1964.

65. D.A. Granger, R.R. Sawtell, and M.M. Kersker; AFS Transactions, 92, pp.579-586, 1984.

66. J.C. Jaquet and W. Hotz; Cast Metals, Vol.4, pp.200-225, 1992.

67. G. Gustafsson, T. Thorvaldsson, and G.L. Dunlop; Metall. Trans., vol 17A, 1986, pp45-52.

68. J.N. Pratt, and G.V. Raynor; J. Inst. Met., 1951, vol 79, pp211.

69. I. Obinata and N. Komatus; Nippon Kinzoku Gakkai-Si, 1955, vol 19, pp.197.

70. B. Closset, and J.E. Gruzleski; Metall. Trans., 1982, vol 13A, pp.945.

71. W. Bonsak; ASTM Bulletin 117, pp 45-59, Aug1942; 124, pp41-51 Oct1943

72. L. Grand; Fonderie,vol 217,pp.95-100, March 1964.

73. F.A. Badia; Modern Casting, vol 50, pp.104-115, July 1966.

74. R.S. Archer, and L.W. Kempf; AIMME Transactions, vol 73, pp.581-621, 1926.

75. I. Alfaro, J. Martinez, and C. Hernaiz, Chemical Abstracts, vol 71, No. 6152p, 1969.

76. S. Hajas; Chemical Abstracts, vol 73, No.133571r, 1970.

77. M. Drouzy, and S. Jacob; Fonderie, vol240, pp.50-54, 1966.

78. T. Morigana, T. Takahashi, and T. Saga; Japan Inst. Metals Transactions, vol 6, no.2, pp.72-77, 1965.

79. S.A. Levy; AFS Transactions, &8-22, pp.135-138.

80. Y. Komiyama, K. Vchida, and M. Gunshi; Metals Abstracts, vol 10B, no.310926, 1977.

81. D.L. Colwell, and R. J. Kissling; AFS Transactions, vol 69, pp.610-615, 1961.

82. R.C. Lemon, and H.Y. Hunsicker; AFS Transactions, vol 64, pp.255-260, 1956.

83. A. Couture; AFS International Cast Metals Journal, 6, pp.9-17, 1981.

84. G.K. Sigworth; Modern Casting , pp.23-25, 1987.

85. Ahmed A. Abdel-Hamid; Z. Metallkde., Bd. 80 (1989) H. 8.

86. J.C. Jaquet and H.J. Huber; Geissereiforschung, 38(1), pp 11-20, 1986.

87. G.K. Sigworth; Conf. "International Molten Metal Processing,"American Foundrymen's Society, Des Plaines, IL, pp 75-99, 1986.

88. M. Tsukuda, T. Suzuki, I. Fukui and M. Harada; J. og Japan Inst. of Light Metals, 29(10), pp 437-444, 1979.

89. C. Vass; Conf. "International Molten Metal Processing," American Foundrymen's Society, Des Plaines, IL, pp 101-147, 1986.

90. U. Honma and S. Kitaoka; Aluminum, 60, pp E780-783, 1984.

91. L. Backerud; Light Metal Age, pp 6-12, 1983.

92. G. K. Sigworth and M.M Guzowski; AFS Transactions, 85-94, pp 907-912.

93. D. Apelian and J.J. Cheng; AFS Transactions, 86-94, pp 797-808.

94. J.R. Denton and J.A. Spittle; Materials Science and Technology, vol 1, pp 305-311, April 1985.

95. P.D. Hess and E.V. Blackmun; AFS Transactions, 1975, 83, 87.

96. N. Fat-Hall; "Current Advances in Mechanical Properties and Production III," [Proc. Conf.], Cario, Egypt, pp 28-30, Dec-1985.

97. A. Telli and S.E. Kisakurek; Mater. Sci. Technol., 1988, 4, 153-156.

98. A. Ourdjini, F. Yilmaz, Q.S. Hamed, and R. Elliott; Mater. Sci. Tech., pp774-776, 1992,8.

99. P. Borgeaud, F. Dabel, M. Drouzy, and C. Mascre; AFS int. Cast Metals Jnl., 1963, Sept., 151.

100. S. Venkateswaran, R.M. Mallya, and M.R. Seshadri; Cast Metals, vol.4, number 2, 1991.

101. Bernad Closset; Strontium modification of Al-Si alloys in the presence of antimony, (paper presented at the 2nd International conference on molten Aluminium processing, A.F.S., Orlando, November, 1989, 8.

102. B.L. Tuttle, A. Keslinke, D. Twarog, and E. Danels; AFS Transactions, 89-168, pp.884-902.

103. J.E. Gruzleski; "Modification and the porosity problem", Paper presented at the 2nd Int. Conf. on Molten Aluminium Proc., A.F.S. Orlando, Nov. 1989, 1.

104. Q.T. Fang and D.A. Granger; AFS Trans., 97(1989), 989-1000.

105. D. Argo and J.E. Gruzleski; AFS Trans., 96, 1988.

106. JR. Denton and J.A. Spittle; Materials Science and Technology, 1 (1985), 305-311.

107. Metal Hand Book, vol 15, ninth edition, American Society for Metals, 1988.

108. B. Closset, R.A.L. Drew, and J.E. Gruzleski; AFS Transactions, 94, pp 9-16, 1986.

109. F.N. Rhines and M. Aballe; Met. Trans. A, 17A, pp 2139-2152, 1986.

110. T.J. Shin, D.N. Lee, and J. Korean; Inst. Met., 23(10), pp1116-1122, 1985.

111. P.Y. Zhu, Q.Y. Liu, and T.X. Hou, AFS Transactions, 93, pp 609-614, 1985.

112. M. Tsukuda, S. Koike, and M.Harada; Journal of Japan Inst. of Light Metals, 28(1), pp 8-14, 1978.

113. R.A. Quadt, and N.J. Barber; SS, pp351-356, 1947.

114. G.S. Ghate, S.S. Murthy, and K.S. Raman; Aluminum, 60, pp E18-19, 1984.

115. B. Chamberlin and V.J. Zabek; AFS Transactions, 81, pp 322-327, 1973.

116. P.R. Beeley; Foundry technology, Butterworth Scientific Monograph, 1982.

117. Metals Hand Book, vol 4, fourth edition, American Society for Metals, 1988.

118. M.R. Javidi; Ph.D. thesis, Unveristy of Manchester/UMIST, 1989.

119. S.M.D. Glenister; Ph.D. thesis, Unveristy of Manchester/UMIST, 1979.

120. Q.S. Hamed; M.Sc. Dissertation (UMIST), 1989.

121. Q.S. Hamed, R. Elliott and P.S. Cooper; TMS Light Metals Cast Shop Technology Conf., New Orleans L A, 17 Feb., 1991.

122. Radhakrishna, K., Seshan : Cast Metals, Vol. 2, 1989, P34.

123. T. F. Bower, H. D. Brody, and M. C. Flemings : Trans. AIME, 236:624 (1966).

124. Brown and Adams : Trans. Am. Foundrymen Society, 1961, Vol. 69, P879.

125. Michael and Bever : AIME Trans., 1954, Vol. 200, P47.

126. Reed : S. B. Thesis, Dep. of Metalurgy, M. I. T., 1960.

127. Harawth and Mondolfo : Acta Met., 1962, Vol. 10, P1037.

128. Gu Genda, Chen Yuyon, An Geing : Solidification processing, Sheffield, 1987.

129. A. A. Chernov : Kristallografiya, 1, 1955, 583.

130. R. Grugel and W. Kurz: Metall. Trans., 18A, pp.1137, 1987.

131. G. K. Sigworth and M.M Guzowski; Metals and Castings, Sept-Oct, 1988, pp. 46.

132. D. Apelian and J. Allen Cheng; Proc. Int. Molten Aluminium Processing Conf., City of Industry, California, Feb.1986.

133. P.A. Tφndel and L. Arnberg; Proc. 3rd Int. Conf. on Aluminium Alloys, Their Physical and Mechanical Properties, Trondheim, Norway, Jun 1992, Vol. 1, pp. 129.

134. Dogan ; MSc. Dissertation (UMIST), 1992.

135. F. Yilmaz and R. Elliott; J. Materials Science, 1989, 24, 2065.

136. S. Khan; Ph.D. Thesis, Manchester, 1990.

137. S. Khan, A. Ourdjini and R. Elliott; Materials Sci. & Tech., pp 516-522, July, 1992.

138. Junmin Lio, Yaohe Zhou, and Baolu Shang; Acta Metall. Mater. Vol.38, No 9,pp.1631-1634, 1990.

139. K. A. Jackson, and J. D. Hunt; Trans. Metall. Soc. A.I.M.E. 234, pp.1129, 1966.

140. L.F. Mondolfo; Aluminum Alloys: Structure & Properties; Butterworths & Co.Ltd., 1976.

141. J. Sulinski; AFS Transactions, 75,pp548-566, 1967.

142. A. Wickbert, G. Gustafsson, and L. E. Larsson; in Proc. Conf. SAE International Congress and Exposition,Detroit, Feb. 27- March 2, 1984, Society of Automotive Engineers.

143. M. K. Supappa, E. W. Blank, and J. C. Jaquet; Microstructural approach to deformation and fracture of cast Al-7Si-0.3Mg alloy.

144. C.W. Meyers and J.S. Chou; AFS Transactions, pp 175-186, 91-139.

145. J.S. Chou and C.W. Meyers; AFS Transactions, pp 165-173, 91-138.

146. P.Y. Zhu, Q.T. Liu and T.X. Hou; AFS Transactions, pp 604-614, 1985.

LIST OF PUBLICATIONS

1) Q.S. Hamed, R. Elliott and P.S. Cooper; "Solidification Characteristics of Sodium and Strontium Modified Aluminium-Silicon Casting Alloys", Proc. of TMS Light Metals Cast Shop Technology Conference, pp 1391, 1992.

2) A. Ourdjini, F. Yilmaz, Q.S. Hamed and R. Elliott; "Microstructure and Mechanical Properties of Directionally Solidified Al-Si Eutectic Alloys with and without Antimony", Materials Science and Technology Journal, 1992,8, pp 774-776.

3) Q.S. Hamed and R. Elliott; The Dependence of Secondary Dendrite Arm Spacing on Solidification Conditions- I. Untreated Al-7 Si-0.5 Mg Alloys, Cast Metals Journal, to be published in 1993.

4) Q.S. Hamed and R. Elliott; The Dependence of Secondary Dendrite Arm Spacing on Solidification Conditions- II. Al-7 Si-0.5 Mg Alloys Treated with Sr and Sb, Cast Metals Journal, to be published in 1993.

5) Q.S. Hamed M. Dogan and R. Elliott; The Dependence of Secondary Dendrite Arm Spacing on Solidification Conditions-III. Al-7 Si-0.5 Mg Alloys treated with TiBAL Cast Metals Journal, to be published in 1993.

6) S. Khan, A. Ourdjini, Q.S. Hamed and R. Elliott; Hardness-Mechanical Properties Relationships in Aluminium Silicon Eutectic Alloy with different Eutectic Si morphologies, Submitted to Journal of Materials Science.

SOLIDIFICATION CHARACTERISTICS OF SODIUM AND STRONTIUM MODIFIED ALUMINIUM-SILICON CASTING ALLOYS

by

Q.S. Hamed, R. Elliott and P.S. Cooper

Q.S. Hamed and R. Elliott are in the
Materials Science Centre, University of Manchester, U.K.
and
P.S. Cooper is with
London & Scandinavian Metallurgical Co Limited, Rotherham, U.K.

ABSTRACT

Controlled solidification experiments are described for aluminium-silicon alloys of hypoeutectic and eutectic composition and reveal distinct differences in solidification behaviour when sodium and strontium are used as modifiers. With sodium modified alloys a rapidly developed eutectic shell moved radially inwards during growth with a smooth solid-liquid interface over a wide range of cooling rates. In contrast, strontium modified alloys developed a pronounced scalloped interface during growth at rates likely to be encountered in medium to heavy sand castings. Directional solidification studies with strontium modified alloys identified the influence of solidification conditions on the development of the scalloped interface and associated porosity. Temperature gradient was shown to play an important role. This undesirable aspect of strontium modification can be overcome with suitable changes to the solidification pattern.

INTRODUCTION

It is good foundry practice to treat liquid aluminium-silicon alloys with a modifying agent. This changes the growth morphology of the silicon phase from flake to fibres with an accompanying increase in mechanical strength and elongation. Originally sodium was used almost exclusively as a modifying agent. However, strontium offers several advantages including less burn off, less attack on refractories and it does not fade as quickly as sodium. These advantages have led to the gradual replacement of sodium by strontium. However, several foundries in the U.K. have reported a significant increase in porosity causing an increased rejection rate when strontium has been substituted for sodium.

The origin of porosity during solidification is usually attributed to the rejection of gas from solution and/or the inability of liquid to feed through solid+liquid regions to compensate for the volume shrinkage that accompanies the phase change. Neglecting pore formation due to entrapped air which is a consequence of bad casting design and practice, the ease of pore formation can be described by the equation:

$$P_g + P_s > P_{atm.} + P_h + P_{s\text{-}l} \qquad (1)$$

where P_g is the equilibrium pressure of dissolved gases in the liquid,
P_s is the pressure drop due to shrinkage,
$P_{atm.}$ is the pressure of the atmosphere over the system,
P_h is the pressure due to the metallostatic head and
$P_{s\text{-}l}$ is the pressure due to surface tension at the pore-liquid interface.

The parameters P_h and $P_{atm.}$ are constant for a given casting design. The dissolved gas pressure, P_g, is a major driving force in microporosity formation. If an aluminium melt contains excessive amounts of dissolved gas, particularly hydrogen, the decrease in solubility on solidification can be sufficient to cause pore formation and gas porosity. It has been shown that modification with strontium can increase both pore size and volume (1). However, the gas content of a melt can be reduced by degassing and held to a predetermined level before casting. Shrinkage porosity pressure, P_s, which is directly related to the ease of interdendritic feeding is not as easy to control. Contraction during solidification leads to microshrinkage particularly in interdendritic areas. Often gas and microshrinkage porosity occur simultaneously. The remaining parameter is $P_{s\text{-}l}$, the surface tension effect. Modifiers are known to reduce surface tension and hence, promote pore formation. However, the relative effects of strontium and sodium have not been reported.

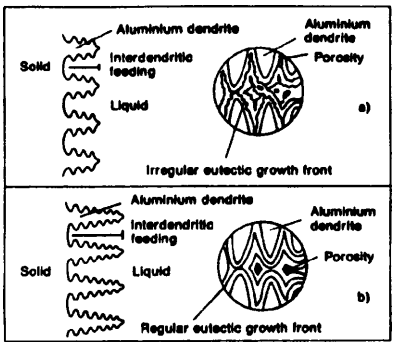

Figure 1: The different modes of microshrinkage porosity in unmodified and modified hypoeutectic alloys.

We are concerned with microshrinkage effects in this communication. Argo and Gruzleski (2) measured microshrinkage quantitatively with a Tatur mould for unmodified and strontium treated aluminium-silicon alloys at a constant gas pressure. Bars were sand cast with a graphite chill and the porosity distribution was examined in both alloys. Modification increased microshrinkage as a percentage of the total shrinkage from 7.27 to 9.7% and decreased the pipe volume by 44%. Modifying agents decrease the eutectic temperature and, hence, extend the freezing range and the length of the mushy zone, increasing both feeding distance and difficulty. The decrease in pipe volume is evidence of an increase in feeding difficulty. Radiographs of the sand cast bars showed that microshrinkage was located mainly in one area in unmodified bars but was distributed more widely in the modified bars. These observations led to the picture of microshrinkage formation in hypoeutectic alloys depicted in figure 1. The shorter freezing range of unmodified alloys means a shorter interdendritic feeding distance. Easier feeding concentrates microshrinkage into the last areas to solidify. The eutectic liquid in these areas solidifies with a flake morphology at a non-isothermal interface. Small pockets of eutectic become trapped behind this advancing, irregular interface to produce fine porosity concentrated in the last areas to solidify. Good feeding practice can locate these areas into the feeder promoting casting soundness. Feeding is more difficult in the modified alloy with the possibility of the formation of larger isolated pockets of eutectic liquid between dendrite arms. This results in widely dispersed, isolated solidification cells which can solidify with an isothermal, regular interface. Thus pores in modified alloys are likely to be larger and more dispersed. Gruzleski (3) has reported Tatur mould measurements for sodium modified aluminium-silicon alloys. The microshrinkage percentage of the total shrinkage was found to increase from 7.27 to 14.7%. These measurements were made on A 356 alloy at constant hydrogen concentration. Consequently these measurements show sodium modified alloys to be more porous and do not offer any evidence for strontium modified alloys being more prone to microshrinkage porosity.

Denton and Spittle (4) have reported that the regular interface of the modified alloy may develop a scalloped interface at slow cooling rates and that this may occur under different solidification conditions in sodium and strontium modified alloys. Deep liquid channels were observed to extend back to the mould wall creating areas of microshrinkage. We report the stability of the regular eutectic interface assumed in the discussion of the Argo and Gruzleski model of microshrinkage porosity.

EXPERIMENTAL PROCEDURE

Denton and Spittle's observations concerning the interface shape of modified alloys were examined in more detail. Small ingots of unmodified, strontium and sodium modified hypoeutectic and eutectic composition alloys were solidified at cooling rates in the range 2 to 31°C min^{-1}. The base alloy was melted in a graphite crucible, 5cm high and 2.5cm in diameter under a protective argon atmosphere. Sodium modification was induced using a LiF/NaF/KF flux in the molar ratio 4.5/1.0/ 4.5. Strontium modification was achieved by adding an aluminium-10%strontium master alloy, supplied by the London & Scandinavian Metallurgical Co Limited to a concentration of 0.025% strontium. Additions were made at 720°C. The temperature of the solidification furnace was maintained at 700°C for 15 minutes prior to controlled cooling. This was achieved by programming the furnace temperature to decrease at the constant rate required to produce the selected cooling rate. Thermocouples placed close to the mould wall and in the ingot centre at a height of 2.5cm were used to record cooling and heating curves. Once these curves had been recorded, the ingot was cooled again at the same rate and the whole assembly was quenched at a predetermined time during solidification to define the interface profile. This was revealed by sectioning transversely just below the thermocouples.

In a second series of experiments unmodified and strontium modified alloys of eutectic composition were directionally solidified in a thermal valve apparatus in order to define the influence of growth velocity and temperature gradient in the liquid on the eutectic interface stability.

EXPERIMENTAL OBSERVATIONS AND DISCUSSION

The small ingot solidification studies confirmed and extended previous studies by Denton and Spittle and Hanna et al. (5). The mode of eutectic solidification was observed to be very similar in aluminium-10% silicon and eutectic alloys. Consequently, after initial experiments most studies were made on alloys of eutectic composition. Figure 2 illustrates the mode of solidification in unmodified, strontium and sodium modified eutectic alloys quenched after 3 minutes solidification at a cooling rate of 7 °C min $^{-1}$. Figure 3 shows the cooling and heating curves for the different alloys. Figure 2a shows that solidification occurs from the mould wall inwards in a radical direction at a very irregular interface as described by Argo and Gruzleski and depicted in figure 1a. Figures 2b and 2c show the different solidification behaviours of strontium and sodium modified eutectic alloys at a cooling rate of 7 °C min $^{-1}$. Figure 2b shows a low density of nucleation sites on the mould wall and one site that may have nucleated in the liquid. This will be discussed later. The grains grow slowly in a hemispherical fashion from the nucleation centres. Lateral growth along the mould wall eventually leads to the joining of grains when growth continues in a radial direction but with a scalloped interface. Figure 4 illustrates this development in a strontium modified alloy cooled at 4 °C min $^{-1}$. It must be emphasised that growth is not steady state in this type of experiment. The reduction in furnace temperature at a constant rate means that growth will occur at an increasing velocity during solidification with the result that the scalloped interface will not develop as solidifaction proceeds to the same extent as in a sand casting in which the growth velocity usually decreases as solidification proceeds. Figure 2c shows the different solidification behaviour of the sodium modified alloy cooled at 7 °C min $^{-1}$. After nucleation at the mould wall lateral growth along the wall has occurred more rapidly than in figure 2b. The cooling curves in figure 3 show that strontium and sodium have different influences on the nucleation and growth processes. They confirm that growth occurs more quickly in the sodium modified alloy.

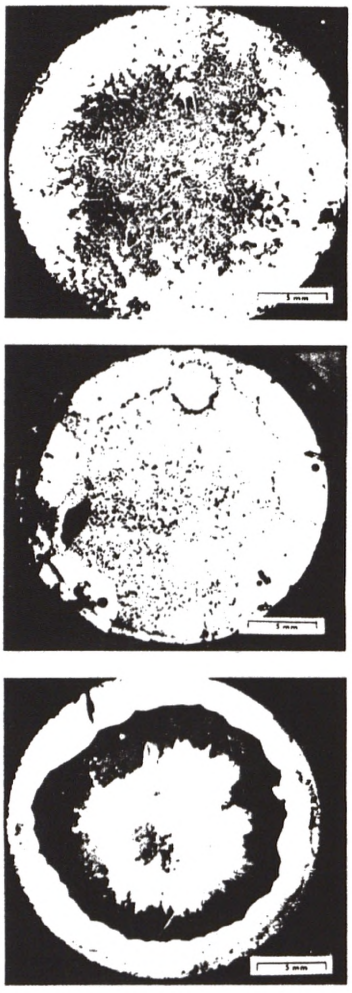

Figure 2: The grain structure in alloys after 3 minutes of eutectic solidification at a cooling rate of 7°C min $^{-1}$.
a) unmodified eutectic
b) strontium modified
c) sodium modified

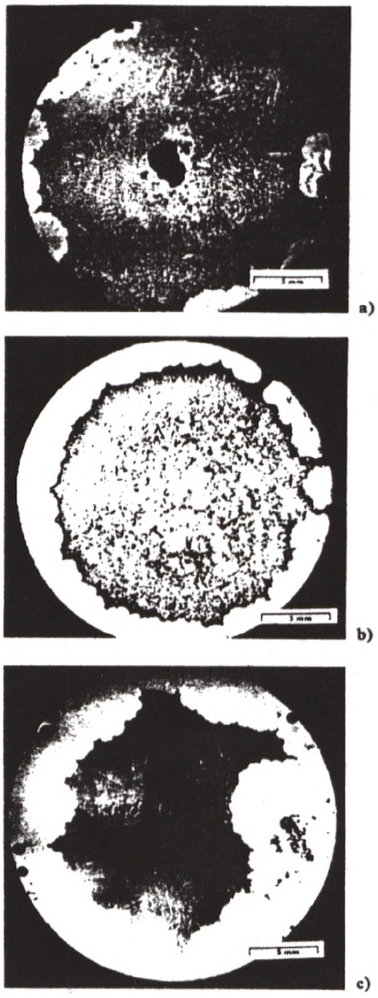

Figure 4: Quenched interfaces showing the development of a scalloped interface in strontium modified eutectic cooled at a rate of 4°C min $^{-1}$.
a) quenched after 2 minutes
b) quenched after 4 minutes
c) quenched after 6 minutes

Figure 3: a) Cooling and heating curves for unmodified strontium and sodium modified eutectic alloys cooled and heated at 7°C min $^{-1}$.
b) Growth undercoolings as a function of cooling rate.

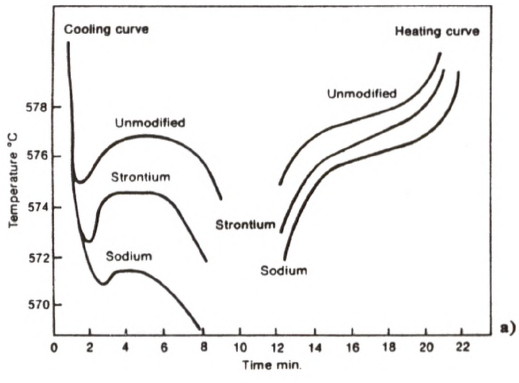

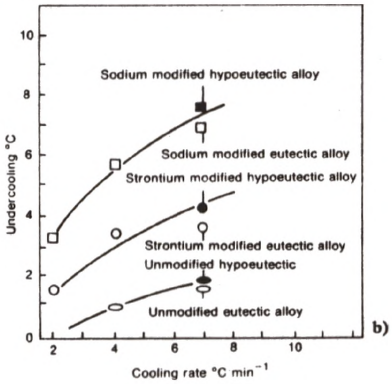

This is probably due to the different behaviours of strontium and sodium in promoting constitutional undercooling. Cooling curves from thermocouples placed at the centre and mould wall indicated that the temperature gradient in the liquid was of the order of 2 °C min $^{-1}$. This rapid lateral growth in the sodium modified eutectic leads to the early formation of a completely solid shell which then advances rapidly with a slightly scalloped interface but without the deep liquid channels observed in the strontium modified alloys. Strontium modified alloys behaved in this manner for cooling rates in excess of 7 °C min $^{-1}$ and the development of a pronounced scalloped interface was not observed in sodium modified alloys until the cooling rate was below 2 °C min $^{-1}$. Figure 5 shows liquid channels and associated microshrinkage porosity in hypoeutectic and eutectic aluminium silicon alloys. Figure 6 details the microstructure characteristics of strontium modified eutectic alloys solidified under steady state conditions with growth velocities in the range 10 to 200 μm s $^{-1}$ and temperature gradient in the liquid between 1.8 and 75 °C cm $^{-1}$. As the G/v ratio decreases, constitutional undercooling increases and the eutectic interface becomes more unstable.

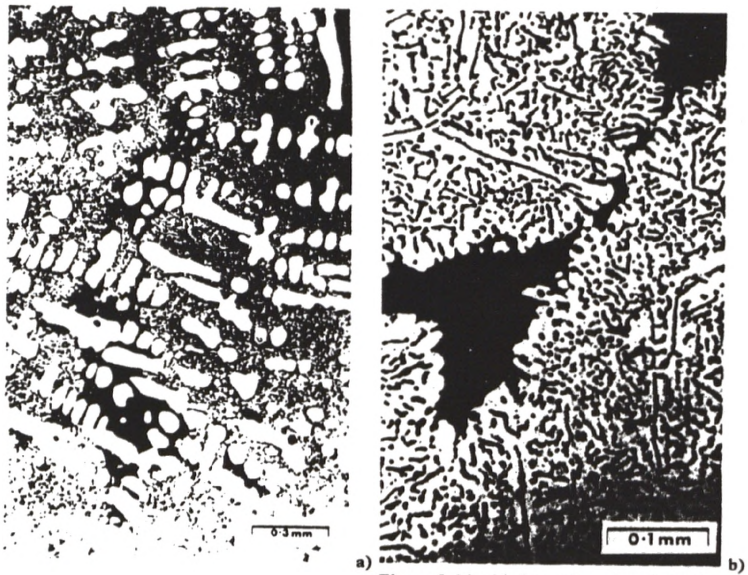

Figure 5: Liquid channels and pockets of porosity in alloys cooled at 4°C min $^{-1}$.
a) hypoeutectic alloy
b) eutectic alloy

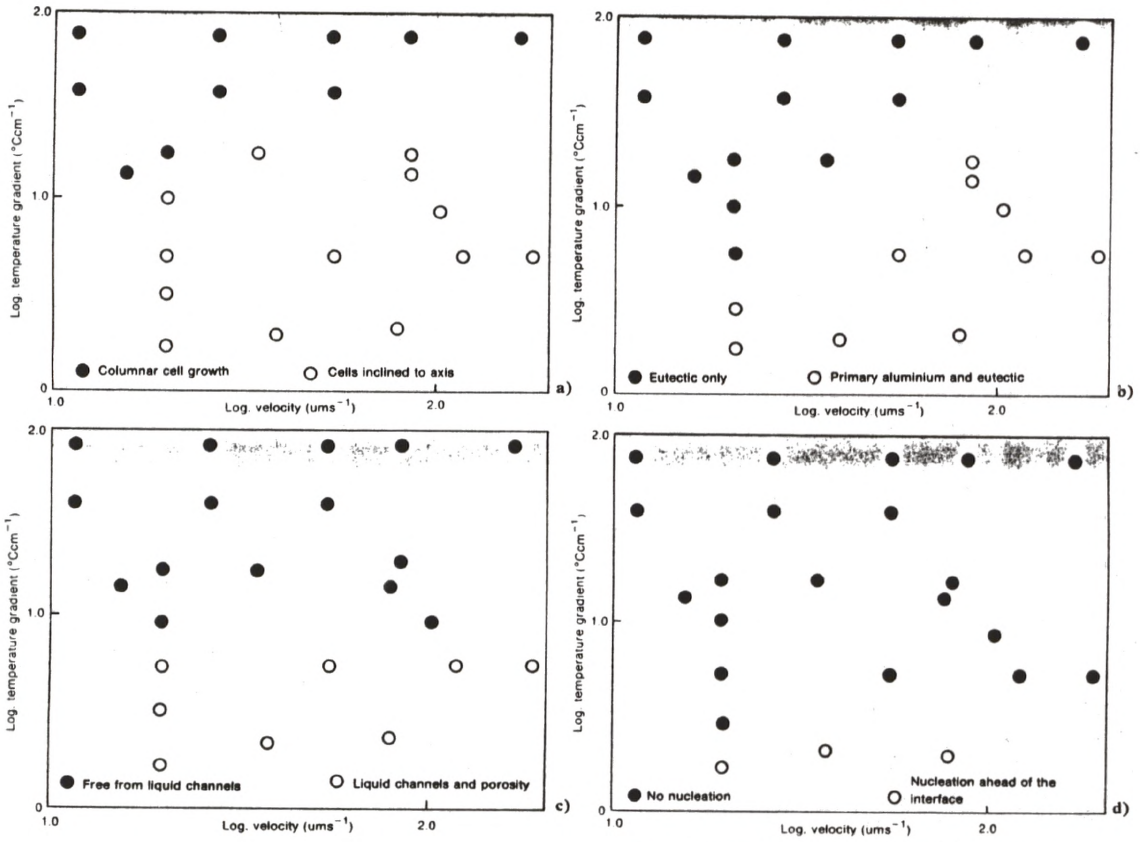

Figure 6: The structural features of strontium modified eutectic alloys as a function of growth velocity and temperature gradient in the liquid.
a) columnar cell growth with boundaries aligned in the growth direction
b) occurrence of primary aluminium dendrites
c) occurrence of liquid channels and porosity
d) nucleation of eutectic grains ahead of the interface.

Figure 6 shows that at high G/v ratios the interface is near isothermal and regular as depicted in figure 1b. As G/v decreases, the interface becomes cellular. Initially, the cell boundaries are shallow and are easily fed so there is no microshrinkage associated with them. However, as G/v decreases further, the cell boundaries deepen and become inclined to the growth axis. Primary dendrites of aluminium form. These changes result in an increased difficulty in feeding and microshrinkage porosity formation. Eventually, at very low G/v ratios, eutectic grains nucleate ahead of the interface and microshrinkage voids can form in areas where these grains meet. Some of these microstructural features are shown in figure 7.

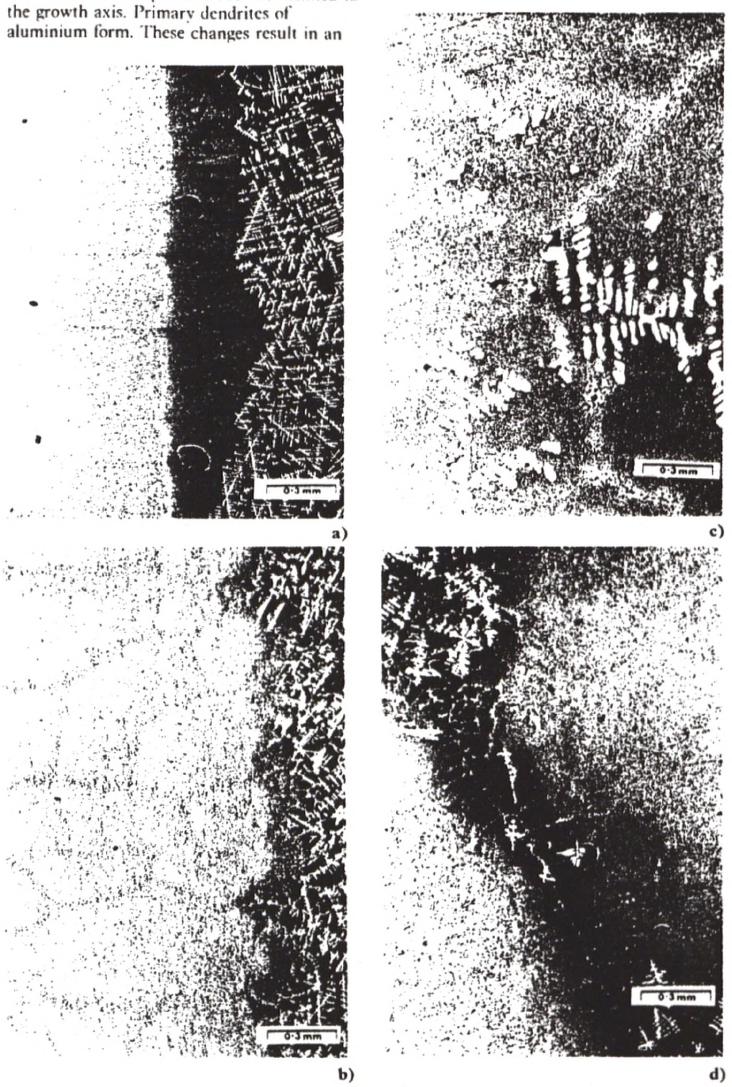

Figure 7:
Microstructural features observed in directionally solidified strontium modified eutectic alloys as the G/v ratio and the temperature gradient in the liquid decreases.
a) near isothermal regular interface with very shallow cell boundaries, v=54 μm s^{-1}; G=75°C cm^{-1}
b) more irregular interface with deeper cell boundaries, v=105 μm s^{-1}; G=8.5°C cm^{-1}
c) primary phase, misaligned cells and porosity, v=20 μm s^{-1}; G=5°C cm^{-1}
d) a eutectic grain nucleated ahead of the interface butting against the interface, v=20 μm s^{-1}; G=1.8°C cm^{-1}.

CONCLUSIONS

The present observations have shown that the regular interface assumed by Argo and Gruzleski for modified aluminium silicon eutectic alloys and depicted in figure 1b may become unstable under solidification conditions corresponding to a low G/v ratio. Deep liquid channels have been observed under these conditions for strontium and sodium modified alloys and to have porosity associated with them. These structural features develop under different solidification conditions for sodium and strontium. The observations offer a possible explanation for the increased rejection rates experienced by some foundries when strontium has been substituted for sodium. Liquid channels have been observed in rejected castings in studies conducted by the London & Scandinavian Metallurgical Co Limited and the Manchester Materials Centre. Figure 6 shows that the temperature gradient in the liquid plays a significant part in the development of these undesirable structural features and success has been achieved in preventing their formation by ensuring that the temperature gradient in the liquid remains high during solidification. This has been achieved with suitable adjustments to running gating and feeding systems.

REFERENCES

1. Q.T. Fang, and D.A. Granger, "Porosity Formation in Modified and Unmodified A 356 Alloy Castings," **Trans. A.F.S.** 97(1989), 989-1000.

2. D. Argo, and J.E. Gruzleski, "Porosity Formation in Modified Aluminium Alloy Castings," **Trans. A.F.S.** 96(1988), 65-74.

3. J.E. Gruzleski, "Modification and the Porosity Problem," (Paper presented at the 2nd International Conference on Molten Aluminium Processing, A.F.S., Orlando, November, 1989), 1.

4. J.R. Denton, and J. A. Spittle, "Solidification and Susceptibility to Hydrogen Absorption of Al-Si Alloys containing Strontium," **Materials Science and Technology**, 1(1985), 305-311.

5. M. D. Hanna, S. Lu, and A. Hellawell, "Modification in Aluminium-Silicon System," **Met. Trans.** A, 15A(1984), 459-469.

Microstructure and mechanical properties of directionally solidified Al–Si eutectic alloys with and without antimony

A. Ourdjini, F. Yilmaz, Q. S. Hamed, and R. Elliott

Hardness H, interflake spacing λ, and tensile properties are reported for Al–12·7Si and Al–12·7Si–0·2Sb (all wt-%) eutectic alloys directionally solidified at growth velocities of up to 250 μm s^{-1} and under temperature gradients in the liquid of up to 12·9 K mm^{-1}. The hardness is related to interflake spacing by the equation $H = H_0 + K\lambda^{-0.5}$, where H_0 is the initial hardness of the alloy. This behaviour contradicts previous results, which suggest that a Hall–Petch relationship is followed. The tensile properties are shown to follow similar behaviour, confirming that hardness shows the same dependence as proof stress on interflake spacing. However, the nature of the relationship depends on the Si morphology and caution should be exercised in using hardness or interflake spacing to indicate proof stress. MST/1585

© *1992 The Institute of Materials. Manuscript received 18 November 1991; in final form 21 January 1992. At the time the work was carried out the authors were in the Manchester Materials Science Centre, University of Manchester/UMIST. Dr Yilmaz is now in the Department of Metallurgy, Technical University of Istanbul, Sakarya Campus, Adapazari, Turkey.*

Introduction

The mechanical properties of *in situ* composites have often been discussed (e.g. Ref. 1). Telli and Kisakurek[2] have presented hardness measurements, tensile properties, and structural features of directionally solidified Al–Si eutectic alloys with and without Sb. They reported that hardness and tensile properties, i.e. ultimate tensile strength (UTS) and 0·2% proof stress, show similar dependences on growth velocity and Si phase interflake spacing. In particular, they concluded that the relationships between interflake spacing, growth velocity, temperature gradient, and concentration of Sb are such that a single relationship exists between the mechanical properties and interflake spacing, for example, as shown between the 0·2% proof stress and interflake spacing in Fig. 1. This relationship is of the Hall–Petch type and it was suggested that it can be used to describe the mechanical properties in the presence and absence of Sb and independently of the Sb concentration and temperature gradient in the liquid. This implies that Sb increases the mechanical properties of the eutectic only by structural refinement. If the relationship in Fig. 1 and the corresponding relationships between UTS and hardness and spacing are valid, they represent a very useful means (either by hardness or spacing measurements) of assessing the mechanical properties of Al–Si or Sb refined Al–Si flake eutectic alloys without knowledge of the solidification conditions. Two of the present authors have recently presented hardness measurements for Al–Si eutectic alloys and have questioned the existence of a Hall–Petch relationship.[3] A more detailed study including the effect of additions of Sb is presented here and used to assess more fully the ideas suggested by Telli and Kisakurek.[2]

Experimental procedure

Alloys of eutectic composition (12·7 wt-%Si) were prepared using metals of 99·999% purity. Weighed amounts of Al and Si were melted under argon and after melt homogenisation for 15 min were sucked into alumina tubes 200 mm in length and of 7 mm o.d. The melt remaining was quenched and used for Si analysis. All alloys were remelted in a vertical Bridgman directional solidification apparatus and after allowing 20 min for melt stabilisation were solidified by withdrawing the specimen into a water cooled, water reservoir at a constant traction velocity in the range 10–300 μm s^{-1}. Fine thermocouples embedded in the specimen were used to measure the growth velocity and temperature gradient in the liquid: the latter was varied from 3·2 to 12·9 K mm^{-1}. These measurements established that the growth velocity and traction velocity were the same after 60 mm of growth. Longitudinal and transverse sections were cut from the specimens after 60 mm of growth and prepared for optical microscopy. A linear intercept method was used to measure the average eutectic interflake spacing. Hardness measurements were made on transverse sections using a Vickers Pyramid Hardness machine and an applied load of 1 kg. This experimental procedure was repeated for Al–12·7Si–0·2Sb (wt-%) alloys. Finally, larger specimens were grown in a thermal valve furnace to allow machining of specimens for tensile tests.

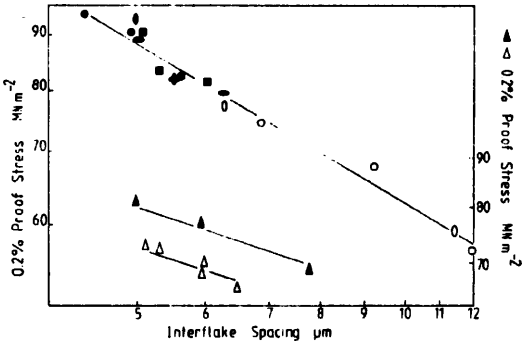

Symbol	Sb, wt-%	G, K mm^{-1}
Ref. 2		
	0	4·0
●	0·1	4·0
■	0·2	4·0
⬬	0·5	4·0
○	0	1·0
◖	0·1	1·0
Present work		
Δ	0	1·5
▲	0·2	1·5

1 Variation of the 0·2% proof stress with interflake spacing for Al–Si eutectic alloys with and without Sb (*G* is temperature gradient)

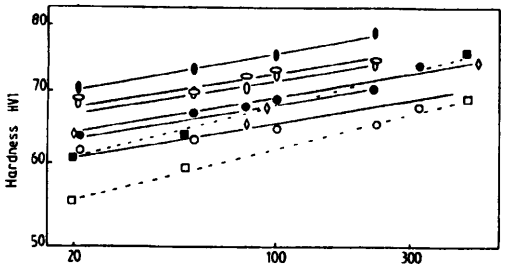

Symbol	Sb, wt-%	G, K mm⁻¹
Ref. 2		
□	0	4·0
■	0·2	4·0
Ref. 3		
◇	0	12·5
Present work		
○	0	3·2
●	0·2	3·2
⊘	0	8·2
◐	0·2	8·2
⊖	0	12·9

2 Variation of hardness (HV1) with growth velocity for Al–Si eutectic alloys with and without Sb

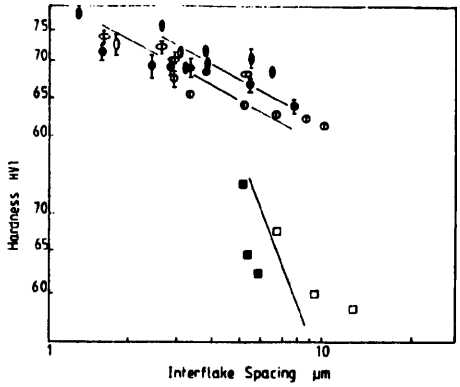

Symbol	Sb, wt-%	G, K mm⁻¹
Ref. 2		
□	0	4·0
■	0·2	4·0
Present work		
○	0	3·2
●	0·2	3·2
⊘	0	8·2
◐	0·2	8·2
⊖	0	12·9

3 Variation of hardness (HV1) with interflake spacing for Al–Si eutectic alloys with and without Sb

Experimental results and discussion

Hardness measurements H made on Al–12·7Si and Al–12·7Si–0·2Sb alloys directionally solidified at different temperature gradients G in the liquid and at various growth velocities v are shown in Fig. 2, which also includes the relationship between hardness and growth velocity from previous studies.[2,3] The present results, in common with those of Telli and Kisakurek,[2] show that the hardness increases with increasing growth velocity, and the hardness of alloys containing Sb is greater for the same solidification conditions. The present results for Al–12·7Si alloys solidified at a constant temperature gradient can be described by an equation of the form

$$H = H_0 + Kv^n \quad \ldots\ldots\ldots\ldots\ldots\ldots \quad (1)$$

where H_0 is the initial hardness of the alloy and $n = 0{\cdot}04$. A similar result was found by Yilmaz and Elliott.[3] It can be seen in Fig. 2 that a slightly higher value of n (0·08) describes the measurements made by Telli and Kisakurek.[2] The present measurements for Al–12·7Si–0·2Sb alloys can be described by equation (1) with a slightly higher value of H_0. The present measurements also show that the hardness of both Al–12·7Si and Al–12·7Si–0·2Sb alloys depends on the temperature gradient in the liquid for a constant growth velocity. As the temperature gradient increases, the hardness increases for both alloys.

The dependence of interflake spacing λ on growth velocity and temperature gradient is required to examine whether or not the changes in hardness can be attributed totally to variations in the scale of the microstructure. Telli and Kisakurek consider that the relationship between interflake spacing and growth velocity is described by an equation of the form

$$\lambda = K_1 v^{-m} \quad \ldots\ldots\ldots\ldots\ldots\ldots \quad (2)$$

with $m = 0{\cdot}19$ for the Al Si eutectic alloys. Kisakurek[4] shows that the addition of Sb produces a stronger effect in refining the eutectic phase at lower growth velocities and with increasing Sb concentration. He suggested that the interflake spacing–growth velocity relationship can be described by equation (2) with $m = 0{\cdot}06$ and 0·12 for alloys containing 0·1 and 0·2%Sb, respectively. He also suggested that the interflake spacing for both Sb containing and Sb free alloys shows negligible dependence on the temperature gradient in the liquid. Using equations (1) and (2), Telli and Kisakurek show that the hardness is related to the interflake spacing for Sb containing and Sb free alloys by the equation

$$H = H_0 + K_2 \lambda^{-0{\cdot}5} \quad \ldots\ldots\ldots\ldots\ldots\ldots \quad (3)$$

This relationship is shown in Fig. 3.

The relationship between 0·2% proof stress and interflake spacing obtained by Telli and Kisakurek is shown in Fig. 1. All their measurements can be fitted to a relationship of the form

$$\sigma_{0{\cdot}2} = \sigma_0 + K_3 \lambda^{-0{\cdot}5} \quad \ldots\ldots\ldots\ldots\ldots\ldots \quad (4)$$

where σ_0 is the initial flow stress of the alloy.

Equations (3) and (4) show that hardness displays a similar dependence on interflake spacing as the 0·2% proof stress and that the relationship is of the Hall–Petch type, implying a dislocation pile-up mechanism of strengthening.

Measurements of interflake spacing in the Al Si eutectic have been reported on several occasions in the literature.[5–7] All the values have been described in terms of equation (2) with values of m varying from 0·33 to 0·50. The various microstructural models of the eutectic reaction also predict a value of m in this range. Interflake spacing measurements made in the present study on Al–12·7Si alloys are shown in Fig. 4 as a function of growth velocity. The relationship follows equation (2) with a value of $m = 0{\cdot}42$. It can also be seen that contrary to Telli and Kisakurek, but in agreement with previous studies,[5–7] there is a strong temperature gradient dependence of the interflake spacing. The refinement of the flakes by the addition of Sb is also indicated. The relationship for Sb containing eutectics at constant temperature gradient can be described by equation (2) with $m = 0{\cdot}42$. As for the Sb free alloys, there is evidently a temperature gradient dependence of the interflake spacing. There is also evidence that the refinement of the spacing is greater at the lower temperature gradient. These studies confirm that Sb refines rather than modifies the eutectic structure. Energy dispersive X-ray analysis on longitudinal sections of specimens quenched during direc-

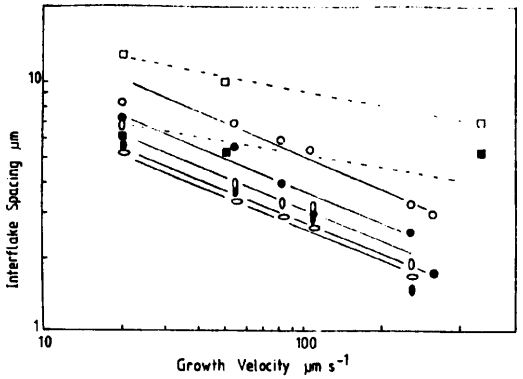

Symbol	Sb, wt-%	G, K mm⁻¹
Ref. 2		
□ - - -	0	4·0
■ - - -	0·2	4·0
Present work		
○	0	3·2
●	0·2	3·2
0	0	8·2
0	0·2	8·2
○	0	12·9

4 Variation of interflake spacing with growth velocity for Al–Si eutectic alloys with and without Sb

tional solidification have shown[8] that an Sb rich boundary layer forms in the liquid at the interface during solidification. This is consistent with the Sb refinement arising from interfacial undercooling promoted by constitutional undercooling. This is consistent with the increased refinement observed at the lower temperature gradient in the present study, but not with the Kisakurek[4] observation of greater refinement at lower growth velocities.

The present interflake spacing measurements show a dependence on growth velocity and temperature gradient that is in good agreement with previous measurements,[5–7] but contradicts the dependence shown by Telli and Kisakurek. This different interflake spacing growth velocity relationship leads to the hardness interflake spacing dependence shown in Fig. 3, which is of the form

$$H = H_0 + K_4 \lambda^{-0.2} \quad \ldots\ldots\ldots\ldots \quad (5)$$

Two parallel relationships are drawn in Fig. 3 distinguishing between the closed symbols corresponding to Sb containing alloys and the open symbols describing Sb free alloys. The slightly increased hardness of the alloys refined with Sb is attributed to a slight solid solution hardening of the Al phase. This relationship is not of the Hall–Petch type.

The present results of the tensile tests are shown in Fig. 1. These results can be described by an equation of the form

$$\sigma_{0.2} = \sigma_0 + K_5 \lambda^{-0.2} \quad \ldots\ldots\ldots\ldots \quad (6)$$

with a slightly higher proof stress for alloys containing Sb. These measurements do not follow a Hall–Petch relationship.

From equations (5) and (6), the factor for converting hardness to proof stress (in units of kg mm^{-2}) is 0·11 compared with a value of 0·13 suggested by Justi and Bragg.[9] The present tensile tests do not reveal as great an improvement in mechanical properties by Sb refinement as suggested by Telli and Kisakurek.[2] In this context, it is shown elsewhere[10] that a significant contribution to the strengthening of a similar alloy LM 25 by Sb additions can be attributed to the refinement of the secondary dendrite arm spacing.

Conclusions

The present study has shown that a relationship exists between hardness and 0·2% proof stress and interflake spacing. It is of the same form, but slightly different, for Sb containing and Sb free Al–Si eutectic alloys. It is not of a Hall–Petch type. Although a definite relationship exists between the proof stress and Si interparticle spacing, previous studies have shown that it is of a different form for different Si morphologies. Consequently, it is not a universal relationship and should only be used when the alloy displays a single Si morphology.

Acknowledgments

The authors would like to thank Professor F. R. Sale for providing research facilities. One of the authors (AO) would like to thank the British Council and the Algerian Government for financial support. Another of the authors (RE) would like to thank Alcoa for sponsoring research on the solidification of Al alloys.

References

1. R. ELLIOTT: 'Eutectic solidification processing'; 1983, London, Butterworths.
2. A. I. TELLI and S. E. KISAKUREK: *Mater. Sci. Technol.*, 1988, **4**, 153–156.
3. F. YILMAZ and R. ELLIOTT: *J. Mater. Sci.*, 1989, **24**, 2065.
4. S. E. KISAKUREK: 'Solidification processing', 48; 1987, London, The Institute of Metals.
5. B. TOLOUI and A. HELLAWELL: *Acta. Metall.*, 1976, **24**, 565.
6. R. ELLIOTT: in Proc. 2nd Int. Conf. on 'Aluminum melt treatment', paper 10; 1989, Des Plaines, IL, American Foundrymen's Society.
7. S. KHAN, A. OURDJINI, and R. ELLIOTT: *Mater. Sci. Technol.*, 1992, **8**, (4), 516–522.
8. S. KHAN: PhD thesis, University of Manchester, 1990.
9. S. JUSTI and H. BRAGG: *Metall. Trans.*, 1978, **9A**, 515.
10. Q. S. HAMED and R. ELLIOTT: submitted to *Cast Met. J.*